Measurements of Prompt Gamma Rays Emitted in Fission of ^{23} U and ^{23} Pu Induced by Fast Neutrons from the LICORNE Neutron Source

Liqiang Qi

NNT : 2018SACLS320

Measurements of Prompt Gamma Rays Emitted in Fission of ^{238}U and ^{239}Pu Induced by Fast Neutrons from the LICORNE Neutron Source

Thèse de doctorat de l'Université Paris-Saclay
préparée à l'Université Paris-Sud

École doctorale n°576 PHENIICS
Particules, Hadrons, Énergie, Noyau,
Instrumentation, Imagerie, Cosmos et Simulation
Spécialité de doctorat : Structure et réactions nucléaires

Thèse présentée et soutenue à Orsay, le 3 Octobre 2018, par

Liqiang QI

Composition du Jury :

Pr Tiina Suomijarvi Professeur, Université Paris-Sud, IPN	Présidente
Pr Stephan Pomp Professeur, Université Uppsala, département de physique et d'astronomie	Rapporteur
Dr Xavier Ledoux Ingénieur de recherche, GANIL	Rapporteur
Dr Fanny Farget Directrice de Recherche, CNRS	Examinateur
Dr Jonathan Wilson Directeur de recherche, Université Paris-Sud, IPN	Directeur de thèse
Dr Matthieu Lebois Maître de conférences, Université Paris-Sud, IPN	Co-Directeur de thèse

Acknowledgments

The completion of the thesis is attributed to many people's support.

First of all, I would like to thank my jury members: Prof. Stephan POMP, Dr. Xavier LEDOUX, Prof. Tiina SUOMIJARVI, and Dr. Fanny FARGET, for their insightful comments and precious suggestions. I would like to thank especially Prof. Stephan POMP and Dr. Xavier LEDOUX for being my reporters and reviewing my manuscript.

I would like to express my deep gratitude to my thesis director Dr. Jonathan WILSON for the continuous support and encouragement. Without him, the thesis is difficult to be completed. I also want to thank him for giving me the opportunities to attend various conferences, workshops and other scientific activities, which broadens my research horizons from various perspectives.

I would also like to express my great appreciation to my thesis co-director Dr. Matthieu LEBOIS for his guidance and help in the experiments and data analysis, as well as his advice and comments on this manuscript. It is appreciated that he shared with me all his knowledge and experiences in nuclear physics.

I am thankful for the assistance given by all the collaborators. My special thanks are given to Stephan OBERSTEDT and Andreas OBERSTEDT for their enormous contributions to the experiments. I enjoy working and discussing with them. I appreciate the fruitful discussions with Christelle SCHMITT especially on the fission model calculations. I also want to thank the PARIS Collaboration. My thanks are extended to other collaborators including Angelique GATERA, Alf GÖÖK, Deepika CHOUDHURY, Benoit LAURENT, Barbara WASILEWSKA and Michal CIEMALA.

I am grateful to all the NESTER group members, especially the secretary Celine GAUBERT-ROSIER for her help in the missions and other administrative work. I thank Iolanda MATEA for the help with PARIS phoswich detectors. I thank Guillaume MAVILLA for the help in TANDEM. I thank Louis OLIVIER, Claire PORTAIL, Mathieu BABO, Nikola JOVANCEVIC for sharing the same office, and nice discussions from time to time. I would also like to thank other PhD students including Anne MEYER, Ian MURRAY, Liss VAZQUEZ-RODRIGUEZ, Clément DELAfOSSE and Anastasia GEORGIADOU.

I want to thank my classmates and friends from Master Nuclear Energy. I would like

to thank my parents for their love and encouragement during my study. Finally, I would like to express my special thanks to my wife, Luting MA, for always being by my side and supporting me in the last few years in France.

Contents

Introduction

Fission was discovered in December 1938 by Otto Hahn and Fritz Strassmann [1]. They found that the heavy nuclides Uranium broke and split into two lighter nuclides when bombarding neutrons on them. Two months later, it was explained theoretically by Lise Meitner and Otto Robert Frisch [2] by using the liquid drop model. Based on Albert Einstein's mass-energy equation $E=mc^2$, the fission process releases a large amount of energy. Besides the immediate and massive energy release, another characteristic of the fission process is the emission of neutrons, *i.e.* every two or three neutrons emitted per fission. These features make a self-sustaining chain reaction possible. Very soon after the discovery of the fission process, scientists started experiments and tried to make use of it in the nuclear applications. In 1940, Enrico Fermi built the first nuclear reactor. Since then, the nuclear power industry has grown rapidly worldwide. It has become one important component of the world's electricity production nowadays.

A nucleus about to fission will undergo shape evolution. Eventually, the nucleus ruptures at the a critical point, and two fission fragments are generated in a excited, rotational state. The two fission fragments are accelerated under the repulsive Coulomb forces and emitted in opposite direction. The excitation energy and spin of the fission fragments will be released by emitting prompt neutrons and prompt γ-rays, until the ground states are reached. Since fission fragments are generally neutron-rich nuclides, they will undergo radioactive decay process β^- until the valley of stability.

Prompt fission γ-ray spectrum (PFGS) and its spectral characteristics, namely γ-ray multiplicity, total γ-ray energy release and average photon energy, are crucial nuclear data for reactor physics. Prompt fission γ-rays (PFG) have a wide range of energy, from few tens of keV to few tens of MeV. They can escape the reactor core and deposit energy in the instrumentation and shielding materials. Gamma heating of these materials is dominant over neutron heating [3], which needs to be predicted with reasonable accuracy to avoid possible fracture and failure. But in some recent reactor experiments, γ heating was shown to be underestimated by up to 28% [4]. In addition, the development of Generation IV reactors, aiming for improved safety, demand the measurement of more precise PFGS and spectral characteristics.

On the other hand, more precise PFGS information is also useful from a fundamental

physics point of view. Nowadays, several competitive calculation codes are trying to reproduce all the properties of the fission fragments and the emitted particles (neutron and γ-ray) for a wide range of fissioning systems. These codes include GEF [5–7], FREYA [8–13], CGMF [14–17], FIFRELIN [18–20], etc. Many assumptions and models are made in these codes, which still remain controversial. PFGS contains a large amount of information about the fission process and neutron rich nuclides (*i.e.* fission fragments). It can lead to a better understanding of the excitation energy sorting mechanism between the nascent fission fragments [5, 18, 21], angular momentum generation mechanism of nascent fission fragments at scission [7, 13, 16, 18] and neutron/γ competition during de-excitation process of the fission fragments [22–24].

In recent years, a series of measurements have been performed to obtain more precise values of the spectral characteristics in the thermal-neutron induced fission [25–27] and spontaneous fission [28, 29]. Very little PFG information exists for fast-neutron induced fission. The development of LICORNE neutron source [30–32], by producing intense, kinematically forward focused fast neutrons, makes the study of fast-neutron induced fission more accessible. In this work, we aimed to measure and study the PFGS of fast-neutron induced fission of ^{238}U and ^{239}Pu. ^{238}U and ^{239}Pu are important nuclides in a reactor core. These results also provide information of PFGS characteristics for fast-neutron induced fission in general.

In this thesis, the mechanism of the fission process is described in Chapter 1. The description of the LICORNE setup is presented in Chapter 2. The experimental setup and corresponding data analysis of PFGS measurements are explained in Chapter 3 and Chapter 4, respectively. In Chapter 5, we discuss the obtained PFGS and spectral characteristics from this work and compare the results with those from GEF and FREYA calculations.

Chapter 1
Mechanism of the nuclear fission process

Since the discovery of the fission process in 1938, the theoretical interpretation as well as the measurements have helped enormously the understanding of this complex problem. However, even though it has been nearly 80 year since the discovery of fission, the fission theory is more interpolative than predictive. There is a lack of overall theory to predict the fission observables, *e.g.* the isotopic yields of fission fragments for different fissioning systems, especially in the regions where nuclear data are scarce. That is because nuclear fission is a time-dependent many-body problem with no analytical solution in terms of the current computational ability. The many-body interaction is complicated, especially at large deformations. It is usually fitted by the experimental data and many types of correlations are neglected to simplify the problem. In addition, it is also an open system, *i.e.* the fragments can emit particles and radiation. As a consequence, all these reasons make the exact theoretical calculation of the fission process extremely difficulty.

At first, nuclear fission can be viewed as a shape evolution, see Figure 1.1. The fission process can be separated in two steps: firstly the fissioning system undergoes deformation until the "scission point" (point where the nucleus breaks apart and two nascent fission fragments are generated). This step is described using collective model to reproduce the collective behaviour of the nucleons. The second step, after "scission point", is the de-excitation process of the fission fragments. Several statistical models are dedicated to generate large numbers of fission events, containing all the information of the energy and momentum of the fission fragments as well as emitted particles (prompt neutrons and prompt γ-rays), in a reasonable short time.

The first section will present a macroscopic-microscopic model [33]. It combines liquid drop description of the nucleus (macroscopic) and the information extracted from the shell structure and pairing effect (microscopic). This is a relatively easier calculation approach compared to a purely microscopic model. It provides a powerful and quantitative theoretical tool for studies of low-energy fission dynamics, where the influence of nuclear structure is strong. The second section will focus on several important ingredients in the post-scission phase including the excitation energy sorting and angular momentum gener-

ation mechanism, prompt neutron and prompt γ-rays emission. Several competing fission models, dedicated for the description of post-scission systems, will be also presented, including GEF, FREYA, CGMF and FIFRELIN. In this work, if not specified, only binary fission is discussed.

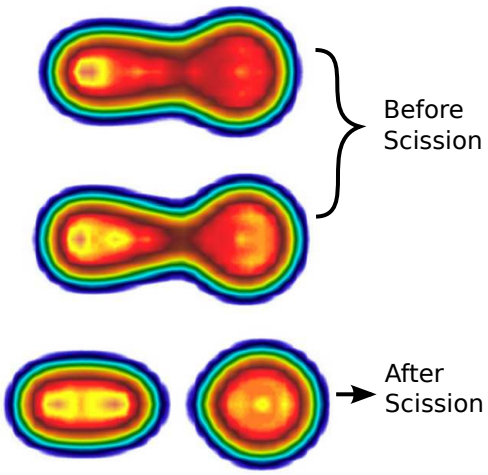

Figure 1.1 – Schematic view of the shape evolution of the compound nucleus ^{240}Pu in the binary fission process [34]. The three main steps of the fission (from top to bottom): pre-scission, "scission point" and post-scission are represented.

1.1 Description of the pre-scission step in the fission mechanism

Fission is a large amplitude collective motion, which can be viewed as an evolution of the nuclear shape, from a spherical or close-spherical shape to two separated nuclei. A nucleus about to fission will stretch until it reaches a critical deformation, *aka* the "saddle point". Beyond the "saddle point", repulsive Coulomb forces become dominant over surface tension. Then, the nucleus forms a dumb-bell configuration with two fission fragments joined by a thin neck. Eventually, the neck ruptures at the "scission point".

The evolution of the nuclear shape is driven by a few collective variables $\mathbf{q}\equiv(q_1,...,q_N)$, which are often some deformation parameters characterizing the nuclear shape. A series of shapes has to be fixed firstly based on parameterizations with finite collective variables, *i.e.* determine the degree of freedom for the calculation. Based on different nuclear shapes as specified by $\mathbf{q}$, the energy of the nuclear system, namely the potential energy U(Z,N,$\mathbf{q}$), is then calculated. In the macroscopic-microscopic model, the potential energy is represented as a sum of a smooth term, E_{macro}(Z,N,$\mathbf{q}$), and a fluctuating correction term, E_{s+p}(Z,N,$\mathbf{q}$). The smooth term (macroscopic energy) is based on the liquid drop model, which successfully describes the smooth trend of the binding energy as a function

of mass number A and atomic number Z. The fluctuation term (microscopic energy) reflects the shell and pairing effects due to the irregularities in the single-particle energy levels. Once the potential energy as a function of the nuclear shape has been established, the time evolution of the nuclear shape $\mathbf{q}(t)$ is then calculated by using the Langevin equation. One fission event is generated when the shape propagates from ground state until "scission point".

1.1.1 Nuclear shape parameterization

Different parametrization methods can be used to describe the nuclear shape along the fission path that one can expect, *e.g.* spheric harmonic functions expansion in spherical coordinate system [35] and three-quadratic-surface parametrization in cylindrical coordinate system [36].

Naturally, an expansion in multipoles over the Legendre polynomials can be used to describe $R(\mu)$, the distance from the nuclear center to the surface, for axially symmetric shapes in the vicinity of a sphere (up to the fourth terms):

$$R(\mu) = \lambda R_0(1 + \sum_{n=2}^{\infty} a_n P_n(\mu)) \tag{1.1}$$

where μ=cosθ and θ is the polar angle, λ is the normalization parameter to ensure the constant volume. Coefficients a_2 represents the quadrupole moment, a_3 the mass asymmetry, and a_4 the neck thickness - *cf.* Figure 1.2. This shape parametrization works for a slightly deformed nucleus, but fails when close to the scission configuration, *i.e.* many terms are required for the description of the shape.

Instead, three-quadratic-surface parametrization is capable of representing the nuclear shape from originally sphere through the saddle and scission shapes, to the fragments at infinity. Even though the results from this parametrization are not satisfactory for small deformations compared to expansion in spherical harmonics, it is not problematic in the description of the large deformation motion as it is the case of fission. J.R. Nix [36] describes the nuclear (axially symmetric) shape by three smoothly joined portions of quadratic surfaces, *e.g.* two spheroids connected by a hyperboloidal neck. The form in a cylindrical coordinate system is:

$$\rho = \begin{cases} a_1^2 - (a_1^2/c_1^2)(z - l_1)^2 & l_1 - c_1 \leqslant z \leqslant z_1 \\ a_2^2 - (a_2^2/c_2^2)(z - l_2)^2 & z_2 \leqslant z \leqslant l_2 + c_2 \\ a_3^2 - (a_3^2/c_3^2)(z - l_3)^2 & z_1 \leqslant z \leqslant z_2 \end{cases} \tag{1.2}$$

Where, the left-hand surface is denoted by the subscript 1, the right-hand one by 2 and the middle one by 3 and z_1 and z_2 are the values of z at the intersections of the middle surface

with left-hand and right-hand surfaces, respectively, see Figure 1.2. These parameters are dependent to make sure that different parts are joined smoothly and the nuclear volume must remain constant during the shape change. Consequently, J.R. Nix introduced six dimensionless parameters in description. These parameters are detailed in Ref. [36].

To summarize, a proper shape parametrization has to be determined firstly depending on the calculation situations, *e.g.* Legendre polynomials expansion for the deformation energy calculation of the fragments at scission (small-deformation approximation) and three-quadratic-surface parametrization for the description of fission (large amplitude collective motion).

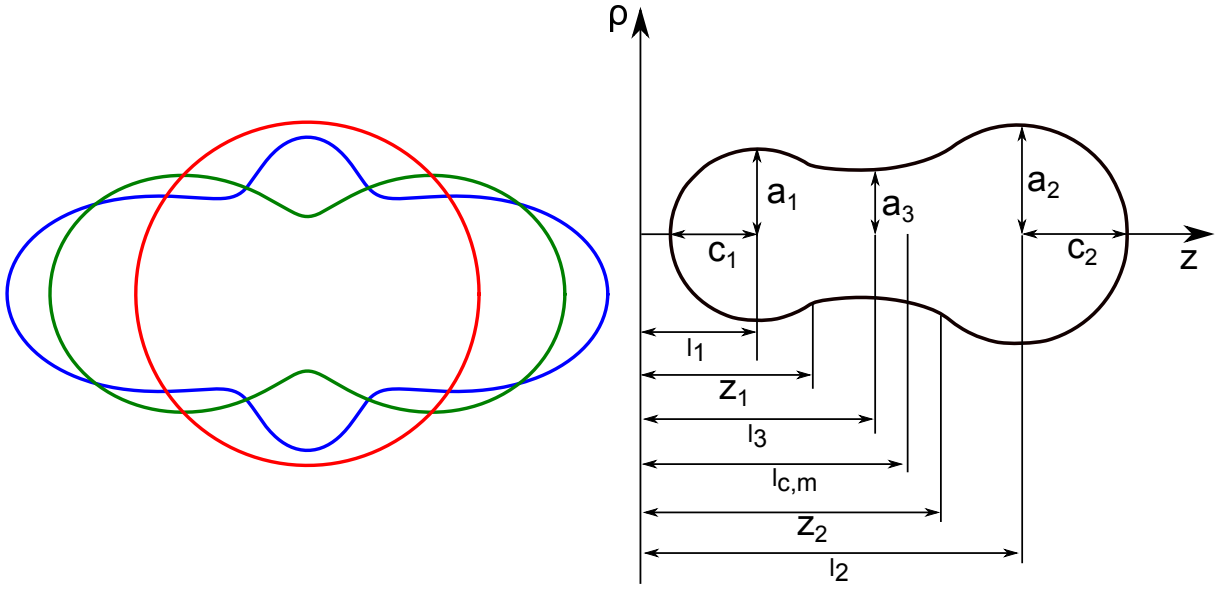

Figure 1.2 – (a) Contour plots of spheres with different kinds of deformation: no (red), quadrupolar (green) and octupolar (blue) deformation, with an expansion over the Legendre polynomials $R(\mu)=\lambda\ R_0(1+a_2P_2(\mu)+a_4P_4(\mu))$. (b) The three-quadratic-surface parameterization in representing the nuclear shape for the tabulation of macroscopic-microscopic potential energy surface (PES) [36].

1.1.2 The macroscopic energy: liquid drop model energy

The liquid drop model (LDM) was proposed by G. Gamow [37] in 1930. According to the model, the behaviour of the nucleus is analogue to a drop of liquid, where neutrons and protons are hold together by the nuclear forces (made of the residual strong force and Coulomb repulsion). Given enough excitation energy, the spherical nucleus may undergo deformations and then may split into two smaller drops. The experimental observations, that nucleus is filled with incompressible substance and there are short range nuclear forces amongst the nucleons which are saturated, are compatible with this picture of the nucleus as a liquid drop. In other words, it was a successful model, especially in the

explanations of the nuclear binding energies. For example, the Weizsäecker Formula (or the semi-empirical mass formula) [38], proposed by Carl Friedrich von Weizsäcker in 1935 based on the liquid drop model, successfully describes the smooth trend of the binding energy as a function of mass number A and atomic number Z:

$$m(Z,N) = Zm_p + Nm_n - \frac{E_b}{c^2} \tag{1.3}$$

$$E_b(MeV) = a_V A - a_S A^{2/3} - a_C \frac{Z^2}{A^{1/3}} - a_A \frac{(A-2Z)^2}{A^{1/3}} \pm a_\delta A^{-3/4} \tag{1.4}$$

Where, $a_V A$ is the volume term corresponding to the attractive strong forces in a limited range. $-a_S A^{2/3}$ is the surface term as a correction to the volume term due to an overestimation of the attractive strong forces in the surface (the surface tension effect). $-a_C \frac{Z^2}{A^{1/3}}$ is the Coulomb term caused by the Coulomb repulsion between protons. $-a_A \frac{(A-2Z)^2}{A^{1/3}}$ is the asymmetry term due to the fact that neutrons provide attractive forces in the compensation of Coulomb repulsion between protons. $\pm a_\delta A^{-3/4}$ is the pairing term since nuclei with an even number of protons and an even number of neutrons are more stable.

The surface term and the Coulomb term are the most important ingredients because they are in competition as the nucleus is deformed from originally sphere. For example, at the quadrupole deformation a_2 of a liquid drop, according to Bohr and Wheeler in 1939 [35], it depicts that the surface energies $E_S(a_2)$ and Coulomb energies $E_C(a_2)$ are changed to:

$$E_S(a_2) = E_S(0)(1 + \frac{2}{5}a_2^2) \tag{1.5}$$

$$E_C(a_2) = E_C(0)(1 - \frac{1}{5}a_2^2) \tag{1.6}$$

where $E_S(0)$ and $E_C(0)$ are the surface and Coulomb energies of the original spherical nucleus, respectively. The Coulomb energy is decreased due to the decrease of the average distance between protons in deformation, while the surface energy is increased since the increase of the surface in deformation. It indicates that there will be a macroscopic fission barrier as long as $2E_S(0) > E_C(0)$, *i.e.* $E_{def} = U(a_2) - U(0) > 0$, which is the case for the atomic number up to 126, because the nucleus tends to have the lowest potential energy in favour of stability (see Figure 1.3).

The LDM has been improved since the end of 1970s and then the finite-range liquid drop model based on the Yukawa-plus-exponential potential was developed [40]. It had being employed in the modern calculations with the form of:

$$\begin{aligned} F(A,Z,\mathbf{q},T,L) = {} & -a_v(1-k_vI^2)A + a_s(1-k_sI^2)B_n(\mathbf{q})A^{2/3} + c_0A^0 \\ & + a_c\frac{Z^2}{A^{1/3}}B_c(\mathbf{q}) - a_c\frac{5}{4}\Big(\frac{3}{2\pi}\Big)^{2/3}\frac{Z^{4/3}}{A^{1/3}} + \frac{\hbar^2L(L+1)}{2J(\mathbf{q})} \end{aligned} \tag{1.7}$$

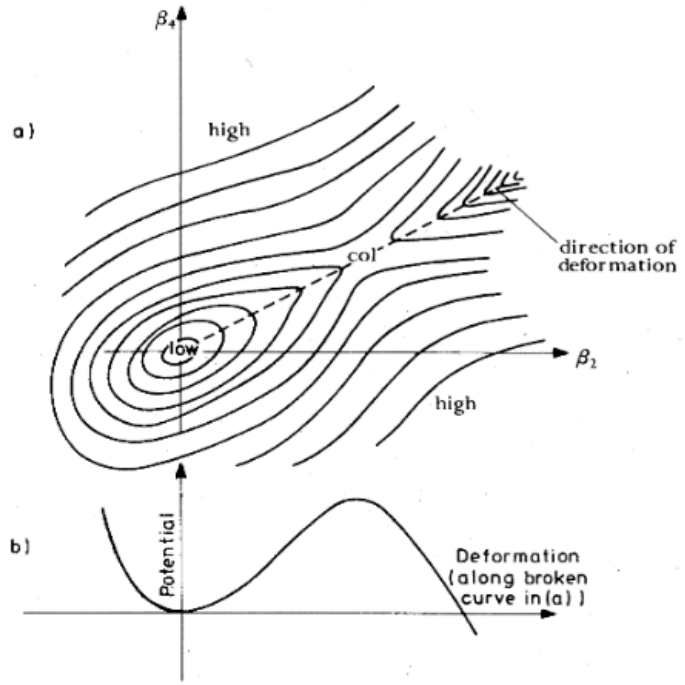

Figure 1.3 – (a) Schematic two-dimensional diagram of potential energy surface of a fissionable nucleus. (b) The potential energy along the minimum energy trajectory for increasing elongation [39]. A fission barrier is observed along the trajectory.

where a_v, a_s and a_c are the usual volume, surface and Coulomb energy parameters and k_v and k_s are the corresponding volume and surface asymmetry parameters. The deformation dependence is taken into account through the shape functions $B_n(\mathbf{q})$, $B_c(\mathbf{q})$ and $J(\mathbf{q})$ (see Ref. [40] for the details). The last term represents the rotational energy with the shape-dependent rigid-body moment of inertia.

1.1.3 The microscopic energy: shell-plus-pair energy

The liquid drop picture of the nucleus was very successful but could not explain all the phenomena, *e.g.* the existence of shape isomers, *i.e.* long-lived states characterized by a large quadrupole moment [41]. Nevertheless, The macroscopic-microscopic approach incorporates information about the shell effects and pairing effects (microscopic) into the liquid drop description of the nucleus (macroscopic).

The description of nuclear structure, presented by M.G. Mayer in 1948 [42], suggested that the nucleons inside a nucleus occupy single-particle orbitals. The distribution of single-particle orbitals is not uniform and there exists gaps in the distribution, *e.g.* the doubly closed shell nuclei ^{132}Sn. The single-particle level schemes also depend on the nuclear shape, see Figure 1.4. The irregularities in the single-particle energy levels accounts for the fluctuation part of the total binding energy. The pairing effect plays a central role

in nuclear physics, in particular for identical particles, it makes up large fractions of the correlations among particles. It is responsible for the explanation of many nuclear properties, *e.g.* binding energy in this case. In the shell model, two protons (or two neutrons) with the same quantum numbers except spin projection (up and down respectively) to respect the Pauli exclusion principle, will have completely overlapping wave-functions and thus greater interaction between them. It makes an even number of protons and/or of neutrons nuclei more stable than odd-odd nuclei.

The shell-plus-pairing energy are obtained by solving the one-body Schrödinger equation:

$$\Big(-\frac{\hbar^2}{2m}\nabla^2 + V(\mathbf{q})\Big)\Psi_n(\mathbf{r}) = \epsilon_n \Psi_n(\mathbf{r}) \tag{1.8}$$

where V($\mathbf{q}$) is the effective single-particle potential depending on the nuclear shape, including the mean-field, the spin-orbit and the Coulomb (for protons) potential. Collective variables $\mathbf{q}$ define the shape of the potential, which in turn changes the single particle energy distribution.

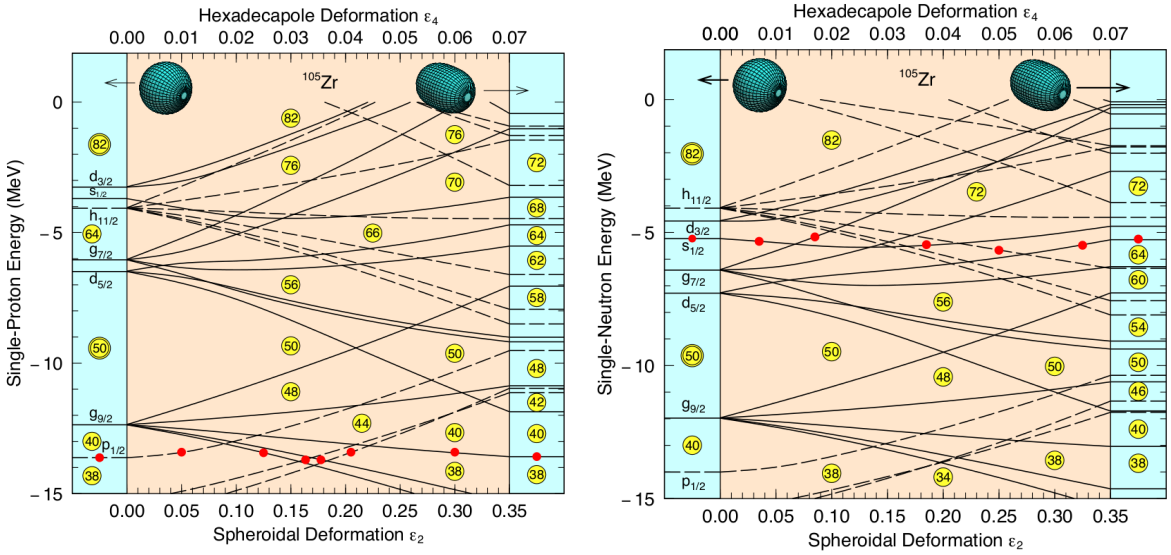

Figure 1.4 – The single-particle energies plotted as a function of the deformations for proton (left) and neutron (right), respectively (corresponding to ^{105}Zr) [43]. The red dots represent the Fermi levels for ^{105}Zr. The well-known "magic numbers" corresponding to particularly large gaps are noted at zero deformation. When the nuclear shape becomes deformed, the spherical shell gaps disappear and new "magic numbers" show up.

1.1.4 Fission dynamics

According to the last two subsections, the macroscopic and microscopic energy are introduced, respectively. Then, the potential energy of a nuclear system can be represented as a sum of a smooth term, E_{macro}(Z,N,$\mathbf{q}$), and a fluctuating correction term, E_{s+p}(Z,N,$\mathbf{q}$), at different shapes characterized by finite collective variables $\mathbf{q}$:

$$U(Z,N,\mathbf{q}) = E_{macro}(Z,N,\mathbf{q}) + E_{s+p}(Z,N,\mathbf{q}) \tag{1.9}$$

The calculated potential energy U(Z,N,$\mathbf{q}$) constitutes the potential energy surface (PES), *i.e.* the energy changes with the deformation of the fissioning nucleus, see Figure 1.5. The local gradient of the potential energy $\mathbf{F}(\mathbf{q}) = -\partial U(\mathbf{q})/\partial\mathbf{q}$ gives a driving force in the calculation of the dynamical evolution of the nuclear shape, which is in favour of the lowest energy of the system. Starting from some initial conditions (shape $\mathbf{q}_0$ and momentum $\mathbf{p}_0$), *e.g.* around the ground-state minimum, the time evolution $\mathbf{q}$(t) can be calculated with the Langevin equation [44]:

$$\frac{dq_i}{dt} = (m^{-1})_{ij}p_j \tag{1.10}$$

$$\frac{dp_i}{dt} = -\frac{\partial U}{\partial q_i} - \frac{1}{2}\frac{\partial}{\partial q_i}(m^{-1})_{jk}p_j p_k - \gamma_{ij}(m^{-1})_{jk}p_k + g_{ij}R_j(t) \tag{1.11}$$

where q_i is the collective variable, p_i is the momentum conjugate to q_i, m_{ij} is the mass tensor and i, j corresponds to the collective coordinates in corresponding shape parametrization. The first term in the right-hand side of the second equation corresponds to the potential energy gradients, the second term the kinetic energy, the third term the friction tensor and the forth term a random force in nuclear shape motion. The friction tensor represents the energy exchange between the collective degrees of freedom and the intrinsic degrees of freedom (dissipation). The presence of the random force (last term of Equation 1.11) allows to simulate quantum tunneling effects.

Different trajectories of the shape motion can occur in the PES. One path may end up with fission, *i.e.* the neck ruptures at the "scission point" and two fission fragments are produced. With sufficient sampling of the fission events, the quantities of the primary fragments can be extracted, including the isotopes distribution, excitation energy sharing between two fragments and spin-parity distribution. These information are the initial conditions for the de-excitation process of the fission fragments, as well as can be used as the validation of the theoretic calculations when compared to the experimental results.

The macroscopic-microscopic method is relatively computationally cheap compared to a purely microscopic method and serves as the major theoretical tool for the fission calculation since the last century. Nevertheless, the energy exchange between collective degree of freedom and intrinsic degree of freedom is not clear, especially when close to the

"scission point". Sharp nuclear surfaces are incompatible with the experimental evidence, *i.e.* scission occurs before one expects. In the last two decades, with the increase of the computational power, the microscopic methods are becoming more and more competing compared to the macroscopic-microscopic method, *e.g.* the time-dependent density functional theory (TDFT). It can help understand more about the fission process in the future.

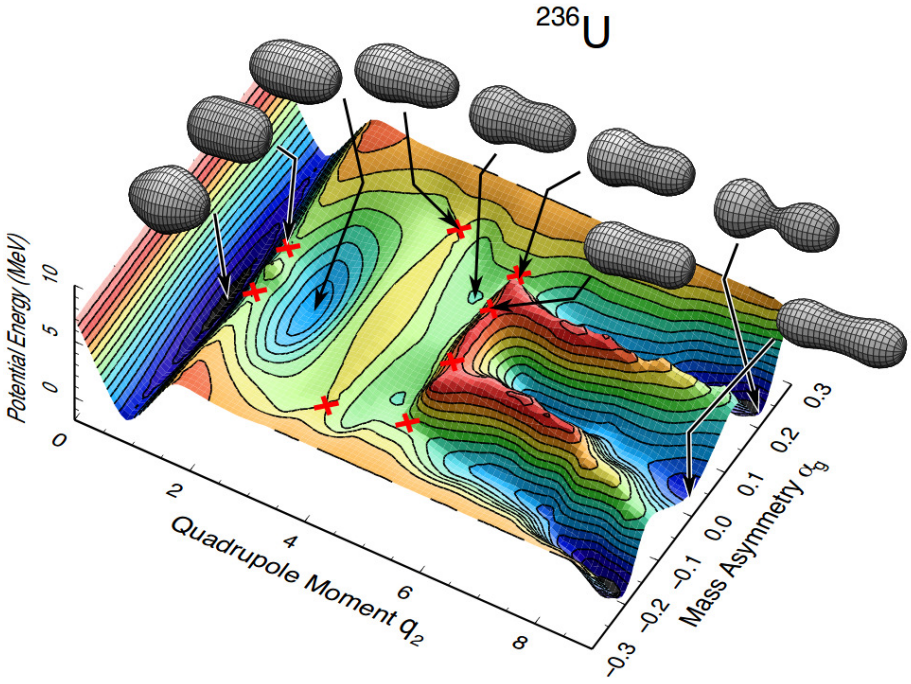

Figure 1.5 – The 5D potential energy surface calculated from macroscopic-microscopic method is projected into quadrupole moment q_2 and mass asymmetry α_g to present some major features of fission in actinides region, taken from [45]. It explains the existence of the shape isomers (around $q_2 = 2$) in terms of a double-humped fission barrier which turns out for most actinide nuclei, and the mass asymmetry of the fission fragments due to shell effects, which can not be explained by LDM.

1.2 Description of the post-scission step in the fission mechanism

A nucleus about to fission will undergo shape change from "saddle point" to "scission point". Eventually, the neck ruptures at the "scission point", and two fission fragments (called primary fission fragments at the "scission point") are produced in an excited and rotated state. This process takes $\sim 10^{-21}$ s according to the fission dynamic calculations. Under the effect of the repulsive Coulomb forces and total momentum conservation, the

two primary fragments are accelerated and emitted in opposite direction. The characteristic time of the acceleration phase is $\sim 10^{-20}$ s based on kinematics calculation under Coulomb repulsion. Since primary fragments are often excited and rotating, these energy and spin will be released by emitting prompt neutrons and prompt γ-rays. Fission fragments after prompt neutron emission are called secondary fission fragments and after prompt γ-ray emission are called primary fission products. According to Heisenberg's uncertainty relation, the decay time τ for evaporated neutrons and γ-rays can be estimated to be 10^{-18} s-10^{-14} s and 10^{-14} s respectively, with the formula:

$$\tau_{n\ or\ \gamma} = \frac{\hbar}{\Gamma_{n\ or\ \gamma}} \tag{1.12}$$

where Γ_n is the neutron or gamma width of the states of the fission fragments. Finally the primary fission products undergo radioactive decay process β^-, because they are usually neutron rich nuclei far from the valley of stability. The radioactivity decay process are accompanied by emission of γ-rays, neutrons and anti-neutrinos $\bar{\nu}_e$, which are called delayed particles since the time scale is several orders of magnitude larger. See a schematic view of the fission process in a characteristic time scale in Figure 1.6.

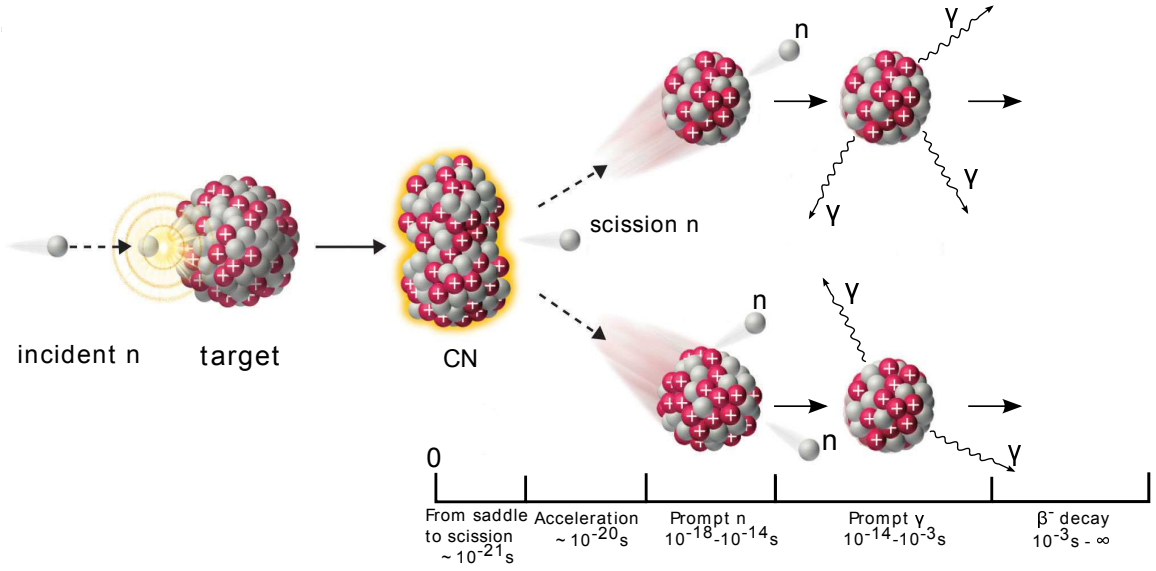

Figure 1.6 – Schematic view of the fission process in a characteristic time scale. Modified according to the original figure from [46].

The total energy released, given by the reaction Q-value, in neutron-induced fission can be calculated according to the mass differences, with the formula (in case of binary fission):

$$Q = m_{CN}c^2 - m_{light}c^2 - m_{heavy}c^2 \tag{1.13}$$

$$E_n + B_n + Q = TKE + TXE \tag{1.14}$$

where the masses m_{CN}, m_{light} and m_{heavy} are corresponding to the rest mass of the compound nucleus and nascent primary fission fragments, E_n is the kinetic energy of the incident neutron and B_n is the neutron binding energy $B_n=m_nc^2+m_{target}c^2-m_{CN}c^2$. According to the energy conservation law, the available energy will be shared between the total kinetic energy (TKE) and total excitation energy (TXE) of the fission fragments. TXE comprises the energy stored in each fragment from both collective and intrinsic degrees of freedom [47]. The energy associated with intrinsic degrees of freedom corresponding to the excitation of nucleons is denoted as intrinsic excitation energy $E^{*,SC}$. The part of the energy corresponding to collective degrees of freedom includes deformation energy $E^{def,SC}$ and rotational energy $E^{rot,SC}$. After the full acceleration of the fission fragments, the deformation energy $E^{def,SC}$ is transformed into intrinsic excitation energy $E^{*,SC}$. Thus only intrinsic and rotational energy are left, as the initial condition for the later-on de-excitation process. This section will detail the discussions of intrinsic excitation energy sorting and angular momentum generation mechanism at "scission point", as well as prompt neutron and prompt γ-rays emission of the fully accelerated fission fragments.

1.2.1 Models for the post-scission description

Instead of reproducing the dynamic evolution of the nuclear shape, various models were designed to generate large numbers of fission events, including all the information on the energy and momentum of the fission fragments as well as emitted particles (prompt neutrons and prompt γ-rays), in a reasonably short time (few seconds for 10^5 events), which can be incorporated into other transport code, *e.g.* MCNP and GEANT4. These models include GEF [5–7], FREYA [8–13], CGMF [14–17,48] and FIFRELIN [18–20]. The average values of fragment mass A, charge Z, TXE, TKE, average neutron multiplicity $\langle\nu\rangle$, neutron energy in the laboratory frame $\langle E_n^{lab}\rangle$, average photon multiplicity $\langle\nu_\gamma\rangle$ and photon energy in the laboratory frame $\langle E_n^{lab}\rangle$ are tabulated for the FREYA and GEF codes in terms of the light and heavy fragments individually as well as the weighted average of the two, see Table 1.1. These two codes will be discussed mainly in this work.

GEF, developed by K.H. Schmidt, is an open source available on [49]. It includes a model of the PES of the compound nucleus (before fission), which is used to obtain the fragment yields in mass and charge. It also includes some physical models, *e.g.* excitation-energy-sorting mechanism and statistical model for angular momentum generation, to determine the initial properties of the fission fragments at scission. The fragments are then de-excited by neutron emission and subsequent photon emission. The neutron emission is described by evaporation models, including neutron-γ competition. The γ-rays emission is calculated in a fully analytical formalism, in terms of the electric dipole E1 and electric quadrupole E2 transitions. The electric dipole transitions are calculated according to a black-body spectrum with a giant dipole resonance (GDR) form factor. The electric

quadrupole transitions are calculated according to the moment of inertia and the spin of the fragments.

In contrast, FREYA (available on [50]) requires fission fragment yields and the total kinetic energy of the fragments as inputs, in order to extract the initial intrinsic and rotational excitation energy of the two fragments. The fragments are then de-excited by neutron emission and subsequent photon emission. The neutron emission is described by evaporation models and it stops when no more neutron emission is energetically possible (no neutron-gamma competition included). Then photons emission is calculated first statistically with a black-body spectrum by a giant dipole resonance form factor and then follows the experimental data form RIPL-3 [51] in low-energy region. It combines the analytical formalism and experimental nuclear structure information.

In addition, CGMF and FIFRELIN builds the full level scheme with energies, spin and parity from RIPL-3 data base or calculations if not available experimentally and then apply complete Monte Carlo Hauser-Feshbach method to simulate the prompt neutron and prompt γ-rays decay cascade to the discrete states and finally to the ground state.

Table 1.1 – Summary of the average quantities calculated for the light and heavy fragments individually as well as the weighted average of the two, in case of spontaneous fission ^{252}Cf, from the two competing codes FREYA and GEF. The lower energy limit for photon properties is 100 keV.

FREYA	All Fragments	Light Fragments	Heavy Fragments
A	126.00	108.47	143.53
Z	49.00	42.18	55.82
TXE or XE(MeV)	33.32	19.59	13.74
TKE or KE(MeV)	184.30	104.82	79.48
$\langle\nu\rangle$	3.74	2.17	1.57
$\langle E_n^{lab}\rangle$ (MeV)	2.29	2.63	1.81
$\langle\nu_\gamma\rangle$	8.31	4.35	3.95
$\langle E_\gamma^{lab}\rangle$ (MeV)	0.85	0.84	0.87

GEF	All Fragments	Light Fragments	Heavy Fragments
A	126.00	108.14	143.86
Z	49.00	42.65	55.35
TXE or XE(MeV)	37.89	18.31	19.57
TKE or KE(MeV)	186.49	106.28	80.21
$\langle\nu\rangle$	4.37	1.97	2.40
$\langle E_n^{lab}\rangle$ (MeV)	2.20	2.51	1.96
$\langle\nu_\gamma\rangle$	7.17	2.86	4.31
$\langle E_\gamma^{lab}\rangle$ (MeV)	0.91	1.06	0.81

1.2.2 Excitation energy distribution and angular momentum generation in the primary fission fragments

One of the open questions about the fission process is how the TXE is partitioned between the two fission fragments. It effects the prompt neutron multiplicities distribution as a function of the primary fragment mass, see Figure 1.7, which gives the well-known "saw-tooth" like behaviour. The energy sorting mechanism still remains controversial for the model calculations. Several methods have been proposed in the past few years.

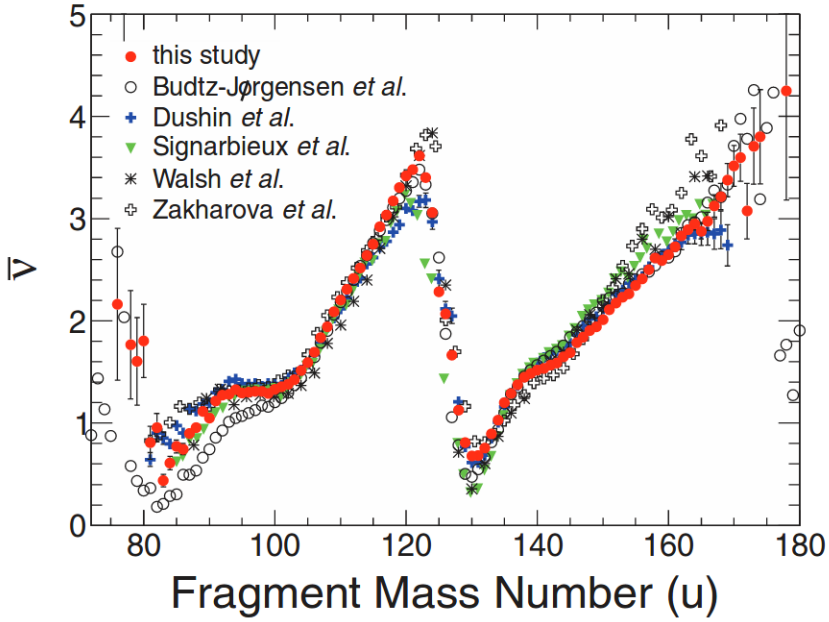

Figure 1.7 – Average prompt neutrons multiplicities distribution as a function of the primary fragment mass from spontaneous fission ^{252}Cf [52]. The minimum close to A=130 is due to the shell closures N=82, Z=50 that leads to spherical fission fragments. And thus the fission fragments have less excitation energy available for the neutron evaporation.

The model calculations, FREYA [8] and Los Alamos model [21], assume that the light and heavy fragment have the same residual nuclear temperature and the partition of the intrinsic excitation energy $E^{*,SC}$ at scission is proportional to the heat capacity $\partial E_i^{*,SC}/\partial T_i = 2a_iT_i$, based on the well know relations $E^* = aT^2$, where a_i is the Fermi gas level density parameter, T is the nuclear temperature. GEF also assumes independent fission fragments and thermal equilibration between the fragments at scission [5]. But it applies the constant-temperature level density function instead of Fermi gas level density function, and the intrinsic excitation energy at scission is shared between the two fragments according to the probability distribution of the available micro-states, which is given by the total nuclear level density.

Other model calculations, CGMF [48] and FIFRELIN [18], proposed that the mass-

dependent temperature ratio between the heavy and light fragments sets the excitation energy sharing. The temperature of the two fragments is not necessarily equal for all the masses. For example, in low-energy fission with the asymmetric fission yields, the temperature of heavy fragments is generally lower than the temperature of the light fragment due to the shell effect, *e.g.* doubly magic heavy fragment with A_H=132 (lower temperature) and complementary highly deformed light fragment (higher temperature) with A_L=120.

On the other hand, the energy sorting can be deduced from experimental measurements regardless any assumptions in the scission configuration, as is proposed by Ref. [53] with $\frac{E_L^*}{E_H^*} = \frac{\nu_L}{\nu_H}$. However, there is a lack of experimental measurements of neutron multiplicity distribution for different fissioning systems.

Another open question is the initial spin distribution of the fission fragments at scission, which can not be directly measured experimentally and by far can not be calculated precisely. The angular momentum generation mechanism still remains unclear, see Figure 1.8. Even though it is not sensitive for the prompt neutron observables, it is of great importance for the prompt γ-rays observables.

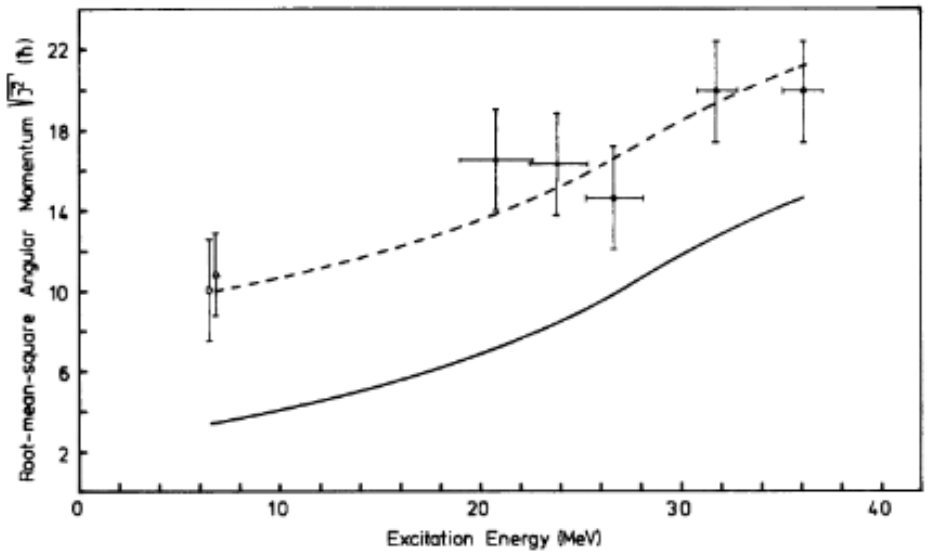

Figure 1.8 – The spin distribution (dashed line) of the fission fragment ^{148}Pm as a function of the excitation energy of the compound nucleus ^{236}U* [54]. The solid line represents the spin distribution for the compound nucleus. Extra spin ($\sim 7\hbar$) is generated during the fission process.

In the absence of detailed information, it is usually sampled from semi-empirical statistical model (in GEF, CGMF and FIFRELIN), with the form [7]:

$$N(J) = (2J+1)exp(-\frac{J(J+1)}{2b})^2 \tag{1.15}$$

where J is the angular momentum and b is the so-called spin cut-off parameter. The spin cut-off parameter defines the width of the distribution and is related to the root-mean-square angular momentum by $J_{rms} = b/\sqrt{2}$, which is a function of the effective moment of inertia and nuclear temperature of the compound nucleus. Other similar distributions can be found in Ref. [16,18] with the spin cut off parameter either specified or taken from the RIPL-3 data library.

On the other hand, model calculation, FREYA [13], takes into account different modes of dinuclear rotation, *i.e.* wriggling and bending, in which the fragments rotate in same or in the opposite sense around the axis perpendicular to the dinuclear axis (fissioning axis). The spin corresponding to each mode also needs to be sampled from a statistical distribution, which introduces a free parameter "spin temperature" T_s to be adjustable.

1.2.3 Description of prompt neutron emission

Prompt neutrons may be emitted at different stages of the fission process. Different models and formalisms have to be applied depending on the production mechanism. There are five sources that contribute to the prompt neutron production: pre-fission neutrons, ternary fission neutrons (scission neutrons), post-scission neutrons from ternary fission fragments, evaporated neutrons during the acceleration of the fission fragments and from the fully accelerated fission fragments. The prompt neutrons are mainly referred to the ones from the fully accelerated fission fragments, while the others have negligible contributions.

Pre-fission neutrons are emitted prior to the fission in multi-chance fission. Above the second-chance fission threshold, *e.g.* $E_n \approx 6$ MeV in case of ^{238}U(n,f), the compound nucleus can decay by emission of a neutron then followed by fission (n,n'f). Below this second-chance fission threshold, the excitation energy of the residual nucleus left after neutron emission is too low to undergo fission. In fact, the pre-fission neutrons are not related to the fission process itself.

In most of time, fission is a binary process, *i.e.* only two primary fission fragments are formed. Once every few hundred fission events, more than two particles are formed. When there are three primary fission fragments, it is called a ternary fission event. About 90% of the ternary fission particles are α-particles and 7% tritons. The remaining particles can include a large variety of species, including neutron emitter, *e.g.* ^{5}He$\rightarrow$ ^{4}He+n ($T_{1/2}$=7.03$\times10^{-22}$s). Consequently, post-scission neutron from ternary fission fragments is a negligible component.

The neutron width of the states in fission fragments are usually around few tens of keV, corresponding to a characteristics time of $\sim10^{18}$ s. As a result, the characteristic decay time of the prompt neutron emission is larger than the period of the acceleration of the primary fission fragments ($\sim10^{20}$s) and thus the evaporated neutrons are mainly coming from the fully accelerated fission fragments instead of during the acceleration phase.

Unlike the four sources of prompt neutrons discussed above, the existence of ternary fission neutrons, also called scission neutrons, is still an open question. That's because the adiabatic assumption is not validated any more in the scission configuration, where the neck between the fragments ruptures and quickly absorbed by the fragments. Several models are dedicated to this kind of calculations [55] based on Halpern's Sudden Approximation. There is a lack of precise experimental data to validate the theoretical calculation, where the main difficulty is to differentiate between scission neutrons and evaporated neutrons experimentally. The angular distribution of the scission neutron is a key issue in the separation. Because the evaporated neutrons are emitted from the moving fission fragments, which are kinematically focused onto the fission axis when transformed form the center of mass frame to the lab frame. And theoretical calculation reveals that the scission neutrons are emitted mainly perpendicularly to the fission axis, which has an opposite effect. However, the evaporated neutrons are not uniformly emitted from the fragments in center of mass system due to the angular momentum effect [56, 57], which adds extra difficulties in the separation between evaporated neutrons and scission neutrons.

According to the discussion above, the evaporated neutron from the fully accelerated fission fragments is the main source for prompt fission neutron spectra (PFNS), and the scission neutrons is still controversy, which in turns can be a very good observable in understanding the dynamic process in the scission configuration. Eventually, PFNS are described by various models, including Maxwellian, Watt, Los Alamos model (extension Point-By-Point model) and statistical Hauser-Feshbash model (CGMF and FIFRELIN codes). For example, the earliest and simplest model is the single parameter Maxwellian-Boltzmann distribution, which is a good approach to evaporation spectrum of Weisskopf [58], with the form:

$$N(E) = \left(\frac{2}{\sqrt{\pi}}\right) \times \left(\frac{\sqrt{E}}{T^{2/3}}\right) e^{-\frac{E}{T}} \tag{1.16}$$

where T is the temperature parameter. It relies on the fit to the experimental data, *e.g.* in case of ^{252}Cf(sf), T=1.42 MeV, corresponding to an average energy $<E_n>=\frac{3}{2}T=2.13$ MeV. The transformation of the Maxwell spectrum into center of mass system yields a Watt spectrum. It is implemented in many model calculations due to its good description of the experimental data, see Figure 1.9. However it has been well known that it can not describe the experimental result above 6 MeV since it neglects the physical aspects of the fission process. Given the initial conditions of the primary fission fragments (excitation energy and spin), the kinetic energy of the emitted neutron can be sampled from one of the distributions mentioned above and the process stops when no more neutron emission is possible, namely excitation energy below the neutron separation energy S_n.

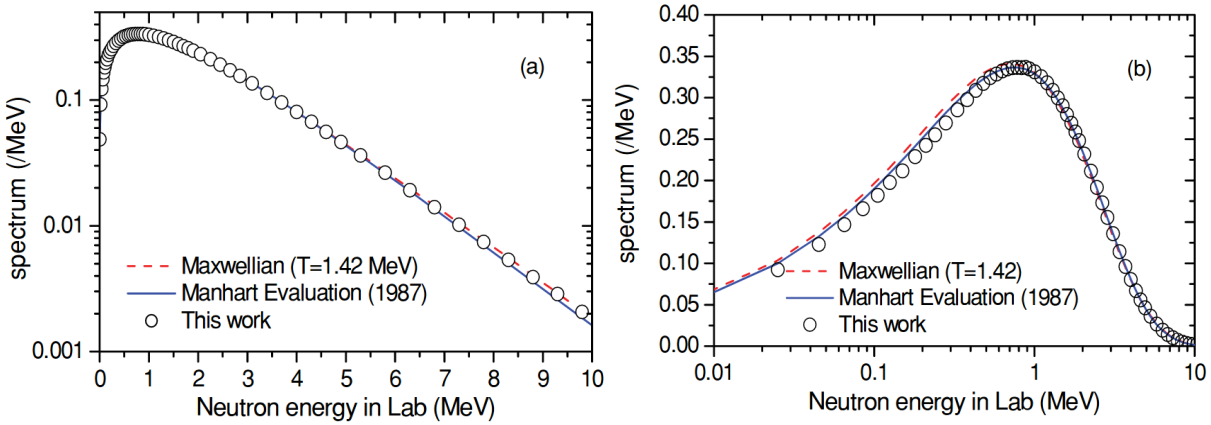

Figure 1.9 – Comparison of prompt neutron spectrum among the calculations from FIFRELIN, a Maxwellian and the Manhart evaluation in a linear (a) and a logarithmic (b) neutron energy scale [18].

1.2.4 Description of prompt γ-rays emission

When the excitation energy has fallen below the neutron separation energy after the prompt neutron emission, prompt γ-ray emission takes over. Prompt fission γ-rays are emitted in characteristic times 10^{-14}s to 10^{-3}s. At the early stage, γ-ray emission may compete with the last neutron emission, which still remains unclear [22–24]. About 95% of the prompt PFG are emitted within 3 ns after fission [59,60] and it is the main subject of study of this work. γ-rays emitted in times $>$ 50 ns up to 1 ms is called "late" γ-ray, which stem from the de-excitation of the shape isomers. The γ-rays emitted after 1 ms are called delayed γ-rays in order to be distinguished from prompt γ-rays and "late" γ-rays. The time evolution of relative yields of γ-ray energy and multiplicity has been experimentally measured, see Figure 1.10.

The early analysis of fission fragment de-excitation assumed that the neutron emission was taking place whenever energetically possible. The residual energy then evacuated by prompt γ-rays emission. However, the high yield of prompt γ-rays from the measurement suggests that there may exist a competition between neutron and γ emission, *e.g.* at times about 10^{-14}s, high-energy γ-rays of giant resonances may compete with the last neutron emission. Neutron emission is efficient in taking away excitation energy (typical neutron separation energy is $\sim$8 MeV) but not angular momentum. Then it is highly possible to leave the nucleus at low excitation energy but high spin. It gives γ-rays a better chance to compete neutron emission and to exhaust the remaining angular momentum, because the level densities at low energy but high spin are low and neutron evaporation to final states is delayed. Experiments have shown [22] that the total γ-ray energy is almost linear with the excitation energy and could be related to the average number of neutrons emitted by

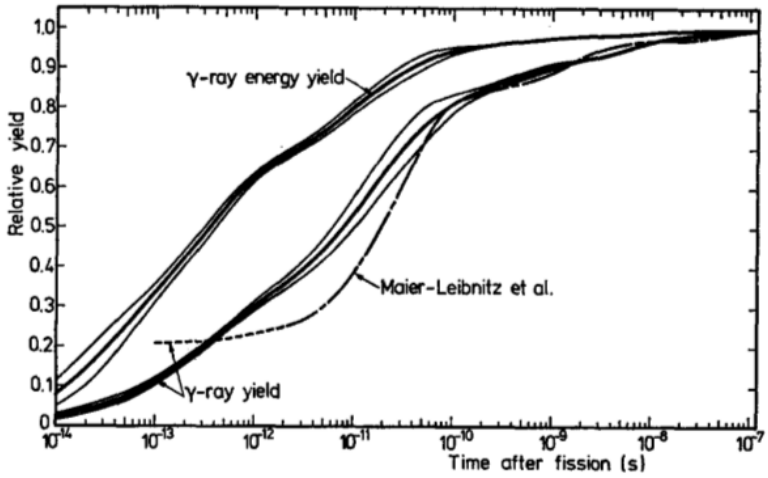

Figure 1.10 – The time evolution of relative yields (to the total production) of γ-ray energy and multiplicity since fission occurs [59]. The fact that the total photon energy increases faster with time than the multiplicity indicates that early γ-rays have higher energies.

the fragments. The relation is:

$$< E_\gamma >= 0.75 < \nu > +4MeV \tag{1.17}$$

where $< E_\gamma >$ is the average total γ-ray energy release per fission and $< \nu >$ the average prompt neutron multiplicity. It has been explained as the linear increase of the spins of the fragments as a function of the excitation energy, to be closely related to the deformation. Nevertheless, the branching ratio between the neutron and γ-ray emission at high excitation energy $P_n = \Gamma_n/(\Gamma_n + \Gamma_\gamma)$ for different fission fragments still remains unknown (where Γ_n, Γ_γ is the neutron width and gamma width), and more experimental information is clearly needed.

The angular distribution of prompt γ-rays emission is non-isotropic relative to the fissioning axis, see Figure 1.11. The anisotropy A (defined as [W(0deg)-W(90deg)]/W(90deg)) is negative when the γ-ray energy is lower than 200 keV, namely more γ-rays emitted at the directions perpendicular to the fissioning axis than along the fissioning axis. It changes to positive when the γ-ray energy is larger than 200 keV. The calculations [61] indicate that the statistical dipole and the quadrupole radiation components are about equally strong at high γ-ray energies, the dipole component predominant at low-energy region and the quadrupole component at intermediate energies. The quadrupole radiation can be assumed to be E2. The dipole radiation can be assumed to be M1 at low energies and E1 at high energies. In addition, components of stretched E2 cascades are seen in the energy ranges 0.15-0.24 MeV and 0.35-0.96 MeV. It leads to the basic picture of the de-excitation process of the fission fragments in the (E^*, J) plan, see Figure 1.12.

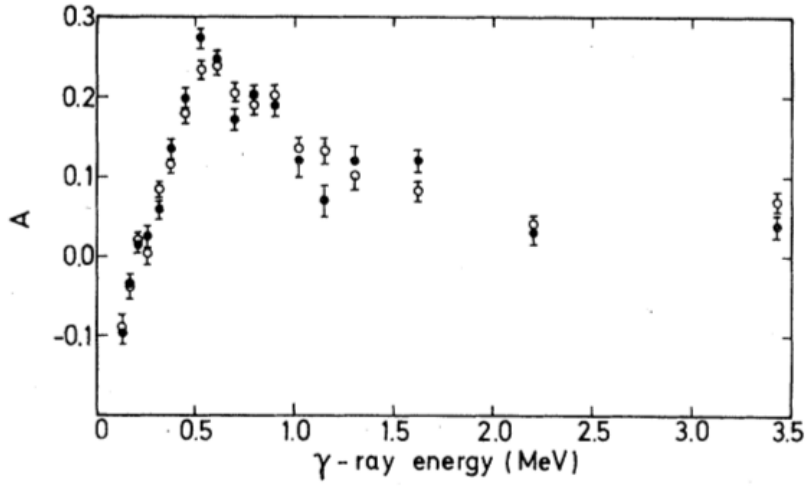

Figure 1.11 – The anisotropy versus γ-ray energy from the measurements with Pt (circles) and Ni (dots) backing [61].

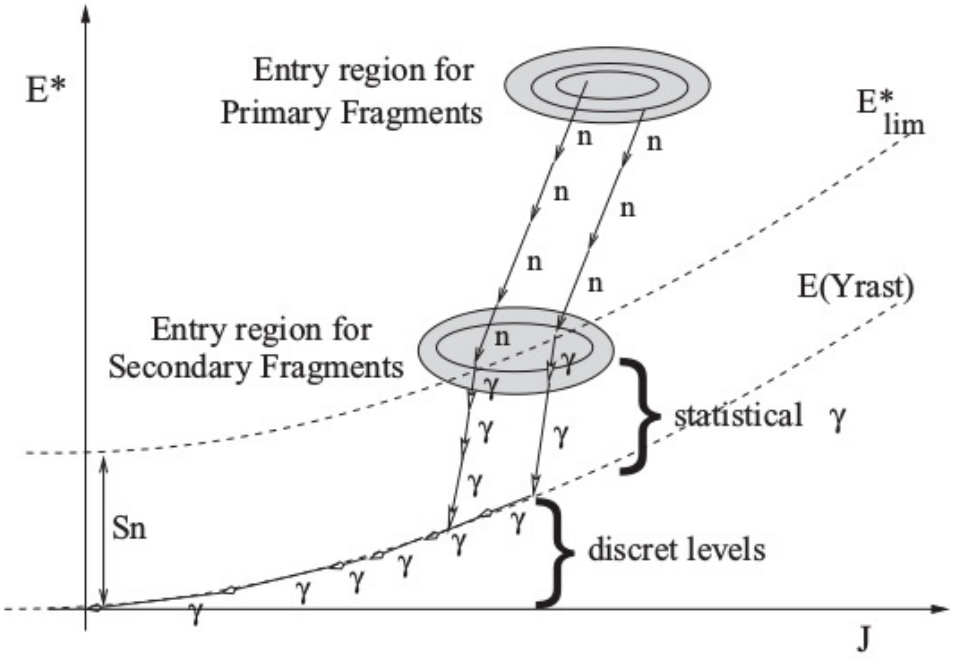

Figure 1.12 – Schematic view of the de-excitation process of the fission fragments in the (E*, J) plan [18]. The primary fission fragments firstly evacuate the excitation energy by neutron emission, and then followed by γ-rays emission including statistical γ-rays and discrete γ-rays.

The information of PFG is one of the least understood part of the fission process due to the experimental difficulties related to the wide ranges of γ-ray energies (few tens of keV to tens of MeV) and wide emission time range. Recent instrumental advancements

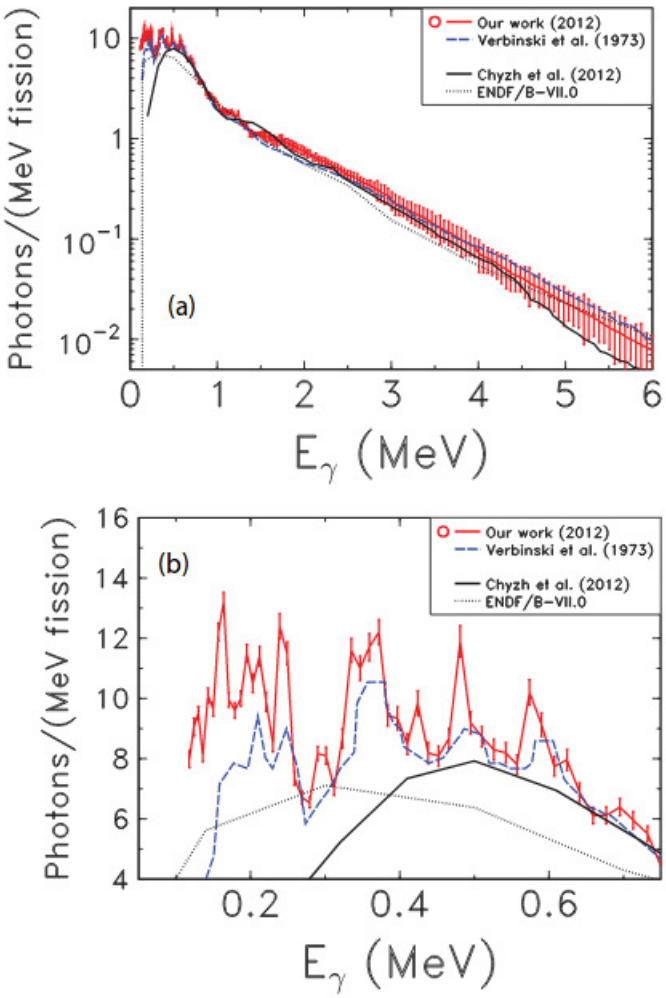

Figure 1.13 – The prompt fission γ-ray emission spectrum from the work [62] by using $LaBr_3$ scintillation detectors, in comparison with earlier measurements and evaluated data.

have made it possible to perform more precise measurements of PFGS from spontaneous, thermal- and fast-neutron induced fission of a large variety of actinide systems. Recently, several measurement programmes on PFG characteristics, namely the multiplicity, total energy released and average photon energy per fission, have been performed by JRC (Geel). For example, the γ emission from ^{252}Cf(sf) was studied and compared to the data taken 40 years earlier by using various types of γ-ray detectors [62]. More structures at low-energy region have been observed, see Figure 1.13. In order to extend the nuclear data library of PFGS, which are important for fundamental physics and nuclear applications, this work has measured the prompt fission γ-rays from various fissioning systems. These fissioning systems include ^{252}Cf(sf), ^{238}U(n,f) and ^{239}Pu(n,f). The experimental aspect of this work will be discussed in the following chapters.

Chapter 2
The fast neutron source - LICORNE

As mentioned in the first chapter, fast-neutron-induced fission of ^{238}U and ^{239}Pu will be studied in this work. Due to the fact that the fission cross section in fast-neutron region is three orders of magnitude lower than that in the thermal neutron region, it requires an intense neutron source to cumulate reasonable statistics for the study of the PFGS. Fast neutrons are currently produced using either "white" neutron sources or mono-energetic/quasi mono-energetic neutron sources. "White" neutron sources offer the ability to provide neutrons from sub-thermal energies to GeV, for example n-TOF facility at CERN [63]. However, the use of collimated long flight paths, which are necessary to obtain better energy resolution using time of flight (TOF) measurement, result in limited neutron fluxes. Mono-energetic or quasi mono-energetic neutron sources are generally produced through light ion reactions such as T(d,n), T(p,n), D(d,n), ^{7}Li(p,n) and ^{9}Be(p,n), and are generally good sources for fast neutron measurements. They are used for example at the Van de Graaff facility in JRC (Geel) [64]. Nevertheless, inverse kinematics such as p(^{7}Li,n), p(^{9}Be,n) and p(^{11}B,n) can be used to kinematically focus the outgoing neutrons into a small angular range around zero degree with respect to the beam axis direction. The advantages from inverse kinematics reactions are that the shielding materials for beam collimation are not needed, thereby limiting the background of scattered neutrons, and the neutron flux is greatly increased. In this chapter, the fast neutron source LICORNE (which stands for Lithium Inverse Cinematiques ORsay NEutron source) [30–32], developed at the ALTO facility of the IPN Orsay, will be presented.

2.1 General characteristics of the LICORNE neutron source

The LICORNE neutron source generates fast neutrons which can be used to bombard an actinides sample and induce fission. LICORNE produces intense, kinematically focused, quasi mono-energetic beams of neutrons or "white" neutrons, by using the p(^{7}Li,n)^{7}Be or p(^{11}B,n)^{11}C reaction. The heavy projectile (^{7}Li or ^{11}B), produced by the

Tandem in ALTO facility [65], interacts in a cylindrical hydrogen gas cell, producing naturally collimated neutrons. This allows placement of detectors close to a sample to be irradiated without being affected by the neutrons from the source. As a consequence to this naturally collimated neutron cone, there is no need for the shielding of the neutrons and the neutron flux is enhanced by the kinematic focusing on the sample. Another key feature is that the LICORNE device is placed in a big experimental hall without a roof, which decreases the back-scattered neutron background in the region of the irradiated samples. Thus the neutron background, especially thermal neutrons, is very low. It has been proved experimentally that the thermal neutron background is five orders of magnitude lower, which allows the study of fissile material in fast-neutron region reliable.

A schematic view of the LICORNE device can be seen in the Figure 2.1. A reaction chamber was designed to couple the pressurized gas cell to the Tandem vacuum beam line. The entry point of the cell consists of a drilled hole and a Tantalum foil pinched between the cell and the reaction chamber exit flange. The foil thickness may vary from 2.0 µm to 2.8 µm. Tantalum and other high-Z materials are essential to eliminate all potential sources of fusion-evaporation reactions along the beam trajectory. Low-Z materials are avoided. Parasitic fusion-evaporation reactions are unwanted because they emit neutrons isotropically and at undesired energies, destroying the advantage of the inverse kinematics. In addition they emit background γ-rays. The Coulomb barrier heights of different structural materials for the primary beam ^{7}Li and ^{11}B are listed in Table 2.1, respectively, and determine the energy regime within which LICORNE can operate at very low background. Inside the LICORNE chamber, a fluorescent foil and a camera are used to help tuning the incident beam to pass through the 4.5 mm hole. Obtaining high transmission of the primary beam into the cell is of utmost importance. The end of the gas cell is coated with 100 µm Lead or 25 µm gold foil to stop the primary beam. The gas cell is surrounded by Lead or Tungsten shielding (not represented in the schematic view) in order to attenuate the flux of the 478 keV γ-rays emitted from radioactive decay of residual nuclei ^{7}Be and inelastic scattering ^{7}Li(p,p') reaction (in case of ^{11}B, 511 keV annihilation γ-rays from radioactive decay and 2125 keV γ-rays from ^{11}B(p,p') reaction).

Table 2.1 – Coulomb barrier of the structural materials along the beam trajectory (^{27}Al, ^{181}Ta and ^{208}Pb) for the primary beam (^{7}Li and ^{11}B), respectively.

	$V_{C,^{7}Li}$ (MeV)	$V_{C,^{11}B}$ (MeV)
^{27}Al	2.68	9.13
^{181}Ta	22.32	44.52
^{208}Pb	24.79	48.90

It is essential to understand the neutron flux distribution and energy distribution in the space in order to predict the fission rate of the actinides samples, neutron damage on the

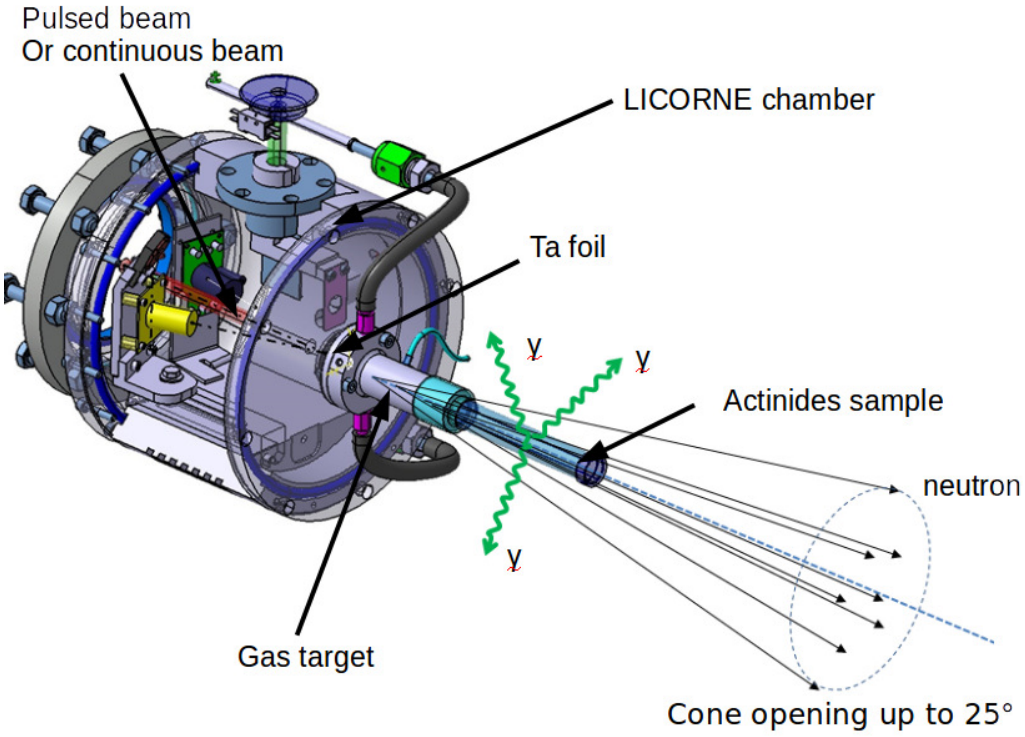

Figure 2.1 – A schematic view of the LICORNE facility with an actinides sample placed after the hydrogen gas cell. The Tantalum foil separates the vacuum in LICORNE chamber and the pressurized gas cell [66].

gamma ray detectors and scattered neutron background etc. A simulation code has been developed based on GEANT4 [67]. This program aims to simulate the coupling between the energy loss process of ^{7}Li or ^{11}B in Tantalum foil and hydrogen gas, and the neutron production reaction of p(^{7}Li, n)^{7}Be or p(^{11}B, n)^{11}C, as well as the neutron transportations in space. The kinematics calculation of the two reactions had to be incorporated into the GEANT4 tool-kit, which doesn't include these reactions in the standard list of physics processes. Kinematics calculations were performed using TGenPhaseSpace class [68] from ROOT [69]. However this class assumes that the differential cross section in center of mass system (CM) is uniform. In order to improve the calculations, two-body phase calculation had to take into account the differential cross section of the two reactions, obtained from experiments [70,71]. Since the total cross sections of the two reactions are very low, around several hundreds of millibarns, it needs a lot of calculation time to decrease statistical fluctuations in the results. In order to accelerate the simulation, some general options can be considered, *e.g.* higher physical cut limits (namely energy threshold) applied to particles whose tracking are not interesting like beryllium and electron. However, the effect of these operations is limited. Instead, more efficient event-biasing techniques have been implemented into the GEANT4 simulation to accelerate the calculations without changing the tool-kit itself and the code has been validated in different types of experiments.

2.2 Simulations of the neutron production

2.2.1 Kinematics calculations

The physics list is a key issue in GEANT4. It includes the modelling of interactions of different particles in matter, *e.g.* photons and neutrons. In the version 9.6, the processes of inverse kinematics for light ions are not included. For this reason, this section describes the creation and implementation of the process of inverse kinematics into reference physics lists in GEANT4, *i.e.* "IonPhysics". Similar to photon Compton scattering, the p(^{7}Li,n)^{7}Be reaction is described in "DiscreteProcess". The process has three methods which play an important role in tracking, "PostStepDoIt", "ComputeCrossSectionPerAtom" and "GetMeanFreePath". The physical interaction length, namely the distance at which the process will make an interaction, is calculated by the multiplication of the mean free path (obtained from "GetMeanFreePath" and "ComputeCrossSectionPerAtom") and the number of mean free path (sampled random number). The process with shortest interaction length is invoked and corresponding states are changed according to "PostStepDoIt" class. The principle of the processes for the p(^{7}Li,n)^{7}Be and p(^{11}B,n)^{11}C reactions is the same. So only the formula for p(^{7}Li,n)^{7}Be reaction is shown in the following discussion.

The "ComputeCrossSectionPerAtom" and "GetMeanFreePath" methods give the mean free path in certain materials, which is defined as:

$$\lambda = \frac{1}{\sum_H N_H \cdot \sigma_H(E)} \tag{2.1}$$

where N_H is the number of hydrogen atom per volume and $\sigma_H(E)$ is the total cross section of the process. The total cross section as a function of the incident beam energy needs to be provided by the user according to the experimental data [70, 71], see Figure 2.2 for the cross section of the p(^{7}Li,n)^{7}Be and p(^{11}B,n)^{11}C reactions as a function of the kinetic energy of the projectile, respectively.

The details of the interaction, including the change of the particle's energy, momentum, direction and position, and information of secondary particles etc., are implemented in the method of "PostStepDoIt", *i.e.* the phase calculations in this case. The multi-bodied phase calculation firstly generates an effective mass M_{eff}, conserving total energy and momentum. And then the effective mass is sequentially "decay" *via* two-body modes, giving decay products with an angular distribution in their own center of mass system. Then the neutron momentum $P_{n,cm}$ in center of mass system can be easily deduced from

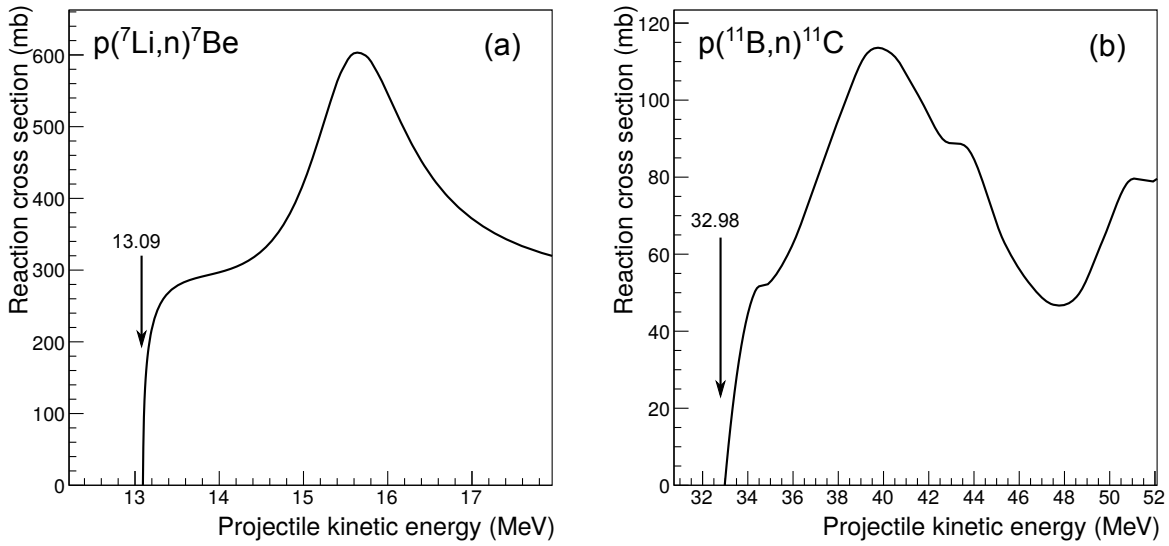

Figure 2.2 – Total cross sections for the (a) p(^{7}Li,n)^{7}Be and (b) p(^{11}B,n)^{11}C reactions, respectively, as a function of the incident projectiles' energy. The reaction threshold for the two reactions has been pointed out in the figure.

the total energy of the neutrons $E_{n,cm}$, with the formula:

$$M_{eff} = m_{Li} + KE_{Li} + m_p + KE_p \tag{2.2}$$

$$E_{n,cm} = \frac{M_{eff}^2 - m_{Be}^2 + m_n^2}{2M_{eff}} \tag{2.3}$$

$$P_{n,cm} = \sqrt{E_{n,cm}^2 - m_n^2} \tag{2.4}$$

where m_{Li}, m_p, m_{Be}, and m_n are the rest mass of ^{7}Li, proton, ^{7}Be and neutron, respectively. In the previous work, "TGenPhaseSpace" class [68] form ROOT tool-kit was used, in the assumption that the direction of outgoing neutrons is uniformly distributed in center of mass system. However, it is not the case according to the experimental results [70, 71] (see Figure 2.3 for the distribution at different projectile energies, which have been scaled for easier reading) and the angular distribution changes dramatically especially at high energies of the projectiles. The differential cross section is described with Legendre polynomials:

$$\sigma(\theta) = \sum A_n P_n(\cos\theta) \tag{2.5}$$

where θ is the outgoing angle of neutron in center of mass system, $P_n(\cos\theta)$ is the Legendre polynomial coefficient and A_n is the coefficient fitted from experimental data as a function of incident particle energy. Due to the fact that the differential cross section data were obtained from direct reaction ^{7}Li(p,n)^{7}Be, the energy of proton has to multiply the mass

ratio between lithium and proton to get the corresponding lithium energies, with the cross section to be conserved in inverse kinematics. And the $(180° - \theta)$ is the outgoing angle of neutron in the differential cross section distribution of inverse kinematics by replacing the original angle θ.

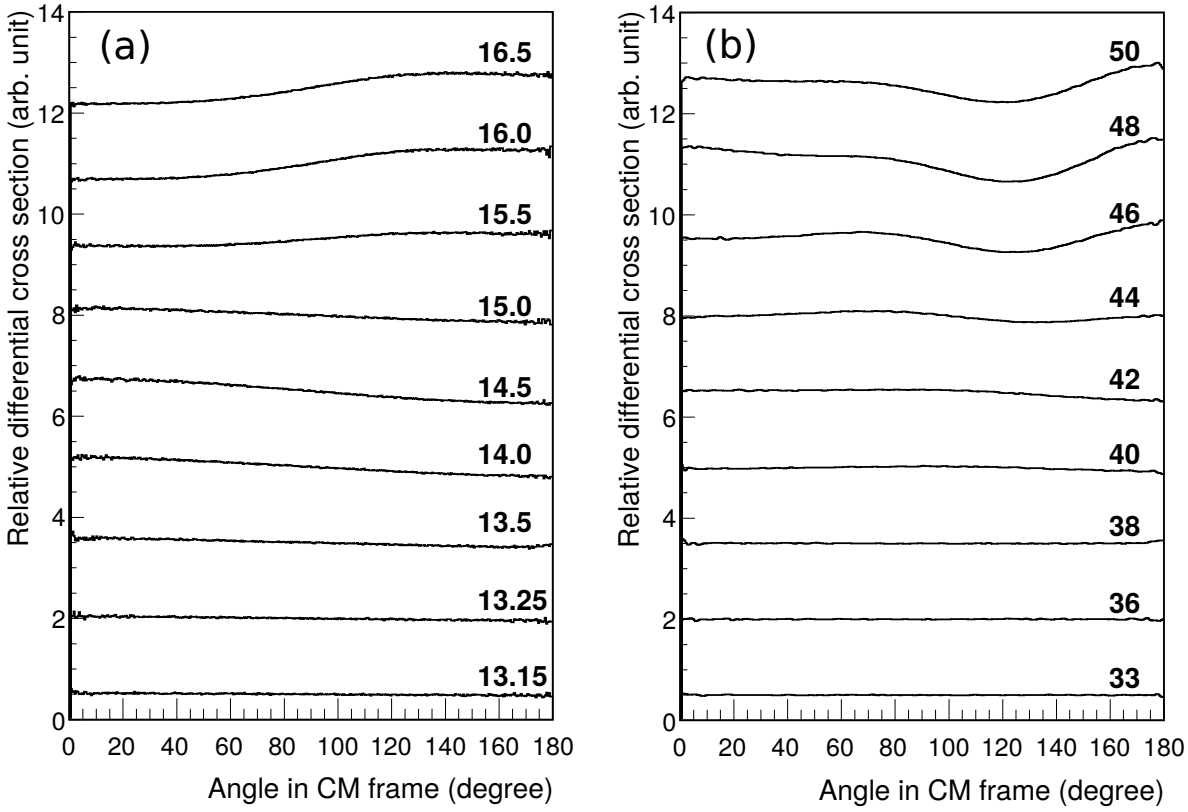

Figure 2.3 – Differential cross section distribution in CM system at different projectile energies for the (a) p(^{7}Li,n)^{7}Be and (b) p(^{11}B,n)^{11}C reactions, respectively. The cross section has been scaled for better visualization. Non-uniform distributions are observed for ^{7}Li energies from 13.15 MeV to 16.5 MeV and ^{11}B energies from 33 MeV to 50 MeV, especially at high-energy region.

Instead of a uniform distribution, *i.e.* cos(θ)=rand() and α=2$\pi\times$rand(), non-uniform sampling in angle θ according to experimental distribution can be obtained for the outgoing neutrons. As a consequence, the corresponding momentum of the neutrons are then be able to be modified according to the neutron realistic kinematics:

$$P_{n,cm,x} = P_{n,cm} \times \sin\theta\cos\alpha \tag{2.6}$$

$$P_{n,cm,y} = P_{n,cm} \times \sin\theta\sin\alpha \tag{2.7}$$

$$P_{n,cm,z} = P_{n,cm} \times \cos\theta \tag{2.8}$$

Finally, the kinematics properties need to be described in the laboratory (LAB) system using the Lorentz boost. The boost velocity is that of the mother nucleus (assumed as the compound nucleus) in lab frame

$$\boldsymbol{V}_{CN,lab} = \boldsymbol{P}_{CN,lab}c^2/E_{CN,lab} \tag{2.9}$$

where $\boldsymbol{P}_{CN,lab} = \boldsymbol{P}_{Li,lab}$ and $E_{CN,lab} = M_{eff}$. The components of the ejectile momentum parallel and perpendicular to the boost velocity are

$$P^{\parallel}_{n,cm} = \boldsymbol{P}_{n,cm} \cdot \hat{\boldsymbol{v}}_{CN,lab} \tag{2.10}$$

$$\boldsymbol{P}^{\perp}_{n,cm} = \boldsymbol{P}_{n,cm} - P^{\parallel}_{n,cm}\hat{\boldsymbol{v}}_{CN,lab} \tag{2.11}$$

respectively, where $\hat{\boldsymbol{v}}_{CN,lab}$ is the unit vector of the boost velocity. According to the Lorentz transformation, the perpendicular component is not affected by the Lorentz boost and the parallel component in lab frame is

$$\boldsymbol{P}^{\parallel}_{n,lab} = \gamma(P^{\parallel}_{n,cm} + V_{CN,lab}E_{n,cm}/c^2)\hat{\boldsymbol{v}}_{CN,lab} \tag{2.12}$$

$$\boldsymbol{P}^{\perp}_{n,lab} = \boldsymbol{P}^{\perp}_{n,cm} \tag{2.13}$$

where $\gamma = 1/\sqrt{1 - V^2_{CN,lab}/c^2}$. The summation of the two vector components (parallel and perpendicular) gives the final momentum in the lab frame. Also Lorentz boost matrix is available in the class of "TLorentzVector" from ROOT tool-kit, which can be easily applied in the code.

The results of relativistic kinematics calculation are plotted in Figure 2.4. For each energy of incident projectile, two energies of neutrons appear in one specific angle in LAB system, except the maximum angle of the neutron cone. That's because in the inverse kinematics, the forward and backward outgoing neutrons in CM system are projected into the same angle of LAB system, which leads to a primary energy (at higher energy) and a "satellite" energy at an angle in LAB system. This correlation is illustrated in Figure 2.5 when $\Gamma > 1$ in case of A(a,b)B reaction, where Γ is defined as $\Gamma = \left(\frac{A_aA_b}{A_AA_B} \cdot \frac{E'}{E'+Q}\right)^{1/2}$, and $E' = \frac{1}{2}\frac{m_am_A}{m_a+m_A}v_a^2$ is the kinetic energy of the center of mass (non-relativistic kinematics is used for this illustration).

In addition, when the energy of projectile is higher than the threshold (16.51 MeV) for the reaction p(^{7}Li,n)^{7}Be*, where ^{7}Be* stays in the first excited state, the equation 2.3 has to be changed as:

$$E_{n,cm} = \frac{M^2_{eff} - (m^2_{Be} + 429.08[keV]) + m^2_n}{2M_{eff}} \tag{2.14}$$

Thus the available energy for neutron production is decreased and two types of kinematics

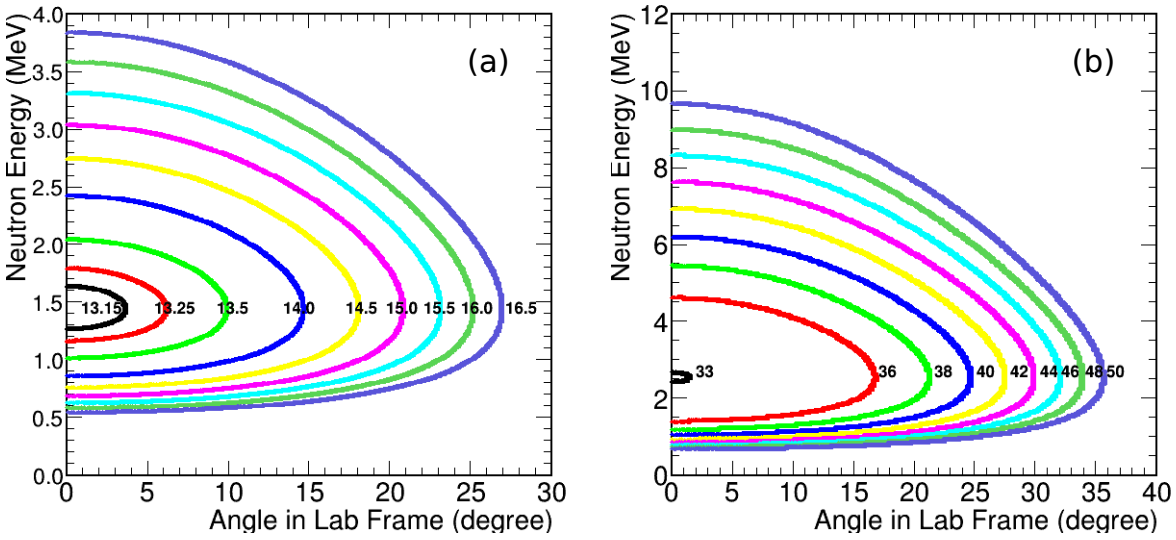

Figure 2.4 – Kinematics curves of the neutron energy vs. the angle of outgoing neutron in the LAB frame with respect to the projectile's direction for different projectile energies, calculated using two-body relativistic kinematics. (a) ^{7}Li energy ranges from 13.15 MeV to 16.5 MeV, (b) ^{11}B energy ranges from 33 MeV to 50 MeV.

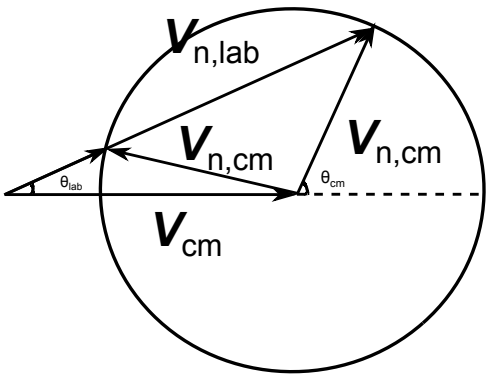

Figure 2.5 – The correlation between $\boldsymbol{V}_{n,cm}$, $\boldsymbol{V}_{n,lab}$ and $\boldsymbol{V}_{cm}$ when $\Gamma > 1$. See text for the definition of Γ.

curves are generated for one incident lithium energy. Since the ratio of the macro cross section for the two reactions are known, this part of calculation can be incorporated into the same DiscreteProcess by changing the equation 2.3. In reality, the lithium energy has to be operated below the threshold of the reaction p(^{7}Li,n)^{7}Be*, because in most cases LICORNE serves as a quasi mono-energetic neutron source.

2.2.2 Description of the event biasing

As mentioned before, the total cross section for the p(^{7}Li,n)^{7}Be and p(^{11}B,n)^{11}C reactions is small, *i.e.* less than 1 barn, according to the Figure 2.2. It gives a much larger mean free path compared to other interactions in the gas cell. It is rarely chosen in GEANT4 Monte Carlo selection of the physics processes. As a result, the analogue simulation for small cross section processes usually takes a lot of calculation time. In order to accelerate the simulation, event-biasing technique is often needed by sampling particle histories in the regions of interest. Since version 10.0, GEANT4 incorporates a new approach, allowing biasing of processes interaction and final state, together with splitting, killing etc. However, the validation of the new approaches is still ongoing. In addition, version 9.6 is used in this work. So event-biasing technique was performed by wrapping the processes for the p(^{7}Li,n)^{7}Be and p(^{11}B,n)^{11}C reactions (the creation and implementation discussed in the previous section), that have been inserted into reference physics list, without changing the GEANT4 tool-kit itself. Two main methods of event-biasing techniques: particle splitting and importance biasing, are discussed hereafter.

The first method, called particle splitting technique, splits the tracking into two branches. One contains the interaction products and the other contains the original particle. It is widely used in MCNP code [72], and is also known as force collision. It may be necessary to remember that ^{7}Li is continuously loosing its energy over its trajectory in the gas cell. Unlike dealing with neutral particles, charged particles' transportation has strong coupling between the energy loss process in the hydrogen gas cell, which is a continuous process, and neutron production process, *i.e.* p(^{7}Li,n)^{7}Be or p(^{11}B,n)^{11}C reaction, which is a discrete process. Despite the continuous loss of energy, the step-size is limited in GEANT4 so that cross section can be assumed constant during the step [73]. As a result, force collision can be applied in GEANT4 by adding secondaries (*e.g.* neutrons) at the end of each step, see Figure 2.6(a). Proper weight has to be given to compensate the splitting process:

$$W'(x) = W(x - \Delta x) \cdot \left[1 - e^{\sigma(x-\Delta x)\cdot\Delta x}\right] \tag{2.15}$$

$$W(x) = W(x - \Delta x) \cdot e^{\sigma(x-\Delta x)\cdot\Delta x} \tag{2.16}$$

where $W(x - \Delta x)$ and $W(x)$ is the weight of the original incident particles (^{7}Li) in the previous step and current step, $W'(x)$ is the weight of the outgoing neutron generated in this force collision, $\sigma(x - \Delta x)$ is the cross section in this step and Δx is the step length. Similar to the particle splitting, the final state of discrete processes can also be modified. It means that instead of generating one neutron in analogue simulation, hundreds of neutron can be generated following the same kinematics calculation, see Figure 2.6(b). The statistical weight of these neutrons will be divided by the splitting factor. This technique was firstly used in the example of Bremsstrahlung splitting [74].

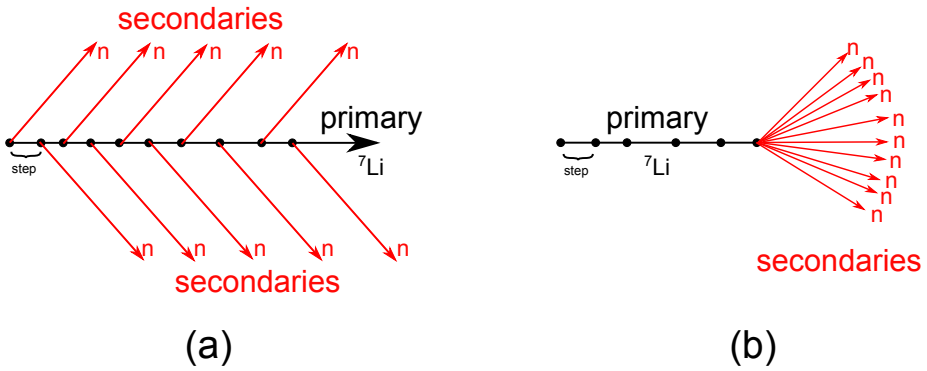

Figure 2.6 – Schematic view of the principle of multi-level splitting techniques applied in GEANT4: (a) force collision; (b) secondaries splitting.

Instead of splitting particles, the cross section for potentially interesting processes can be modified to be more favourable in the selection of different processes. The increase of the cross section leads to higher probability in getting small step-size samples, which results in the p(^{7}Li,n)^{7}Be or p(^{11}B,n)^{11}C reaction to be more favourable for high-energy projectiles, *i.e.* at the beginning of the hydrogen gas cell. This phenomenon is called beam depletion. This un-physical phenomenon needs to be corrected by introducing a proper weight factor to compensate the artificial increase of the cross section. The weight is deduced from the derivative form of interaction probability ($dN/N = -\Sigma dx$), with the formula:

$$W(x) = W(x - \Delta x) \cdot e^{(b-1)\cdot\Delta\lambda} \tag{2.17}$$

where $W(x)$ and $W(x - \Delta x)$ are the weight of the incident particles (^{7}Li) in the previous step and current step, b is the biasing factor, $\Delta\lambda$ is the number of interaction lengths traversed in this step. This method is the so-called importance biasing [75]. Figure 2.7 gives the number of interactions for the p(^{7}Li,n)^{7}Be reaction at different positions in the hydrogen gas cell, with and without weight correction. It depicts that the interaction in the latter part of the gas cell has greater importance (weight) due to the increased cross section.

Both splitting and importance biasing techniques are tested in the simulation. Figure 2.8 shows that both splitting method and importance biasing method are in good agreement with the analogue simulation. At the same time, it decreases computation time dramatically. In terms of figure-of-merit (FOM), defined as FOM $= 1/(\sigma \cdot T)$ where σ is the statistical error and T is the calculation time, it has been increased more 20 times compared to analogue simulation. As a result, the final strategy is the combination of the particle splitting technique and the importance biasing to make use of all the advantages,

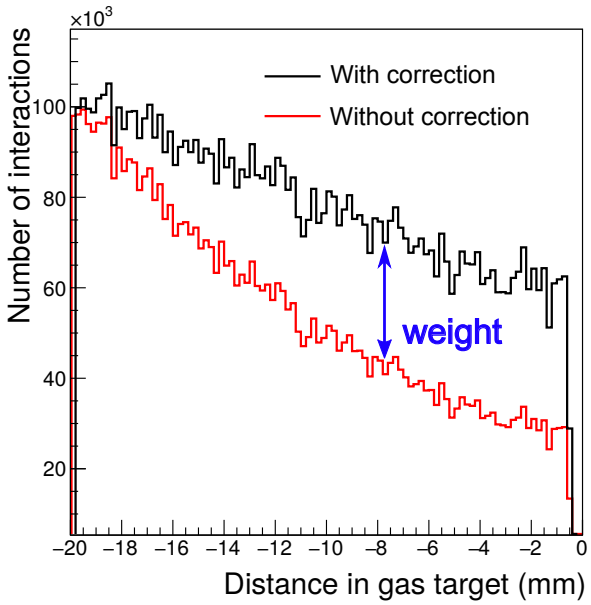

Figure 2.7 – Comparison of the number of interactions versus the depth in the gas cell with (black) and without (red) the weight correction. -20 mm represents the entry of the gas cell and 0 mm the exit of the gas cell. Uncorrected curve exhibits the beam depletion phenomenon.

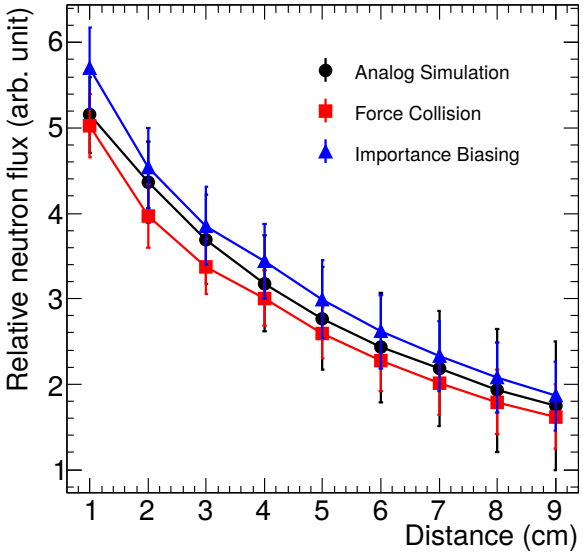

Figure 2.8 – Comparison of the neutron flux at different distances after the LICORNE setup, calculated by the two major event-biasing techniques (force collision and importance biasing) and the analog simulation (without any variance reduction applied). The agreement validates the GEANT4 code in the use of these two event-biasing techniques.

i.e. increase the cross section by a factor of 10000 and increase the neutron yields by a factor of 100 at the same time in default configuration.

2.3 Simulation results and comparisons with experiment

2.3.1 Energy loss process

In this code, an user interface has been created to take all the parameters of the setup into account, *i.e.* thickness of the Tantalum foil, pressure of the hydrogen gas, length of the gas cell and the incident beam energies (see Appendix. A). All these parameters could have impact in the energy loss of ^{7}Li or ^{11}B in the setup and thus the outgoing neutron spectrum.

The incident beam firstly bombards on the tantalum foil, which separates the vacuum in LICORNE chamber ($<10^{-5}$ atmosphere) and the pressurized hydrogen gas cell (1.0 - 1.7 atmospheres). There are two limit values for the tantalum foil thickness available at the moment, 2.0 µm and 2.8 µm. The foil needs a certain thickness to resist the force caused by the pressure difference on both sides. The main interactions between primary beam and the tantalum foil are inelastic collisions with the atomic electrons and elastic scattering with the nuclei. Inelastic collisions with the atomic electrons make negligible deflection but mainly cause a loss of energy. It causes energy straggling because the energy loss process in nature has statistical fluctuations in the number of collisions and energy transfer in each collision. Elastic scattering mainly deflects the primary particles from its incident direction and introduces spacial spreading of the beam profile. The maximum cone angle is increased compared to pure kinematics calculations. As a consequence, the scattered primary particles can hit the Aluminium wall and make fusion-evaporation reactions since the kinetic energy of the primary particles is generally larger than the Coulomb barrier height, see Figure 2.9(a). Extra Lead or Gold foil can be coated around the inside of the gas cell to avoid the fusion-evaporation reactions.

After going through the tantalum foil, the incident particles undergo further energy loss in the hydrogen gas cell. In the gas cell, the spatial spreading is negligible, see Figure 2.9(b), because ^{7}Li projectile is heavier than the proton target such that the ^{7}Li are hardly deflected. And the energy straggling depends on the pressure and the length of the gas cell (thickness), according to the formula calculated by Bohr [76]:

$$\sigma_0^2 = 4\pi N_a r_e^2 (m_e c^2)^2 \rho \frac{Z}{A} x = 0.1596 \rho \frac{Z}{A} x [MeV^2] \tag{2.18}$$

where σ_0 is the standard deviation of the energy distribution of the incident particle at the end of the gas cell, ρ the density and x the thickness of the gas cell. It depicts that the

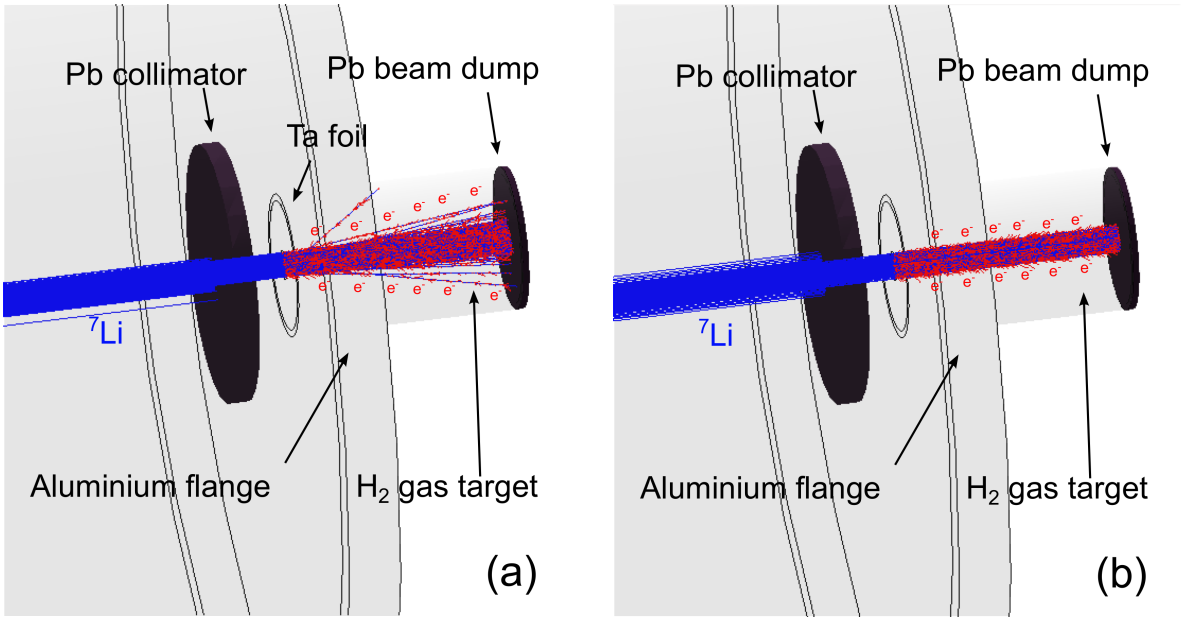

Figure 2.9 – Comparisons of the ^{7}Li trajectories in LICORNE setup (a) with and (b) without the Tantalum foil, simulated in GEANT4. The spacial spreading of the projectile trajectories is mainly due to the presence of Tantalum foil.

higher the pressure (*i.e.* larger ρ), the greater is the stopping power of the gas and thus wider the energy spread of the incident particles at the end. The longer the gas cell x, the incident particles lose more energy and thus wider the energy spread. As a consequence, the wider of the incident particles' energy distribution induces a wider distribution of neutron spectrum.

Given all the information of the LICORNE setup, the spacial spreading and energy straggling are simulated in the GEANT4 code. Assuming that the incident beam has a two-dimensional Gaussian distribution (σ_0=1.0 mm) before the collimator ($\oslash$=4.0 mm, see Figure 2.9), the distribution of the beam at the end of the gas cell has been calculated to be σ_x=1.17 mm for 2.0 µm thick tantalum foil, and σ_x=1.26 mm for 2.8 µm thick tantalum foil, respectively. Table 2.2 summaries the change of quantities during the energy loss process in LICORNE setup.

Table 2.2 – Summary of the projectile quantities at different positions, including energy and space distributions. 0 stands for the position before the Pb collimator, 1 stands for the beginning of gas cell (right after Ta foil) and 2 for the end of gas cell. Other LICORNE setup parameters are gas cell length L=3.5 cm and pressure P=1.5 atm.

Ta thickness d(µm)	E_0(MeV)	E_1(MeV)	E_2(MeV)	σ_0(mm)	σ_1(mm)	σ_2(mm)
2.0	16.95	15.57±0.04	13.95±0.06	1.00	0.83	1.17
2.8	17.50	15.58±0.05	13.96±0.06	1.00	0.83	1.26

2.3.2 Neutron production and transportation

As mentioned in the kinematics calculations section 2.2.1, the energy spectrum of the outgoing neutrons is dependent on the energy of incident particles, *i.e.* energy distribution of the incident particles in the gas cell, characterized by its pressure and length. A typical kinematics curve is plotted in Figure 2.10, showing a coupling between the energy loss process of incident particles in hydrogen gas cell (continuous process) and neutron production reaction (discrete process), *i.e.* p(^{7}Li,n)^{7}Be or p(^{11}B,n)^{11}C. A sample placed few centimetres after the LICORNE source usually covers several degrees of polar angle with respect to the beam axis in the LAB system. And the projection of this part to the y-axis is the neutron spectrum seen by the sample. Several neutron spectra are plotted at different projectile energies in Figure 2.11 for the two neutron production reactions, respectively.

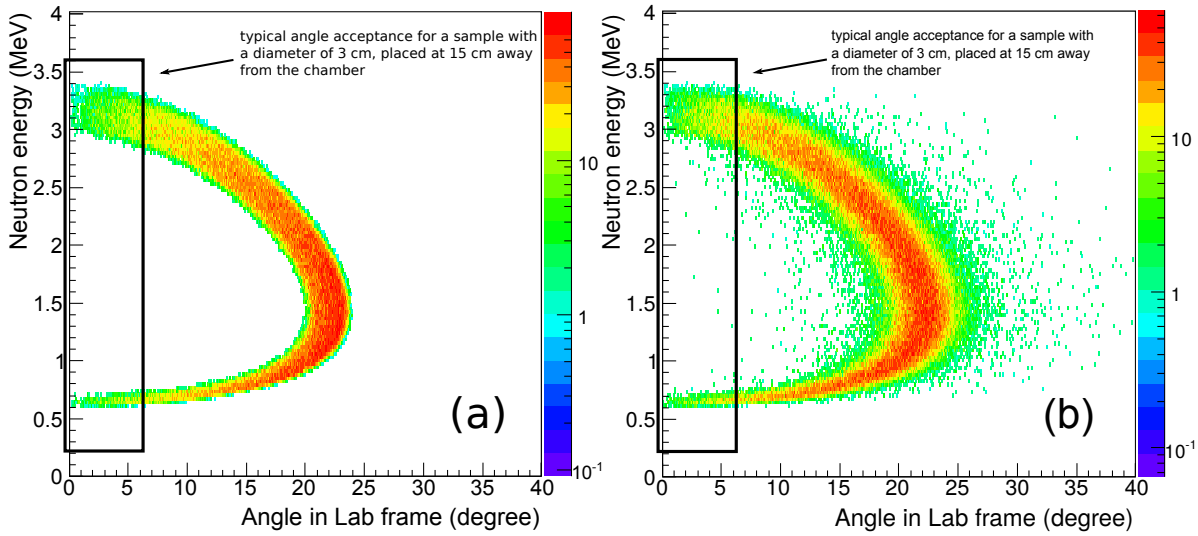

Figure 2.10 – Kinematics curves obtained from the LICORNE simulation with the parameters L=2.0 cm, P=1.1 atm, d=2.8 µm and E_0=17.5 MeV. (a) Correlation between neutron energy and the angle with respect to the projectile's direction in LAB system; (b) Correlation between neutron energy and the angle with respect to the z direction (beam direction) in LAB system.

By changing the energy of incident particles, various outgoing neutron energies are obtained, from 0.5 MeV to 4 MeV for p(^{7}Li,n)^{7}Be in a <25° neutron cone and 0.5 MeV to 7 MeV for p(^{11}B,n)^{11}C in a <35° neutron cone. In terms of using LICORNE as a quasi mono-energetic neutron source, the kinetic energy of primary beam is contraint by two factors: one is to avoid fusion-evaporation reactions with Tantalum on the beam trajectories and the other is to avoid the opening of other reaction channels with protons, *e.g.* p(^{7}Li,n)^{7}Be* reaction. Consequently, the upper limit of the primary beam energy is

16.5 MeV for Lithium and 44.0 MeV for Boron. The width of the neutron peaks depends on the thickness of the Tantalum foil, pressure and length of the gas cell, as discussed in Section 2.3.1. The primary and "satellite" neutron peaks are visible in the spectra (Figure 2.11). For fast-neutron-induced fission, *e.g.* ^{238}U(n,f), the energy threshold is by convention considered to be 1.4 MeV. So the "satellite" neutron peak brings a negligible contribution to the fission of the system. On the other hand, when the energy of incident particles is close to the threshold of the reaction, the neutron cone becomes very narrow and the two neutron peaks very close to each other. 10^5 n/cm^2/s to 10^6 n/cm^2/s are typical neutron flux available at 100 nA beam intensity of Lithium, when using LICORNE as a quasi mono-energetic neutron source.

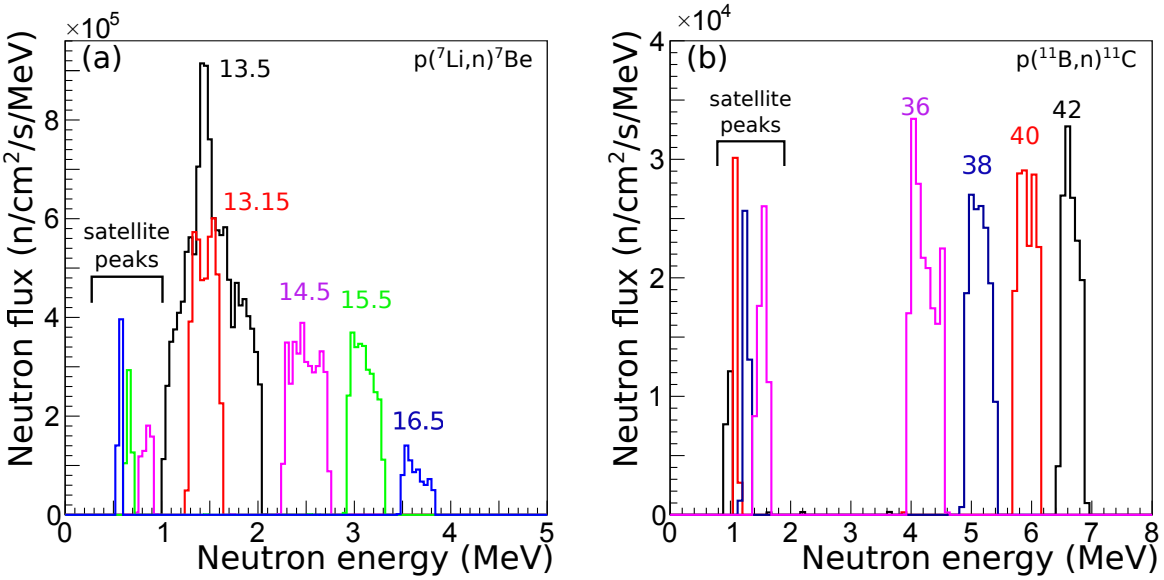

Figure 2.11 – Quasi mono-energetic neutron mode: neutron spectrum seen by a thin actinide sample (⌀=1.0 cm) placed 10 cm after the LICORNE gas cell (L=2.0 cm, P=1.1 atm, d=2.8 µm) at different incident particle's energy. (a) ^{7}Li energies E_1 range from 13.15 MeV to 16.5 MeV; (b) ^{11}B energies E_1 from 36 MeV to 42 MeV. The neutron flux is normalized to the beam intensity of 100 nA.

Contrary to a quasi mono-energetic neutron source, LICORNE can serve as a "white" neutron source. In some industrial applications, the neutron energy distribution in few MeV region dose not affect the results significantly, *e.g.* testing of electronics in extreme neutron irradiation environments. In such cases, the upper limit of the primary beam energy is only limited by avoiding fusion-evaporation reactions on Tantalum, *i.e.* the primary beam energy can extend up to 22.3 MeV for Lithium. Consequently, a long gas cell can be used to maximize the probability of neutron production reactions along the beam trajectory. One example has been presented in Figure 2.12. In addition, thanks to the recent upgrade on ion source in ALTO facility, the primary beam intensity provided

can extend to 1 µA for Lithium without having any window melting problem. Thus, the neutron flux with 1 µA beam intensity of Lithium can reach up to 7×10^7 n/cm^2/s at 0.5 cm far away from the gas cell.

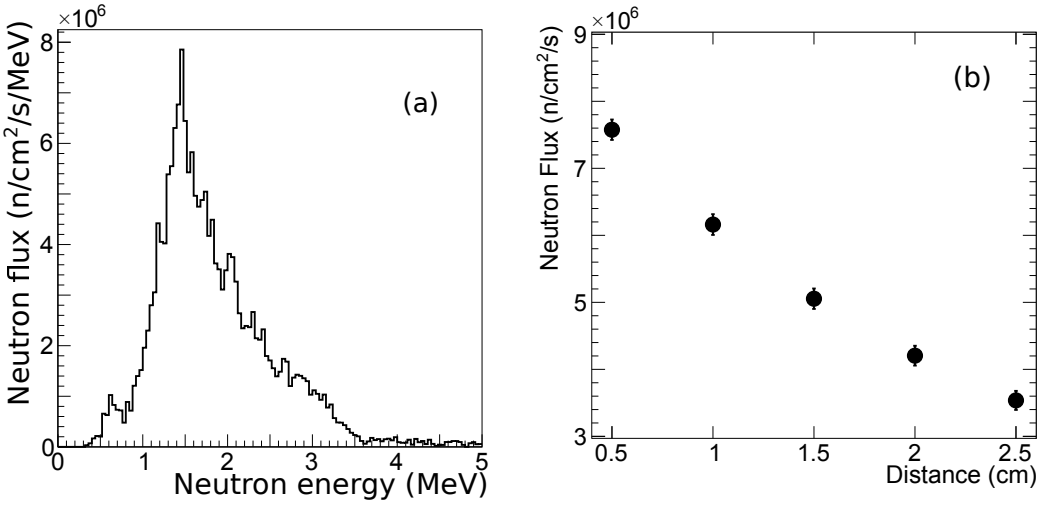

Figure 2.12 – "White" neutron mode: (a) neutron spectrum seen by a thin sample (⌀=2.0 mm) placed 0.5 cm after the LICORNE gas cell (L=20.0 cm, P=1.6 atm, d=2.0 µm). The Lithium energies are E_0=22.30 MeV, E_1=21.11±0.04 MeV and E_2=12.30±0.13 MeV, respectively. (b) The neutron flux distribution at different distances after the LICORNE setup. The neutron flux is normalized to the beam intensity of 100 nA.

The calculation of neutron transportation in the experimental hall is also included in the GEANT4 code. The tracking of the neutron trajectories is stored in the format of TTree, containing spacial coordinates, momentum, kinetic energy and weight (correction to event biasing) of the neutrons. It allows extraction of the information at any place of the experimental hall from the root file without re-doing the simulation, which saves time. For example, the neutron flux in space is plotted in Figure 2.13, which has been normalized to 100 nA beam intensity. The neutron flux is at the order of 10^6 n/cm^2/s in few centimetres after the gas cell. Though the deflected neutrons and even back-scattered neutrons broaden the cone, neutron flux at positions Y=150 mm is at least 4 orders of magnitude lower than that of 10^6 n/cm^2/s. The neutron damage for HPGe detectors placed at certain distances can then be estimated according to this flux distribution, which is crucial in the experiment design.

By coupling the neutron flux with a fission chamber or a liquid scintillator neutron detector, the fission rate of certain actinide or the time-of-flight spectra can be calculated. Figure 2.14 plots the comparison between simulation results and experimental measurements (details in Chapter 3 and Chapter 4) with different techniques, *via* TOF and fission rate measurements. TOF spectra were measured in the liquid scintillation neutron de-

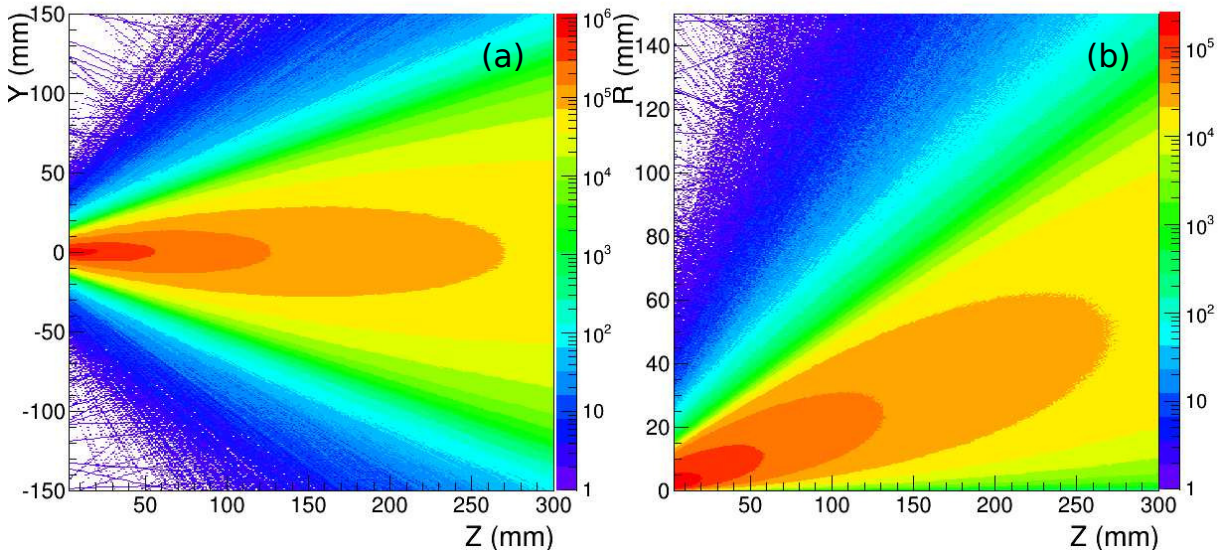

Figure 2.13 – Neutron transportation in air after the LICORNE setup in (a) Cartesian coordinate system and (b) cylindrical coordinate system. The parameters of the LICORNE setup are L=3.5 cm, P=1.5 atm, d=2.8 µm and E_0=16.75 MeV. Neutron flux can be easily extracted from figure (a). And figure (b) gives a hint on the actinides sample design in terms of maximizing the fission rate, *i.e.* conical shape.

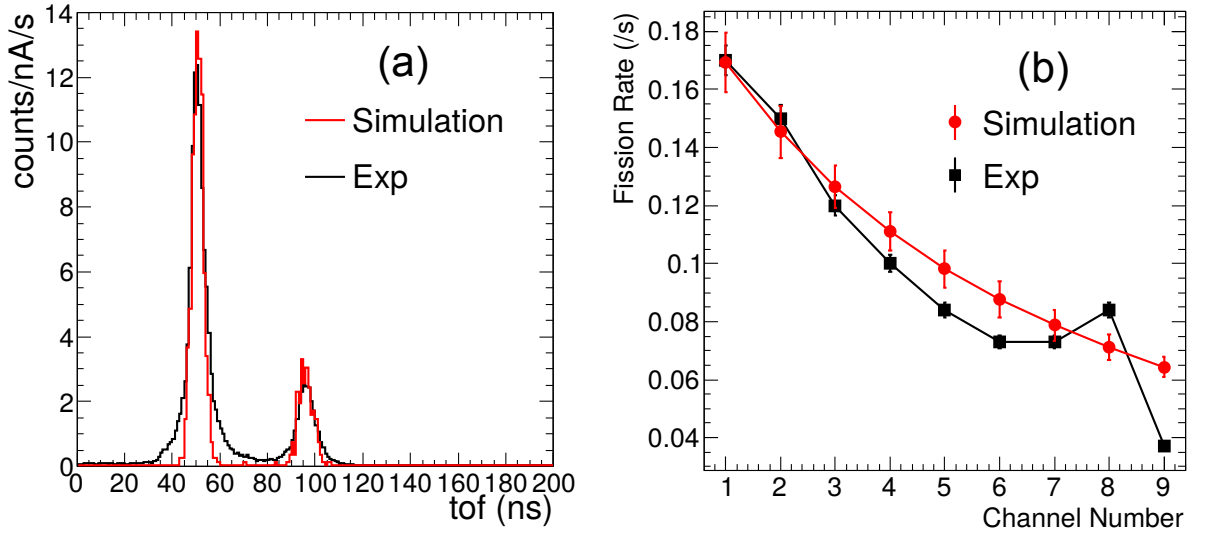

Figure 2.14 – (a) Comparison of the simulation and experimental TOF spectrum in a liquid scintillation detector placed 1.5 m after the LICORNE setup. (b) Comparison of simulation and experimental fission rate measurement in each channel of an ionization chamber containing ^{238}U samples.

tector, placed at zero degree with respect to the beam axis. It is plotted in the left of Figure 2.14. The primary beam ^{7}Li is a pulsed beam of 400 ns period and 2 ns width. The arrival of neutrons in the neutron detector gives the start signal and the beam pulsing signal provides the stop signal. The positions of the primary peak and "satellite" peak have good agreements with the simulations, while the width of the peaks vary due to the lack of the time resolution information of the neutron detector. The fission rate distribution at different distances relative to the LICORNE gas cell (Figure 2.14(b)) was obtained by using a multi-sample ionization chamber. It contained fissionable nuclides ^{238}U and was placed in the neutron probe to be irradiated. The fission events were extracted by excluding the α particles. The tendency of the fission rate distribution has been reproduced by the simulation. Some discrepancies are observed in the last few channels, which may depends on the differences of the sample masses and the discrimination between the fission fragments and α particles.

To summarize, a code in GEANT4 is developed to simulate the LICORNE setup. It is able to reproduce the neutron energy and flux distribution in space at different setup configurations. The calculation time is decreased with the implementation of event-biasing techniques. The code has been validated by experimental measurements with reasonable agreements.

2.4 Examples of LICORNE neutron source use

The main advantage of the LICORNE neutron source is the collimated neutron cone. Thanks to the collimated neutron cone, the flux is kinematically enhanced at short distances and the detectors are allowed to be placed closer to the irradiated samples. With the help of the calculations mentioned above, a better knowledge of the neutron flux and energy distribution in the space is obtained. It opens up probabilities for different kinds of experiments, *e.g.* imaging, cross section measurement and nuclear structure study. These experiments have been performed successfully in the last few years.

2.4.1 Fast neutron tomography

Accelerator based fast neutron tomography (FNT) is a new technique dedicated to produce images of the insides of dense materials. It can be a complementary technique to X-ray computerized tomography (CT), due to neutron penetrative property in dense material and sensitivity to low Z material. In a proof-of-concept experiment, performed in December 2016, the reaction p(^{7}Li,n)^{7}Be was used and the incident lithium (pulsed beam) was set closely to the reaction threshold (13.09 MeV) to minimize the opening neutron cone (<5 degrees). In the experimental setup, a scanning table with rotational and transitional movement, two high purity Germanium (HPGe) detectors and nineteen

liquid scintillator neutron detectors called NEDA were placed, as shown in Figure 2.15. The HPGe detectors were used to detect the γ-rays from the (n,n'γ) reactions on the materials, which in principle allows identification of the insides materials. The attenuation of neutrons was measured by the NEDA array and used to reconstruct the image inside a sealed box. A recently developed data acquisition system called FASTER was adopted for the signals treatment. The apply of simultaneous iterative reconstruction technique (SIRT) successfully produces the images of the internal structures.

Figure 2.15 – Experimental setup of fast neutron tomography by using LICORNE neutron source, including a scanning table (left) and a neutron detection array NEDA (right).

2.4.2 Chronological dating

Argon–argon (^{40}Ar/^{39}Ar) dating is a radiometric dating method invented to supersede potassium-argon (K/Ar) dating in accuracy for geological, planetary and archaeological materials. The ^{39}K(n,p)^{39}Ar and ^{39}K(n,α)^{36}Cl reactions are of great importance for the ^{40}Ar/^{39}Ar dating technique. However the cross section at energy range from 1 to 4 MeV of the two reactions is not well known. With the advantages of the LICORNE neutron source, the cross sections can be measured easily at these energies, with the "satellite" energy below the reaction threshold. The experimental setup (see Figure 2.16) includes a sample holder, a neutron detector and a HPGe detector. In the sample holder, metallic foils (In and Au) were attached behind the sample (KBr or KNO_3). The absolute neutron fluence is mainly monitored by activation of metallic foils (In) and measuring the decay γ-rays, through ^{115}In(n,n')^{115m}In reaction ($T_{1/2}$=4.5 h, cross section around 310-340 mb). After each irradiation, the In and Ag foil were taken off and put in front of the HPGe detectors to measure the decay gamma rays. A neutron detector was placed 3 m away from the LICORNE chamber, in order to monitor the beam fluctuation during the irradiation, which then gives a correction factor for the neutron fluence. At the end of irradiation,

analysis of ^{39}Ar and ^{36}Cl were performed by noble gas mass spectrometry and accelerator mass spectrometry, respectively.

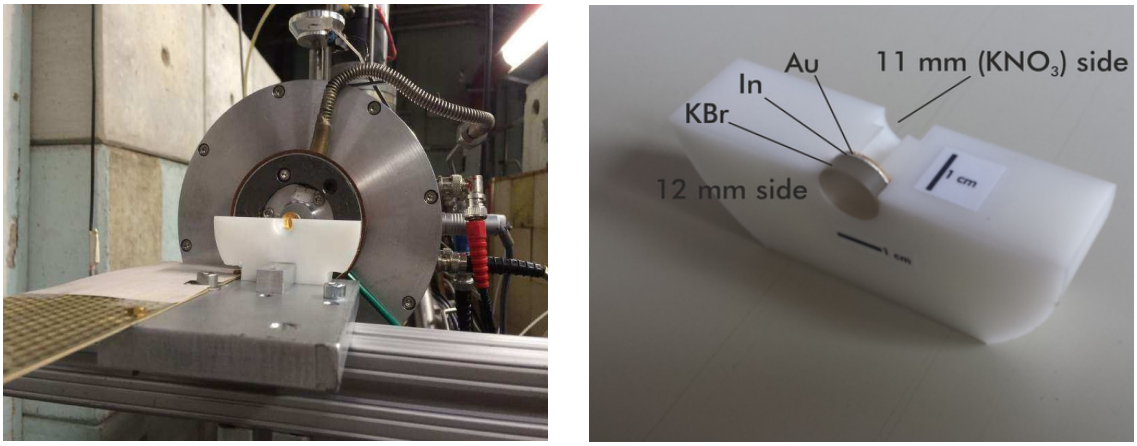

Figure 2.16 – Experimental setup of the cross section measuremnt in the key reaction for ^{40}Ar/^{39}Ar dating technique. The neutron fluence is monitored by mesuring the decay γ-rays of the In and Au foil.

2.4.3 Nuclear structure studies

The nuclear structure of the neutron-rich nuclei is of great interests in nuclear physics since the high neutron/proton ratio can be an interesting environment to study the nuclear force between nucleons. In the past, other experiments have sought to produce neutron rich nuclei by using nuclear fission. The spectrometers used to identify the hundreds of fission fragments (neutron-rich nuclei) produced were those used in the EUROBALL and EXILL experimental campaigns, with great success. However, only a limited subset of neutron-rich nuclei can be obtained from these experiments. The LICORNE neutron source was coupled to the MINIBALL γ-ray spectrometer to investigate fission fragments produced by fast-neutron-induced fission of ^{238}U (E_n = 1.72 MeV), which allows access to more neutron-rich nuclei.

The lithium energy (pulsed beam, E_0 = 16.75 MeV) and gas cell (3.5 cm and 1.5 atmosphere) were chosen to maximize the flux for the opening angle of the neutron cone less than 20 degrees. The Uranium sample was placed 1.5 cm away from gas cell, and was a half cylinder of Uranium metal with a diameter of 1.2 cm and length of 3.0 cm. The MINIBALL array was placed 14 cm away from the Uranium sample to detect γ-rays, which consisted of 24 high-purity Germanium detectors clustered in 8 cryostats without BGO shields. The experimental setup can be seen in Figure 2.17. By using γ-γ and γ-γ-γ coincidence techniques, starting from first and second excited states, the partial level schemes of fission fragments after pre-emission can be built.

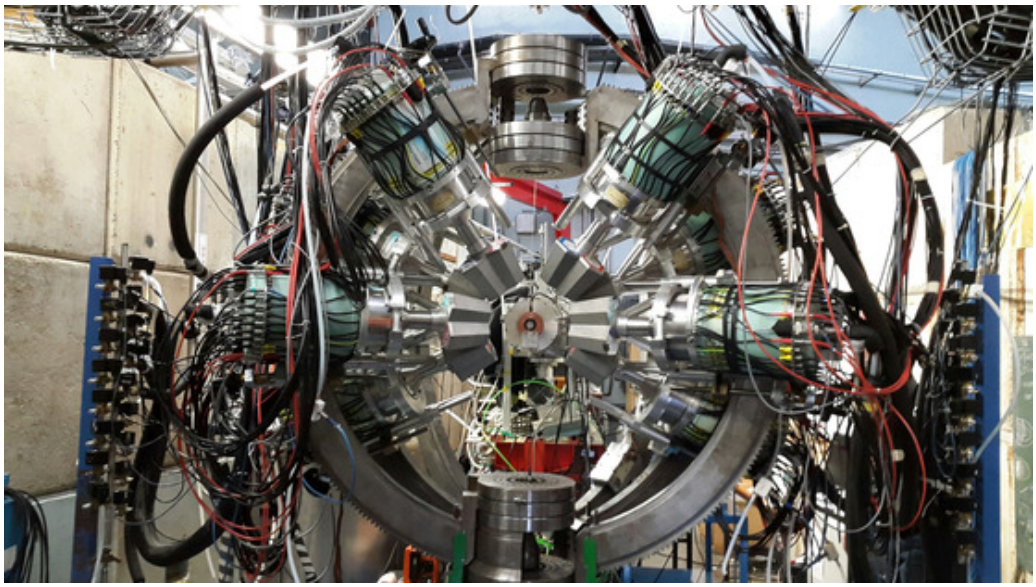

Figure 2.17 – Experimental setup of the MINIBALL γ-ray spectrometer coupled with the LICORNE neutron source, dedicated to measure the decay γ-rays of fission fragments (neutron-rich) in the reaction ^{238}U(n$_{fast}$,f).

Since its creation in 2013, the LICORNE neutron source has now become an essential tool for the ALTO facility. This simulation code, developed in this work, has been used for the LICORNE experiments and is now accessible. Recently, a powerful γ-ray spectrometer, called ν-ball, is coupled to the LICORNE neutron source for various fundamental physics research.

Chapter 3

Measurements of PFGS in ^{238}U(n,f) and ^{239}Pu(n,f) reactions

In recent years, the development of Generation IV reactors revived the measurement of prompt fission γ-ray spectra, especially for fast-neutron-induced fission. The spectral characteristics, such as γ-ray multiplicity, total γ-ray energy release and average photon energy, are crucial nuclear data. These information are also useful from a fundamental physics point of view, where results can be compared with theoretical predictions to refine fission models. They are as well of great importance for reactor physics, *e.g.* they are used as inputs for γ heating calculations. With the development of LICORNE neutron source, the study of PFGS in the fast-neutron region becomes more practicable.

Two experiments dedicated to measure the prompt fission γ-rays of ^{238}U and ^{239}Pu in fast-neutron region were performed at the tandem of the ALTO facility in IPN Orsay, by using LICORNE neutron source, see Figure 3.1. Fission events were detected with an ionization chamber containing actinide samples, placed in the neutron beam, and the emitted prompt fission γ-rays were measured using a number of $LaBr_3$ scintillation detectors and a cluster of 9 phoswich detectors from the PARIS array [77–79]. Prompt fission gamma rays were discriminated from prompt fission neutrons using the time-of-flight (TOF) technique over distances of about 35 cm. In addition, liquid scintillation detectors were placed along the beam axis 1.5 m away from the LICORNE source to characterize neutron spectra *via* the TOF technique and to monitor the produced neutron flux. In both experiments, detector pre-amplifier signals were processed using the digital acquisition system FASTER (Fast Acquisition SysTem for nuclEar Research) [80]. In this chapter, a detailed description of all the setup components will be given.

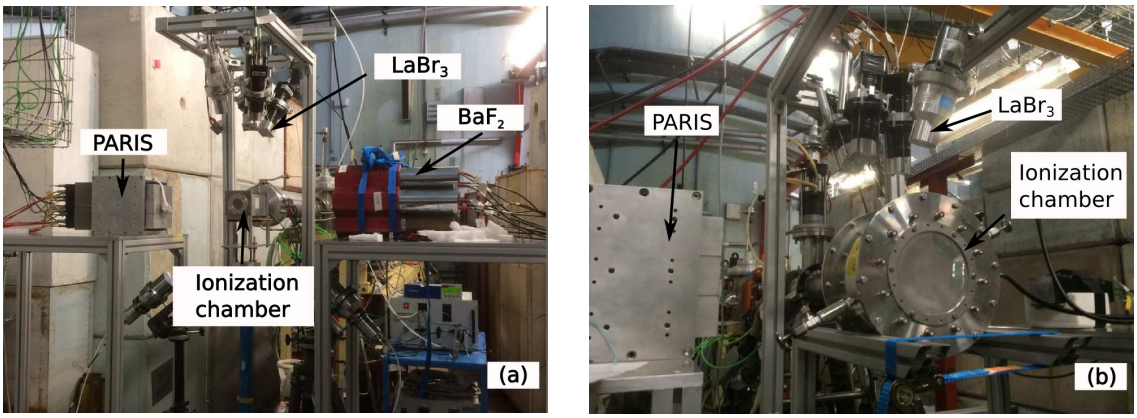

Figure 3.1 – Picture of the two experimental setups, dedicated to measure the PFG of the (a) ^{238}U(n$_{fast}$,f) and (b) ^{239}Pu(n$_{fast}$,f) reactions, respectively.

3.1 Fission fragment detection

3.1.1 Interaction of fission fragments in matter

Fission fragments are charged particles that can be divided into two main groups: the heavy-fragment group around mass number A= 143.53 with an average kinetic energy of 79.48 MeV per fragment and the light-fragment group around mass number A= 108.47 with a kinetic energy of 104.82 MeV per fragment, according to the FREYA calculation in the case of ^{252}Cf(sf). In addition, fission fragments are generally highly excited ionized nuclei, see Table 1.1. The following discussion will focus on the interaction of fission fragments in matter, which is mainly concerned with the collision between the heavy charged particles and the atomic electrons. It is described quantitatively by the stopping power defined as $\frac{dE}{dx}$, *i.e.* the average linear rate of energy loss in a medium (MeV/cm).

Inelastic collision with the nucleus can be important in relativistic energy range. A quantum of electromagnetic radiation is emitted (a photon) in this process, also known as radiative energy loss. However, in this case, β is equal to 0.046 for the light-fragment group, way below the relativistic energy range. Thus the radiative energy loss is negligible.

Consequently, the inelastic collision with atomic electrons through Coulomb force is mainly responsible for the energy loss of fission fragments in matter. It results in excitation or ionization. The excitation process promotes the atomic electron to a higher energy level, followed by characteristics X-rays emission. The ionization process frees the atomic electron creating an electron-ion pair. This is primary ionization. The emitted electron (delta-rays) can have high enough energy to create electron-ion pairs itself, inducing secondary ionization. The total energy and momentum conservation predicts that only a small fraction of the heavy particle's energy is going to be transferred to the light particles (electrons). So the fission fragments travel along an unaltered linear path, gradually losing the kinetic energy. In this region, the stopping power has been well described by the

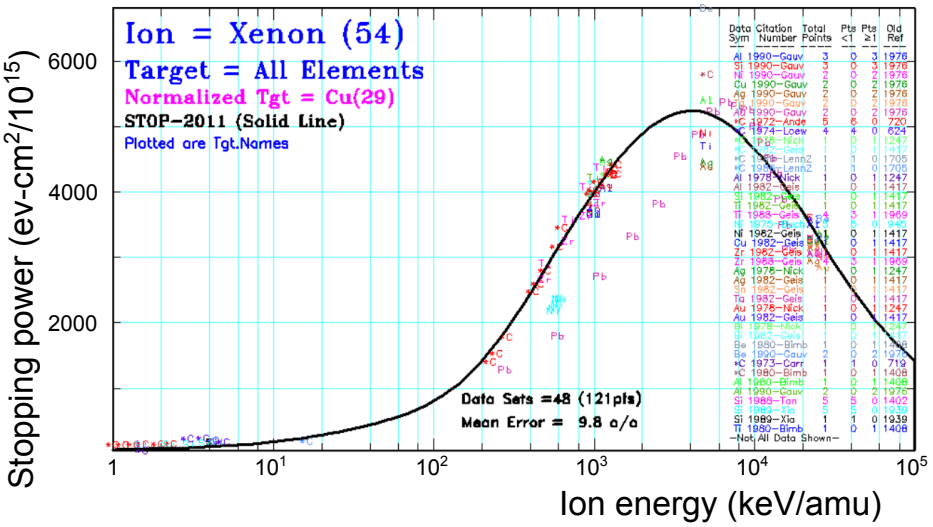

Figure 3.2 – Stopping power of a typical fission fragment Xenon as a function of the ion energy in different targets. The black solid line refers to the calculation result from SRIM [81], as well as different experimental results marked with target name.

Bethe-Bloch formula calculated in quantum mechanics [76]:

$$-\frac{dE}{dx} = 2\pi N_a r_e^2 m_e c^2 \rho \frac{Z}{A}\frac{z^2}{\beta^2}\left[ln\left(\frac{2m_e\gamma^2 v^2 W_{max}}{I^2} - 2\beta^2 - \delta - 2\frac{C}{Z}\right)\right] \tag{3.1}$$

where W_{max} is the maximum energy transfer in a single collision, δ the density effect correction and C the shell correction. Some general properties can be seen from the formula. For example, the property of the medium is described by the Z/A and I, which are roughly the same for all the materials. Thus the stopping power is mainly dependent on the velocity and charge of the incident particles and can be estimated roughly to be -dE/dx $\propto 1/v^2$, see Figure 3.2 in energy range from 10^4 to 10^5 keV/amu.

Table 3.1 – Range calculation results from the TRIM/SRIM codes [81] for a typical fission fragment ^{132}Xe and α particle in different counting gases.

Particle	Kinetic Energy (MeV)	Counting Gas	Density (kg/m^3)	Range (mm)
^{132}Xe	100	CF_4	3.72	8.43
	100	P10	1.59	23.55
	100	P20	1.49	24.72
α	6	CF_4	3.72	17.19
	6	P10	1.59	52.50
	6	P20	1.49	55.22

When the energy of the heavy particles is lower than certain limit, the contribution

of the inelastic collision with atomic electron becomes less important. Because the probability for heavy fragments to capture of the electrons is increasing, thus decreasing the effective charge of the heavy fragment and Coulomb force. In addition, elastic collision (nuclear stopping power) starts to play a role in the interaction in the low-energy region. When the incident particle reaches thermal equilibrium with the medium, the energy is finally transferred to the atoms of the medium in the form of heat. In this region, the Beth-Bloch formula is not applicable (no longer follows $1/v^2$, see Figure 3.2 in energy range from 1 to 10^4 keV/amu) and the theoretical calculations are still not satisfactory with the experimental observations. Several semi-empirical stopping power formulas have been developed [82,83] and implemented in the TRIM/SRIM codes [81]. Table 3.1 includes the calculation results of the stopping ranges by the TRIM/SRIM codes.

3.1.2 Multi-sample fission chamber

The large kinetic energy in fission fragments makes use of gaseous ionization detectors a common technique for fission fragment detection. These gaseous ionization detectors are usually filled with an ionizing gas of a pressure just above 1 atmosphere, and parallel plates consisting of foils of actinides samples and blank foils. The actinide samples are coated on the surface of a thin conductive foil, which can serve as a cathode or an anode. A cathode/anode pair is formed with an adjacent blank or coated foil. The cathode/anode pair is biased with a voltage of about 300 volts, allowing operating in the ionization chamber mode, *i.e.* the charge collected is relatively insensitive to the applied voltage.

Gaseous ionization detectors are sensitive to the movement of charge, *i.e.* electron-ion pairs, produced by ionizing radiation. The average energy to create an electron-ion pair in the gas is called the ionization energy ω, which is at the order of 30 eV. It is not strongly dependent on the type of incident particle, but depends slightly on the type of gas. In case of full-energy deposition, the total number of ionizations N is proportional to the energy of incident particle E_0 [76]:

$$N = \frac{E_0}{\omega} \tag{3.2}$$

It leads to the basic principle that: measuring the total number of ionizations gives access to the energy of the incident particles. The occurrence of the ionization processes is statistical by nature, following a Poisson or Poisson-like distribution. The fluctuation of the distribution is described by [76]:

$$\sigma^2 = FN = F\frac{E_0}{\omega} \tag{3.3}$$

where F is the Fano factor, characterizing the energy loss in a collision not being purely statistical (F<1 for gases and semiconductors). The resolution $R = 2.35\frac{\sqrt{FN}}{N}$ thus improves with larger number of ionizations.

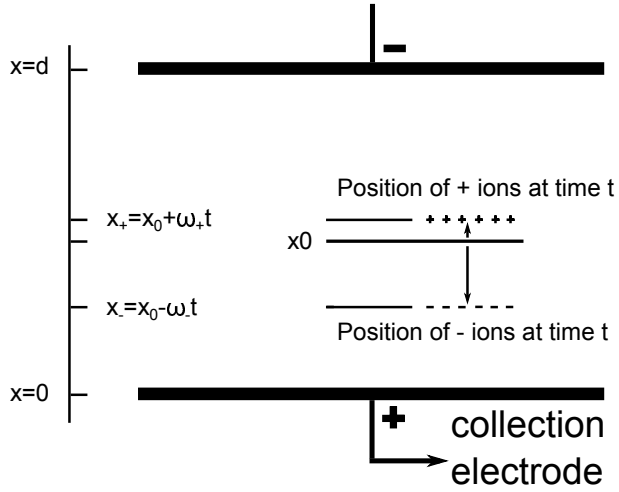

Figure 3.3 – Schematic view of the parallel-plate ionization chamber, taken from [84]. See the text for the explanation of the symbols.

A schematic view of the parallel-plate ionization chamber can be seen in Figure 3.3. The electric field can be assumed to be uniform when the spacing d is small. If N electron-ion pairs are created in position x_0 in the gas, the voltage on the collecting electrode is then [84]:

$$V(t) = \frac{q(t)}{C} = \frac{Ne}{C}\left(\frac{d - x_+}{d} - \frac{d - x_-}{d}\right) \tag{3.4}$$

where $x_+ = x_0 + \omega_+ t$, $x_- = x_0 - \omega_- t$, x_+ and x_- are the positions for ions and electrons at time t and ω is the drift velocity. Since the electron drift velocity is three orders of magnitude larger than that of ions, the pulse from the anode is used in order to achieve better time resolution of the ionization chamber. Therefore the circuit time constant RC is chosen to be slightly larger than the electron collection time t_-, which is much smaller than the ion collection time t_+, *i.e.* the motion of the positive ions is neglected. Thus the voltage turns out to be [84]:

$$V(t) = \frac{Ne}{C}\left(\frac{-x_0 + x_0 - \omega_- t}{d}\right) = \frac{-Ne\omega_- t}{Cd} \tag{3.5}$$

which increases linearly with time until all the electrons are collected. Finally the amplitude of the pulse will be $V(t)=\frac{-Nex_0}{Cd}$, depending where the electron-ion pair was created.

In the experiment to measure ^{238}U(n,f) PFGS, two fission chambers, newly developed at CEA/DAM Bruyère-le-Chatel, were used to study prompt emission in fission [85]. The first chamber contained one cathode supporting a 25 mm diameter ^{252}Cf sample, which is a 60 kBq spontaneous fission source that has been widely studied and serves as a reference to validate the analysis procedure. The second chamber is a multi-sample fission chamber, containing 340 mg Uranium samples over 72 deposits ($\oslash$ = 33 mm) with a compact geometry, see Figure 3.4 for a schematic view. The Uranium was deposited on both sides

of each anode and cathode, except the first and last samples which were only coated on the internal side. The anodes are paired two by two constituting 9 channels for readout of fission fragment detection information. The chambers have been designed with thin Aluminium walls to minimize scattering of prompt γ rays and neutrons emitted in fission and thus have minimum distortion of the γ and neutron spectra. A gas regulation system was used to keep a constant flux and a pressure 50 mb above atmospheric pressure. The key characteristics are the sub-nanosecond time resolution and excellent discrimination between fission fragments and α particles.

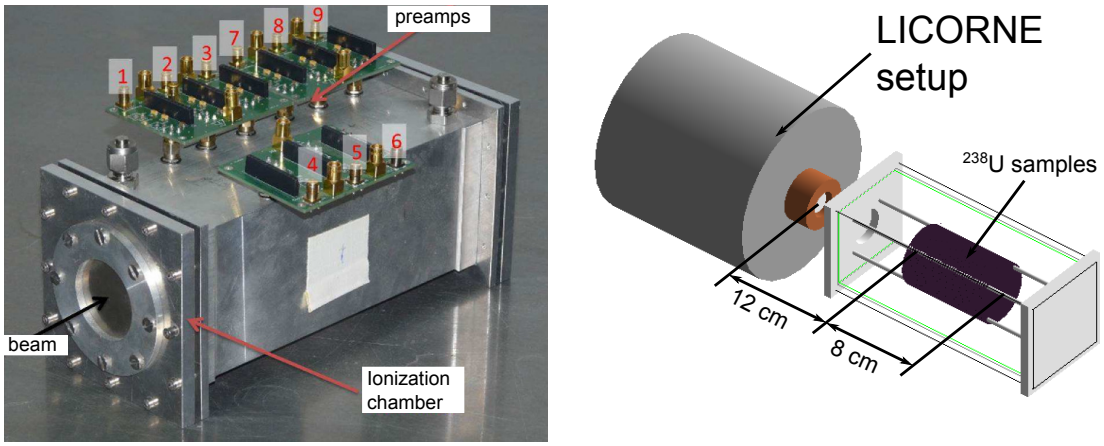

Figure 3.4 – Picture of the multi-sample fission chamber developed in CEA Bruyère-le-Chatel (left) and the corresponding simulation in GEANT4 (right).

The intrinsic time resolution of the fission chamber is the main constraint in this type of experiment. This is because the signal from the fission chamber serves as the "start" of the time-of-flight measurement, while the signal from the γ-ray detectors gives the "stop" signal. In these experiments, the time resolution is around 300 ps for the γ-ray detectors, which is much better than conventional ionization detectors. In order to improve the time resolution of the fission chamber, Tetrafluoromethane CF_4 was used as an ionizing gas. It exhibits a higher electron drift velocity and a higher density compared to typical ionizing gases, *e.g.* P10 (90% Ar, 10% CH_4) or P20 (80% Ar, 20% CH_4). The faster the electron moves, the shorter the rise time of the signal will be. And the high density of the gas allows a short distance between cathode and anode within reasonable pressure for a compact geometry design of multi-sample chamber. In addition to the good drift velocity, corresponding electronics have also been designed to preserve the good time resolution of the chamber [85]. In the end, sub-nanosecond time resolution (732 ps) has been achieved for this type of multi-sample fission chamber.

Another important characteristic is the discrimination between fission fragments and α particles. A clear separation between the alpha decay and fission events is needed, otherwise a false coincidence with the PFG may occur. In addition, the total number of fissions detected in the experiment will be needed to normalize the measured PFGS.

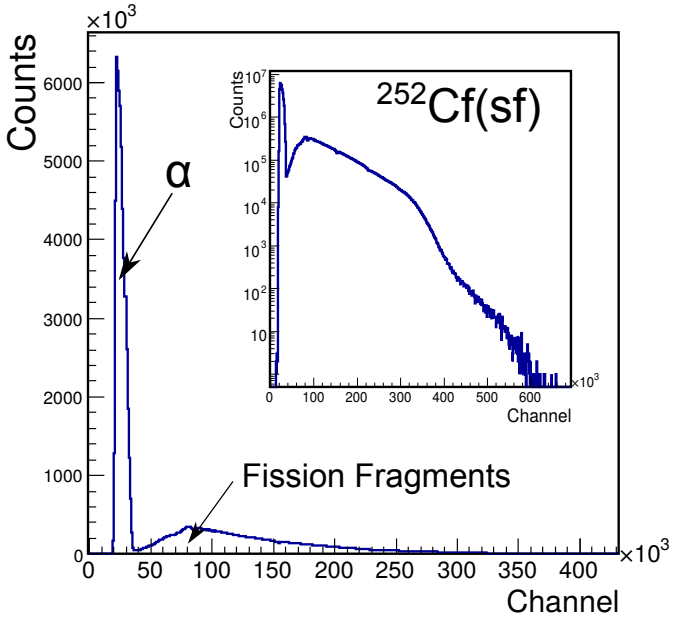

Figure 3.5 – The integrated charge spectrum taken with the CEA multi-sample ionization chamber depicted in linear scale; the inset shows the same distribution in logarithmic scale. In both representations, the separation between fission fragments and α particles is visible.

According to Ref. [85], the gap between the anode and cathode is set to be 2.5 mm, along which the fission fragment induce charge equivalent to energy loss of at least 12 MeV. This value is twice larger than the maximum induced charge of an alpha for actinides (equivalent to ∼6 MeV). A good discrimination between fission fragments and α particles then has been accomplished, see Figure 3.5. The overlapping between α particles and fission events is less than 3% in ^{252}Cf fission chamber. The overlapping is higher in the ^{238}U chamber due to slightly larger thickness of the deposits, but it is still negligible.

In the experiment of ^{239}Pu(n,f) measurement, a fission chamber developed at JRC Geel was used to discriminate α particles and fission fragments and acted as the "start" in the timing measurement (see Figure 3.6). The chamber contained high purity (99.97%) ^{239}Pu samples with a total mass of 3.519 mg. Every two samples were attached to the cathode, forming 4 channels for readout of fission fragment detection information in the anode. A gas regulation system was also used with the ionizing gas being Tetrafluoromethane CF_4. Due to the fact that the half-life of ^{239}Pu (24110 y) is much shorter than ^{238}U (4.468×10^9 y), the α activity of the ^{239}Pu samples is much higher (up to 7 MBq). The pileup of the α particles emission degrades the discrimination between α particles and fission fragments. Instead, pulse shape discrimination (PSD) was applied to improve the discrimination, see Figure 3.7. PSD technique is also used in the organic liquid scintillation neutron detectors. It will be detailed in Section 3.3.2.

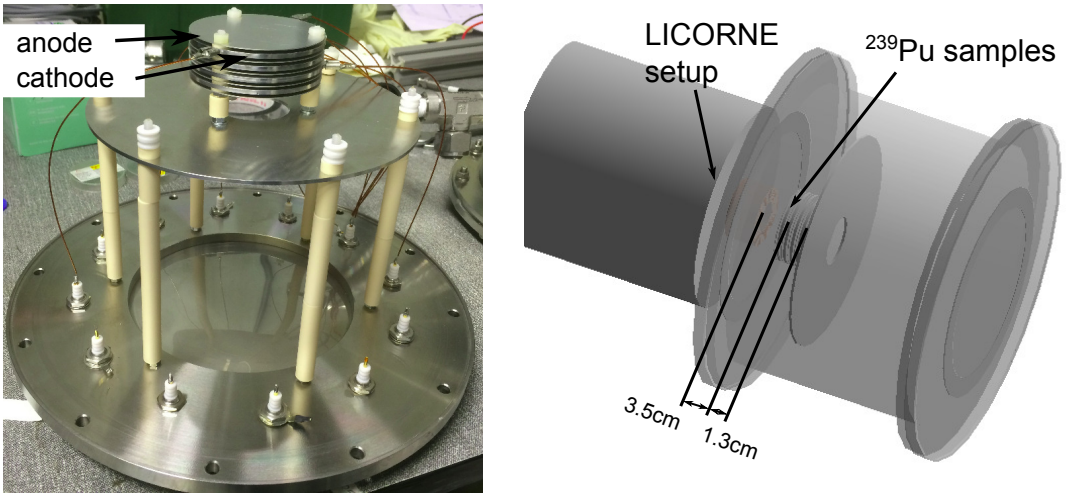

Figure 3.6 – Picture of the multi-sample fission chamber developed in JRC Geel (left) and the coresponding simulation in GEANT4 (right).

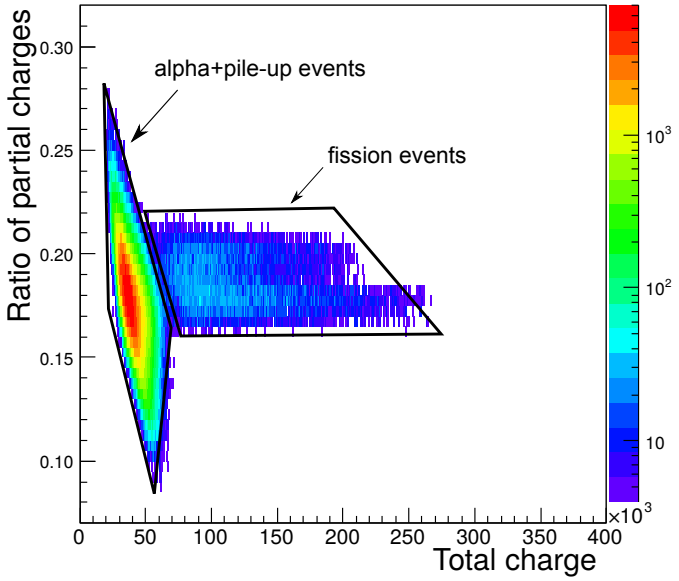

Figure 3.7 – Correlation between the ratio of partial charges and the total integrated charge. PSD improves the discrimination between α particles and FF.

3.2 Prompt fission γ-rays detection

3.2.1 Interaction of γ-rays in matter

Interaction of γ-rays in matter is different from that of charged particles. The number of γ-rays passing through matter follows a decay law. There are a number of known γ-ray interaction mechanisms in matter. The main processes are the photoelectric effect,

Compton scattering and pair production which play important roles in the energy range that we are interested in (few tens keV to 10 MeV). The other processes like Rayleigh scattering have much smaller cross sections and mainly occur at much lower energy. The observed γ-ray spectrum can be complicated for a given type of γ-ray detector, as a result of the various interactions with matters [86]. One typical spectrum for 2.5 MeV incident γ-ray energy has been plotted in Figure 3.8.

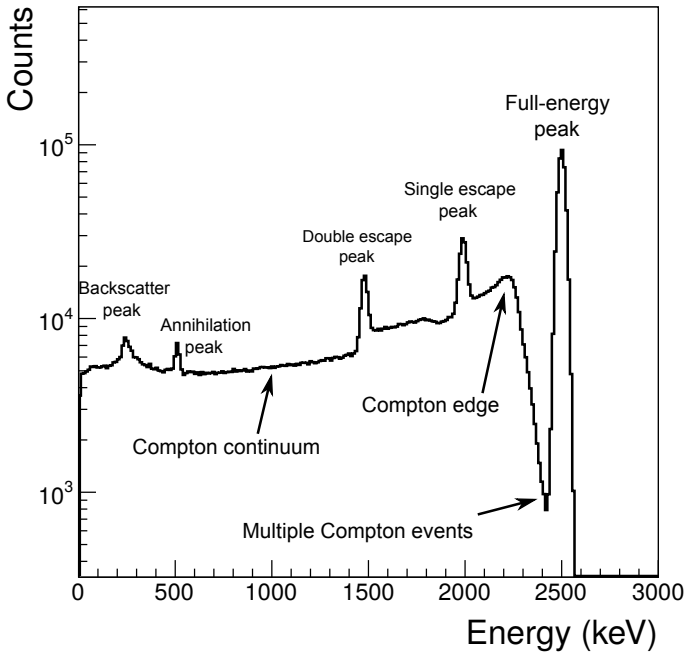

Figure 3.8 – Typical response of a single $LaBr_3$ scintillation detector (surrounded by some Lead shielding) to a mono-energetic γ-ray source of 2.5 MeV, obtained from GEANT4 simulation. Several key components are pointed out. See text for the details of different structures.

In the low photon-energy region, the photoelectric effect is dominant (see Figure 3.9). Part of the incident γ-ray energy is transferred to an atomic electron to free the atomic electron. The remaining energy is transferred to the kinetic energy of the electron. In the second step, outer shell electrons may cascade to the lower atomic energy levels and emit characteristic X-rays (fluorescence). Or outer shell electrons may exhaust the atomic excitation energy and be emitted, *i.e.* Auger electrons. In both cases, the neutral particles transfer all their energy to secondary charged particles (electrons), which can be then collected to measure the incident photon energy. Thus, the photoelectric mechanism is one of the main component of the full-energy peak in the Figure 3.8.

In the intermediate photon energy region, the Compton scattering effect becomes important (see Figure 3.9). The Compton scattering is the inelastic scattering of a photon off an quasi-free electron. The electron is ejected from the atom and the photon is scattered

with a reduced energy. The energy transferred to the electron can vary from zero to a large fraction of the incident photon, following the formula:

$$E_f = \frac{E_i}{1 + \frac{E_i}{m_e c^2}(1 - cos\theta)} \tag{3.6}$$

where E_i and E_f are the initial and scattered photon energy, respectively. When the angle θ between the initial and scattered photon is 180°, the transferred energy is the maximum, corresponding to the Compton edge in the Figure 3.8. The energy distribution of Compton scattered electrons is nearly a constant, exhibiting an almost flat plateau (Compton continuum) from zero energy up to the Compton edge. And due to the fact that the function cosine changes slowly around 180° and 0°, two sharp fringes are observed. However, if the secondary γ-ray deposits its energy in the detector, then the incident γ-ray energy has been measured. This event will then be represented in the full-energy peak.

When the γ-ray energy is larger than 1.022 MeV, pair production starts to play a role, *i.e.* creation of an electron-positron pair (see Figure 3.9). The electrons deposit the energy as described previously. In addition, the positron will annihilate with another electron in the crystal and then produce two photons with energy 0.511 MeV in each. These photons will interact or not inside the crystal. In the case of one photon escape, the detector would then have collected the initial energy minus 0.511 MeV. In the case of two photon escape, the detector would then have collected the initial gamma energy minus 1.022 MeV. The consequence is the appear of single-escape peak and double-escape peak, separated by 0.511 MeV and 1.022 MeV with respect to the full-energy peak, respectively.

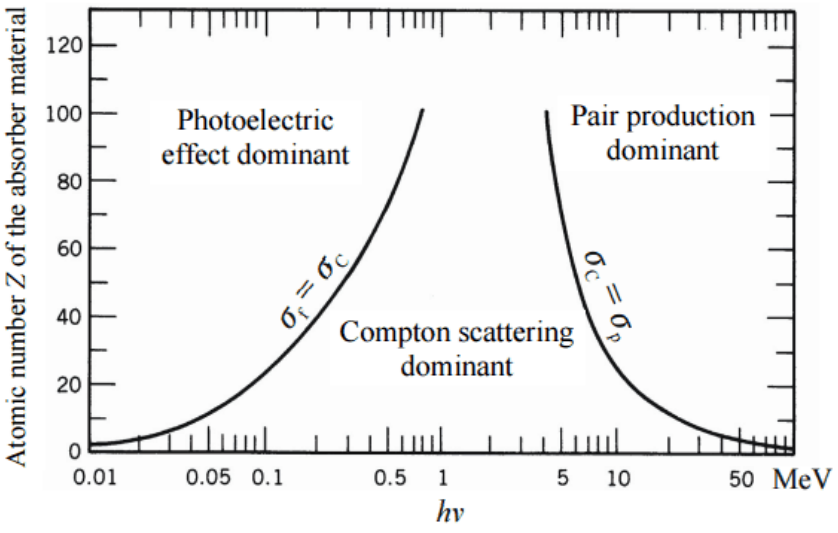

Figure 3.9 – The relative importance of various processes of gamma radiation interaction with matter [87].

Actually, the spectrum is even more complicated because of multiple Compton scatterings, secondary electron escape, bremsstrahlung escape, characteristic X-ray escape and

effect of surrounding materials. The response function of a detector at a given energy is determined by all these different interactions that the radiation can undergo in the detector and the property of the corresponding detector (*i.e.* material composition and geometry). It is usually simulated using Monte Carlo codes in modern calculations, by taking all the possible physical processes and detector properties into account.

3.2.2 Inorganic scintillation γ-ray detector

The scintillation detector is widely used in radiation detection. In terms of γ-rays detection properties, inorganic scintillators are preferred when compared to organic and plastic scintillators, because of the greater light output, higher density and higher atomic number. Above a certain minimum energy (few tens of keV), most inorganic scintillators exhibit a linear relationship between the light output and the incident particle energy. They have fast response and short decay time, *i.e.* good time resolution, small dead time and high counting rate acceptance. In addition, pulse shape discrimination technique (PSD) can be applied to distinguish between different types of incident particles or different types of scintillators [76].

Figure 3.10 is a representative diagram of a scintillation detector. It is mainly composed of scintillator and an associated photomultiplier tube (PMT). The two are connected by a light guide. The inorganic scintillators are mainly crystals of Alkali Halides containing a small fraction of activator impurity. The γ-rays entering the scintillator crystal can ionize the crystal by exciting an electron from the valence band to the conduction band. It creates a freely moving electron-hole pair. Or it can create an exciton by exciting an electron to the exciton band (a loosely bound electron-hole pair). Excitons can migrate through the crystal and be captured by impurity centers, exciting the latter to certain radiative states (fast component). On the other hand, free electron-hole pairs are captured successively resulting in the excitation of certain metastable states (slow component). The time evolution of this emission process is described by linear combination of two exponential decay with the decay constant from the fast and slow component. Thus a single high-energy gamma ray entering the scintillator produces a flash of low-energy photons with two components in terms of the characteristics decay time. These photons are directed to the photosensitive surface (photo-cathode) of a photomultiplier tube, where they eject electrons *via* the photoelectric effect. The number of electrons are then multiplicated in several dynodes and finally collected in the anode to yield a current pulse.

There are three most important properties of a scintillation detector, which need to be taken into account when choosing proper detectors in any experiment: energy resolution, intrinsic detection efficiency and time resolution. The ability to resolve the small differences in the particle energy is referred to the energy resolution. It is characterized by the full width half maximum (FWHM) of the full-energy peaks, which mainly depends

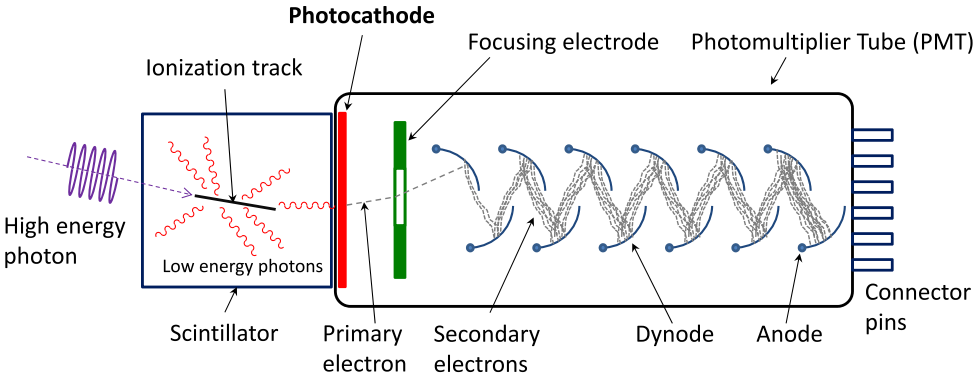

Figure 3.10 – Schematic view of a scintillation detector, including the scintillator and PMT. The high-energy photons hit the scintillator and release low-energy photons, which are then converted into photoelectrons and multiplied in the PMT.

on the light output of the scintillator and corresponding PMT and electronics. Since the mean free path of un-charged γ-rays is large in the material, especially for high-energy γ-rays, a reasonably high efficiency is favourable in consideration of the statistics. Larger density, higher atomic number and larger size increase the detection efficiency. In addition, time resolution is also important, *e.g.* in case of the TOF measurement. The decay time of the scintillator is the main impact factor, especially the fast component, for the time resolution. A number of properties are listed in Table 3.2 for common scintillators used in nuclear physics.

Table 3.2 – Properties of the scintillators used for the γ-ray measurement. Part of data taken from Ref. [88]

	BGO	BaF_2	NaI	$LaBr_3$
Light yield (ph/keV)	9	9	38	60
Primary decay time (ns)	300	600	250	16
ΔE/E(%) at 662 keV	10	13	6	3
Density (g/cm^3)	7.13	4.88	3.67	5.08

In this experiment, three types of fast scintillation detectors were used to measure the PFG: 7 individual Cerium-doped Lanthanum Bromide $LaBr_3$(Ce), a cluster of 9 phoswich detectors from the PARIS array [77–79] and a cluster of 7 Barium Fluoride BaF_2 from the Chateau de Cristal array [89]. The state-of-the-art scintillation detectors made of $LaBr_3$(Ce) (50.8 mm $\times$ 50.8 mm and 76.2 mm $\times$ 76.2 mm in diameter and length) have excellent time resolution ($\sim$300 ps for coincidence gamma rays from ^{60}Co) and good energy resolution ($\sim$3% at 661 keV). These detectors were used in several recent measurements of PFGS from different fissioning systems [25–28]. As their response function is well understood, they are used in this work as the main reference detectors to facilitate the

comparison.

PARIS is an array of a new type of $LaBr_3$(Ce)-NaI(Tl) phoswich detectors, see a photograph in Figure 3.11. The inner shell is $LaBr_3$(Ce) cubic crystals (50.8 mm × 50.8 mm × 50.8 mm) and the outer shell consists of NaI(Tl) rectangular crystals (50.8 mm × 50.8 mm × 152.4 mm). Both crystals are encapsulated in an Aluminium can, sharing one common photomultiplier tube. According to the difference of the decay times of the phoswich scintillators, it is possible to apply PSD (PSD details in Section 3.3.2) to distinguish events occurring in the two layers, see Figure 3.12. In this way, PARIS phoswich detectors benefit from superior energy and time resolution of the $LaBr_3$(Ce) part, and

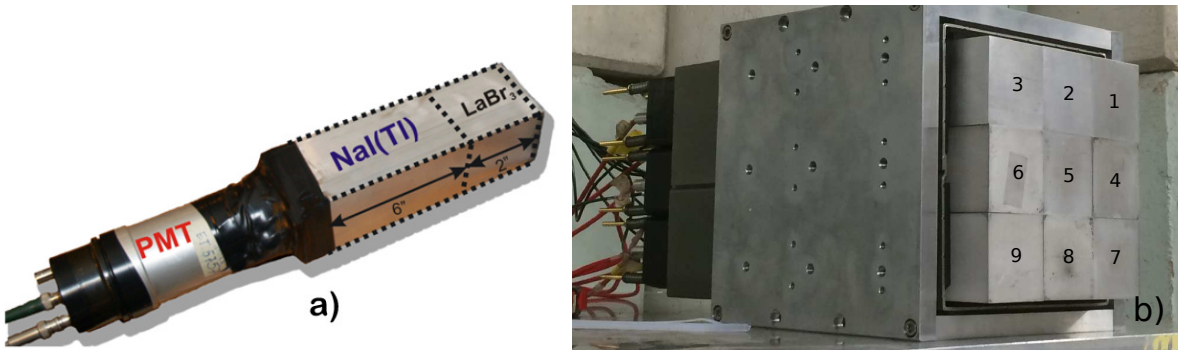

Figure 3.11 – (a) A single PARIS phoswich detector, containing $LaBr_3$(Ce) and NaI(Tl) crystals. The two crystals share one PMT. (b) A cluster of 9 PARIS phoswich detectors used in this work.

increased efficiency, particularly at high energy, from the NaI(Tl) part with larger detection volume. It has lower economical cost than pure $LaBr_3$(Ce) of identical size. Even though the energy resolution is slightly degraded due to this specific design (∼5%), it is not the main constraint in the statistical study of the PFGS and it is still able to resolve the fine structure in the low-energy region.

The BaF_2 scintillators were chosen thanks to their larger stopping power and larger crystal size. However, the energy resolution (∼15%) is much worse compared to $LaBr_3$ and PARIS phoswich. The main drawback is that they have a high detection threshold at around 400 keV, excluding a large part of the information embedded in PFGS.

3.3 Neutron detection

3.3.1 Interaction of neutrons in matter

Neutrons are neutral particles that are insensitive to Coulomb interactions with atomic nucleons and nuclei. The main interaction is through the strong force with the nuclei.

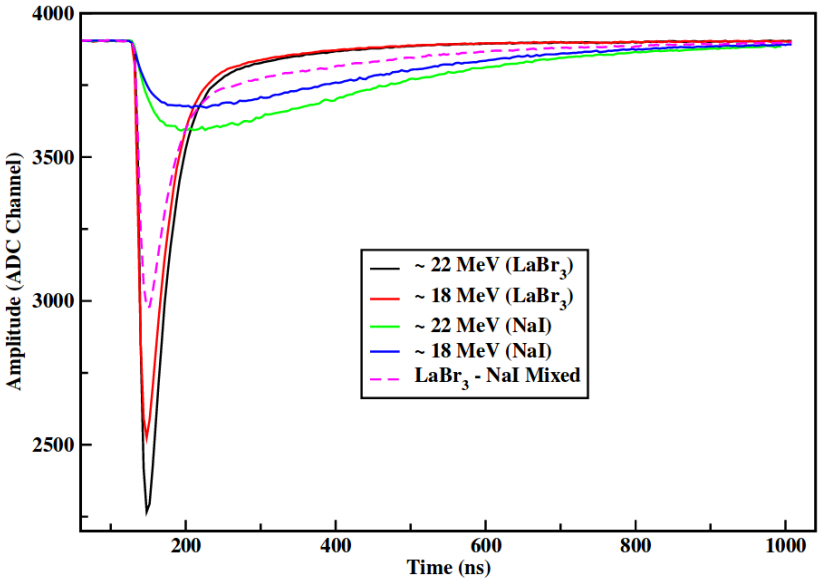

Figure 3.12 – High-energy γ-rays pulses corresponding to different components of PARIS ($LaBr_3$, NaI and mixed) [79].

Due to the short range of this force, the cross section of neutron interactions in matter is small, especially for fast neutrons in the MeV range (the typical energy range generated by the LICORNE neutron source), the cross section usually has only few barns up to few tens of barns, depending on the material. The total probability for a neutron to interact in matter is the cross section summation of all individual reaction channels:

$$\sigma_t = \sigma_s + \sigma_{s'} + \sigma_\gamma + \sigma_f + \cdots \tag{3.7}$$

where σ_s, $\sigma_{s'}$, σ_γ, σ_f are the cross section for elastic scattering, inelastic scattering, capture and fission reactions, respectively [76].

The cross section is strongly dependent on the kinetic energy of the neutron for a given target. In the low-energy region, such as thermal neutrons, the cross section is inversely proportional to neutron velocity $\sigma(E) \propto \frac{1}{v}$. In the high-energy region (MeV), the cross section tends to be constant. This can be explained by considering the wavelength of the neutrons and the radius of the target. Neutron has a de Broglie wavelength $\lambda = \frac{h}{\sqrt{2mE}}$. And the geometric interpretation of the cross section is $\pi(R + \lambda(E))^2$. For neutrons of wavelength much larger than typical radius of atomic nuclei, R can be neglected, which yields the law of 1/v. On the other hand, for neutrons of wavelength is much smaller than radius R, the cross section is only related to $4\pi R^2$, which is a constant and independent of the neutron energy. In addition, neutron resonances peaks are observed, when the energy of the neutron is that a compound nucleus can be formed at a certain excitation state.

In the MeV energy range of fast neutrons, the primary mechanism of energy loss is the elastic scattering and inelastic scattering, until it reaches thermal equilibrium with the

surrounding atoms. The neutrons may undergo a nuclear reaction or be captured before reaching thermal energy due to the 1/v dependence of the cross section, especially if a resonance peak is present.

3.3.2 Organic liquid scintillation neutron detector

Neutron detection is a very difficult task in nuclear physics experiments since neutrons are very penetrating neutral particles. Unlike γ-rays, neutrons have more complicated reaction channels with matters and much smaller cross section in case of depositing all the kinetic energy to charged particles. Alternatively, the time-of-flight (first interaction) of the neutrons can be measured instead of the energy deposition, as a common technique in nuclear physics experiments to measure precisely their energy. Thus organic liquid scintillator detector is usually chosen for this kind of measurement, because they are hydrocarbons, containing a huge amount of hydrogen, and have good n/γ discrimination ability, based on the pulse shape difference. In this experiment, a cylindrical EDEN detector (20 mm $\times$5 cm), filled with NE213 liquid scintillator, was used to detect the neutrons from the LICORNE source. It served as two main functions. One is to obtain the neutron energy using time-of-flight technique and the other is to monitor the beam intensity fluctuation. In addition, NEDA detectors [90] were also tested and used in the ALTO facility.

In neutron detection, γ-rays have to be excluded firstly because γ-ray background is not negligible in the experimental hall and without discrimination, γ-rays hinder the measurement of neutrons. As is mentioned in the last section, the scintillation process in inorganic scintillator is due to the electric band structure found in crystals, while it arises from transitions in the energy levels of a single molecule in organic materials [76]. The time evolution of the pulse from the organic liquid scintillators also has fast and slow components. The fast components corresponds to the photon emission from an excited singlet state (fluorescence) and the slow component corresponds to the photon emission from a converted triplet state (phosphorescence). The proportional of the fast component to the slow component is related to the dE/dx (or ionization density), thus to the nature of the incident particles. In organic scintillator, a high dE/dx produces a high density of excited molecules and hinders the fluorescence process. When a photon interacts in the scintillator, the recoil particle is an electron. While for a neutron interaction, the recoil particle is generally a proton or carbon. Heavy charged particles generally have larger dE/dx compared to light charged particle, see Bethe-Bloch formula 3.1. As a result, the pulse shape induced by neutron interaction always has a high proportion of slow component, while γ-ray interaction exhibits the opposite effect, which allows the discrimination between neutron and γ-rays (see Figure 3.13).

A practical way to discriminate neutron and γ-ray is to plot charge ratio versus total charge, see Figure 3.13. Different integration gates are defined in the left of Figure 3.13.

Q_{tot} is the total charge of the signal, the gate starting before the pulse and ending after the pulse. $Q_{delayed}$ is the delayed part of the charge and the starting point of the delayed gate is crucial to achieve good n-γ discrimination. The point where the neutron signal crosses the γ signal is usually an optimum value. The charge ratio is then defined as the ratio between the delayed charge and the total charge. One example is plotted in the right of Figure 3.13 with NEDA detectors (BC537) used in fast neutron tomography experiment. Another work [91] uses the charge ratio between delayed and quasi-total charge to discriminate neutrons and γ-rays for the liquid scintillator BC501A, with typical gates being total charge [-20 ns,160 ns], delayed charge [-15 ns,160 ns] and quasi-total [-3 ns,160 ns].

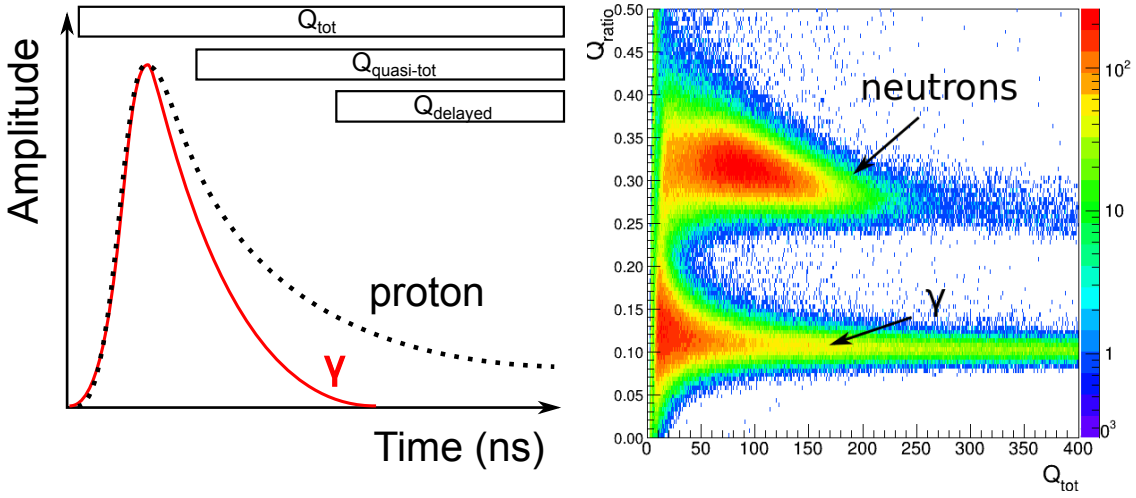

Figure 3.13 – Left: Schematic view of the oscilloscope signal for γ-rays and protons (or neutrons), taken from [86]. The signal induced by neutron interaction always has a higher proportion of slow component compared to γ-rays. Right: n/γ discrimination by plotting the ratio of charges vs. the total charge. Here, the charge ratio is defined as the ratio between the delayed charge and the total charge. See text for the explanation of the definitions.

In addition, an external module, MESYTEC MPD-4 [92], was also used to perform the n/γ discrimination in multi-channel liquid scintillation neutron detectors. It has one PMT signal input and four output signals including integrated PMT charge (Ampl), ratio of fast and slow component of signal (TAC), logic signal with particle selection (n/g-Trig) and without particle selection (Gate). Several parameters including threshold, walk and gain are available for tuning in n/γ discrimination. In the end, the logic signal n/g-Trig is sent to scaler for the beam monitoring, see Figure 3.14.

The energy of neutrons is calculated according to the measurement of the TOF. In the few MeV range of neutrons, the relativistic corrections is negligible and the energy of

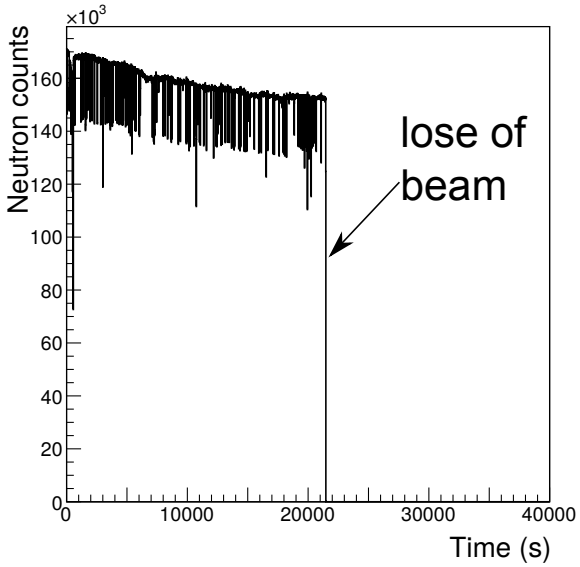

Figure 3.14 – Time evolution of the number of neutrons detected (after n/γ discrimination) in the organic liquid scintillation detector, which represents the fluctuation of the beam intensity in TANDEM.

neutron is simply calculated with the formula:

$$E = \frac{1}{2} m_n v^2 \tag{3.8}$$

$$v = \frac{l}{t} \tag{3.9}$$

where l is the known distance between the target and the scintillator (*e.g.* 1.5 m) and t is the time difference between a start signal and a stop signal. Here, the start signal is given by PMT of the detector when an interaction of neutrons happens in the scintillator. And the stop signal is given by the radio-frequency signal coming from the accelerator that is used to pulse the beam. A schematic view is plotted in Figure 3.15. The radio-frequency signal provided by the IPN Tandem has a width of 2 ns and a period of 400 ns. Both signals are sent to the data acquisition system FASTER and an algorithm is implemented to calculate the time difference between the neutron scintillation detector signal and radio-frequency signal in the corresponding pulse. Finally, the correlation between the TOF versus the charge ratio is plotted in Figure 3.16. The TOF spectra with γ-ray background subtracted can then be obtained.

There are two important properties for the liquid scintillator neutron detector: energy resolution and detection efficiency. According to the formula mentioned above, the neutron energy E is proportional to $\frac{l^2}{t^2}$. Thus the relative error of the neutron energy is [76]:

$$\frac{\Delta E}{E} = \frac{2\Delta t}{t} + \frac{2\Delta l}{l} \tag{3.10}$$

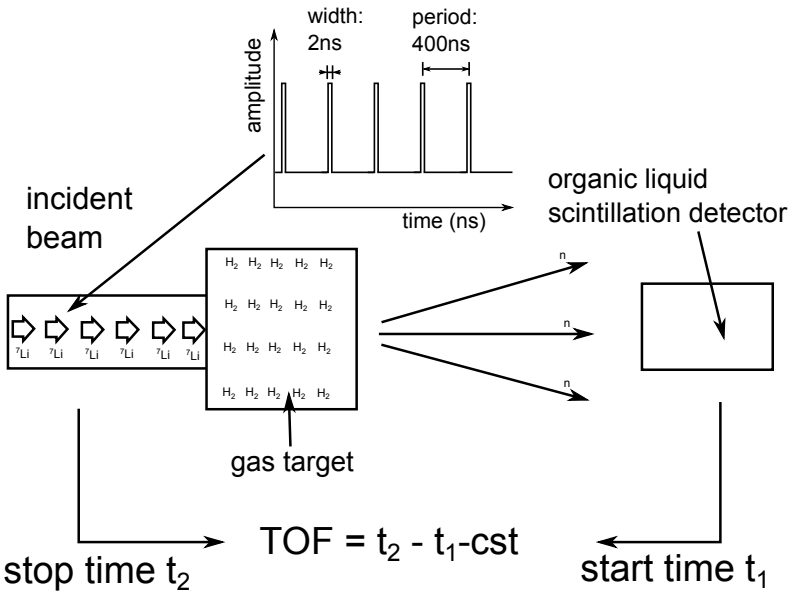

Figure 3.15 – Schematic view of the system of time-of-flight measurement. The arrival of neutrons in the organic liquid scintillation detector gives the start signal and the beam pulsing signal provides the stop signal. A constant offset (cst) is always present due to the time ^{7}Li travels from the beginning to the gas cell and the difference of cable length.

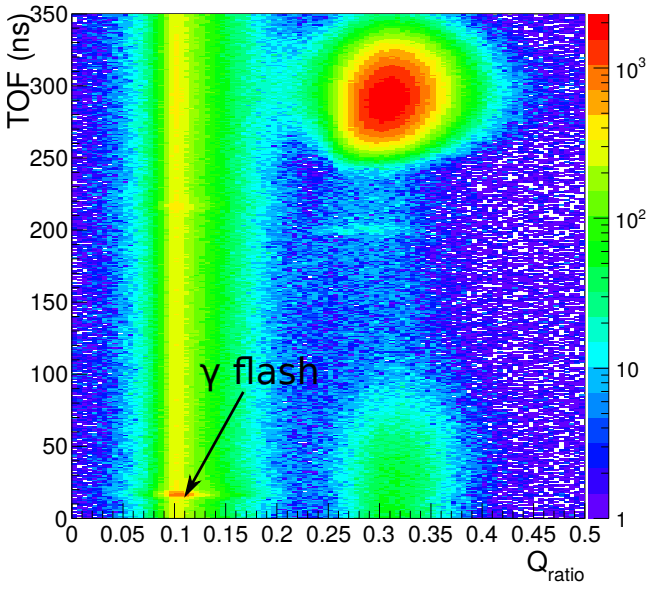

Figure 3.16 – Correlation between TOF and charge ratio in the n/γ discrimination. The γ flash origins from neutron inelastic scattering in coincidence with the beam pulse, which is perfectly known (16.67 ns for a detector placed at 5 m for example) and provides opportunity for the correction of the constant time offset.

It depends on the relative uncertainty of the time-of-flight and the distance measurement. The uncertainty of the distance measurement mainly depends on the spatial distribution of the neutron production in the LICORNE gas cell and the neutron interaction in the EDEN detector. The uncertainty of the time-of-flight measurement includes the width of the neutron pulse, time response of the inorganic scintillator and intrinsic time resolution of the data acquisition system. Thus increasing the distance l (at the same time, t is also increased) improves the energy resolution. On the other hand, the detection efficiency per energy $\frac{\Delta N}{\Delta E}$ is proportional to the geometric factor l^{-2}. As a consequence, the distance has to be compromised between the energy resolution and detection efficiency. In this case, since the neutron energy distribution generated in LICORNE source is not complicated (primary plus satellite neutron energy in general), the task is simply to separate the two neutron peaks, *i.e.* the energy resolution is not the main constraint, and the EDEN detector was placed 1.5 m away from the LICORNE source in the zero degree with respect to the beam axis.

3.4 Data acquisition system

In this experiment, FASTER (Fast Acquisition System for nuclEar Research) [80], a new digital modular acquisition system developed at LPC, was used to treat the signals. It provides CARAS daughter board with 12 bits and a sampling rate of 500 MHz to perform charge and time measurement. Different algorithms can be implemented into FPGA (Field Programmable Gate Array), such as "QDC" and "RF" module, depending on the experimental task. The system has mainly two components: the FASTER console for the coincidence events decision and all the parameters for tuning in different modules, and the histogram builder RHB for visualization (including the oscilloscope). See Figure 3.17 for the interface of the two parallel independent programs. All the signals coming from the radio-frequency, γ-ray detector, neutron detector and fission chamber are sent directly to the FASTER and immediately digitized. These signals are synchronized with a 2 ns internal clock whose period is perfectly defined by a quartz.

The FASTER has "QDC" module for the charge measurement. The signal processing in the "QDC" module will mainly undergo: dynamic range tuning, polarity tuning, constant or dynamic baseline restoration, CFD or leading edge trigger and charge calculation. The dynamic range of the CARAS daughter card is +/-1.2 V. The dynamic range can be shifted by adjusting an offset to make full use of the range in case of high energy γ-rays measurement. The baseline restoration can be achieved either by subtracting a constant level (constant BLR) or by the low-frequency variations (dynamic BLR). Dynamic BLR is preferred due to higher peak-to-noise ratio, except for the high counting rate situation, which is not the case in this experiment. There are three parameters responsible for the dynamic BLR tuning: threshold, gate and Fc (see details in Figure 3.18). The baseline

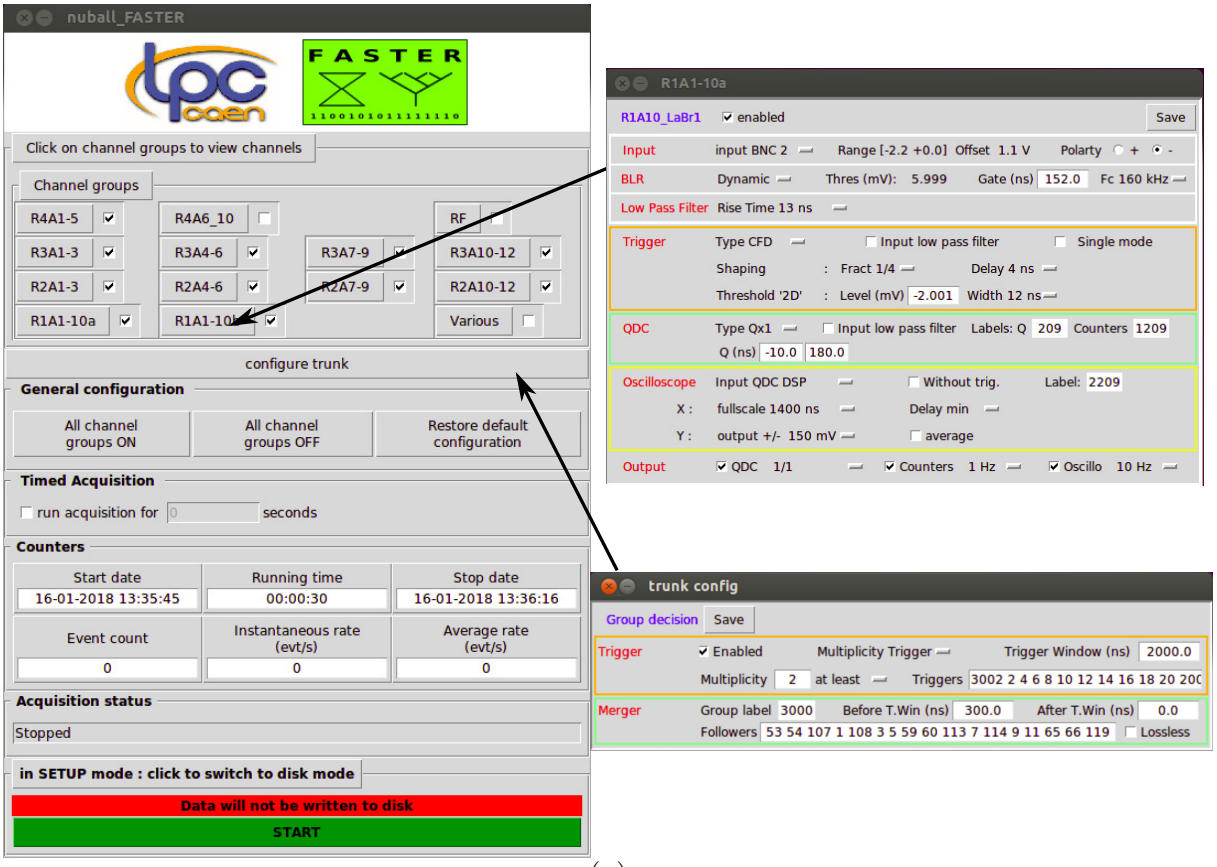

(a)

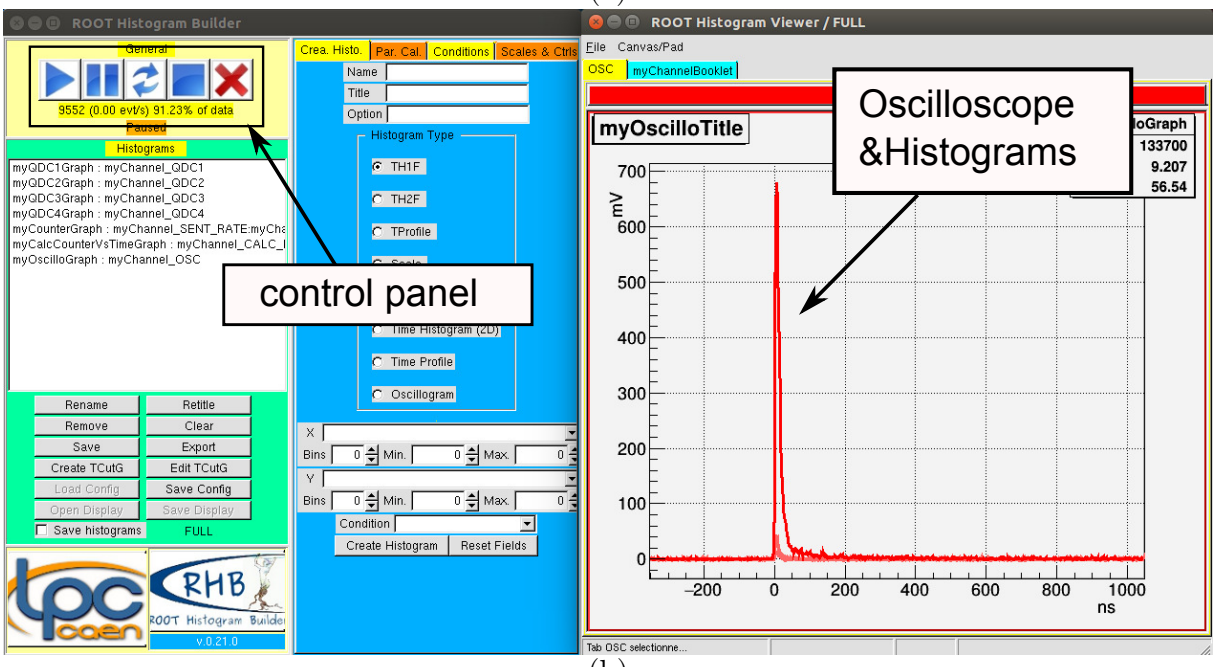

(b)

Figure 3.17 – (a) FASTER console interface; (b) Histogram builder RHB interface.

tracking stops when an event is detected and restarts when the signal is below the threshold and maintain for a duration (gate). The Fc parameter represents the cut-off frequency in the BLR low-pass filter.

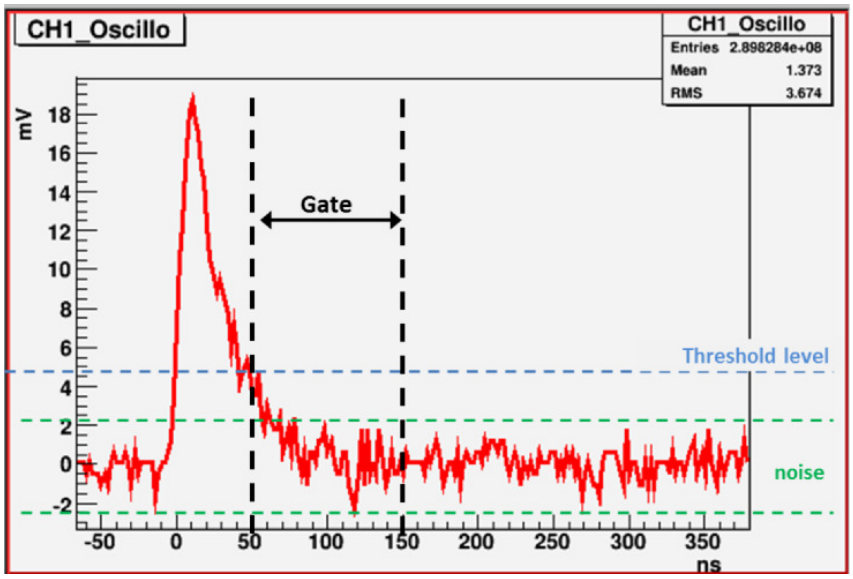

Figure 3.18 – Gate and threshold adjustment in the dynamic base line restoration (BLR) in "QDC" module of FASTER [80].

Each channel in FASTER can apply either internal or external trigger. The internal trigger includes leading edge trigger (threshold) and constant fraction discrimination (CFD) trigger. The CFD trigger minimizes the walk, *i.e.* signals with different energies and same rising time gives different timestamps when using leading edge trigger. It divides the signal into two parts. One is delayed, and a fraction of the other one is subtracted from it:

$$out(t) = f \times in(t) - in(t - \nu) \tag{3.11}$$

where f is the fraction and ν is the delay. The fraction between 0.2 and 0.4 is reasonable for scintillation detector. By definition, the delay time is selected to be equal to the time taken for the input pulse to rise from the fraction (*e.g.* 0.25) of maximum amplitude to maximum amplitude. The attenuated signal is added to the delayed and inverted signal to form a bipolar signal with a zero crossing, see Figure 3.19. This zero crossing is the true time of the event, providing an additional time precision with a 7.8 ps accuracy (based on 2 ns accuracy of the internal clock), as it does not depend any more on the signal rise time. Finally, a 2D threshold, *i.e.* signals under the threshold (level) during a time window (gate), is set on this bipolar signal for internal triggering.

The FASTER has "RF" module to deal with TOF measurement, which is suitable to any cyclotron frequencies ranging from 1 MHz to 100 MHz. It is necessary to know every threshold crossing time, in order to calculate the TOF. But the data acquisition system will be saturated if recording each threshold crossing time with, *e.g.* 2.5 MHz pulsed beam

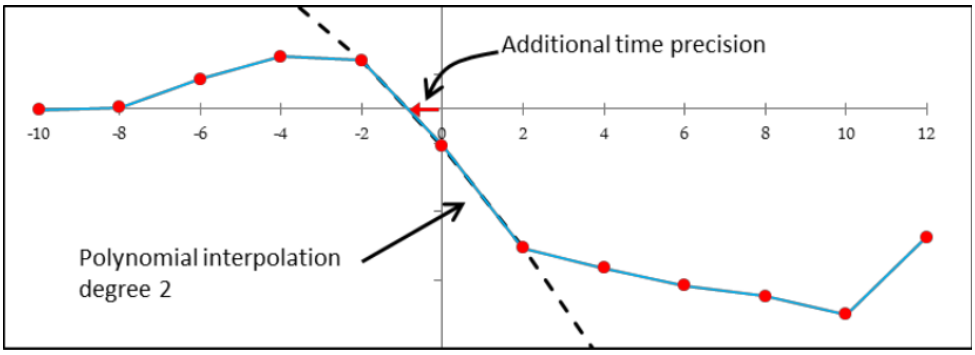

Figure 3.19 – Typical constant fraction discrimination (CFD) signal in "QDC" module of FASTER [80]. A good quadratic polynomial interpolation needs at least 3 points in the zero crossing edge.

in this case. The FASTER has implemented Phase Locked Loop (PLL) to record part of the signals, *e.g.* 1/1000 of the total number of the signals, for the threshold crossing time. Then any threshold crossing time can be deduced with the period of the radio-frequency by the formula:

$$t_n = t_{c1} + nT_{cycl} \tag{3.12}$$

where t_{c1} is the current threshold crossing time, n is the number of period in between and T_{cycl} is the period, more information see Figure 3.20.

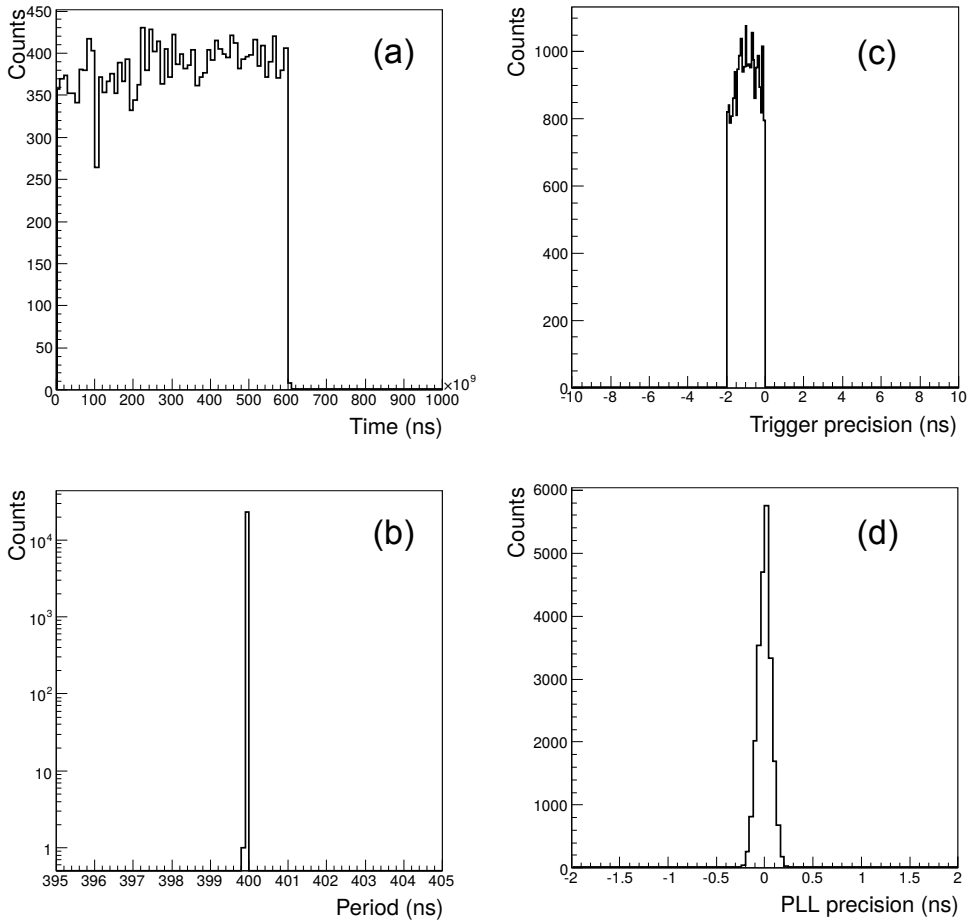

Figure 3.20 – (a) Beam intensity fluctuation as a function of time; (b) Calculated period of the beam pulse; (c) Precision of the threshold crossing time; (d) Precision of the PLL reconstruction algorithm.

In this chapter, the experimental setup has been discussed, including different types of detectors and measurement techniques. The fission fragments are measured in the ionization chamber. High kinetic energy of fission fragments compared to α particles enable fission tagging. The coincident γ-rays are measured in scintillation detectors, including high efficiency gamma detectors PARIS. At the same time, liquid scintillation detectors were used for the LICORNE neutron energy determination and beam intensity monitoring. In the next chapter, the detailed data analysis procedures will be presented.

Chapter 4
Data Analysis

In this chapter, we describe how the prompt fission γ-ray spectrum and its spectral characteristics are obtained from the raw data acquired by FASTER. Firstly, the γ-ray detector is calibrated by using various radioactive sources and neutron activation sources. Detector characteristics from few tens of keV to 9 MeV are presented. Secondly, the incident neutron (from LICORNE source) on actinide samples is characterized by using the liquid scintillation detector and the GEANT4 simulation code, as discussed in Section 2. Thirdly, fission events are selected according to the charge spectrum from ionization chamber. Fourthly, the measured PFG are selected by eliminating the prompt neutron response in the γ-ray spectrometer *via* TOF technique. Then, the measured PFGS are unfolded to recover the complex γ response in each individual detector, whose response function relies on the GEANT4 simulation. Finally, the unfolded spectrum and its spectral characteristics will be presented for different fission reactions, including ^{252}Cf(sf), ^{238}U(n$_{fast}$,f) and ^{239}Pu(n$_{fast}$,f).

4.1 γ-ray detector characterization

4.1.1 Pre-treatment

Rare-earth Halide based scintillation detector (*e.g.* $LaBr_3$(Ce)) is a new generation of scintillation detectors in γ-rays measurement with excellent energy resolution ($\sim$3% at 661 keV), sub-nanosecond time resolution ($\sim$300 ps) and relatively high intrinsic efficiency, compared to the last generation of scintillation detectors such as Sodium Iodine detectors NaI(Tl) and Barium Floride detectors BaF_2. The scintillation detectors made of $LaBr_3$(Ce) used in this experiment have two sizes: 50.8 mm $\times$ 50.8 mm and 76.2 mm $\times$ 76.2 mm in diameter and length, coupled with PMT 7723-100 of Hamamatsu. These detectors were used in several recent measurements of PFGS from different fissioning systems [25–28]. As their response function is well understood, they are used in this work as the main reference detectors to facilitate the comparison.

PARIS is a new type of phoswich detector $LaBr_3$(Ce)-NaI(Tl), where both crystals are encapsulated in an Aluminium can and share one common PMT. Due to the composite in nature, the response of PARIS is more complicated than a pure $LaBr_3$ scintillation detector. Depending on the large difference of the pre-amplifier signal decay times (*i.e.* 16 ns for $LaBr_3$ and 250 ns for NaI), pulse shape discrimination (PSD) can be applied to resolve the event reconstruction of each component (see Figure 4.1). PARIS phoswiches benefit of a better time and energy resolution than a simple NaI and a higher efficiency than a single $LaBr_3$ crystal. A practical way to resolve the events in each component is to plot a two-dimensional histograms of two charges of the signal, see Figure 4.1. The two charges Q_{short} and Q_{long} correspond to two different integration gate on the signal. One with a short gate on the signal of [-20 ns, ∼300 ns] (for $LaBr_3$(Ce) signal) and the other with a long gate of [-20 ns, ∼900 ns] (for both $LaBr_3$(Ce) and NaI(Tl) signals). A first line on the top corresponds to the events of the full γ energy deposition in $LaBr_3$(Ce) part. The second line below corresponds to the events of the full γ energy deposition in NaI(Tl) part. The area between the two stripes corresponds to the events of partial energy deposition in either of them (mixed events).

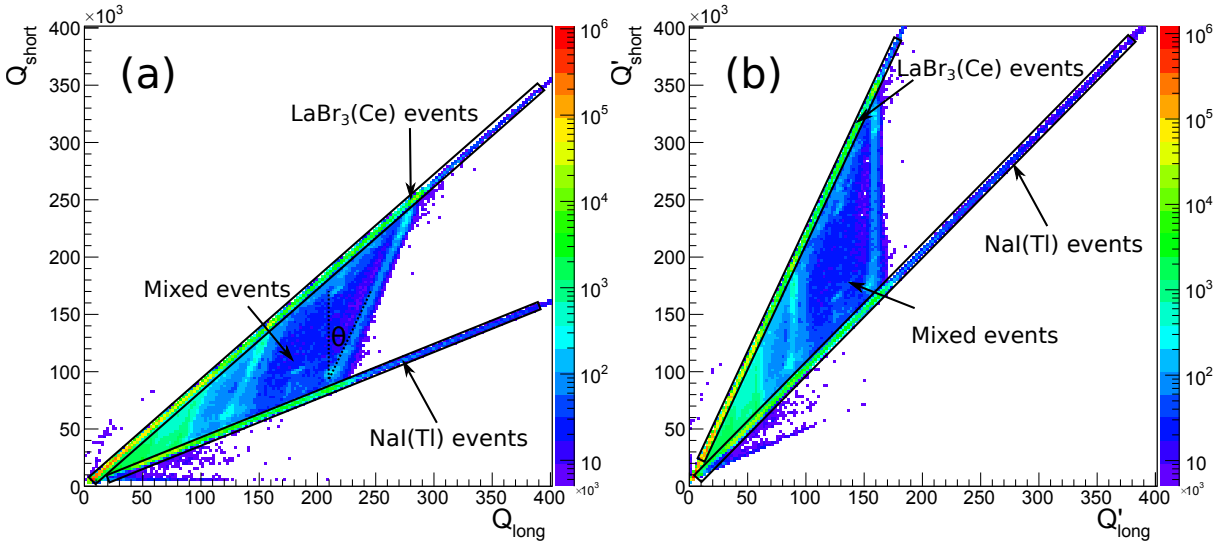

Figure 4.1 – Correlation between Q_{short} and Q_{long} before and after rotation. Q_{short} and Q_{long} represent the integrated charge over the short and long time gates, respectively. A clear discrimination of different events in a PARIS phoswich crystal can be achieved.

In order to make optimal use of a PARIS phoswich detector, the reconstruction of the total energy deposited in $LaBr_3$(Ce) and NaI(Tl) crystals is essential. Figure 4.1 shows that $LaBr_3$(Ce) and NaI(Tl) crystals have different gains. In their work, M. Zieblinski *et al.* [78] has demonstrated that by rotating two-dimensional histogram with a well chosen angle, a same gain can be obtained for both crystals, which facilitates the calibration

procedure. The rotation angle is chosen in order to make mixed events vertical, as represented by θ in Figure 4.1(a). In another work, C. Ghosh [79] proposed an algorithm that reconstructs the energy deposition in the individual $LaBr_3$(Ce) and NaI(Tl) phoswich elements separately.

In this work, in order to improve the energy resolution in the total energy spectrum, the event of energy deposition in $LaBr_3$(Ce) only was extracted directly (no rotation) with a graphic cut (called a ROOT TCUTG [69]) of the stripe and projected to the Q_{short} axis for the subsequent calibration. This calibrated energy of $LaBr_3$ events is denoted as E_1. On the other hand, the mixed events and NaI(Tl) events were extracted by rotating the histogram by an angle θ anti-clockwise (same definition in Ref. [78]) and projected to the Q_{long} axis for calibration. This calibrated energy of NaI(Tl) and mixed events is denoted as E_2. For each event, total energy E_{tot} is then obtained in terms of internal add-back within each phoswich:

$$E_{tot} = E_1 + E_2 \tag{4.1}$$

where E_1 corresponds to $LaBr_3$(Ce) events and E_2 to the mixed events and NaI(Tl) events. Figure 4.2 plots the energy spectrum of different components in the phoswich. The red curves represents the total energy E_{tot} measured in a phoswich, which is the summation of the contributions from $LaBr_3$, NaI(Tl) and mixed events.

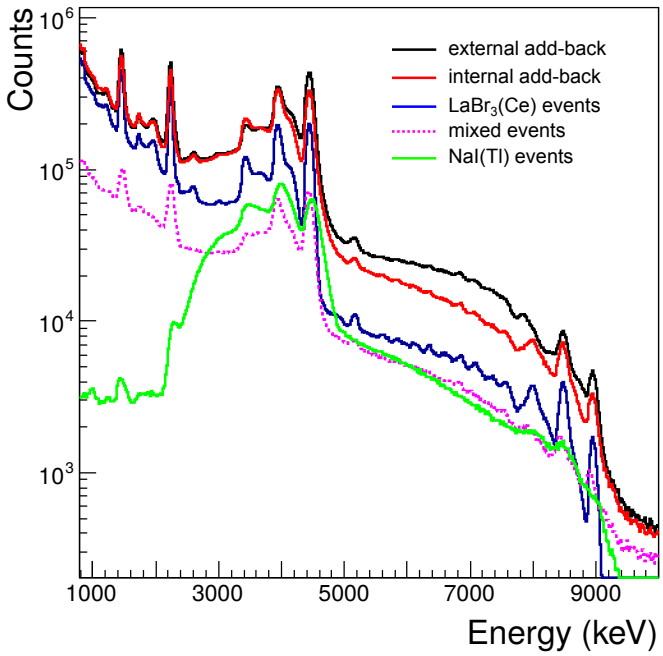

Figure 4.2 – Measured spectrum of 9 MeV γ-ray source (AmBe plus Nickel foils, discussed in the next section) for one single PARIS phoswich. Contributions from different components of the phoswich as well as external add-back have been pointed out.

A cluster of 9 PARIS phoswich detectors were used in this work. The scattered γ-rays between neighbouring phoswich detectors can also be reconstructed by applying external add-back algorithm in the cluster level. When less than 4 phoswich detectors are fired, the γ-ray energies are summed up and attributed to the phoswich detector which has the maximum energy deposition. The black curve in Figure 4.2 represents the energy spectrum for one phoswich after external add-back algorithm.

4.1.2 γ-ray sources

Generally, in nuclear physics spectroscopy experiments, measurements focus on the low-energy γ-rays, *e.g.* up to 3 MeV. As a consequence, the calibration and characterization of the γ-ray detectors are usually performed by using various radioactive sources with low-energy γ-rays, *i.e.* ^{60}Co, ^{137}Cs and ^{152}Eu (see Table 4.1). However, in the study of PFG, the energy range is from a few tens keV up to a few tens MeV, which then requires an extension of the characterization to the high-energy region. It is essential because the scintillation detector may lose its linearity in the high-energy region due to the fact that the high light yield of the crystal may saturate the response of PMT. In addition, the energy resolution and detection efficiency as a function of γ-ray energy up to 10 MeV are needed as an input data for the subsequent γ-ray response function construction. In this work, the characterization and calibration (*i.e.* linearity, energy resolution, time resolution and detection efficiency) of the γ-ray detector are performed with the radioactive sources mentioned in Table 4.1: common γ-ray source (^{60}Co, ^{152}Eu), Thorium decay series, americium-beryllium (AmBe, a mix of ^{241}Am and ^{9}Be) source and γ-rays from thermal neutron capture reaction (n,γ) on Nickel foil, covering an energy range between 40 and 8997 keV.

In thorium decay series, only the gamma line relative intensities are known. The so-called "point-pair" method has to be applied in order to obtain the absolute efficiency at high-energy region [93]. That is to set the lower energy gamma line to the region of known detection efficiency to obtain the absolute intensity, where detection efficiency is already calibrated by other common sources. And the absolute intensity of the higher energy γ-rays in the un-calibrated region is then calculated with the numbers presented in Table 4.1.

High-energy γ-rays are usually obtained in accelerator-based reactions, *e.g.* (p,γ) reactions. In this work, a practical and convenient source of 9 MeV γ-rays [94] was obtained by using AmBe fast neutron source and thermal neutron capture Ni(n,γ) reaction, with the features of low cost, portability, and long-term stability. A box with several pieces of paraffin was built to thermalize the fast neutrons emitted from the AmBe source and the thermal neutrons are then captured on the Nickel foil, emitting 8997 keV γ-rays at a rate of 0.26γ per capture [94]. The thermal neutron flux and capture rate are simulated in GEANT4, see Figure 4.3, which allows the deduction of the absolute intensity of the

8997 keV γ-rays.

Table 4.1 – A list of γ-ray energies and intensities for detector calibration in this work. The 0.583 MeV and 2.614 MeV γ-rays are from β decay of ^{208}Tl ($T_{1/2}$=3.053 min) in ^{228}Th ($T_{1/2}$=1.9116 y) decay chain. The 4.439 MeV γ-ray is due to the de-excitation of $^{12}C^*$, created from the $^{9}Be(\alpha, n)^{12}C^*$ reaction in AmBe source. The 8.997 MeV γ-ray comes from the thermal neutron capture reaction on Nickel foil.

Nuclide	Energy	Intensity	Nuclide	Energy	Intensity
^{137}Cs	661.66	0.8510	Th chain	238.63	-
^{60}Co	1173.24	0.9997		473.00	-
	1332.50	0.9998		510.77	-
^{152}Eu	40.93	-		583.19	0.8506*
	76.20	-		794.95	-
	121.78	0.2858		911.20	-
	244.70	0.0758		2614.51	0.9975*
	344.28	0.2650	AmBe	3416.91	-
	411.12	0.0223		3927.91	-
	443.96	0.0281		4438.91	0.56**
	778.90	0.1242	Ni(n, γ)	7975	-
	867.38	0.0424		8486	-
	964.08	0.1460		8997	0.26***
	1408.01	0.2100			

*"point pair" method to get the absolute efficiency at 2614.51 keV [95]; **The 4.439 MeV γ-ray to neutron ratio for the AmBe neutron source [96]; ***The 8.997 MeV γ-ray per capture ratio in Ni(n,γ) reaction [94];

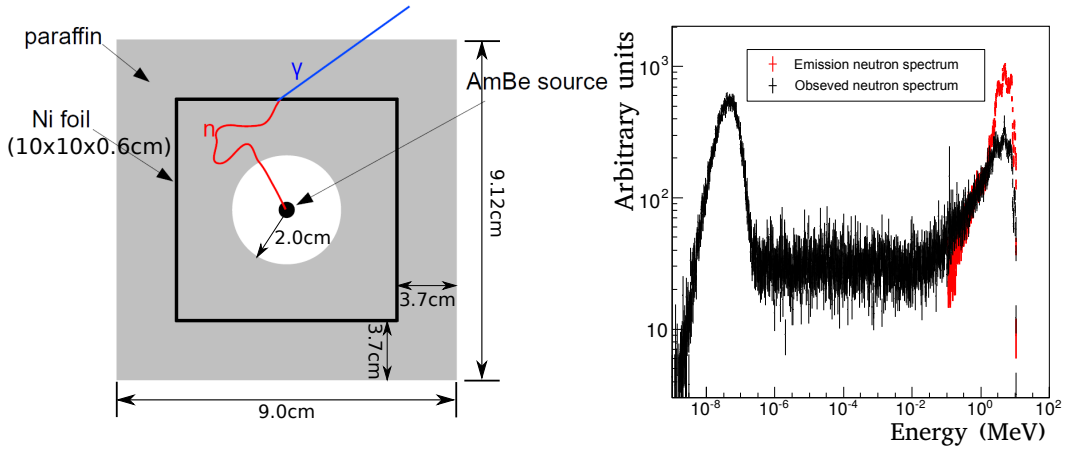

Figure 4.3 – Left: Schematic of the 9 MeV γ-ray source, consisting of AmBe source, paraffin and Nickel foils. Right: Emission neutron spectrum from the AmBe source and observed neutron spectrum in the Nickel foils. The fast neutrons from the AmBe source are thermalized by the surrounding paraffin, and then captured on the Nickel foils.

4.1.3 Calibrations

The calibration was performed at the beginning and at the end of the experimental with the radioactive sources presented in the previous section, to monitor the gain stability. The high voltage supplies for the γ-ray detectors was tuned to insure that the dynamic range is up to 10 MeV, taking into account that the maximum voltage of the CARAS daughter card in FASTER is 2.4 V (+/-1.2 V). Before each calibration run with the sources, the background was measured without any source in the experimental hall, because $LaBr_3(Ce)$ contains radioactive contaminants that raise the background levels in detector response. During the data analysis, the γ-ray spectrum was firstly background subtracted and then each full energy peak in the spectrum was fitted with a Gaussian function and a linear background, which gives centroid, sigma and height for each peak. One example of the fitting process, on the ^{137}Cs full energy peak at 661.7 keV, is plotted in the Figure 4.4.

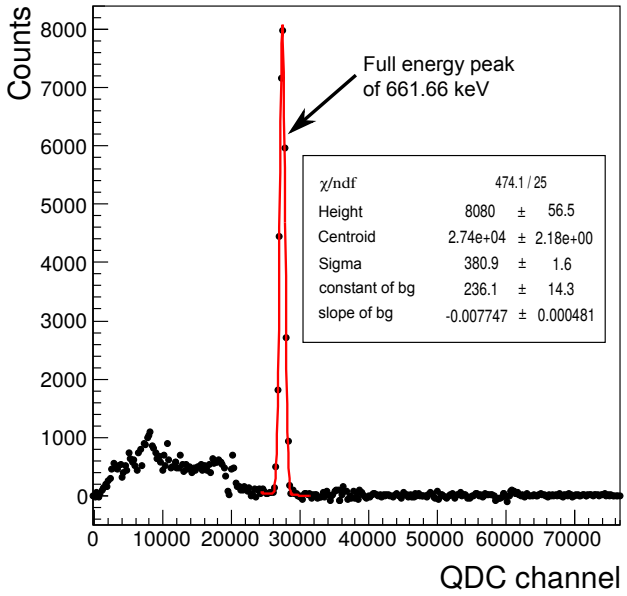

Figure 4.4 – Background subtracted γ-ray spectrum of ^{137}Cs source for $LaBr_3(Ce)$ detector Q5414. The full energy peak has been fitted with a Gaussian function and a linear background, and the fitting results are noted.

The centroids obtained as a function of the γ-rays energy indicate the linearity of the energy response of the detector, whose slope is the so-called gain. The non-linearity α is estimated as the deviation of the channel to a linear fit with the experimental results. The quantity of non-linearity has been summarized in Table 4.2 at two γ-ray energies, 4.438 MeV and 8.997 MeV respectively. Up to the γ-ray energy of 4.438 MeV, the non-linearity is under the energy resolution (except few detectors like Q5414, Paris3 and Paris7). It shows that the linearity is acceptable for both $LaBr_3$ and PARIS phoswich

detectors up to γ-ray energy 4.438 MeV with the current PMT. In practical, a second order polynomial function can be applied to the experimental data to achieve better fit, see one example in Figure 4.5. It constrains the relative deviation to be within the detector resolution at both low-energy region and high-energy region.

Table 4.2 – The summary of non-linearity α of the γ-rays detectors at E_γ = 4.438 MeV and 8.997 MeV, respectively.

Detector	α(%) @4.438 MeV	α(%) @8.997 MeV	Detector	α(%) @4.438 MeV	α(%) @8.997 MeV
Thalia	0.42	1.88	Paris1	1.67	4.26
Aglaea	0.54	1.27	Paris2	0.94	0.76
Euphra	0.09	1.23	Paris3	3.57	6.63
Q5414	3.38	5.41	Paris4	0.64	3.16
Q9624	2.86	2.41	Paris5	1.54	3.29
Q9625	2.18	1.94	Paris6	1.50	4.26
			Paris7	4.19	6.75
			Paris8	2.36	5.16
			Paris9	2.61	5.55

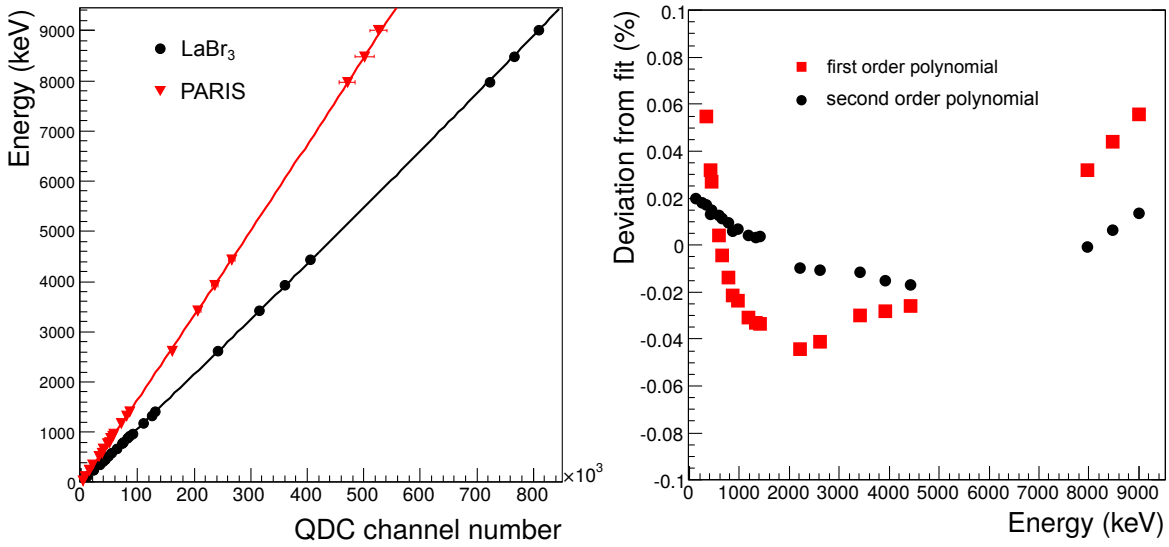

Figure 4.5 – (a) Energy response of the scintillation detector $LaBr_3$ and phoswich detector PARIS, respectively, *i.e.* correlation between γ-ray energy and QDC channel number; (b) Relative residuals of the linear fit to the experimental data of one $LaBr_3$ detector in the energy range from 0.1 MeV to 9.0 MeV.

The full width half maximum (FWHM) of a peak is used to define the energy resolution of a detector. The energy resolution resolves the small differences in the incident particle

energy. When using Gaussian functions to fit the full energy peaks, the obtained sigma can be easily transformed to the FWHM by:

$$FWHM = 2\sqrt{2ln2}\ \sigma \approx 2.3548\sigma \tag{4.2}$$

For comparison with other detectors, the relative energy resolution (FWHM/E) at 661.66 keV (^{137}Cs) is used as a reference. The measured energy resolution are listed in Table 4.3 for each detector. It is also plotted as a function of the γ-ray energy in Figure 4.6. This dependency can be described by the function:

$$(\frac{FWHM}{E}) = \sqrt{\alpha^2 + \frac{\beta^2}{E} + (\frac{\gamma}{E})^2} \tag{4.3}$$

where α represents the light transmission from the scintillator to the photo-cathode, β represents the statistical nature of the light production, attenuation, photon–electron conversion and electron amplification, and γ is the noise term due to the photomultiplier tube and the electronic amplification [97].

Table 4.3 – Summary of the energy resolution in terms of relative FWHM at γ-ray energy of 661.66 keV from ^{137}Cs source.

Detector	$\frac{dE}{E}$ (%)
Thalia	3.29
Aglaea	3.48
Euphra	3.25
Q5414	3.26
Q9624	2.86
Q9625	3.02

Detector	$\frac{dE}{E}$(tot) (%)	$\frac{dE}{E}$($LaBr_3$) (%)	$\frac{dE}{E}$(NaI) (%)
Paris1	5.82	5.13	8.92
Paris2	6.29	5.71	10.87
Paris3	5.92	5.56	9.59
Paris4	4.70	4.40	12.22
Paris5	4.93	4.82	10.52
Paris6	4.79	4.56	7.87
Paris7	6.13	5.30	8.98
Paris8	6.25	5.74	9.49
Paris9	5.82	5.36	9.16

The detection efficiency is another important aspect of a γ-ray spectrometer. Especially in this type of experiment, the fission cross section in the fast-neutron region is very low - three orders of magnitude lower than thermal-neutron-induced fission - and thus the statistics of PFG emitted is limited. Detection efficiency is generally defined as the ratio of the number of counts in full-energy peak by the number of photons emitted from the source, also known as the full-energy peak efficiency. It depends on the geometrical conditions and intrinsic properties of the detectors, as well as γ-ray energy. It can be described as a production of the geometrical efficiency ϵ_g and intrinsic efficiency ϵ_i. The geometrical efficiency ϵ_g is the ratio of the number of photons emitted towards the

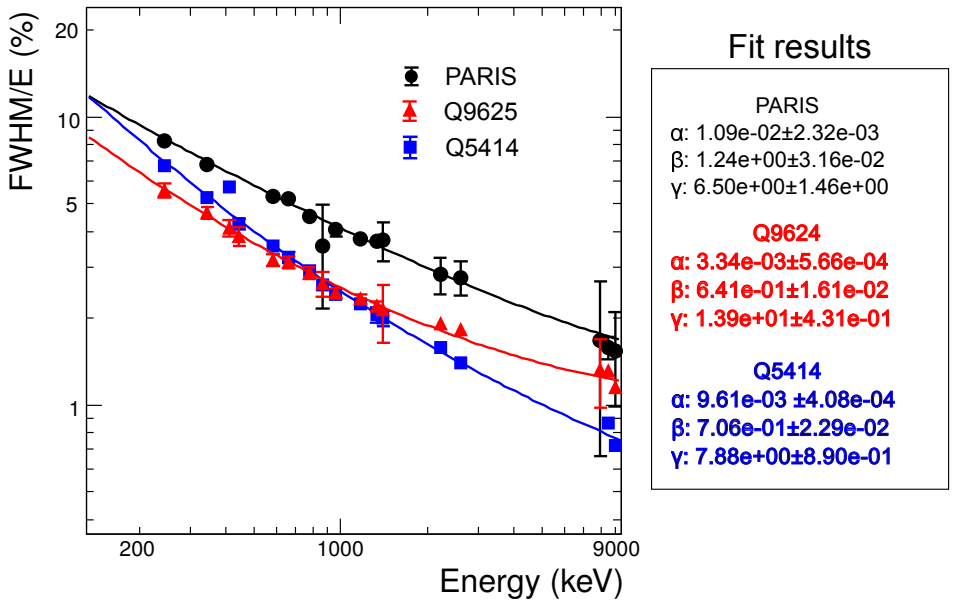

Figure 4.6 – Relative FWHM evolution as a function of the γ-ray energy for a single PARIS phoswich, $LaBr_3$ detector Q9625 (76.2 mm × 76.2 mm) and Q5414 (50.8 mm × 50.8 mm), respectively.

detector by the number of photons emitted by the source:

$$\epsilon_g = \frac{1}{2}\left(1 - \frac{d}{\sqrt{d^2 + r^2}}\right) \tag{4.4}$$

where d is the distance between the detector and source, r is the radius of the front surface of the detector. The intrinsic efficiency is the ratio of the number of counts in full-energy peak by the number of impinging photons, which depends on the photon transmission through the front window and interaction in the scintillator. It is difficulty to calculate the intrinsic efficiency and generally simulated in Monte Carlo codes, *e.g.* GEANT4.

The full-energy efficiency, obtained from different radionuclides mentioned before, needs to be fitted with mathematical functions in order to estimate efficiency at any energy. The dependency between full-energy efficiency and γ-ray energy is fitted according to the function that has been widely used for HPGe detectors [98] with the form:

$$\ln \epsilon(E) = \exp\left(a_0 + a_1 \ln E + a_2 (\ln E)^2 + a_3 (\ln E)^3\right) \tag{4.5}$$

The polynomial degree is adjusted to three according to the reduced chi-square values at different degrees. A smooth shape can be seen in Figure 4.7 in log-log scale with the polynomial fitting function.

Apart from the linearity, energy resolution and efficiency calibration, the time reso-

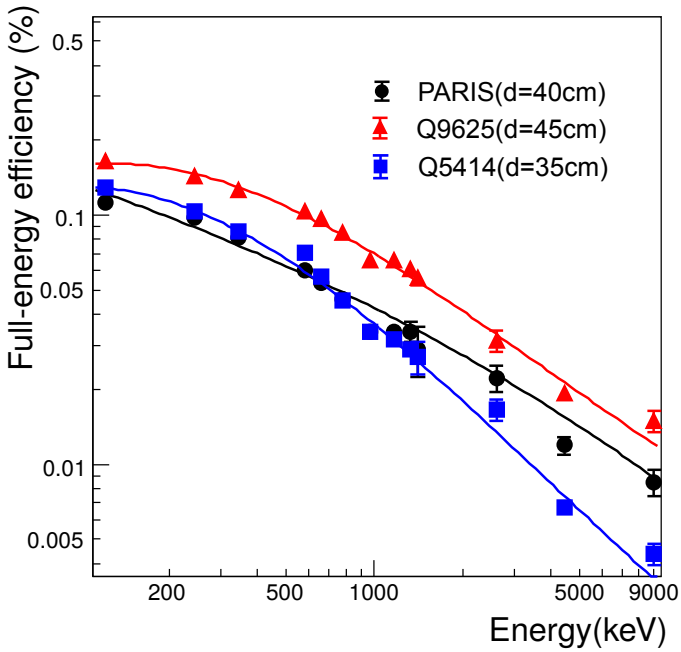

Figure 4.7 – Full-energy detection efficiency evolution as a function of γ-ray energy for a single PARIS phoswich, $LaBr_3$ detector Q9625 (76.2 mm $\times$ 76.2 mm) and Q5414 (50.8 mm $\times$ 50.8 mm), respectively.

lution measurement for the γ-ray detectors also needs to be performed. In this work, production of two coincident photons from ^{60}Co source (E_γ 1.17 MeV and 1.33 MeV) was used to perform such kind of characterization. One $LaBr_3$ that had been proved with good time resolution (~300 ps) in previous experiment was used as a reference detector. The coincidence time spectrum of the prompt cascade was then obtained whenever these two photons are measured at the reference detector as well as any other detector at the same time.

The obtained coincidence time spectrum is a superposition of the delayed and anti-delayed time distributions. The delayed time distribution corresponds to decay transition gated on stop detector and the anti-delayed time distribution corresponds to decay transition gated on start detector. The centroid shift of the delayed and anti-delayed time distribution equals to 2τ, where τ is the mean lifetime of the state (τ=1.30 ps for the $I^\pi = 2^+$ level at 1332.5 keV in ^{60}Ni). The superimposed spectrum of the delayed and anti-delayed time distribution (Figure 4.8) exhibits one Gaussian-like peak with the current binning. The width of the superimposed spectrum is a measure of the time resolution of the detectors. The obtained FWHM equals to 364 ps for $LaBr_3$ (50.8 mm $\times$ 50.8 mm), 725 ps for $LaBr_3$ (76.2 mm $\times$ 76.2 mm) and 417 ps for PARIS phoswiches, see one example in Figure 4.8.

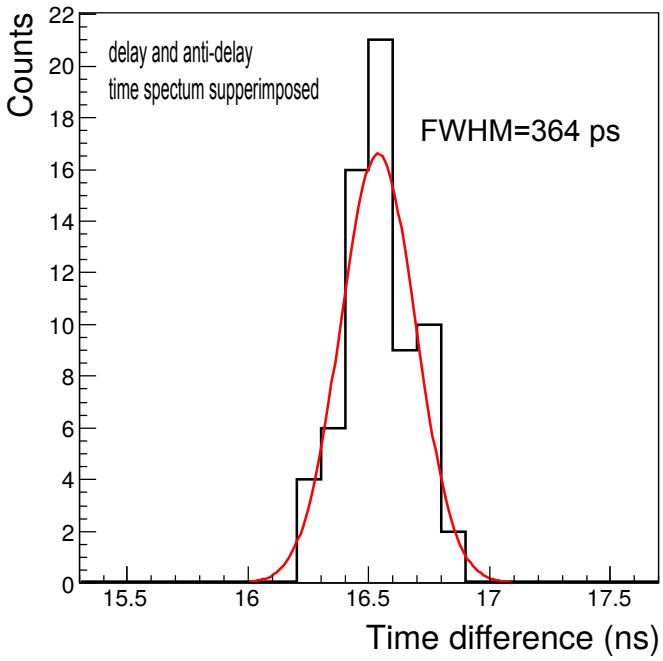

Figure 4.8 – Coincidence time spectrum of the prompt cascade from ^{60}Co source (E_γ 1.17 MeV and 1.33 MeV). The delayed and anti-delayed time distribution are superimposed and the FWHM gives the characteristic time resolution.

4.2 Neutron energy determination

The LICORNE neutron source, by using inverse kinematics, has a complex spatial variation of neutron energy spectra compared to direct kinematics, as discussed in Section 2. The neutron spectra seen by the samples vary as a function of the solid angle covered. In addition, the geometrical information of some elements remain uncertain, *e.g.* the thickness of Tantalum foil under deformation from the gas pressure is difficult to estimate. Thus the determination of the incident neutron energy on the actinide samples relies on the simulation of the inverse kinematics inside the hydrogen gas target, as is discussed in the Section 2.2, and a subsequent validation using a neutron TOF measurement at 1.5 metres (or 3.0 meters) from the LICORNE source (Section 2.3).

The TOF measurement had been performed at the beginning of the experiment with the pulsed beam (400 ns period, 2 ns width), with EDEN and NEDA liquid scintillation detectors used in such measurements. The validation is performed through a comparison between simulated and measured TOF spectra in EDEN or NEDA neutron detectors, see Figure 4.9 and Figure 4.10 in the left. The good agreement allows the deduction of the neutron spectra seen by the samples with the same parameters of the LICORNE setup in GEANT4 simulation. Then, the total neutron spectra seen by all the samples

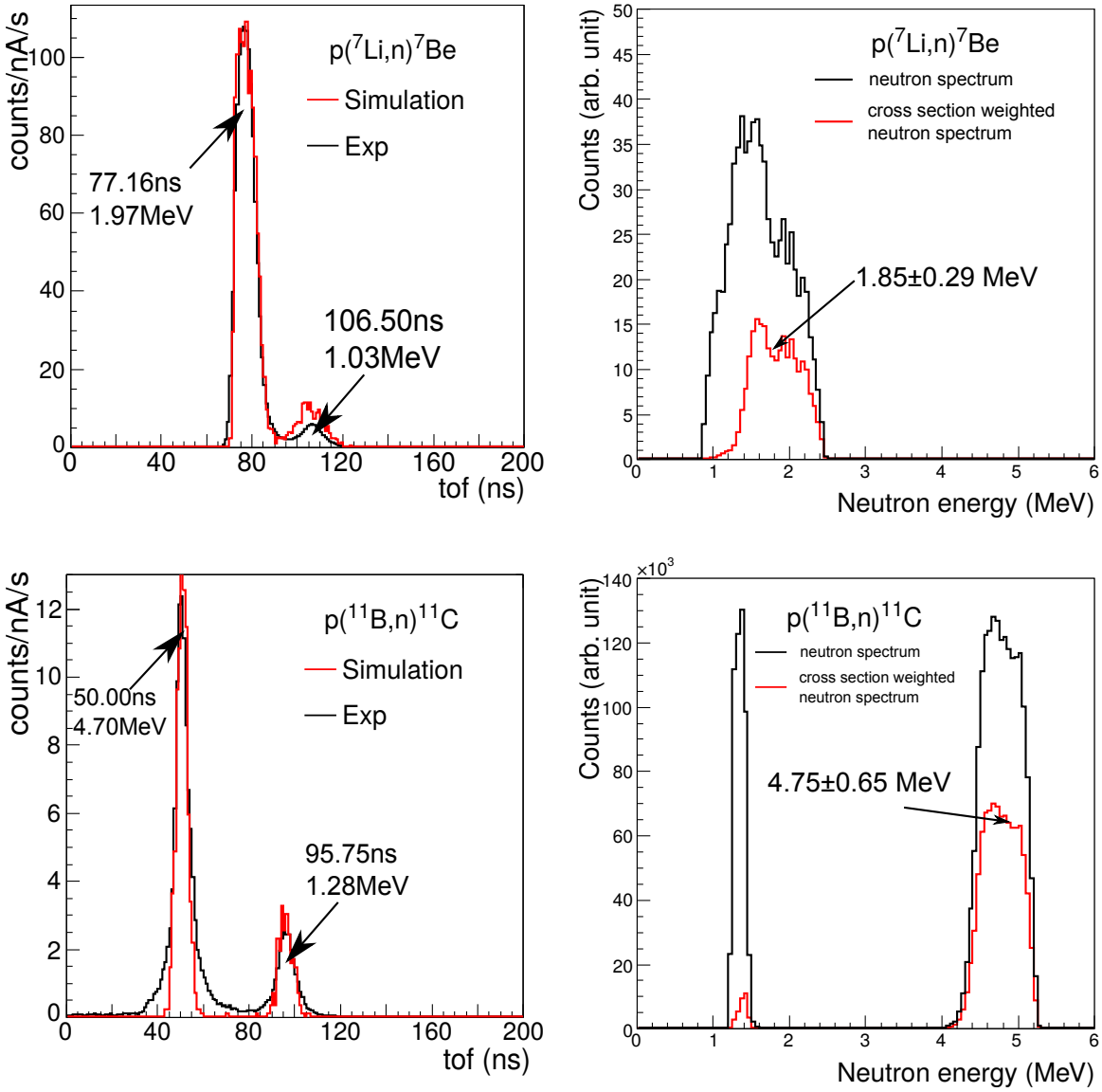

Figure 4.9 – Comparison between simulated and measured TOF spectra in neutron detectors (placed at 1.5 m) in ^{238}U(n,f) reaction at two different energies (left). Simulated neutron spectra seen by all the samples in the ionization chamber, as well as the weighted spectra by the fission cross section.

in the ionization chamber were simulated. Averaged incident neutron energies on the samples, weighted by the fission cross sections, were thus deduced to be 1.9±0.3 MeV and 4.8±0.2 MeV in the ^{238}U(n,f) reaction and 1.8±0.5 MeV in the ^{239}Pu(n,f) reaction, respectively. Once the neutron energy has been determined to be as expected, the beam is then switched to direct mode for subsequent PFG measurement in order to maximize the statistics.

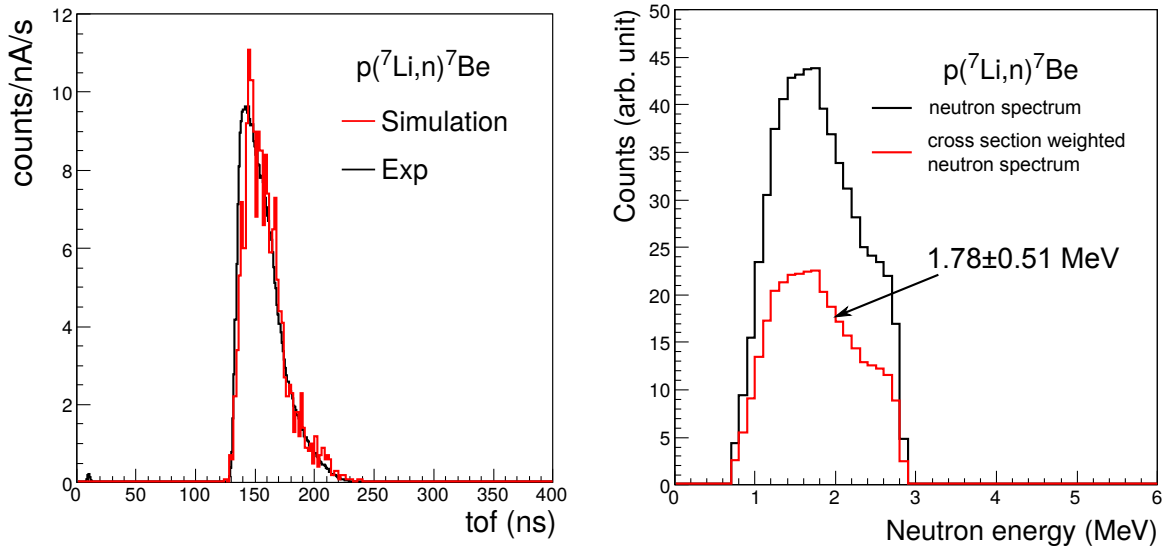

Figure 4.10 – Comparison between simulated and measured TOF spectra in neutron detectors (placed at 3.0 m) in ^{239}Pu(n,f) reaction at two different energies (left). Simulated neutron spectra seen by all the samples in the ionization chamber, as well as the weighted spectra by the fission cross section.

4.3 Fission events selection

Fission events were identified from the charge spectrum of the ionization chamber, depending on the difference of kinetic energy for fission fragments (FF) and α particles (the maximum alpha energy for actinides $\sim$6 MeV, and typical kinetic energy for FF see Table 1.1). A good α/FF discrimination is necessary (see Figure 4.11) because the uncorrelated background γ-rays need to be excluded, the number of fission needs to be extracted for subsequent normalization within reasonable uncertainty and especially no weight on the mass of FF should be introduced.

The number of α particles appearing in the selected FF distribution is obtained by superposing the two charge spectra of the chamber with and without the incident neutron beam. A threshold can be set slightly higher than the maximum energy of α particles to select fission events in the valley between the two distributions. PFGS are then extracted and normalized to the this number of fissions to give average spectral characteristics per fission. The influence of α particles in the FF distribution has been evaluated to be less than 0.5%, which is negligible.

The number of FF under the α particles distribution is estimated by simple extrapolation with Landau function fitted to the left part of the FF distribution. The analytic function is unavailable for the fitting of the FF distribution due to the complexity of the anode signal to the energy deposition of FF. The Landau function was chosen simply according to the reduced chi-square. The total number of fission events is then able to be

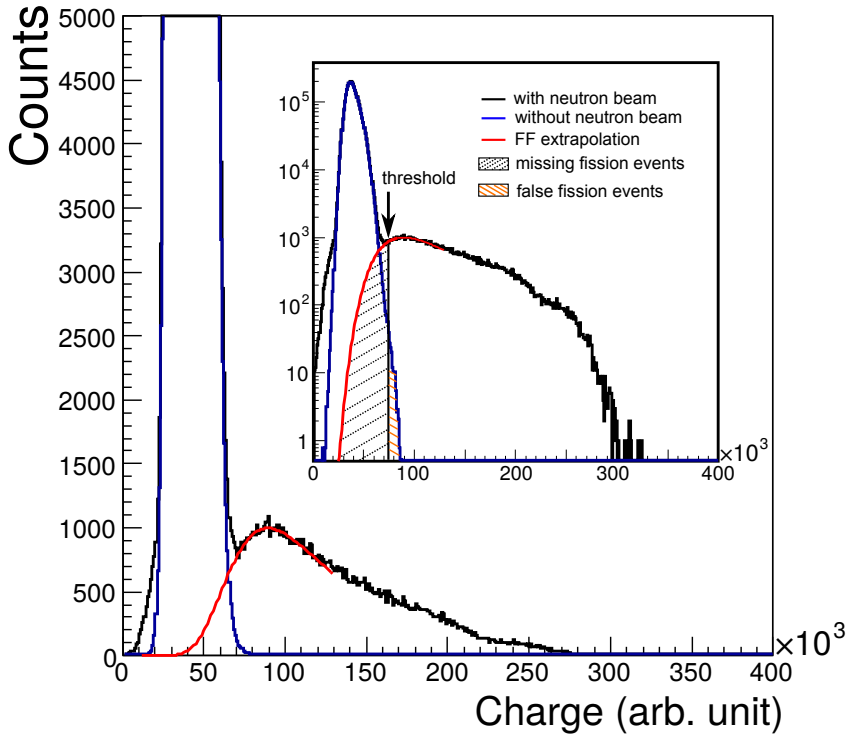

Figure 4.11 – The integrated charge spectrum taken with the JRC multi-sample ionization chamber depicted in linear scale; the inset shows the same distribution in logarithmic scale. α and FF distributions are reconstructed, respectively, giving access to the number of overlapping events.

reconstructed, as well as the estimation of the ratio between the missing events and the total number of fission events. Corresponding numbers of fission events are summarized in Table 4.4. The number of missing events, mainly concerning the low energetic heavy FFs, is less than 3.0% and 7.0% for each type of ionization chamber. Even though the spectral characteristics vary as a function of the FF mass, the effect is not significant. In addition, in each fission event, only one fragment is detected while the other fragment is stopped. Prompt γ-rays from heavy FFs are still be possible to be detected when the complementary light fragment is detected in the ionization chamber. Thus, we conclude from the numbers presented in Table 4.4 that the impact of FF mass on the PFG is negligible for these two types of ionization chambers.

The separation between charge distributions of FF and α particles is excellent in the first experiment (chamber from CEA, measurement of ^{252}Cf(sf) and ^{238}U(n,f)), see Figure 3.5, and hence a very low threshold can be set to select the fission events in one-dimensional charge spectra. However, in the second experiment (chamber from JRC, measurement of ^{239}Pu(n,f)), the high activity of α decays ($\approx$ 7 MBq) induce pile-up in

the charge measurement, which hinders the separation between FF and α particles. PSD was applied to improve the separation by excluding the events of small charge ratio and large charge integration, which is a typical of α-α pile-up, as is has been explained in Section 3.1.2 and Figure 3.7.

Table 4.4 – Summary of the number of fission events selected by using different methods (discussed in the text). The total number of fission events is reconstructed by means of extrapolation.

Measurement	Number of fission		
	1D-threshold	2D-TCUTG	Extrapolation(total)
CEA: ^{252}Cf(sf)	3.739E+07	-	3.769E+07
CEA: ^{238}U($n_{1.9MeV}$,f)	2.857E+06	-	2.941E+06
CEA: ^{238}U($n_{4.8MeV}$,f)	3.346E+05	-	3.444E+05
JRC: ^{239}Pu($n_{1.8MeV}$,f)	5.156E+06	5.575E+06	5.974E+06

4.4 PFG selection

Based on time coincidence, γ-rays can be correlated with the fission events. The characteristic emission time of prompt neutrons and prompt γ-rays is 10^{-18}-10^{-14} s and 10^{-14}-10^{-3} s, respectively. So the experimental setup is not able to discriminate neutron and γ by intrinsic time resolution ($\sim$1 ns). Depending on the difference of the neutron and γ-ray velocity, prompt neutrons and prompt γ-rays can be discriminated *via* TOF technique. For example, over a chamber-detector distance of typically 35 cm, 10 MeV prompt neutrons travel 8 ns, while prompt γ-ray travel 1.2 ns. With the time resolution of the whole experimental setup being $\sim$2 ns, prompt neutrons can be discriminated in the γ-ray spectrometer.

A two-dimensional plot of the TOF between the ionization chamber and the γ-ray detector versus measured γ-ray energy is shown in Figure 4.12. The intense sharp horizontal component is associated to PFG, and defines the "zero time" reference. The broad component at larger TOF (few tens of nanoseconds later) is associated with PFN, which needs to be eliminated in the PFG spectroscopy. Delayed gamma lines starting from the prompt γ-ray structure can also be seen, and are associated with isomeric decays of particular fission fragments. Usually, electromagnetic transitions take place within 10^{-15}-10^{-13} s. However, because of nuclear structure effect, an electromagnetic transition can be delayed and have a "measurable" lifetime of several ns or greater. These transitions are called isomeric transitions (IT) and the originating states are called isomers, *e.g.* 1769 keV gamma line with lifetime 54 ns can be a candidate for ^{146}Ce [99]. Other lines, that appears only in the neutron structure of the two-dimensional plot, can originate from neutron inelastic scattering (n, n$'\gamma$) on materials inside the detectors, *e.g.* γ ray decay of

the first excited states of ^{139}La (165.86 keV), ^{79}Br (217.07 keV) and ^{81}Br (275.99 keV), or materials close to the γ-ray detectors and the ionization chamber, *e.g.* γ ray decay of the first excited states of ^{27}Al (843.76 keV) and ^{56}Fe (846.78 keV). A continuous γ-ray background exists along the whole axis associated with uncorrelated decays in the experimental room, *e.g.* 1435.8 keV intrinsic gamma line from the electron capture on ^{138}La in $LaBr_3$ detectors. Gating on the time window before the prompt γ-ray structure and after the prompt neutron structure allows extraction of this averaged continuous background which must be normalized and subtracted from the measured PFGS. In the end, the measured PFG in each γ-ray detector with respect to each fissioning channel (cathode or anode) was extracted for subsequent unfolding procedure individually, in consideration of slightly differences in the geometry between electrode and γ-ray detector.

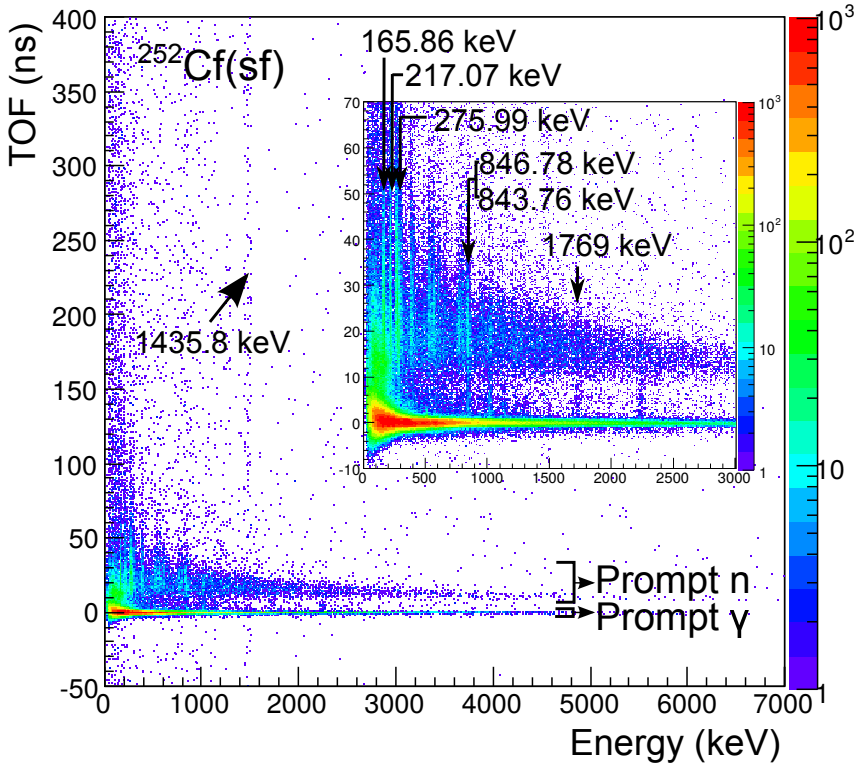

Figure 4.12 – Correlation between the γ-ray energy detected in one gamma detector and the TOF, where the ionization chamber gives the start signal and a gamma detector gives the stop signal. The inset shows the same correlation in low energy part. The time resolution, *i.e.* Full Width Half Maximum (FWHM), of the prompt gamma peaks projected to y-axis is around 1.2 ns for each gamma detector.

In comparison of PFG data with other experimental results and model calculations [26, 62], two conditions have to be considered in the PFG selection: the size of the time window and the energy range. The size of the time window used to select PFG in few

nanosecond after scission is crucial because the detection system only has time resolution of around 1-2 ns. For example, since the time resolution is worse at low energies, more stringent cuts disproportionately affect this part of the spectrum and can have effects on the extracted spectral characteristics, as illustrated in Figure 4.13. For comparison with other experimental results, the time window in this work has been set to be ±2.5 ns in ^{238}U(n,f) reaction and ±3.0 ns in ^{239}Pu(n,f) reaction. Also, it is sensitive to the low energy cut. Because most of the radiated photons are relatively low-energy, the photon multiplicity drops off significantly as the low energy cut increases, see Figure 4.13. Another concern is that the threshold effect and the coincident atomic x-rays can not be well simulated for recovering the emission PFGS. Consequently, the experimental threshold was tuned below 100 keV and for subsequent analysis a typical energy cut is chosen to be 100 keV. On the other hand, the high energy cut is of little relevance to the spectral characteristics due to the exponential decrease in the high-energy part.

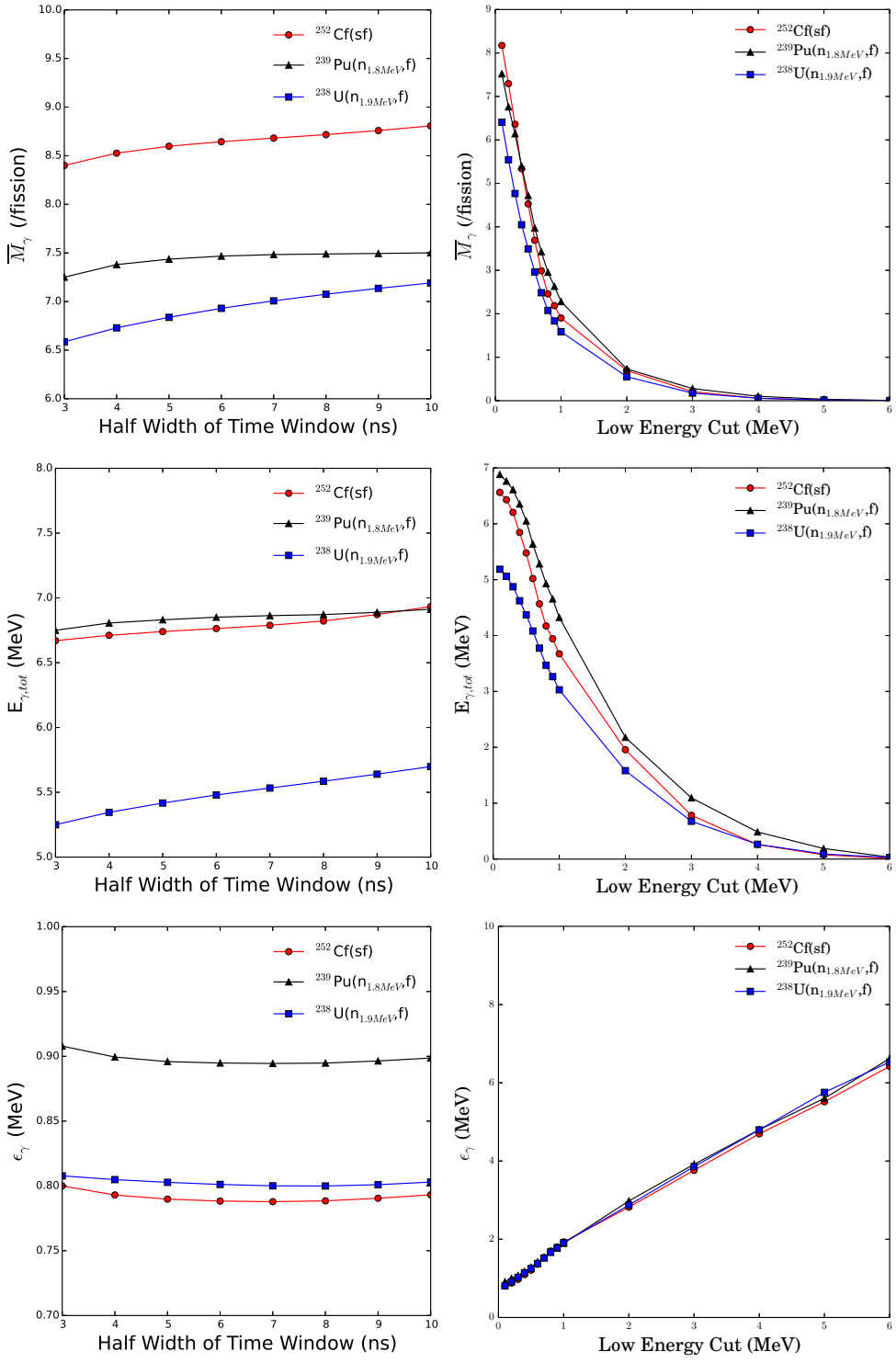

Figure 4.13 – The effect of time window (left) and low energy cut (right) to the prompt γ-ray characteristics per fission. Half width of the time window also corresponds to the time since scission occurs.

4.5 Response function unfolding procedure

In the following section, information on the unfolding procedure is given in some detail in order to understand any potential systematic errors that it can introduce. This is especially important for measured spectra with low statistics, which can be the case for PFG measurements of fast-neutron-induced fission, since cross sections are typically three orders of magnitude lower than those for thermal-neutron-induced fission.

The γ-rays have complicated response in a gamma detector, due to the interactions of Compton scattering, photoelectric effect and pair production. The measured spectrum is not equal to the emitted PFGS. Therefore, the measured spectrum must first be deconvoluted by the detector response to obtain the emitted spectrum. Let f(y) to be the unknown emission γ-ray spectrum of the source, and R(x,y) to be the response matrix. Then, g(x) given by:

$$g(x) = \int_0^\infty R(x,y) f(y) dy \tag{4.6}$$

is the measured spectrum. The challenge is to solve this linear integral equation in order to obtain the emission spectrum f(y) given the measured spectrum g(x) and simulated response function R(x,y), from which the characteristics of each fission event are extracted. This process is called "unfolding" or "deconvolution".

It is well known for being an ill-posed problem [100]. Firstly, the continuous form of the integral equation has to be rewritten into discrete form

$$g_i = \sum_{j=1}^{N} R_{ij} f_j \tag{4.7}$$

because a spectrum has a limited channel and each channel corresponds to an energy range: energy range E_i and E_{i+1}. And the measured spectrum can only be presented in discrete data between energy E_0 and E_N, where E_0 is the lower limit and E_N is upper limit. It is the first limitation in this problem to obtain emission distribution. Secondly, the measured spectrum always accompanies with a noise term, including statistics error ϵ_{g_i} and systematic error δ_{g_i}:

$$g_i = \sum_{j=1}^{N} R_{ij} f_j + \epsilon_{g_i} + \delta_{g_i} \tag{4.8}$$

Thus, a small perturbation in the measured spectrum can cause an arbitrary large perturbation of the solution during inverse process, especially in this work the PFGS has limited statistics. In this specific physical case of unfolding PFGS, a detailed procedure is presented below.

4.5.1 Emission spectrum shape

In some cases, the unfolding process is model dependent. For example, Brunson [101] has established a mathematical model for the prompt γ-ray multiplicity distribution, whose coefficients need to be fitted during the unfolding process. In contrast, the unfolding procedure in this experiment has no prior information (functional form) available and the measured spectrum is unfolded directly with the simulated response function for the γ-ray detectors (model independent).

In the case of PFGS, there is no functional form for the emission spectrum due to the complexity of the process producing the γ-rays. In its low energy part (< 1 MeV), the spectrum is dominated by discrete (mainly E2) transitions, characteristics for the populated fission fragments [102], see inset of Figure 4.14. These low-energy γ-rays sit on a continuous background of statistical γ-rays which are mainly E1 transitions. The latter cover a wide range of energies from few tens keV up to 8 MeV. At even higher energy ranges, the de-excitation of giant resonance (GR) of the fragments was observed [103,104]. In the case of fast-neutron-induced fission, the limited statistics above 6 MeV constrain the study of high energy spectroscopy, which is out of the scope of this study, see Figure 4.14.

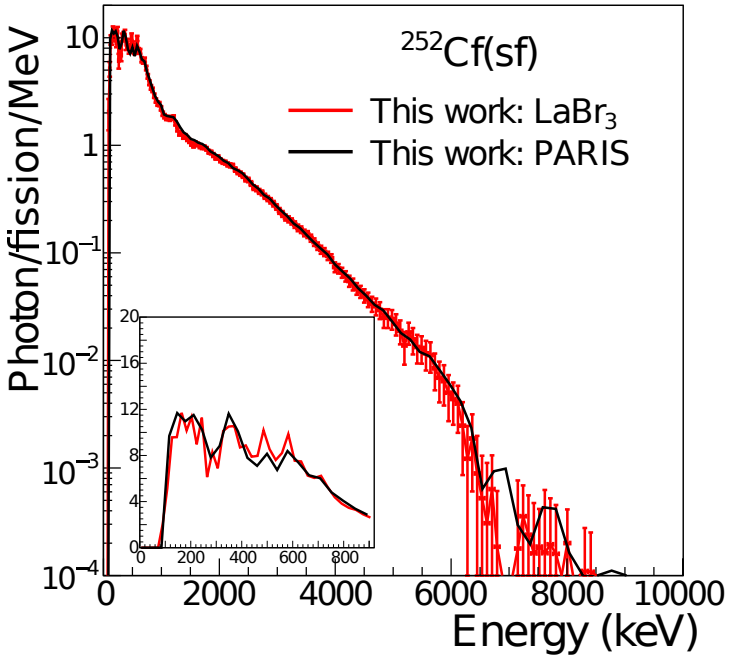

Figure 4.14 – Unfolded spectra with the time window ±2.5 ns from ^{252}Cf(sf) in logarithmic scale as obtained for two different types of gamma detectors (see text for details). The inset shows the region below 900 keV in linear scale.

4.5.2 Response function construction

The response function itself is obtained from detailed GEANT4 simulations of the entire experimental setup using the PENELOPE physics list [105]. The energy deposition of the γ-rays in the detector is scored by G4VSensitiveDetector and hits in GEANT4, see Figure 4.15 for a schematic view of the simulation process. The experimental smearing effect, *i.e.* energy resolution, is also taken into account for γ-ray spectrometer. As discussed in Section 4.1.3, the relative energy resolution (FWHM/E) as a function of the γ-ray energy is obtained from calibration procedure. The energy deposition of the γ-ray is then convoluted with a Gaussian random number, whose sigma follows the distribution of experimental distribution (FWHM/E).

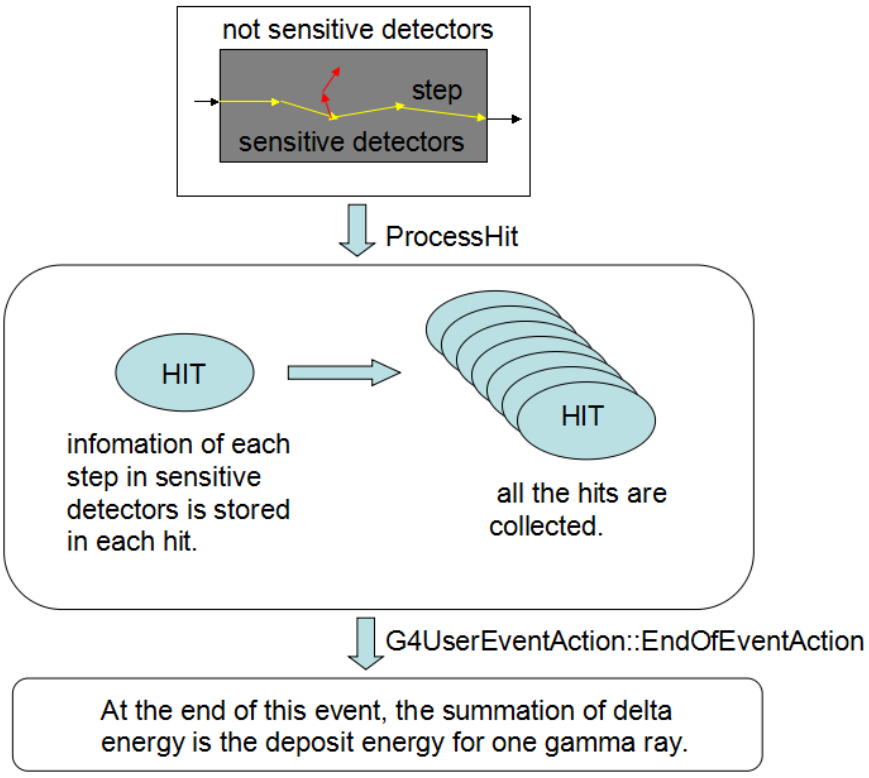

Figure 4.15 – Schematic view of the simulation process in G4VSensitiveDetector of GEANT4.

In the low energy part, the lower limit has been set at 100 keV to avoid threshold effects and exclude atomic x-rays, which cannot be simulated very well. In order to extract the spectral characteristics in the energy range between 100 keV and 6 MeV, the energy range is extended up to 10 MeV in terms of excluding the effect of Compton scattered high energy γ-rays affecting the lower energy region of the spectrum.

A typical simulated response function can be seen in Figure 4.16. The y-axis corresponds to the energy of the emission γ-ray, whose width (binning) is determined according

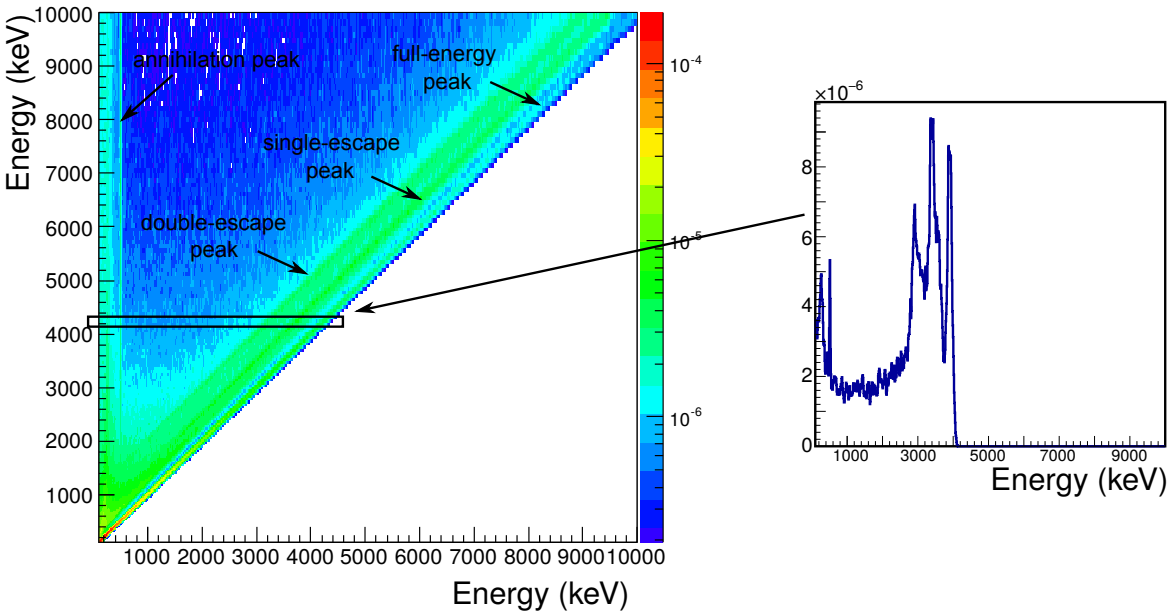

Figure 4.16 – A typical GEANT4 simulated response matrix for different energies of γ-rays. The y-axis corresponds to the emission γ-ray energies and the x-axis the measured γ-ray energies. Different structures are visible in the two-dimensional plot. One slice of the response matrix, corresponding to the emission γ-ray energy around 4 MeV, is plotted in the right.

to the energy resolution as a function of γ-ray energy (Equation 4.3), in consideration of computation capability. The x-axis is the observed γ-ray energy in the detector corresponding to the emission γ-ray. The binning of the x-axis is dependent on the unfolding algorithms (discussed in the next section), *e.g.* symmetric $N \times N$ response matrix for matrix inversion and linear iteration is mandatory. Also other structures are visible in the plot, *e.g.* the double-escape, single-escape peak and annihilation peak (*i.e.* 511 keV).

A validation of the response function was performed by using the detection efficiencies and comparisons between simulated and experimental spectra from conventional γ-ray sources, see Figure 4.17. It confirms that the experimental setup and physical processes are reasonably described in the code, and the response function precise enough for the subsequent unfolding process as a preliminary condition.

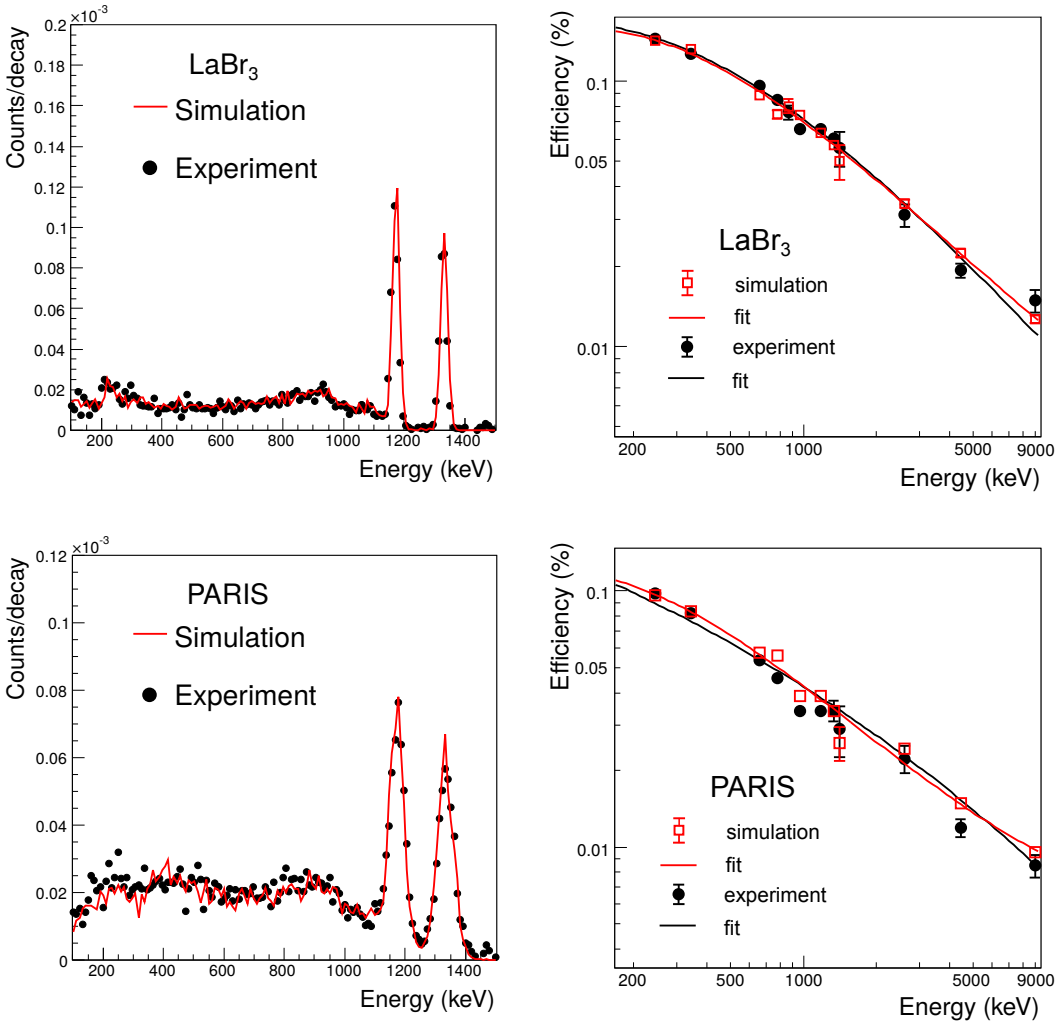

Figure 4.17 – Comparisons of the simulated and experimental γ-ray spectrum in the presence of ^{60}Co radioactive source for one $LaBr_3$ detector and one single PARIS phoswich, respectively (left); Comparisons of full-energy detection efficiency for simulation and experiments respectively, in energy range from 0.1 MeV to 9.0 MeV (right).

4.5.3 Unfolding algorithms

Various unfolding algorithms for recovering the emission PFGS have been developed over the last 50 years. Unfolding algorithms fall mainly into two categories: un-regularized and regularized methods.

The un-regularized methods are most straightforward, including matrix inversion and bin-by-bin method [62]. In the matrix inversion, the emission spectrum and corresponding statistical error can be deduced easily by:

$$f_j = \sum_{i=1}^{N} (R^{-1})_{ji}\ g_i \tag{4.9}$$

$$Cov(f_j, f_k) = \sum_{i=1}^{N} (R^{-1})_{ji} (\epsilon_{g_i})^2 (R^{-1})_{ki} \tag{4.10}$$

where ϵ_{g_i} is the uncertainties of the measured spectrum. However, the inversion of the response matrix is not precise. Precise inversion gives $R^{-1}R = \mathbb{1}$ identical without off-diagonal elements, which is not the case here. And also this method is well known to be fluctuating since it cannot distinguish between widely fluctuation and smooth distribution, and obtains large negative correlations between adjacent bins. The bin-by-bin method obtains a scaling factor from the ratio between the measured spectrum and simulated spectrum and apply a background subtraction to the lower energy part at the same time when starting from the highest energy bin:

$$f_i = \frac{(g_i - g_{bg,i})}{R_{i,i}} \tag{4.11}$$

where $g_{bg,i}$ is the accumulated background. Since the process is purely linear, error propagation formula can be applied. A more practical method was proposed in Ref. [62], which performs a least square or maximum likelihood fit between measured spectrum and simulated spectrum every 3 bins to get the scaling factor and at the same time better eliminate the smearing effect of energy resolution in neighboring bins.

Instead of un-regularized unfolding, a regularization parameter can be introduced, which makes a compromise between the "fit" of the solution to the measured distribution and the "size" of the solution. It is able to wash out the oscillations and transform ill-conditioned problems into well-posed problems, which makes the solution more acceptable and stable. Different methods have different definitions of "fit", "size" and the way to choose the optimum regularization parameter. Tikhonov regularization [106] and singular value decomposition (SVD) regularization [107] are well known methods, implemented in "TUnfold" and "TSVDUnfold" classes of ROOT. Tikhonov *et al.* [106] introduced the regularization theory and methods, which is to solve the minimization problem with the

general form:

$$argmin[\ \parallel Rf - g \parallel_2^2 + \lambda^2 \parallel L(g - g_0) \parallel_2^2\ ,\ \lambda\ ] \tag{4.12}$$

where λ is the regularization parameter. The "fit" is defined as the norm $\parallel Rf - g \parallel_2$ of the residual vector, originating from a fold step from the solution to the measured distribution. The "size" of the solution is defined as the norm $\parallel L(g - g_0) \parallel_2$. The g_0 is 0 when no prior information is available. And the L is identical matrix in standard form. L-curve criteria is available for finding optimal λ, by plotting ($\parallel Rf - g \parallel_2$, $\parallel L(g - g_0) \parallel_2$) in log-log scale.

In addition, iteration is also a regularized method, including linear [108] and non-linear iteration [109]. By avoiding reversing the measured distribution, the corresponding prediction for the solution is computed by a folding step from an initial guess, whose shape is usually not far from the measured distribution. It is then compared to the measured distribution and modified at each iteration, such that the difference between this distribution and the measured distribution is reduced. Andras Laszlo *et al.* [108] suggests a linear iteration algorithm as follows:

$$f_i^{k+1} = f_i^k + N_{col}^{-1} \sum_{j=1}^{N} (R^T)_{ij} g_j - \sum_{j=1}^{N} R_{ij} f_j^k \tag{4.13}$$

where N_{col} is column norm of the response matrix R and R^T is the transposed of the response matrix. Due to the linearity of the method, the statistical error propagation is feasible. And the systematic error of the unfolded distribution has a upper limit [108], as follows:

$$\epsilon_i^{k+1} = \epsilon_i^k + N_{col}^{-1} \sum_{j=1}^{N} R_{ij}^T g_j - \sum_{j=1}^{N} R_{ij} \epsilon_j^k \tag{4.14}$$

$$\delta_{f_i} \leq (1 + ln(k+1) N_{col}^{-1} R_{ii}^T \delta_{g_i}) \tag{4.15}$$

Unlike the linear iteration, all components in non-linear iteration method are scaled to their contribution $R_{ij} f_j^k$ to g_i during the modification process:

$$f_j^{k+1} = \sum_{i=1}^{M} R_{ij} f_j^k \frac{g_i}{\sum_{j=1}^{N} R_{ij} f_j^k} / \sum_i R_{ij} \tag{4.16}$$

Error propagation is not applicable due to the non-linear model. Simple error assignment can be given according to Ref. [109].

The quality of "fit" is described by chi-square $\chi^2 = \sum_{i=1}^{M} \frac{(g_i - t_i)^2}{t_i}$, where $t_i = \sum_{j=1}^{N} R_{ij} f_j^k$ and f^k the unfolded spectrum at kth iteration. When the number of iterations k increases, the

oscillations become larger. It means that the norm of the solution is larger, described by another quantity $X^2 = \sum_i^N \frac{(\hat{f}_i^k - f_i^k)^2}{f_i^k}$, where $\hat{f}_i$ is calculated from toy experiment (unfolded spectra obtained from different sets of measured spectra). A stopping criteria, *i.e.* halt the procedure as soon as the unfolded spectrum properly fits to the measured spectrum, is then used to choose the optimum iteration number, see Figure 4.18.

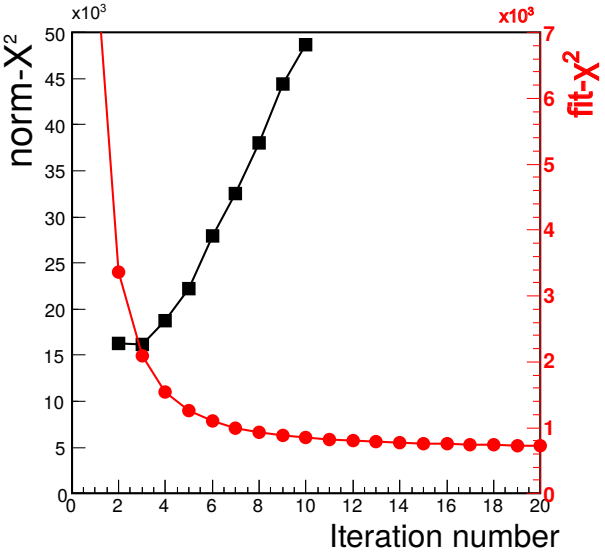

Figure 4.18 – The chi-square χ^2 and norm size X^2 distribution as a function of the iteration number. The optium regularization parameter, namely iteration number, can be chosen according to this plot.

The unfolding code of above algorithms can be found in the link [110]. Even though there are plenty of algorithms developed, there is a lack of knowledge about what kind of systematic effects the different unfolding algorithms have on the unfolded spectrum, especially the spectral characteristics. In addition, the performance of the unfolding procedures needs to be evaluated in low-statistics data sets, which is particularly relevant for fast-neutron-induced fission PFG measurements. By artificially reducing the number of events (selecting a data subset), the impact of low statistics on the extracted average multiplicity has been quantified for each unfolding algorithm. The results, shown in Figure 4.19, demonstrate that the iteration method is the most stable for spectra with the fewest counts. Consequently, it was chosen as the unfolding algorithm in this work.

4.5.4 Observables extraction

Once the unfolding is completed, the spectral characteristics can then be extracted from the unfolded spectra, which are normalized to the number of fissions (as discussed in Section 4.3). The average multiplicity is deduced by integrating the unfolded spectrum.

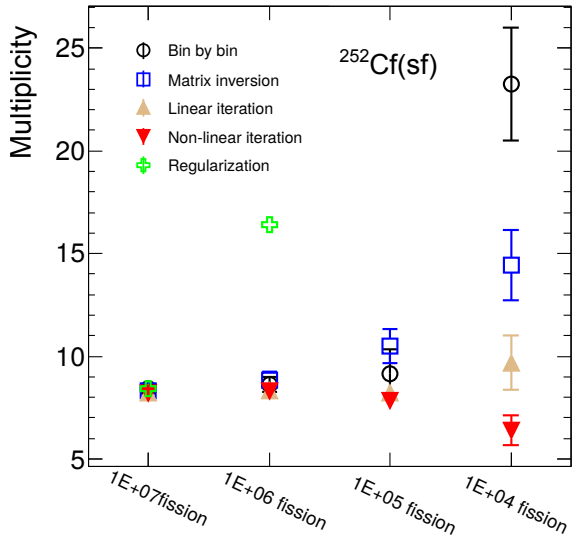

Figure 4.19 – Comparison of different unfolding techniques from the spontaneous fission source ^{252}Cf at different statistical configurations, with the extracted property of γ-ray multiplicity per fission.

The multiplication between the unfolded distribution and the γ-ray energy gives the total energy released. The average photon energy can then be calculated from these two quantities. The calculation of these quantities follows:

$$\overline{M}_\gamma = \int N_\gamma(E_\gamma)\, dE_\gamma \tag{4.17}$$

$$\mathrm{E}_{\gamma,tot} = \int E_\gamma \times N_\gamma(E_\gamma) dE_\gamma \tag{4.18}$$

$$\epsilon_\gamma = \mathrm{E}_{\gamma,tot}/\overline{M}_\gamma \tag{4.19}$$

where $N_\gamma(E_\gamma)$ is the unfolded PFG distribution (normalized to per fission) as a function of the γ-ray energy E_γ.

In order to validate the calculations, simulated data with high statistics are used in case of a discrete (radioactive source ^{152}Eu) and a continuous (energy in exponential, multiplicity in Gaussian) distribution, which are typical of PFGS. Figure 4.20 (using linear iteration algorithm) gives the comparison among measured spectrum, unfolded spectrum and emission spectrum. Even though the unfolded spectrum cannot fully eliminate the energy shearing effect, which causes oscillation in the neighboring bins, the spectral characteristics of the unfolded spectrum very well represents the ones of emission spectrum, see TABLE 4.5. The analysis shows that, for one detector, aforementioned unfolding procedures reasonably reproduce the average multiplicity, total energy released and average photon energy in high-statistics data sets.

Table 4.5 – Summary of the performance of different deconvolution techniques tested on a discrete and continuum distribution (at high statistical situation) [110], respectively. The calculation of the quantities are described in the text.

	$\bar{M}_\gamma$(/fission)	$E_{\gamma,tot}$(MeV)	$\epsilon_\gamma(MeV)$
Bin-by-bin	1.54 ± 0.06	1.09 ± 0.05	0.71 ± 0.04
Matrix Inversion	1.68 ± 0.03	1.19 ± 0.03	0.71 ± 0.02
Linear Iteration	1.65 ± 0.06	1.16 ± 0.02	0.70 ± 0.03
Non-linear Iteration	1.57 ± 0.01	1.11 ± 0.02	0.71 ± 0.01
Regularization	1.59 ± 0.01	1.07 ± 0.02	0.67 ± 0.01
Reference	1.58 ± 0.01	1.11 ± 0.00	0.71 ± 0.01
	$\bar{M}_\gamma$(/fission)	$E_{\gamma,tot}$(MeV)	$\epsilon_\gamma(MeV)$
Bin-by-bin	7.37 ± 0.12	13.09 ± 0.34	1.77 ± 0.05
Matrix Inversion	7.25 ± 0.10	12.89 ± 0.35	1.78 ± 0.06
Linear Iteration	7.28 ± 0.08	12.93 ± 0.07	1.77 ± 0.02
Non-linear Iteration	7.24 ± 0.02	12.83 ± 0.06	1.77 ± 0.01
Regularization	7.27 ± 0.01	13.27 ± 0.04	1.82 ± 0.01
Reference	7.25 ± 0.02	12.86 ± 0.00	1.77 ± 0.00

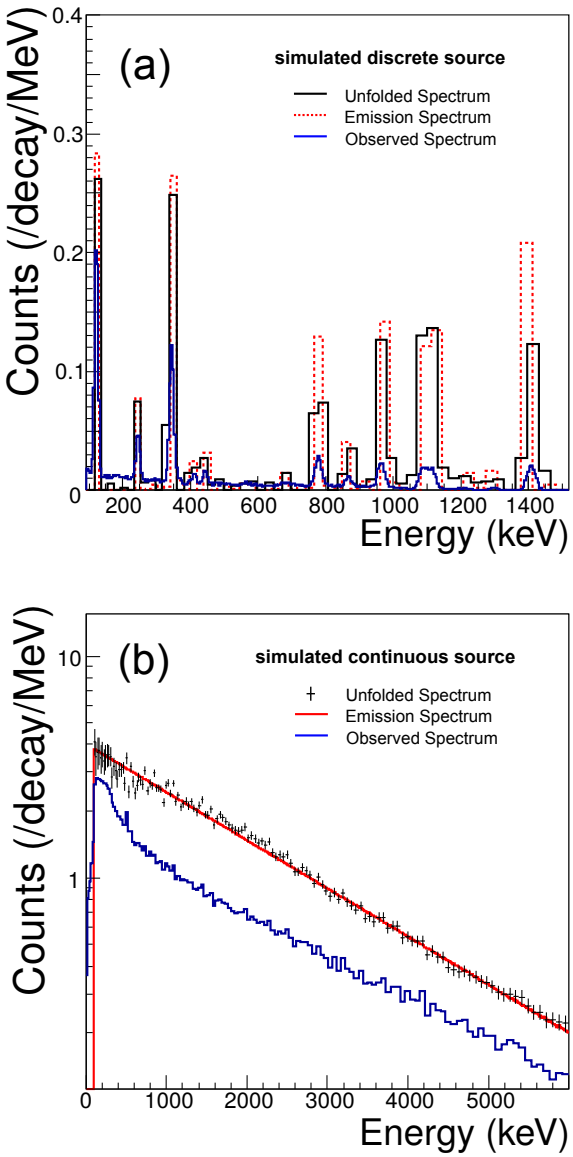

Figure 4.20 – Comparison of the unfolded γ-ray spectra for (a) a discrete gamma source ^{152}Eu and (b) an exponentially distributed gamma source. Each unfolded spectrum is compared to the emission spectrum, as well as the measured spectrum (scaled for better visibility).

4.6 Results

4.6.1 ^{252}Cf(sf)

In the first experiment, two fission chambers from CEA Bruyère-le-Chatel were used to study prompt emission in fission. The first chamber only contained one cathode of ^{252}Cf sample. ^{252}Cf is a spontaneous fission source that has been widely studied and the measured PFGS can be used as a reference to compare with other results and validate the analysis procedure. The measured spectrum of each individual γ detector was unfolded separately, following the unfolding procedure discussed in the previous section. The spectral characteristics are then extracted individually. For each detector, the error bar assignment was performed by taking all the possible sources of uncertainty into account during the data analysis procedure. One example of the error bar assignment is presented in Table 4.6 with corresponding description in below.

Table 4.6 – A detailed decomposition of the uncertainties for the spectral characteristics of PFGS. Relative errors from different sources of uncertainty are presented and the total value is the quadratic sum. It is for one of the γ-ray detectors ($LaBr_3$ Q9625).

Source of uncertainty	Relative error		
	$M_\gamma(/fission)$	$E_{\gamma,tot}(MeV)$	$\epsilon_\gamma(MeV)$
Measured Spectrum	1.46%	2.18%	1.62%
Response matrix statistics	0.66%	0.13%	0.67%
Response matrix systematics	2.61%	0.80%	1.91%
Unfolding systematics	1.87%	1.90%	3.81%
Binning effect	0.26%	1.01%	1.06%
Energy calibration	0.20%	0.44%	0.64%
Fission fragments measurement	0.07%	0.32%	0.32%
Total	3.61%	3.22%	4.78%

Source of uncertainty	Description
Measured Spectrum	samples generation according to Poisson distribution
Response matrix statistics	simulate 10^6 particles per energy
Response matrix systematics	due to measurement: θ, $\phi \pm 10°$, distance $\pm$ 0.25 cm
Unfolding systematics	test arbitrary distribution, e.g. exponential
Binning effect	binning by energy resolution (σ, FWHM and 2×FWHM)
Energy calibration	quadratic fitting error
Fission fragments measurement	∼0.5% uncertainty on FF measurement

The final values are then obtained from the weighted mean and associated uncertainties of spectra from the multiple detectors in the experimental setup, see Figure B.1 in Appendix. B. The values obtained are presented in Table 4.7, compared to other previ-

ous measurements. Δt represents the time window to select the PFG and ΔE represents the energy range when extracting the spectral characteristics. Each individual unfolded spectra from multiple detectors were combined into two averaged unfolded spectrum for different detector types, *i.e.* $LaBr_3$ scintillation detector and PARIS phoswich detector, as is plotted in Figure 4.21.

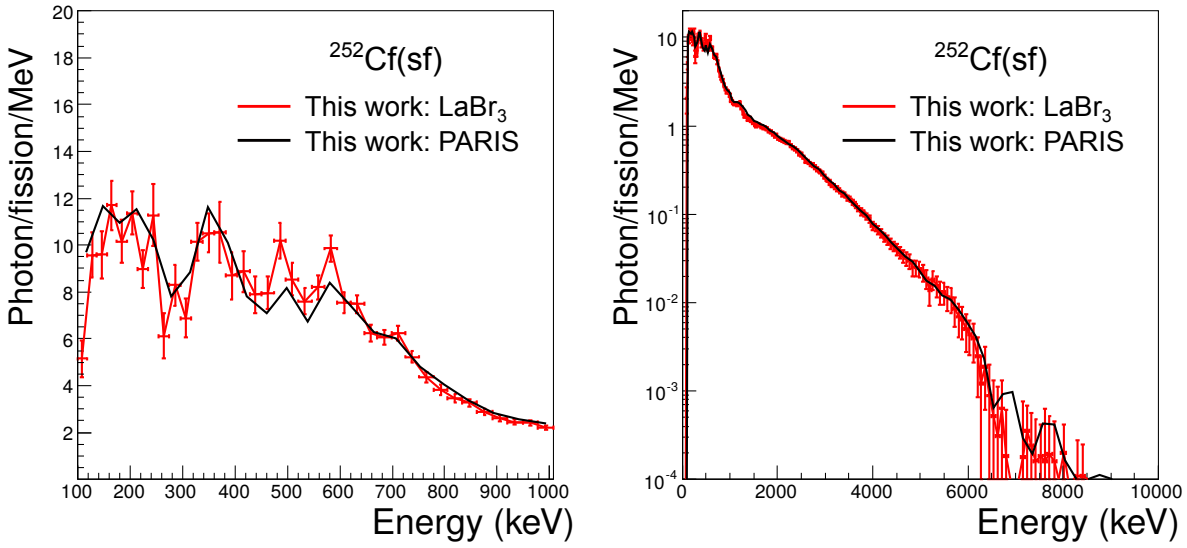

Figure 4.21 – Summed unfolded PFGS of ^{252}Cf(sf) for $LaBr_3$ and PARIS phoswich, respectively.

Table 4.7 – Summary of PFGS characteristics of ^{252}Cf(sf) for $LaBr_3$ and PARIS phoswich, respectively. The width of time window and the energy range have been pointed out if available.

^{252}Cf(sf)	Detector	$\bar{M}_\gamma$ (/fission)	$E_{\gamma,tot}$ (MeV)	ϵ_γ (MeV)	Δt (ns)	ΔE (MeV)
This work	$LaBr_3$	8.30±0.15	6.60±0.15	0.80±0.02	±2.5	0.1-6.0
	PARIS	8.40±0.19	6.70±0.26	0.80±0.02	±2.5	0.1-6.0
R. Billnert *et al.* [62]		8.30±0.09	6.64±0.10	0.80±0.01		
A. Chyzh *et al.* [111]		8.14±0.40	7.65±0.55	0.94±0.05		

The unfolded spectra from the $LaBr_3$ scintillation detectors and the PARIS phoswich detectors are in very good agreement with each other despite the very different γ-ray responses. There is good agreement in terms of both the slope in the high-energy region and the positions of the structures in the low-energy region. There are some small differences observed in the amplitude of the major peaks in the low-energy region, but this may be due to the different energy resolutions of the two detector types and are also within the uncertainties. The spectral characteristics for the two types of the detectors agree well

within 1.5% and are within the error bars (see Table 4.7). This demonstrates a good performance of the PARIS phoswich detectors in this experiment - in fact, it was the first time that these detectors have been used in a physics experiment.

Our results from ^{252}Cf are also in very good agreement with results from previous experiments [62, 111]. Comparisons are given in Table 4.7. We conclude that our analysis procedure is valid and may now be applied to the spectral data obtained in our measurements of PFG from neutron-induced fission of ^{238}U and ^{239}Pu.

4.6.2 ^{238}U(n,f)

In this section, the experimental PFGS results from fast-neutron induced fission of ^{238}U at two different incident energies (1.9 and 4.8 MeV) will be presented. It also aims to examine any potential energy dependence of spectral characteristics below second chance fission.

The ^{238}U ionization chamber used for the measurement had an identical external geometry and was constructed of similar materials compared to the ^{252}Cf chamber. However, the uranium samples were deposited on different cathodes or anodes, positioned between 12 and 20 cm away from the LICORNE gas cell. Due to the slight difference in the source-detector geometry, the response matrix for each γ detector has to be simulated at each positions. The measured PFGS corresponding to each fission position have been unfolded separately, see Figure B.2 in Appendix. B. The final values for the spectral characteristics were then extracted from the weighted mean for each of the relevant quantities, see Table 4.8. To obtain the final unfolded spectrum in Figure 4.22, all the separate unfolded spectra were combined into two averaged unfolded spectrum for different detector types.

Table 4.8 – Summary of PFGS characteristics of ^{238}U(n,f) for $LaBr_3$ and PARIS phoswich, respectively. The width of time window and the energy range have been pointed out if available.

^{238}U	E_n (MeV)	Detector	$\bar{M}_\gamma$ (/fission)	$E_{\gamma,tot}$ (MeV)	ϵ_γ (MeV)	Δt (ns)	ΔE (MeV)
This work	1.9	$LaBr_3$	6.38±0.19	5.15±0.21	0.81±0.02	±2.5	0.1-6.0
		PARIS	6.69±0.19	5.35±0.19	0.80±0.02	±2.5	0.1-6.0
	4.8	$LaBr_3$	7.37±0.49	6.29±0.69	0.85±0.11	±2.5	0.1-6.0
		PARIS	7.25±0.42	6.06±0.60	0.84±0.10	±2.5	0.1-6.0
J.M. Laborie	1.7		7.05±0.20	5.92±0.24	0.84±0.03		
et al. [112]	5.2		7.25±0.35	5.73±0.40	0.79±0.04		

Again, it is visible that the unfolded spectra from the $LaBr_3$ scintillation detectors and the PARIS phoswich detectors are in very good agreement with each other. In addition, a linear fit to the spectral characteristics for the two incident neutron energies in this work has been performed. For example, the trend of the total energy released per fission has a

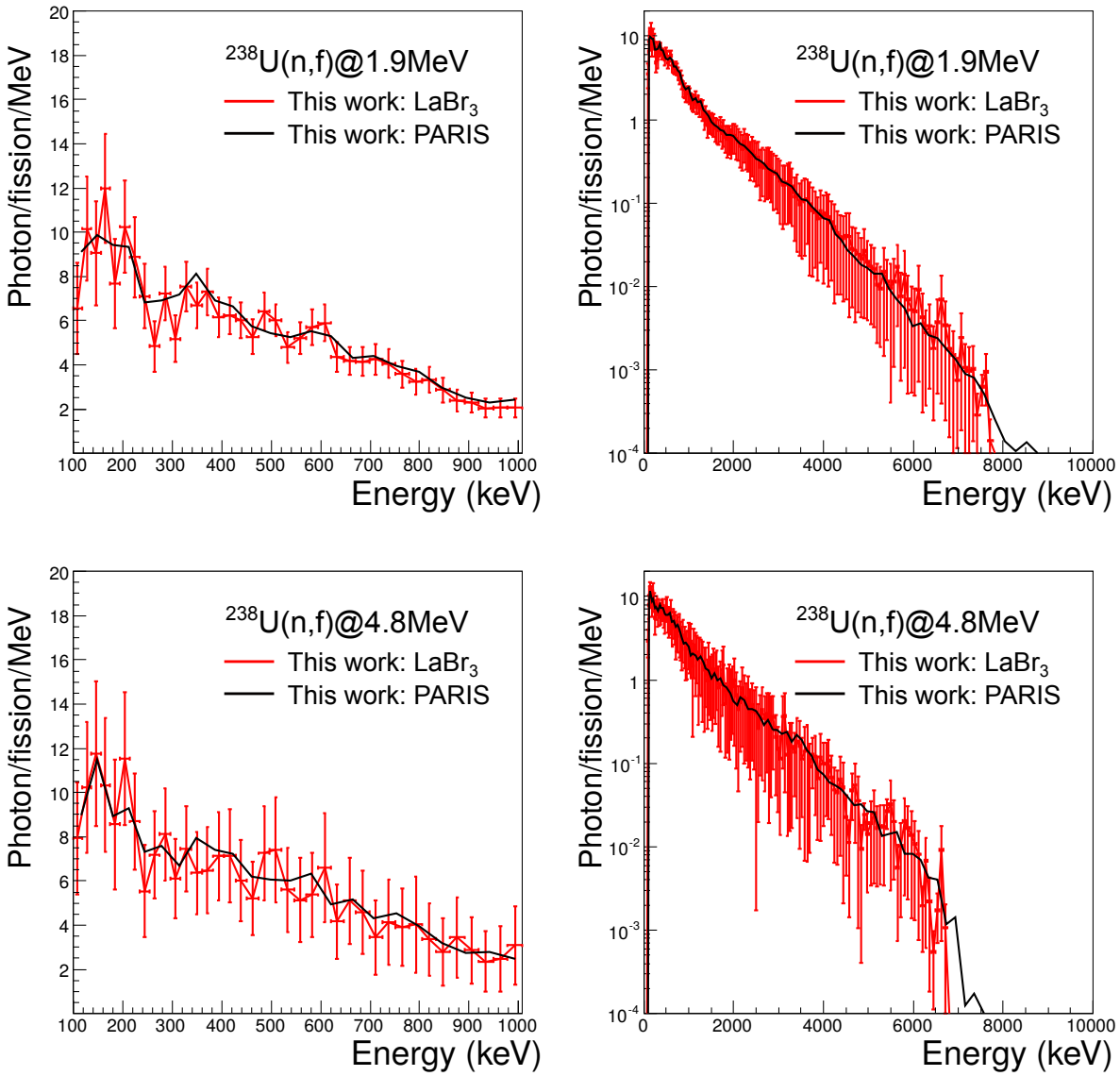

Figure 4.22 – Summed unfolded PFGS of ^{238}U(n,f) for $LaBr_3$ and PARIS phoswich, respectively, at E_n=1.9 and 4.8 MeV.

slope 0.32±0.14 MeV/MeV and an intersection 4.64±0.32 MeV. The experimental results reveal that the spectral characteristics of PFGS, including the average multiplicity, the total energy release as well as the average photon energy, have no significant observable energy dependence when the beam energy is raised from 1.9 to 4.8 MeV. Also no significant observable evolution in the shape of the spectrum is seen.

4.6.3 ^{239}Pu(n,f)

In the second experiment, the PFG of fast-neutron induced fission of ^{239}Pu was investigated, by using an ionization chamber developed in JRC (Geel). The chamber contained

high purity ^{239}Pu samples. Every two samples were attached to the cathode, forming 4 channels for readout of fission fragment detection information in the anode. Similar to the treatment in the case of ^{238}U(n,f), the response matrix for each γ detector is simulated in 4 different positions taking into account the difference in source-detector geometries. The spectral characteristics are summarized in Table 4.9, which are extracted from the weighted mean of each individual unfolded spectra (see Figure B.3 in Appendix. B). The summed unfolded spectra are plotted in Figure 4.23.

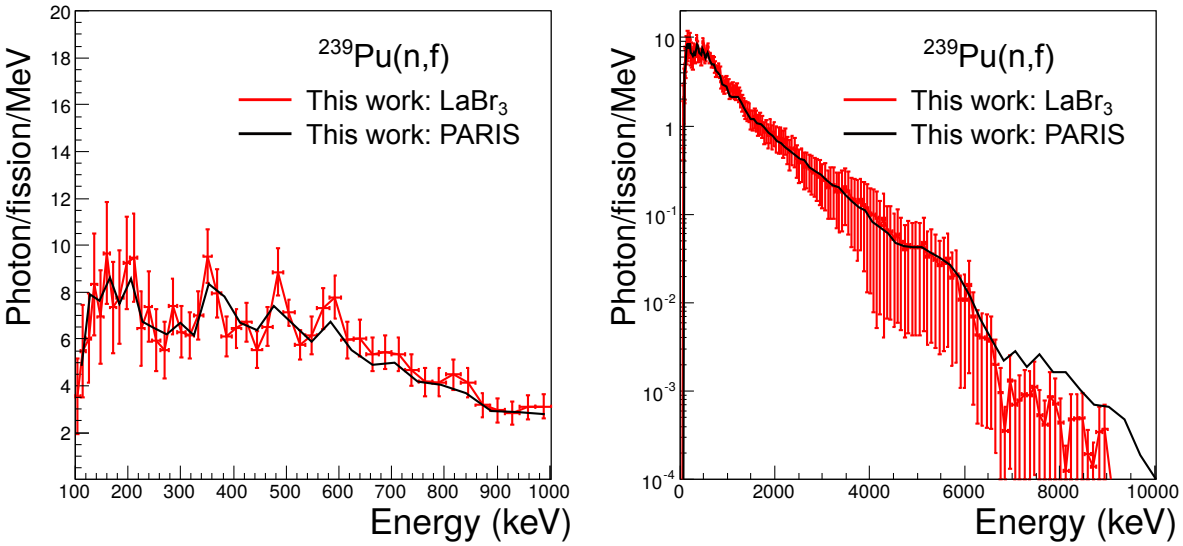

Figure 4.23 – Summed unfolded PFGS of ^{239}U(n,f) for $LaBr_3$ and PARIS phoswich, respectively, at E_n=1.8 MeV.

Table 4.9 – Summary of PFGS characteristics of ^{239}Pu(n,f) for $LaBr_3$ and PARIS phoswich, respectively. The width of time window and the energy range have been pointed out if available.

^{239}Pu	E_n (MeV)	Detector	$\bar{M}_\gamma$ (/fission)	$E_{\gamma,tot}$ (MeV)	ϵ_γ (MeV)	Δt (ns)	ΔE (MeV)
This work	1.8	$LaBr_3$	7.37±0.36	6.75±0.39	0.91±0.04	±3.0	0.1-7.0
		PARIS	7.12±0.40	6.67±0.38	0.91±0.04	±3.0	0.1-7.0
A. Gatera *et al.* [26]	thermal	$LaBr_3$	7.35±0.12	6.27±0.11	0.85±0.02	±3.0	0.1-7.0

In this chapter, the procedure of obtaining the unfolded PFGS and spectral characteristics have been presented step by step. In the end, the spectrum and characteristics, obtained following the same procedure, are either plotted or listed in the table. In the next chapter, the comparisons and discussions about the experimental results, as well as the theoretical calculations, will be detailed.

Chapter 5
Discussions

The spectral characteristics and corresponding spectral shapes of prompt fission γ-rays (PFG) in different fissioning systems have been measured, including spontaneous fission of ^{252}Cf, fast-neutron-induced fission of ^{239}Pu and ^{238}U. The same experimental methods and analysis procedures have been applied to obtain the emission spectra by recovering the complex response functions of different types of γ-ray detectors. Thus the results can be compared in a consistent way to understand what can impact the prompt γ-ray emission.

According to the experimental results in Figure 5.1, the PFGS shows different structures as a function of the γ-ray energy in the range of 0.1 to 10 MeV. In the high-energy region, from 1 MeV to 8 MeV, it is characterized by the exponentially decreasing yields of statistical γ-rays (mainly electrical dipole transitions). An exponential fit of the tail (between 3 MeV to 6 MeV) has been performed, which gives the fitted slope parameter of 1.24 MeV^{-1}, 0.97 MeV^{-1} and 1.20 MeV^{-1} for the fission reactions ^{252}Cf(sf), ^{239}Pu(n$_{1.8MeV}$,f) and ^{238}U(n$_{1.9MeV}$,f), respectively (Figure 5.2). The spectrum of ^{239}Pu(n$_{1.8\ MeV}$,f) is much harder than the two others in this region. At energies below 1 MeV, the discrete characteristic γ-rays along the Yrast lines of rotating fragments dominate the spectrum. In the fission process, a few hundreds of different isotopes are populated. Some of them have close-lying and overlapping γ-ray lines. This feature, combined with the limited energy resolution of our γ-ray detectors (scintillation detectors), creates bunches of lines with similar energies. For example, the gross γ-ray structures of 350 keV, 480 keV and 580 keV are related to the discrete γ lines from $4^+ \rightarrow 2^+ \rightarrow 0^+$ chains of highly populated fission fragments ^{100}Zr and ^{138}Xe, in the case of ^{238}U(n$_{1.9MeV}$,f). Above 8 MeV, the onset of the giant-dipole-resonance (GDR) leads to a slight enhancement of the γ-ray spectrum [103, 104].

In order to identify the different effects that may impact the PFGS emission, the calculations from two fission models, GEF and FREYA, will be used in order to reveal the physics behind the obtained experimental results. GEF code includes a model of the potential energy surface (PES) of the compound nucleus in order to obtain the fragment yields at scission. Several physical models, *e.g.* excitation-energy-sorting mechanism and

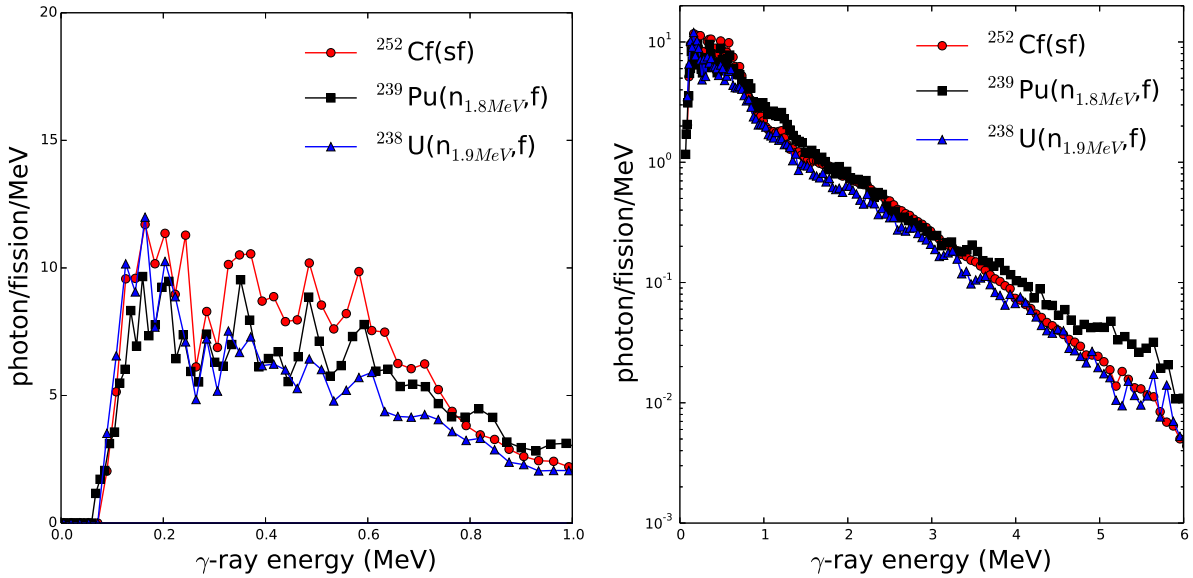

Figure 5.1 – Unfolded prompt fission γ-ray spectra obtained from this work with $LaBr_3$ detectors for different fission reactions: ^{252}Cf(sf), ^{239}Pu(n$_{1.8MeV}$,f) and ^{238}U(n$_{1.9MeV}$,f), respectively.

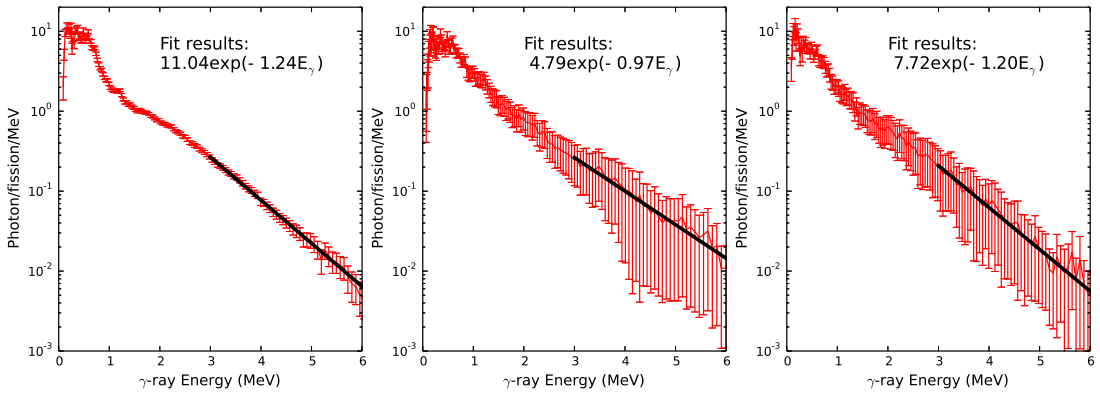

Figure 5.2 – An exponential fit to the high-energy tail between 3 MeV and 6 MeV for the unfolded prompt fission γ-ray spectra obtained from this work, for different fission reactions: ^{252}Cf(sf), ^{239}Pu(n$_{1.8MeV}$,f) and ^{238}U(n$_{1.9MeV}$,f), respectively.

statistical model for angular momentum generation, were proposed to determine the initial conditions of the fission fragments at scission. The fragments are then de-excited by neutron emission and subsequent photon emission. The neutron emission is described by evaporation models, including neutron-gamma competition. The γ-rays emission is calculated in a fully analytical formalism, in terms of the electric dipole E1 and electric quadrupole E2 transitions. FREYA code reads in fission fragment yields and the total kinetic energy of the fragments as inputs. Different excitation-energy-sorting mechanism and angular momentum generation mechanism are implemented for the determination of

the initial conditions of the fission fragments for subsequent de-excitation process, *i.e.* neutron emission and photon emission. The neutron emission is described by evaporation models and it stops when no more neutron emission is energetically possible. Neutron-gamma competition is not included. The photon emission is calculated firstly by the

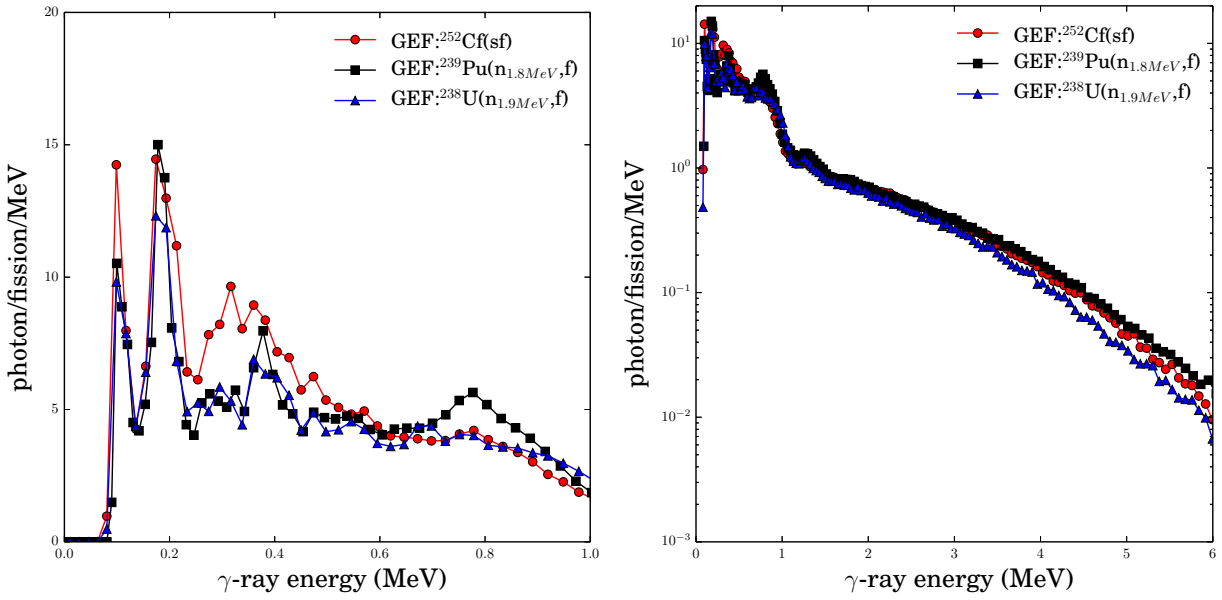

Figure 5.3 – Calculated prompt fission γ-ray spectra in GEF code for different fission reactions: ^{252}Cf(sf), ^{239}Pu(n$_{1.8MeV}$,f) and ^{238}U(n$_{1.9MeV}$,f), respectively.

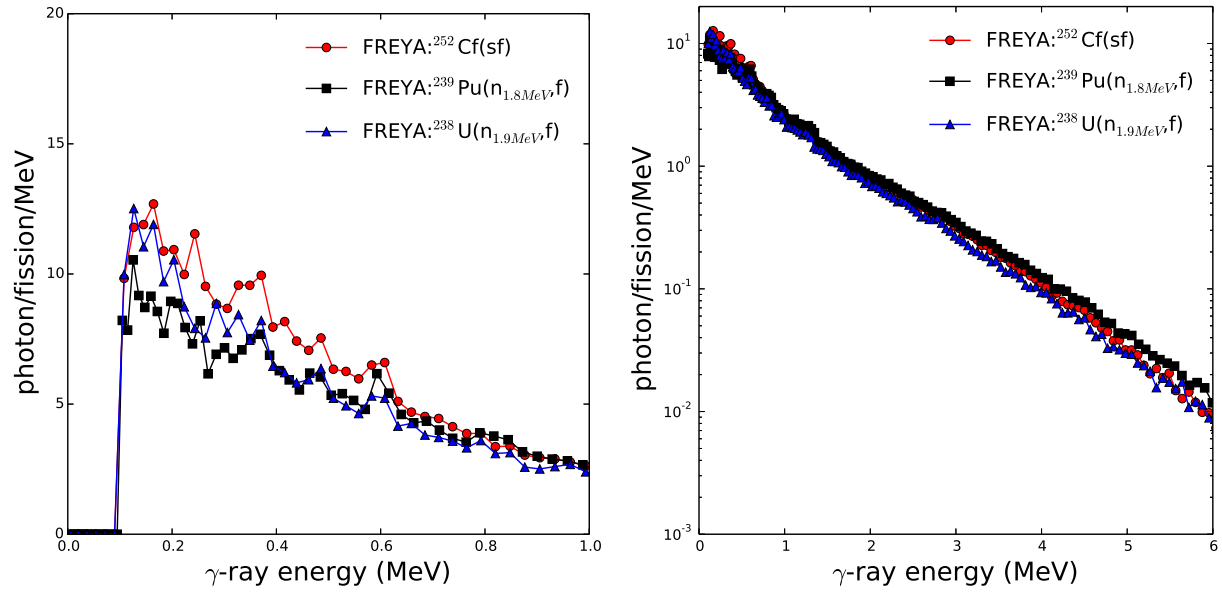

Figure 5.4 – Calculated prompt fission γ-ray spectra in FREYA code for different fission reactions: ^{252}Cf(sf), ^{239}Pu(n$_{1.8MeV}$,f) and ^{238}U(n$_{1.9MeV}$,f), respectively.

statistical transitions (E1) and then follows the experimental data form RIPL-3 in low-energy region.

It has been mentioned above that the lower energy limit and time window to select the PFG are important in comparison between experimental results and theoretical calculations. It is noted that the default lower energy limit for γ-ray in GEF code is 50 keV, which can be set to be a higher value when treating the event-by-event data. In FREYA, this quantity is a tunable input data in the source code, which is set to be 100 keV as is the same in the experiments. The lower energy limit effect strongly influences the PFG characteristics, especially the γ-ray multiplicity and average photon energy per fission. Regarding the time limit for prompt γ-rays emission, the GEF code in default version stops the de-excitation calculation whenever the γ-ray cascade reaches an isomeric state according to JEFF-3.1.1 with lifetime in the order of 10 to 100 ms. In FREYA, the maximum lifetime of isomeric states is set to be 1.5 ns, which is close to the experimental conditions, *i.e.* few nanoseconds of time window. Due to limited time resolution of the whole experimental setup ($\sim$2 ns), the selection of a time window of few nanoseconds strongly affects the experimental spectral characteristics. The calculated results of PFGS are plotted in Figure 5.3 and Figure 5.4. The comparison of the spectral characteristics is presented in Table 5.1.

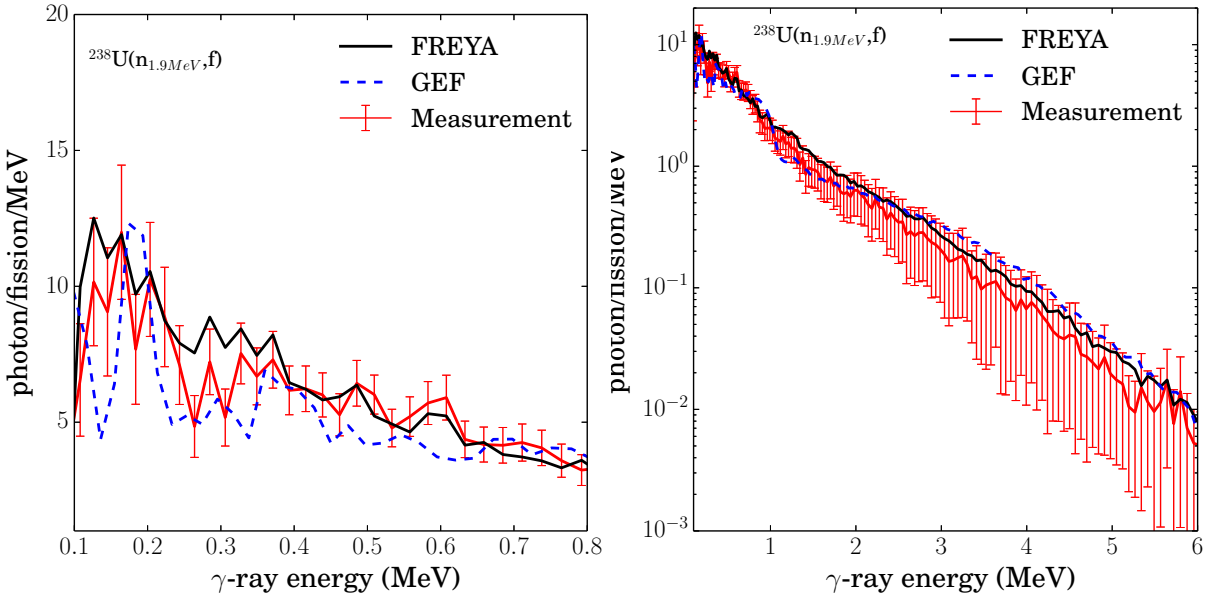

Figure 5.5 – Comparison of prompt fission γ-ray spectra obtained from experimental data, GEF and FREYA calculations for the fissioning system of ^{238}U(n$_{1.9MeV}$,f).

From the comparison (Figure 5.5), we can see that the theoretical calculations cannot fully match the experimental results neither in the low-energy nor in the high-energy regions. In GEF calculations, the discrete γ lines have rather poor agreement with the experimental results since it uses an analytical formula to obtain the electrical quadrupole

Table 5.1 – Comparison of PFGS characteristics between experimental results observed from this work and theoretical calculations from GEF and FREYA, for different fission reactions. The selected time window and the energy range have been also pointed out.

		$\overline{M}_\gamma$ (/fission)	$E_{\gamma,tot}$ (MeV)	ϵ_γ (MeV)	Δt (ns)	ΔE (MeV)
^{252}Cf(sf)	This work	8.35±0.20	6.64±0.21	0.80±0.02	±2.5	0.1-6.0
	GEF	7.17	6.52	0.91	~10^4-10^5	0.1-6.0
	FREYA	8.31	7.10	0.85	1.5	0.1-6.0
^{238}U($n_{1.9MeV}$,f)	This work	6.54±0.19	5.25±0.20	0.80±0.04	±2.5	0.1-6.0
	GEF	6.24	5.84	0.94	~10^4-10^5	0.1-6.0
	FREYA	7.23	6.18	0.85	1.5	0.1-6.0
^{238}U($n_{4.8MeV}$,f)	This work	7.31±0.46	6.18±0.65	0.84±0.11	±2.5	0.1-6.0
	GEF	6.54	6.14	0.94	~10^4-10^5	0.1-6.0
	FREYA	7.30	6.28	0.86	1.5	0.1-6.0
^{239}Pu($n_{1.8MeV}$,f)	This work	7.23±0.37	6.71±0.37	0.91±0.04	±3.0	0.1-7.0
	GEF	6.72	6.76	1.00	~10^4-10^5	0.1-7.0
	FREYA	7.38	7.06	0.96	1.5	0.1-7.0

transition along the Yrast line, while FREYA takes into account the experimental data from RIPL library at the last stage of the prompt γ-ray emission and thus well reproduces the positions of the major bunched γ peaks, even though the amplitudes of these peaks differ. In the high-energy region, the enhanced yield above 3 MeV calculated with the GEF code is not supported by the experimental results and results from FREYA code has better agreement with the experimental results. Nevertheless, both codes depict that the PFGS for ^{239}Pu($n_{1.8MeV}$,f) is clearly harder than that for the two other fissioning systems, which is also observed in the experimental results.

According to the spectral characteristics presented in Table 5.1, the prompt γ-ray multiplicities from FREYA calculations have good agreement with the experimental results generally (except that for the fissioning system of ^{238}U($n_{1.9MeV}$,f), the discrepancy is up to 10%). That is because the free parameters of the FREYA calculations (in default) is tuned by the multiplicity quantity of the ^{252}Cf(sf) reaction, taken from Billnert *et al.* [62]. However, the total γ-ray energy release is in overall higher than the experimental values. The average energy per photon is thus also higher because of the relationship $\epsilon_\gamma = E_{\gamma,tot}/\overline{M}_\gamma$. In terms of the GEF calculations, there are no free parameters for tuning. The obtained total γ-ray energy release has good agreement with the experimental results generally (except that for the fissioning system of ^{238}U($n_{1.9MeV}$,f), the discrepancy is up to 10%). But the prompt γ-ray multiplicity is much smaller than the measured values. Consequently the average energy per photon is much higher.

In this section three potential effects that can influence the spectral characteristics of PFGS will be discussed, including the energetic condition, isotopic yields and angular

momentum of the fission fragments. Due to the fact that all these three effects change with the incident neutron energy, the potential energy dependence of PFGS will also be discussed in the last section.

5.1 Energetics of the fission process

The primary fission fragments at scission are excited and rotating. Their energy and spin will be evacuated by first emitting prompt neutrons, followed by prompt γ-rays, though some competition between neutrons and high-energy γ-rays (de-exciting *e.g.* giant resonances) exists. Generally, the emission of prompt neutrons takes away most of the excitation energy of the fragments and does not modify the spin distribution on average. The leftover excitation energy and spin distribution at scission are the initial conditions for the prompt γ-ray emission. The following discussion includes a complete description of the energetics of the fission process from scission to the start of the prompt γ-ray emission, with the help of the calculation results in GEF and FREYA as well as some experimental evidences.

At the scission configuration, the initial excitation energy E^{SC}_{init} can be described by two components, intrinsic excitation energy $\mathrm{E}^{*,SC}$ and collective $\mathrm{E}^{coll,SC}$:

$$E^{SC}_{init} = E^{*,SC} + E^{coll,SC} = E^{*,SC} + E^{def,SC} + E^{rot,SC} \tag{5.1}$$

The collective excitation energy includes deformation energy $\mathrm{E}^{def,SC}$ and rotation energy $\mathrm{E}^{rot,SC}$. The rotation energy $\mathrm{E}^{rot,SC}$ is due to the angular momentum of fission fragments generated in the scission process, where the mechanism of angular momentum generation is still unknown. According to energy conservation, the total statistical (intrinsic) excitation energy is deduced by [8]

$$E^{*,SC}_{total} = E^{*,SC}_{L} + E^{*,SC}_{H} = M^{gs}_{CN} + E^{*}_{CN} - M^{SC}_{L} - M^{SC}_{H} - E^{rot,SC}_{L} - E^{rot,SC}_{H} - V^{C}_{LH} \tag{5.2}$$

where M^{gs}_{CN} and E^{*}_{CN} is the ground state mass and excitation energy of the compound nucleus, M^{sc}_{i} the mass of the deformed pre-fragments, V^{C}_{LH} the coulomb repulsion between the two deformed pre-fragments of the scission configuration and E^{rot}_{i} the rotational energy of the deformed pre-fragments.

The sharing of this statistical excitation energy $\mathrm{E}^{*,SC}_{total}$ still remains controversial and different methods were applied in various model calculations, as is discussed in Section 1.2.2. In FREYA, $\mathrm{E}^{*,SC}_{total}$ is divided in proportion to the respective heat capacities, *i.e.* the level density parameter $\partial E^{*}_{i}/\partial T_{i} = 2a_{i}T_{i} \propto a_{i}$ according to the well-known relation $E^{*}_{i} = a_{i}T^{2}_{i}$, and assuming the nuclear temperature is equal for the two fragments in a thermal contact. Consequently, the $\mathrm{E}^{*,SC}_{total}$ is divided in proportion to the mass number since $a_{i} \propto A_{i}$. In GEF, the statistical excitation energy is shared according to the proba-

bility distribution of the available micro-states, given by the total nuclear level density [7]. The partition of the statistical excitation energy is not proportional to the mass of the fragments.

The deformation energy at scission plays an important role in the total excitation energy, which in turn depends on the shell structure of the specific nuclides. Thus the mass asymmetry of the pre-scission nuclear shape produces the saw-tooth shape of excitation energy as a function of fragment mass at the scission point, see Figure 5.6. An experimental evidence is the kink around $m_H^* \approx 132$ (^{132}Sn), which corresponds to the stiff doubly magic numbers with small deformation energy, and most of the deformation energy is stored in the shape-distorted complementary light fragments.

The deformation energy at the scission point is transformed to excitation energy when the fragments are fully accelerated. Neutrons are assumed to be evaporated from the fully accelerated fragments, since the neutron characteristic emission time is much larger than the duration of the acceleration phase. Evaporation models for the prompt neutron emission have been proved to be a good approximation since the Maxwell spectrum describes well the measured neutron energy spectra in the laboratory frame (see Figure 1.9), with the formalism:

$$\phi(\epsilon_n) \sim \sqrt{\epsilon_n}\, e^{-\epsilon_n/T} \tag{5.3}$$

where T is the temperature of the daughter nucleus and ϵ the kinetic energy of the emitted neutrons. Even though neutrons evaporated from a rotating nucleus are related to its angular momentum [113], this effect can be neglected in the first-order approximation. The neutron emission is ceased when it is not possible energetically any more, which means that the neutron emission is mainly constrained by the available excitation energy. Thus the initial fission fragment excitation energies $E^{init}(A)$ largely determine the multiplicities and total energy of evaporated neutrons, see Figure 5.6 (top and middle). It is noted that the sawtooth shapes are roughly reproduced in the total energy released by prompt neutron emission $E_{n,tot}(A)$, while the distribution of post-evaporation excitation energy as a function of fragment mass does not conserve the shape any more (bottom in Figure 5.6). The post-evaporation excitation energies correspond to the initial energetic conditions for the subsequent γ-ray emission.

As is seen in Figure 5.6, the distribution of the post-neutron-evaporation excitation as a function of the fragment masses does not have the same shape of the two aforementioned distributions. The distributions also possess more-or-less the same shape for different fissioning systems in each calculation code, though the two different codes produce slightly different distributions. Nevertheless, this result is compatible with the discussions above because prompt γ-ray emission comes mainly after the fission product excitation energy drops below the neutron separation energy S_n by a few MeV, *i.e.* another neutron emission not energetically possible. Therefore, in terms of one fission fragment with certain mass and charge number, the post-evaporation excitation is at a similar level despite the initial

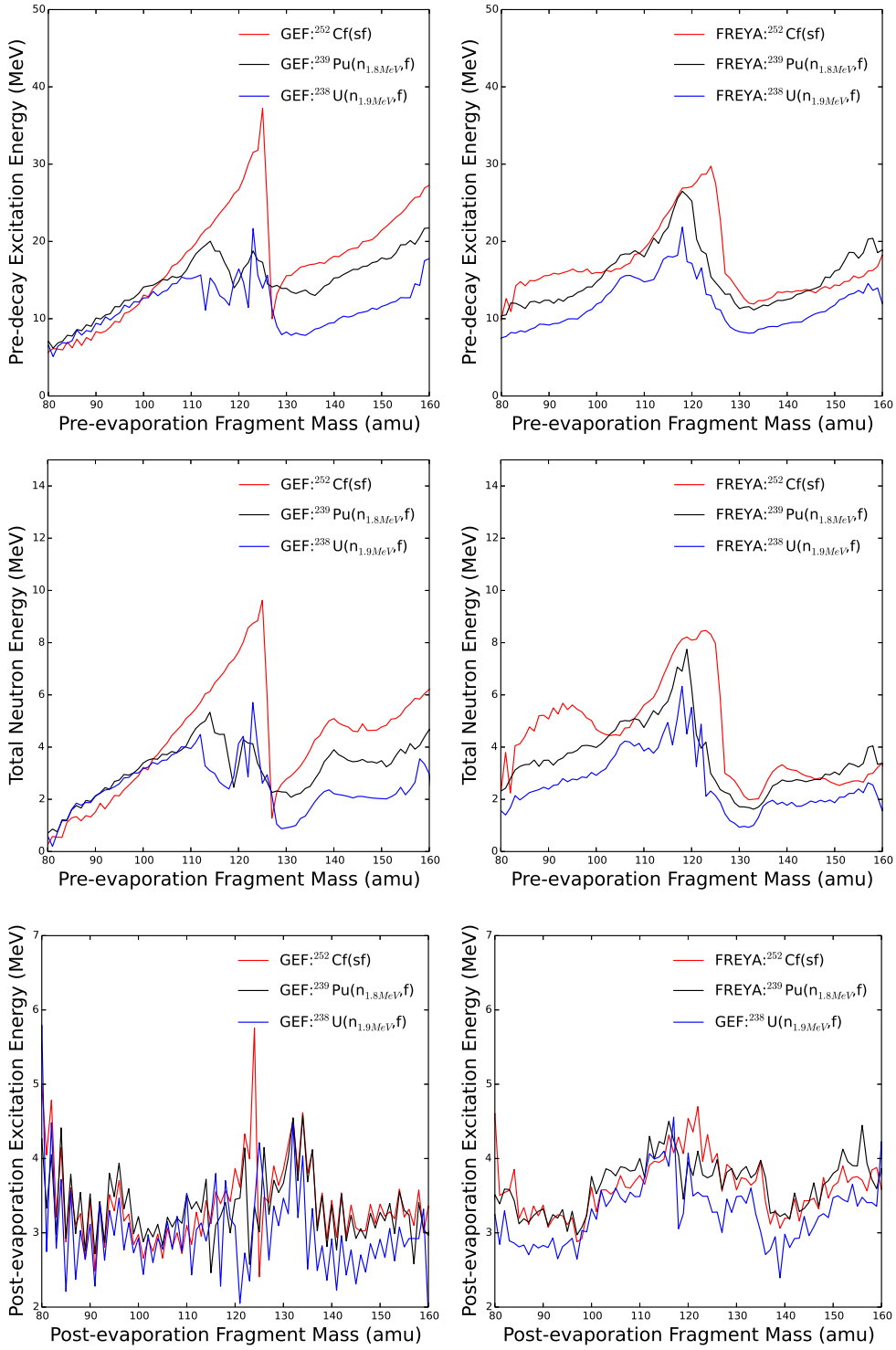

Figure 5.6 – The energetics of the fission process from scission point to the start of the prompt γ-ray emission as a function of fragment mass A for different fission reactions: ^{252}Cf(sf), ^{239}Pu(n$_{1.8MeV}$,f) and ^{238}U(n$_{1.9MeV}$,f), respectively, according to GEF (left) and FREYA (right).

excitation energy and the prompt neutron properties varies significantly with different fission reactions. The neutron separation energy should give a hint on this quantity, which can be easily checked by plotting the neutron separation energy as a function of fragment mass. $S_n(A)$ is weighted over charge yields for each mass number A, see Figure 5.7. This calculation uses nuclear masses from Ref. [114] and independent fragment yields from JEFF-3.3 evaluation [115]. The obtained neutron separation energy $S_n(A)$ changes dramatically at A=100 and A=132 and rather slowly in each individual region. It roughly reflects the shape of the distributions compared to FREYA calculations and the relative level of the neutron separation energy $\overline{S}_n$. $\overline{S}_n$ of ^{238}U($n_{0.4MeV}$,f) is ~0.5 MeV lower than ^{252}Cf(sf) and ^{239}Pu($n_{0.4MeV}$,f), because this reaction produces more neutron-rich fragments than the other two reactions.

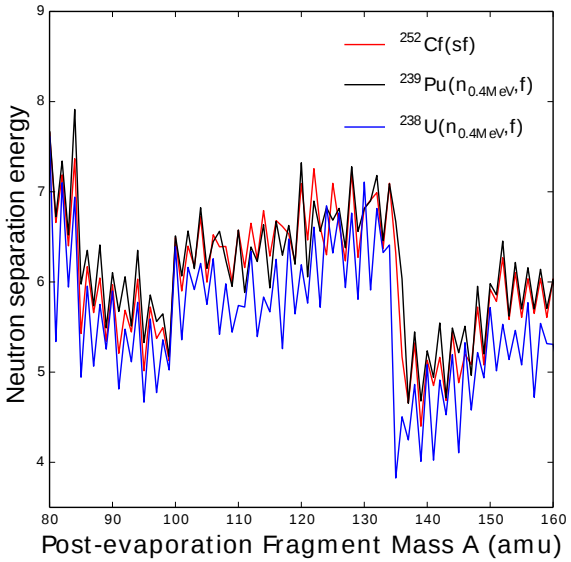

Figure 5.7 – Neutron separation energy distribution as a function of fragment mass A, weighted over the charge yields for each mass number. The charge yields are obtained from JEFF-3.3 library [115] for the available fissioning systems: ^{252}Cf(sf), ^{239}Pu($n_{0.4MeV}$,f) and ^{238}U($n_{0.4MeV}$,f), respectively.

5.2 Fission fragments yields

As mentioned in the previous section, the physical quantities in fission process depend on the fragment mass, *e.g.* the distribution of total γ-ray energy released as a function of the post fission fragments mass (see Figure 5.6). Therefore, in determining the γ-ray characteristics, the fragment mass dependence needs to be coupled with the corresponding mass yields (in fact, charge yields has already been taken into account when obtaining the mass dependences). Generally, the fission fragments yields varies with different fission

reactions and incident neutron energy (for neutron-induced fission), which in essence needs to be taken into account in the calculations and evaluations of the prompt γ-ray characteristics.

It has already been observed in the experiment of the Darmstadt-Heidelberg Crystal Ball spectrometer that there is a strong enhancement of the γ-ray spectra in the energy range between 3.5 MeV and 8.0 MeV due to the strongly reduced level densities in the vicinity of the shell closures at Z=50 and N=82 [116], which in turns gives much larger nuclear temperature T according to $T = \sqrt{E^*/a}$, where E^* is the statistical excitation energy (see Figure 5.8). This phenomenon is well reproduced in the FREYA code, see Figure 5.9, where an enhancement can be seen in the mass region from 130 to 135 in different fissioning reactions (only ^{238}U($n_{1.9MeV}$,f) is shown, similar for other reactions). However, in the GEF code (Figure 5.10), except the enhancement in the mass region of A=128-133, the light fragments also exhibits an enhancement in the high-energy region, which are not supported by the experimental results in Crystal Ball spectrometer. This overestimation might be the origin of the enhanced yields above 3 MeV in the PFGS spectrum when compared to the experimental results obtained from this work (Figure 5.5).

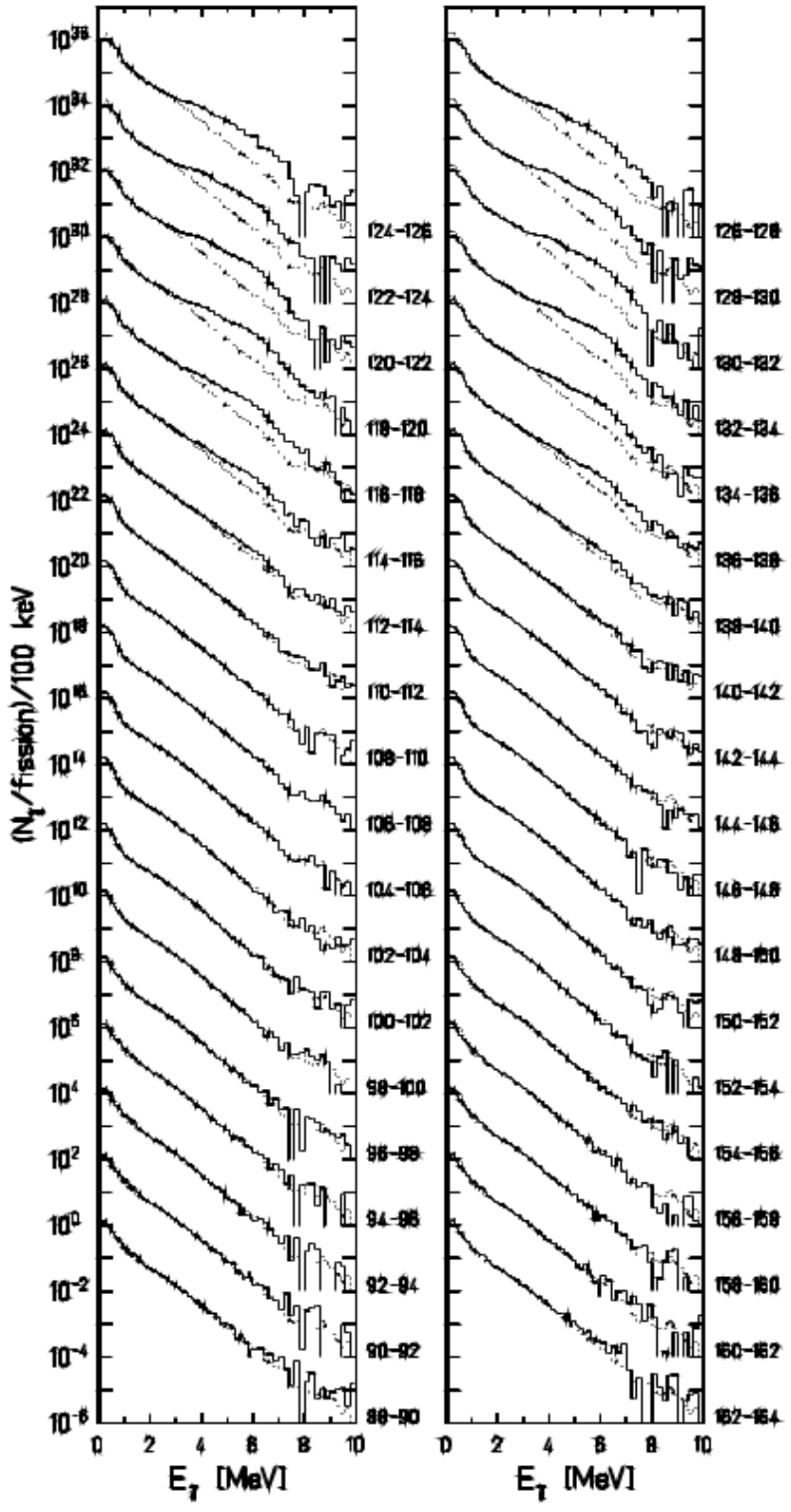

Figure 5.8 – Normalized γ-ray spectra for different fragment mass splits. The spectra have been scaled for better visibility. The dotted line shows the spectrum observed for A_b=106-108. Results taken from Ref. [116].

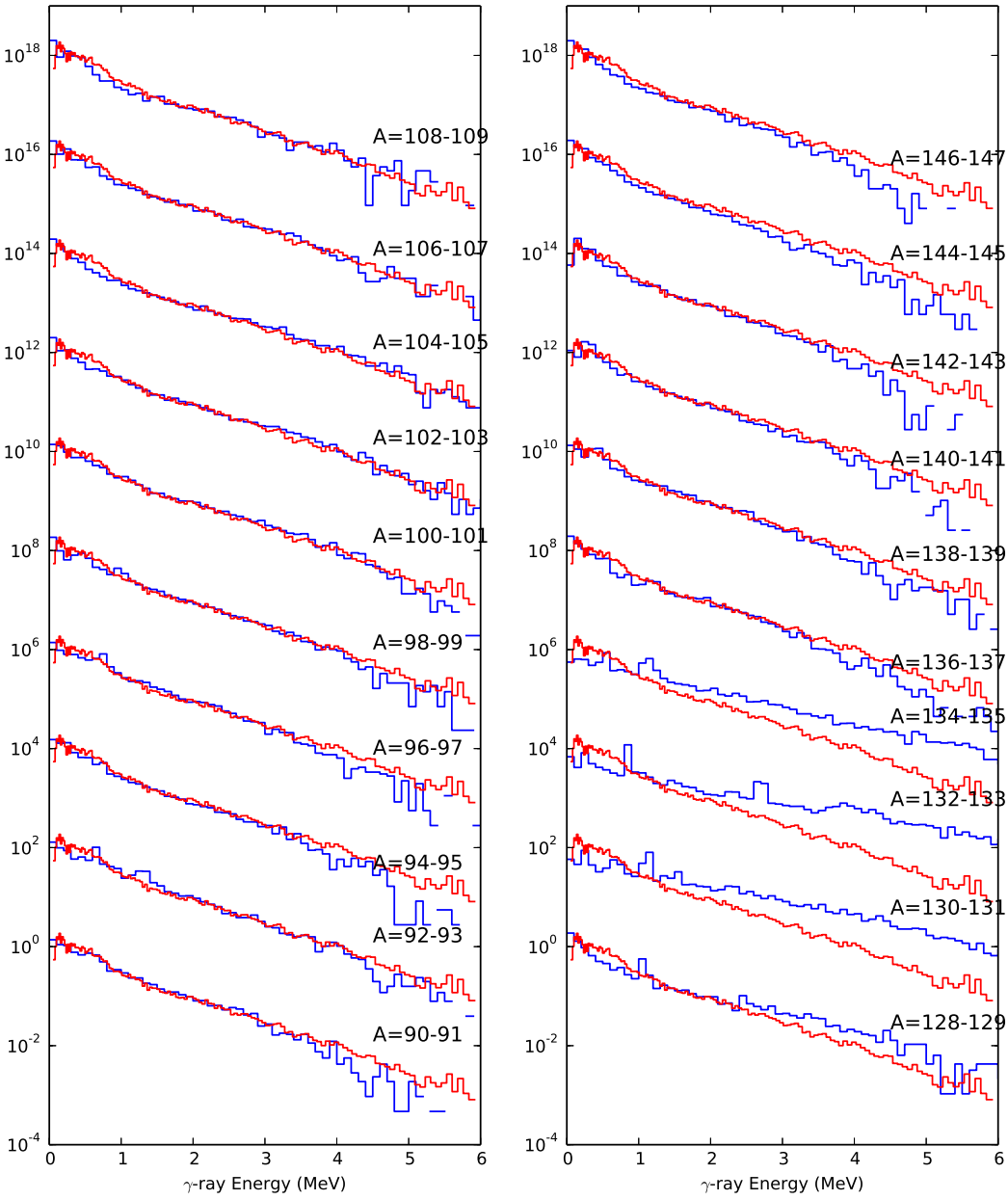

Figure 5.9 – Normalized γ-ray spectra for different fragment mass A in fission reaction ^{238}U(n$_1$.9MeV,f) calculated in FREYA code. The spectra have been scaled for better visibility. The red spectrum represents the PFGS obtained from this work.

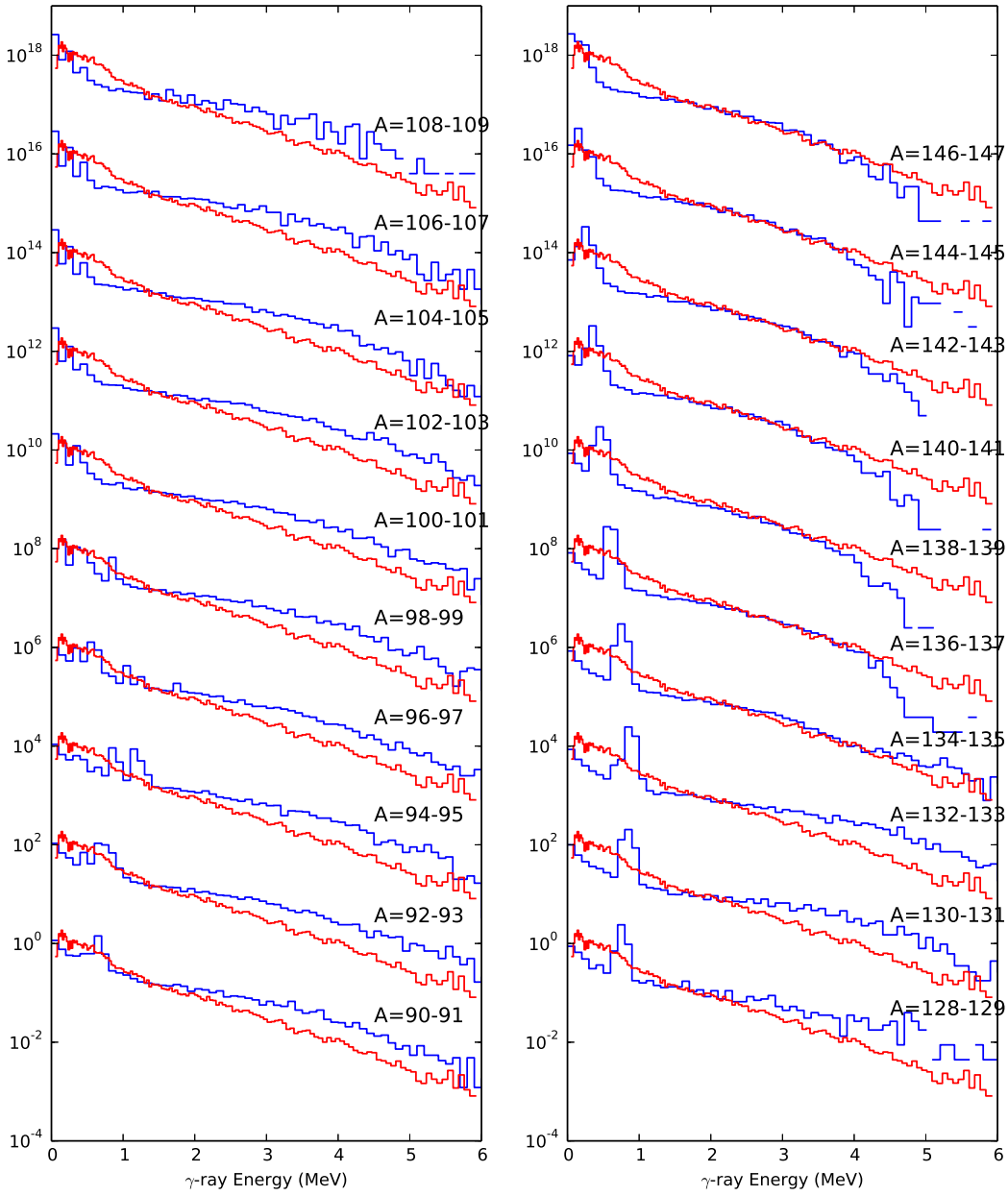

Figure 5.10 – Normalized γ-ray spectra for different fragment mass A in fission reaction ^{238}U(n$_1$.9MeV,f) calculated in GEF code. The spectra have been scaled for better visibility. The red spectrum represents the PFGS obtained from this work.

The leftover excitation energy, after neutron evaporation has ceased, is exhausted by γ-ray emission, including statistical photons mainly from electrical dipole transitions and discrete γ-ray from electrical quadrupole transition. The statistical γ-rays carry away most of the remaining excitation energy of the fragments in a wide energy range, up to 8 MeV ($\sim$neutron separation energy). In both calculations, the energy distribution of statistical photons follows the giant dipole resonance form factor modulated black-body spectrum with slight differences in the formalism [7, 8]:

$$FREYA \ : \phi(\epsilon_\gamma) \sim \frac{\Gamma_{GDR}^2 \epsilon_\gamma^4}{(\epsilon_\gamma^2 - E_{GDR}^2)^2 + \Gamma_{GDR}^2 \epsilon_\gamma^2} e^{-\epsilon_\gamma/T} \tag{5.4}$$

$$GEF \ : \phi(\epsilon_\gamma) \sim \frac{\Gamma_{GDR} \epsilon_\gamma^4}{(\epsilon_\gamma^2 - E_{GDR}^2)^2 + \Gamma_{GDR}^2 E_{GDR}^2} e^{-\epsilon_\gamma/T} \tag{5.5}$$

where Γ_{GDR}^2 is the width of GDR, E_{GDR} the position of GDR, T is the nuclear temperature and ϵ is the γ-ray energy. The magnitude of the angular momentum is reduced by 1 (FREYA) or 0 (GEF) for each statistical photon (mainly E1 transitions) emitted and the remaining excitation becomes $E_f^* = E_i^* - \epsilon_\gamma$. The use of the giant dipole resonance form factor hardens the spectrum, especially in the high-energy region. And this effect is more enhanced for fission fragments with larger mass number, due to the fact that the GDR position follows $E_{GDR}(MeV) = 31.2/A^{1/3} + 20.6/A^{1/6}$ [117], see Figure 5.11(a).

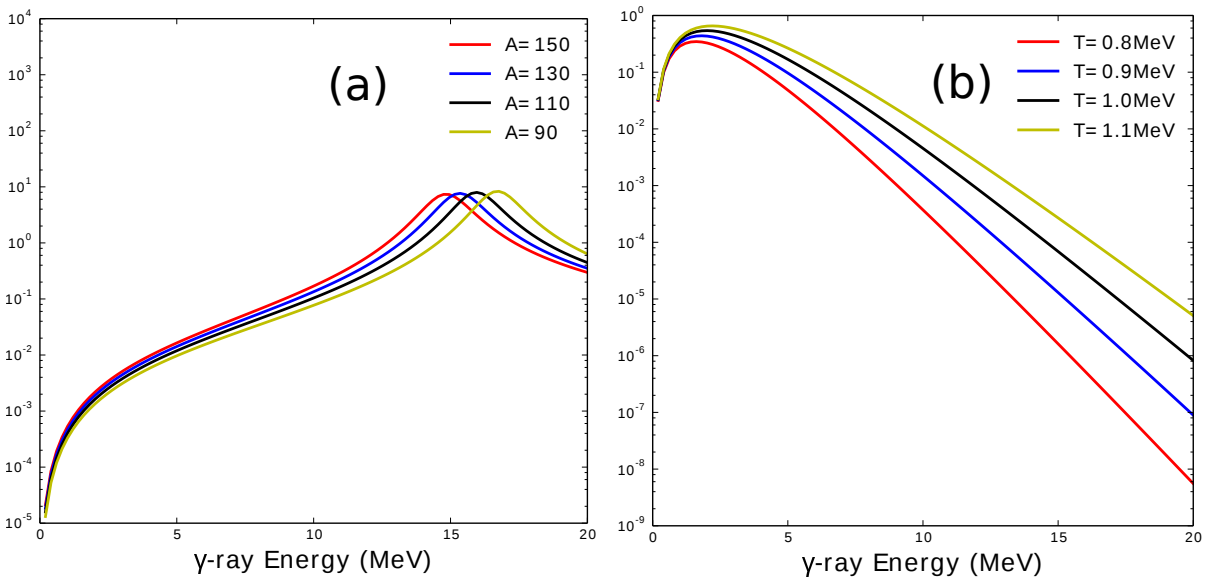

Figure 5.11 – (a) Giant dipole resonance form factor distribution for different fragment masses A; (b) Black-body spectrum with different temperature coefficients.

The nuclear temperature also depends on each individual fragment, *i.e.* the level density parameter [118]:

$$a(U) = a^*\Big\{1 + \frac{\delta W}{U}(1 - e^{-\gamma U})\Big\}, U \equiv E^* - \Delta \tag{5.6}$$

where a* is the asymptotic level density parameter, δW the shell correction energy, γ the damping factor, E* the excitation energy and Δ the pairing energy. The effect of the nuclear temperature in the γ-ray spectra can be seen in Figure 5.11(b), where a larger T harden the spectrum in the high-energy tail.

Once the Yrast line is reached, the remaining rotational energy is evacuated by electrical quadrupole E2 transitions. The magnitude of the angular momentum is reduced by 2 and the corresponding rotation energy disposed is described by the semi-classic expressions:

$$I_f = I_i - 2 \tag{5.7}$$

$$\epsilon_\gamma = \frac{\hbar^2}{2\mathcal{J}} I_i^2 - \frac{\hbar^2}{2\mathcal{J}} I_f^2 \tag{5.8}$$

where I is the angular momentum following the sequence of 0,2,4,..., and $\mathcal{J}$ is the moment of inertia depending on each individual fragment. In FREYA, the calculation also includes the experimental nuclear structure information from RIPL3 [51] data base. In the low-energy region, the calculations follows the tabulated decay rates between the levels from RIPL3 (partially). This is the reason why the low-energy structures in FREYA calculation have better agreement with the experimental results measured in this work, see one example of ^{138}Xe in Figure 5.12.

In this work, the measured PFGS is the summation of the contributions from all the mass splits. The experimental observations [116] reveals that the spectra are similar except for the fragments in the vicinity of the shell closures. This observation is also reproduced in the model calculations. Thus, we can deduce that the slope of the measured PFGS may also largely depends on the fragment yields in the region A=130-135. This is compatible with the experimental results and calculated results in both FREYA and GEF that the spectra of ^{239}Pu(n,f) is harder than ^{252}Cf(sf), due to the fact that the yields in region A=130-135 for the fission reaction ^{239}Pu(n,f) is higher than that in ^{252}Cf(sf), see Figure 5.13 and Figure 5.14. On the other hand, even though the fragments yields is quite similar for the fission reactions ^{239}Pu($n_{1.8MeV}$,f) and ^{238}U($n_{1.9MeV}$,f) (according to FREYA), the γ-ray spectra is much softer in the high-energy region for ^{238}U($n_{1.9MeV}$,f). This is because the initial condition in terms of excitation energy for each fragment is quite different for reactions $^{239}Pu_{1.8MeV}$(n,f) and $^{238}U_{1.9MeV}$(n,f), while similar for $^{239}Pu_{1.8MeV}$(n,f) and ^{252}Cf(sf), see Figure 5.6. One might naively expect that higher initial excitation energy, when prompt γ-rays emission starts, tends to emit more

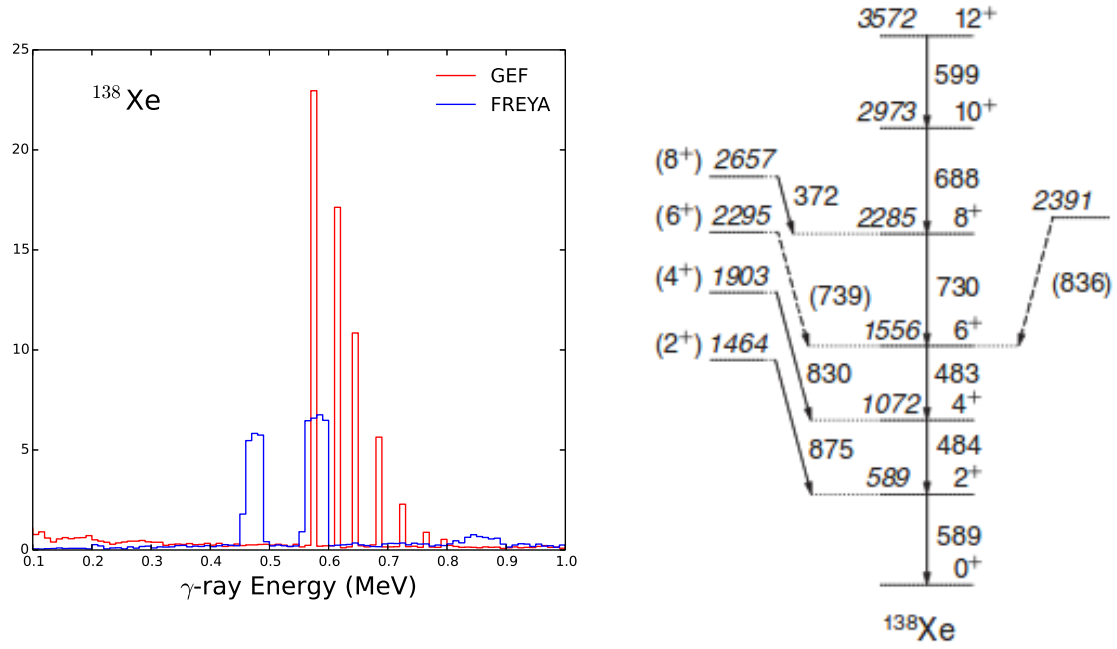

Figure 5.12 – Discrete γ-ray from electrical quadrupole transitions of ^{138}Xe calculated from GEF and FREYA code, as well as partial level scheme of ^{138}Xe deduced from experimental data set [119].

energetic γ-rays. Therefore, the slope of the high-energy tail in PFGS should depend on the initial energetic condition of the fragments when prompt γ-ray emission starts and the fragment yields, especially the fragments close to the vicinity of shell closures.

In the low-energy region of the measured PFGS, the discrete γ-rays mainly from electrical quadrupole transitions E2 along the Yrast line of the fragments lead to another enhancement of the γ-ray spectrum below 1.5 MeV. Due to the large variety of fragment isotopes with their close-lying γ lines and the limited energy resolution of scintillation detectors, broad structures rather than sharp peaks are obtained, see Figure 5.1. For different fission reactions, even though the fragment yields may vary significantly, the major bunched groups of close-lying γ lines stay in the same positions and only the amplitudes vary. In addition, contrary to statistical photons, these discrete γ-rays are also sensitive to the angular momentum due to its nature, *e.g.* the multiplicity of γ-rays from E2 transitions is proportional to the amplitude of angular momentum I. The aspect of angular momentum will be detailed in the next section.

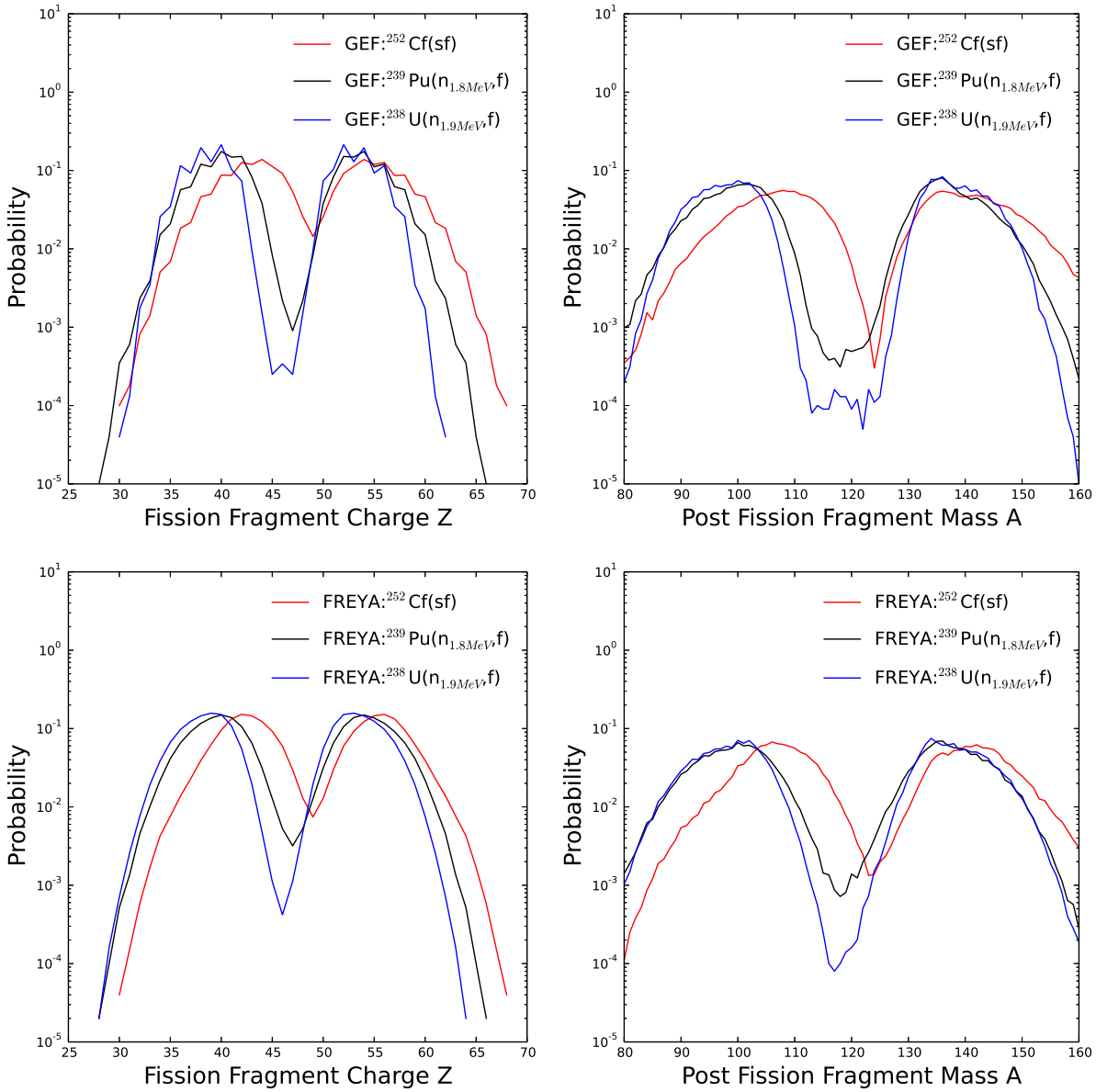

Figure 5.13 – Charge and post-evaporation mass distribution in GEF and FREYA code for different fission reactions. In GEF, the fragment yields as a function of mass and charge is obtained according to the potential energy at scission [7]. In FREYA, the mass and charge distribution of the fragments are determined by first selecting the mass from a probability distribution $P(A_f)$ of five-Gaussian and a subsequent charge selection from a normal distribution [8], with no odd-even staggering.

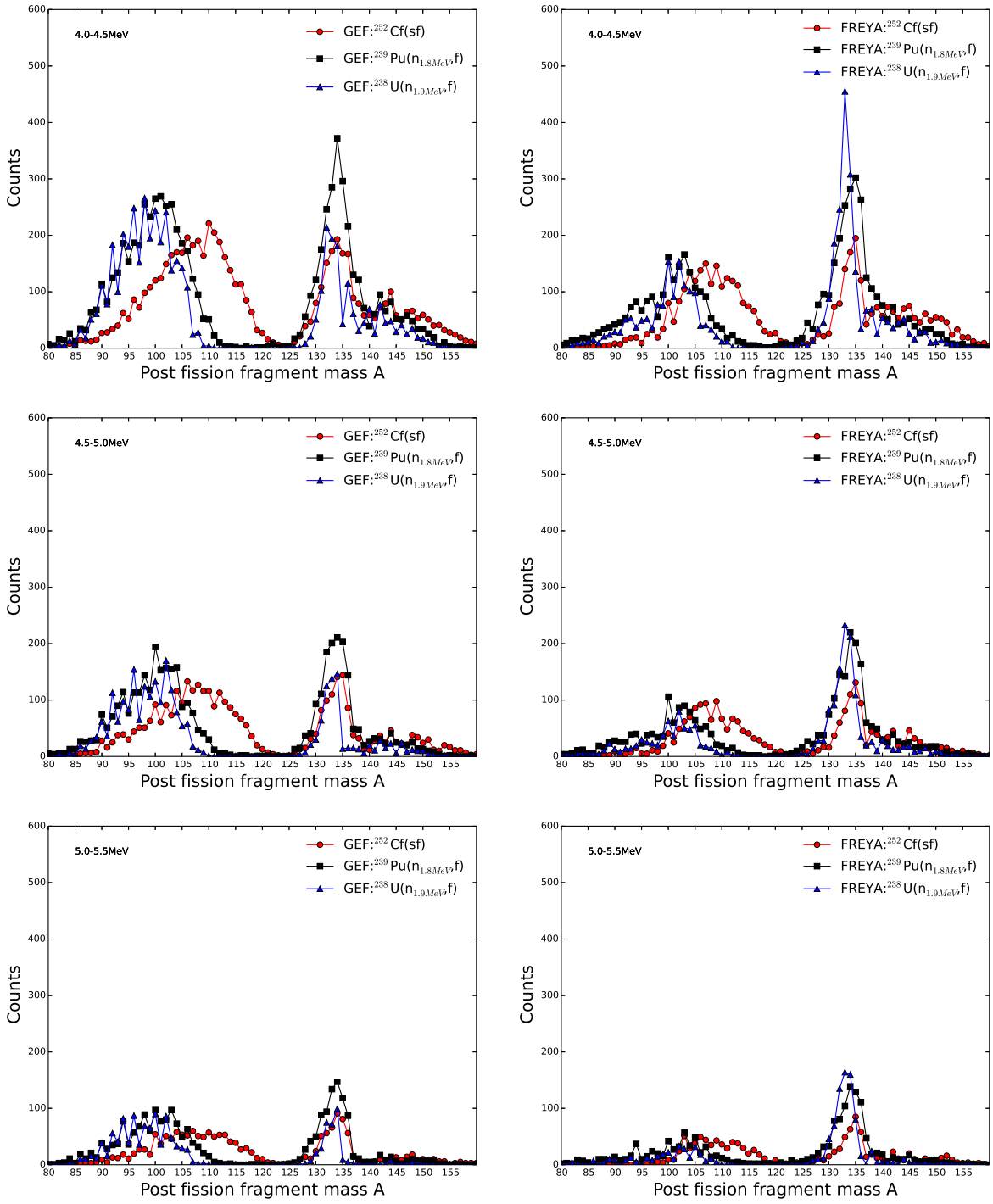

Figure 5.14 – Post-evaporation fragment mass distribution at different energy gates on the prompt fission γ-ray spectrum. The energy gates are [4.0 MeV-4.5 MeV], [4.5 MeV-5.0 MeV] and [5.0 MeV-5.5 MeV], respectively.

5.3 Angular momentum

In addition to the excitation energies and fragments yields, the initial fragment angular momentum distribution is also an important initial condition for the prompt γ-ray emission. Due to the fact that the rotating fragments emit E2 photons to carry away most of the angular momentum, one can naively expect that higher angular momentum generates prompt γ-rays with higher multiplicity and lower energy. On the contrary, the distribution of Yrast states as a function of spin is a very important observable for the study of angular momentum in fission.

Since this experiment does not have mass resolution for the fragment detection nor the energy resolution for the γ-ray measurement, it is difficult to extract sufficient experimental evidence for further detailed study. The only experimental observation is that the amplitudes of the major γ peaks in the low-energy region varies for different fissioning systems in Figure 5.1. According to the Ref. [54], where independent isomeric yield ratio was measured to deduce the average fragment angular momentum, it indicates that the angular momentum varies slowly with the change of the Z, A and excitation energy of the fissioning system. We then conclude that the amplitude difference of the major bunched γ peaks in the low-energy region, is mainly due to the variant excitation energy conditions and fragment yields, rather than the angular momentum, for different fission reactions. The following discussion will only include the difference of the treatment in the angular momentum for the two calculation codes.

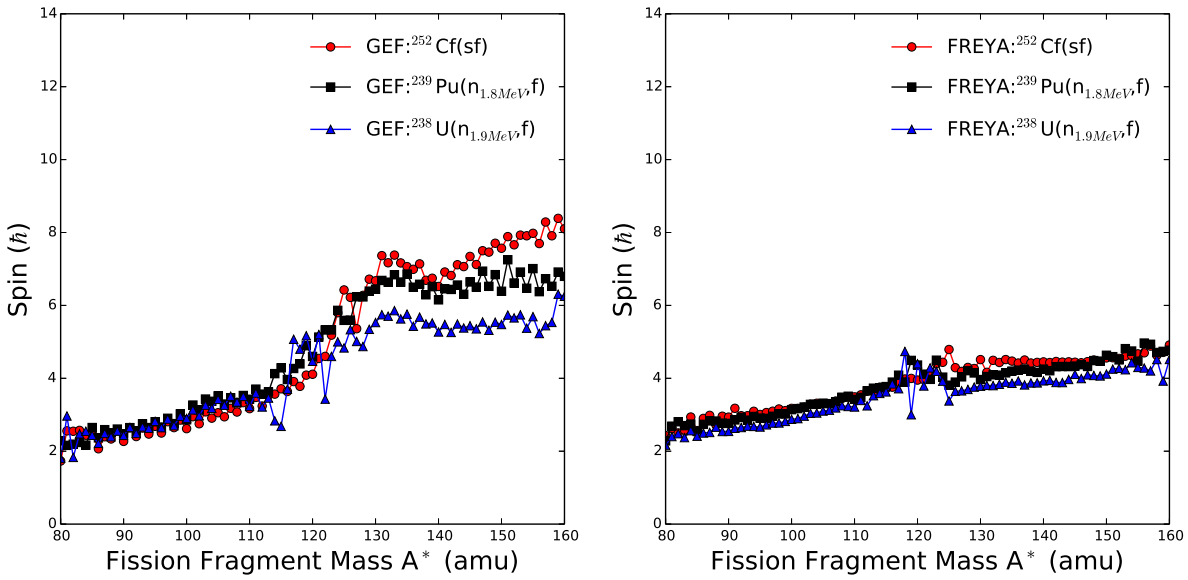

Figure 5.15 – Initial spin distribution of the fission fragments at scission from GEF and FREYA, for different fission reactions.

Generally, the emission of prompt neutrons is assumed not to modify the spin distri-

bution in average. The initial spin distribution of the fragments is thus assumed to be the same at the scission point and post-neutron evaporation. The angular momentum generation mechanism of the fission fragments at scission point is poorly understood. Therefore, it is treated by sampling the spin magnitudes independently for each fragment from the statistical distribution with the form similar to Equation 1.15 in the GEF code. The spin cut-off parameter is dependent on each fragment's moment of inertia and temperature with no adjustable parameter [7]. The FREYA code calculates the angular momentum from the overall dinuclear rotation plus the fluctuating amounts from the wriggling and bending modes in dinuclear rotation. The fluctuation components are the major source of the spin quantity, which are also agitated from the statistical distribution of the similar form mentioned before [117] with an adjustable free parameter. The calculated spin distributions J(A) are plotted in Figure 5.15. It can be seen that the heavy fragments generally have larger spins than the light fragments due to the differences in moment of inertia. The spins calculated in the GEF code are larger than those in the FREYA code.

Figure 5.16 shows the photon characteristics as a function of fragment mass, including the multiplicity and total energy release per fission. Very different multiplicity distributions are observed, *i.e.* the one from GEF calculation reflects its spin distribution while the result from FREYA is close to its total excitation energy distribution (*cf.* Figure 5.6). This is because the different way of treating the statistical photon emission (this part of emission is also noted in Figure 5.16). According to the discussion in the last subsection that the PFGS for each fragment mass does not vary significantly except for the vicinity of shell closures, the statistical photon emission is mainly constrained by the statistical excitation energy and thus the multiplicity distribution follows roughly the shape of its statistical excitation energy. The statistical photons do not modify the spin in GEF and the following E2 radiations follow essentially the Yrast line towards the ground state. So the multiplicity component originating from E2 radiations (proportional to the spin) dominates the distribution. On the contrary, the spin magnitude is decreased by 1 per statistical photon emission in FREYA, *i.e.* large part of the rotational energy is damped into the statistical energy. Thus, the multiplicity distribution is similar to the total excitation energy.

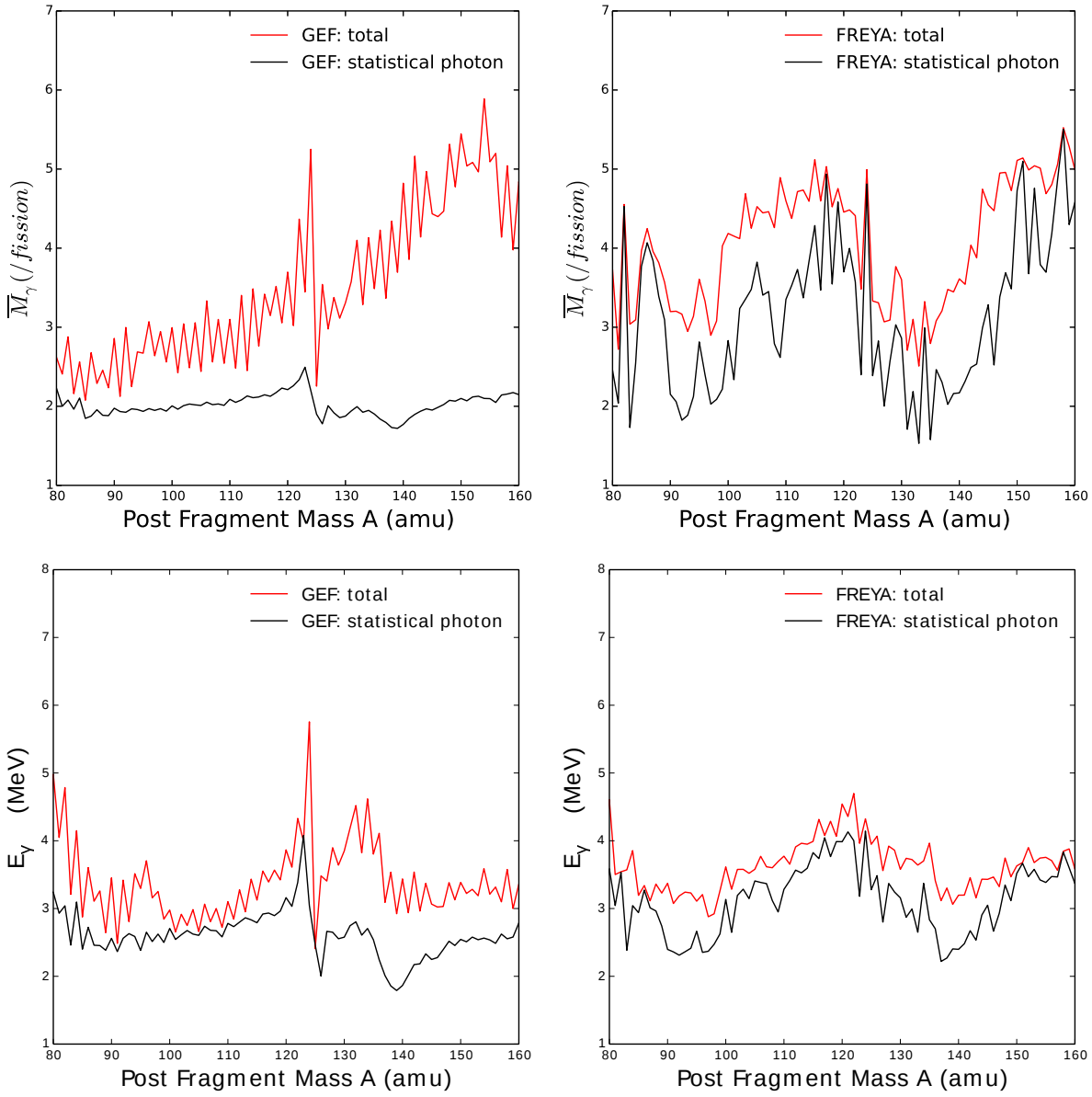

Figure 5.16 – Prompt γ-ray characteristics as a function of post-evaporation fragment mass A from GEF and FREYA, including average γ-ray multiplicity (top) and total energy release (bottom) per fission.

5.4 Incident neutron energy dependence

Changes in the PFG characteristics with incident neutron energy can occur because the three aforementioned aspects depend on the incident neutron energy. It is well known that the relative contributions from each fission fragment in the fission yields to the spectral characteristics of prompt γ-ray change with the incident neutron energy. The extra total fragment excitation energy available will be distributed for both neutron and γ-ray emission (see Figure 5.6), causing both of them to evolve as a function of the incident neutron energy. Finally, the angular momentum distribution ought to change, *i.e.* the average angular momentum of fission fragments is higher in medium-energy-induced fission than low-energy-induced fission [54]. In this work, PFGS from fast-neutron induced fission of ^{238}U at two incident neutron energies 1.9 MeV and 4.8 MeV, and of ^{239}Pu at E_n = 1.8 MeV are measured. There is no evidence for a firm shape change of the PFGS within the precision of the measurement (see Figure 5.17). No significant energy dependence for the spectral characteristics of PFGS below the second chance fission is observed.

Due to the fact that the increase of neutron energy is not very large, namely 2.9 MeV in the ^{239}U* fissioning system and 1.8 MeV in the ^{240}Pu* fissioning system (compared to thermal-neutron induced fission from Ref. [26]), combined with the experimental evidence that the angular momentum is not sensitive to the excitation energy of the compound nucleus [54], it indicates that the energy dependence of the spectral characteristics of PFGS below the second chance fission is mainly depending on the fission yields changes and how the extra excitation energy is distributed between neutron emission and γ-ray emission.

According to the independent yields (after neutron emission and before β-decay) in JEFF-3.3 evaluation data base for the two fissioning systems [115], the isotopic yields do indeed change when the incident neutron energy changes. According to the data available, for example, highly populated fragment Y(A=138) changes from 0.060 % to 0.047 % when incident neutron energy increases from 0.4 MeV to 14.0 MeV in ^{238}U(n,f) and it changes from 0.061 % to 0.058 % when incident neutron energy increases from 0.025 eV to 0.4 MeV in case of ^{239}Pu(n,f). Therefore, it is expected that the low-energy part of the γ-ray spectrum (*i.e.* discrete transitions, characteristic of the populated fragments), and the slope of the high-energy tail (sensitive to the yields of A=130-135), changes with neutron energy. However, changes in these structures are expected to be small over the studied neutron energy range, and we are indeed unable to evidence them clearly with the precision of the current measurement by using scintillation detectors in the case of fast-neutron-induced fission.

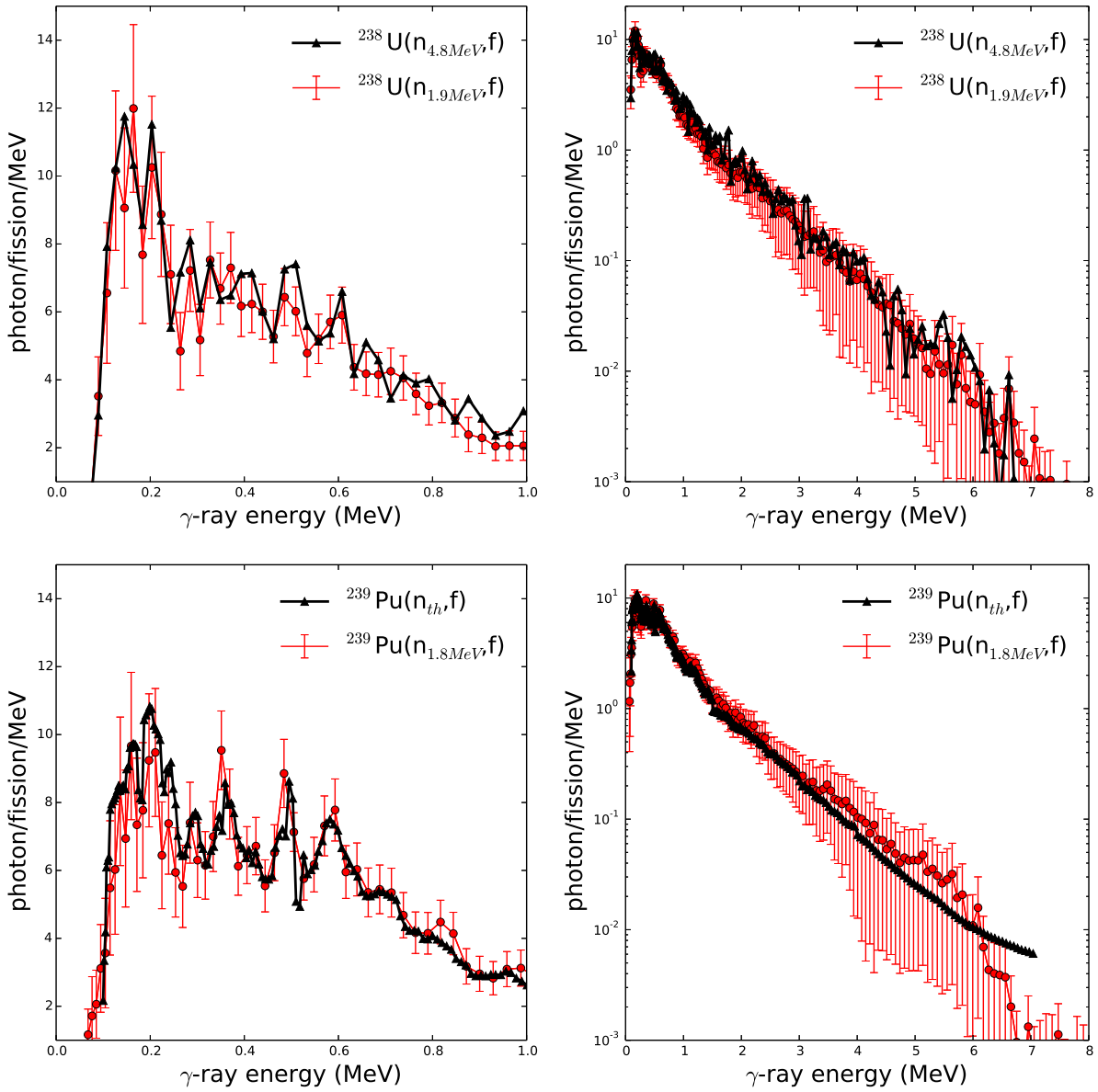

Figure 5.17 – Comparison of experimental prompt fission γ-ray spectra at different incident neutron energies for different fission reactions, respectively. The low-energy part are plotted in the left with linear scale and the total spectrum in the right with logarithmic scale. The error bar of one distribution has been omitted for easier reading.

A detailed comparison in terms of PFGS at different incident neutron energy is performed in Figure 5.18 and Figure 5.19. Both model calculations, from GEF and FREYA, also do not show significant differences at the two incident neutron energies in accordance with the experimental results. It can be explained by the discussions in the previous subsections about the effect of the excitation energy, fragment yields and angular momentum to the prompt γ-ray emission. Figure 5.20 plots the post-evaporation excitation energy, post-evaporation mass distribution and initial angular momentum distribution at neutron incident energy E_n=1.9 MeV and E_n=4.8 MeV, respectively. In GEF calculations, only the mass yields in the symmetric fission region increases by one order of magnitude. Nevertheless, it has negligible contributions to the prompt γ-ray emission, since the absolute value is still 3 orders of magnitude lower than the maximum. The angular momentum of the heavy fragments at scission increases by roughly 1 $\hbar$, due to the excitation energy sorting mechanism implemented [5]. In FREYA calculations, all these distributions do not show significant differences. As a consequence, both GEF and FREYA calculations do not show significant energy dependence for prompt γ-ray emission below the second chance fission.

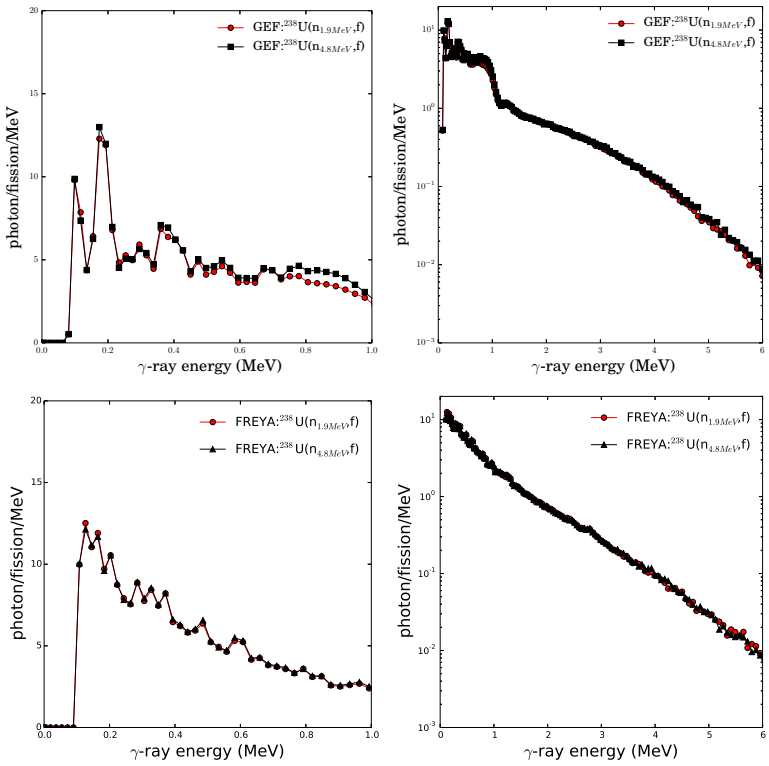

Figure 5.18 – Comparison of prompt fission γ-ray spectra at different incident neutron energies for the fission reaction ^{238}U(n,f) obtained from GEF and FREYA calculations, respectively. The low-energy part are plotted in the left with linear scale and the total spectrum in the right with logarithmic scale.

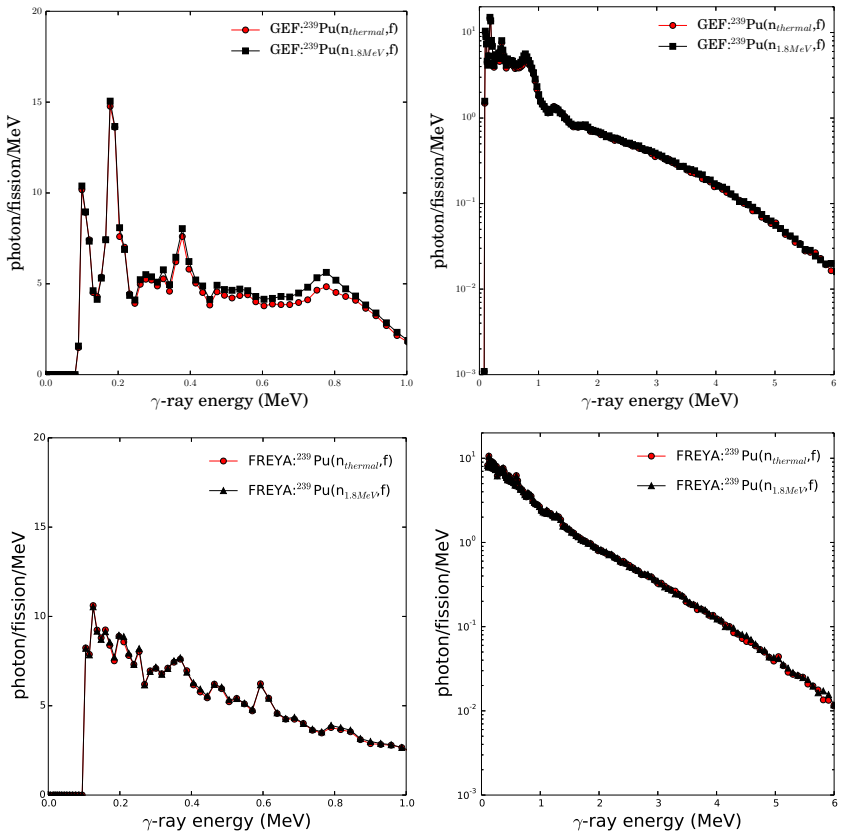

Figure 5.19 – Comparison of prompt fission γ-ray spectra at different incident neutron energies for the fission reaction ^{239}Pu(n,f) obtained from GEF and FREYA calculations, respectively. The low-energy part are plotted in the left with linear scale and the total spectrum in the right with logarithmic scale.

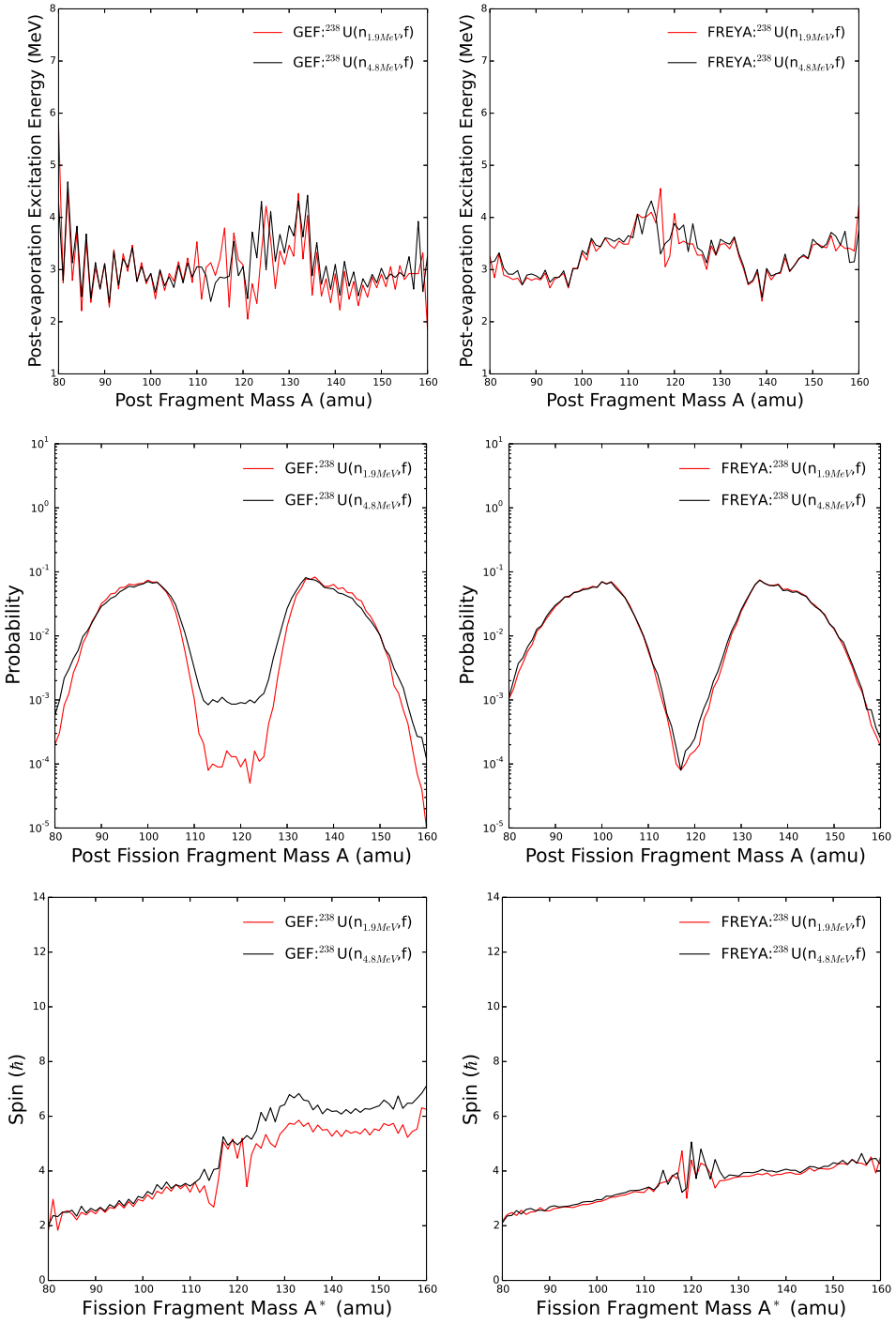

Figure 5.20 – Post-evaporation excitation energy, post-evaporation mass distribution and initial angular momentum distribution at neutron incident energy E_n=1.9 MeV and E_n=4.8 MeV, respectively, for the GEF (left) and FREYA (right) calculations.

On the other hand, the change in incident neutron energy leads to a few MeV of extra excitation energy imparted to the compound nucleus, 2.9 MeV and 1.8 MeV in case of $^{239}U^{*}$ and $^{240}Pu^{*}$ respectively, which is shared between the TKE and TXE of fission fragments. Previous measurements [120–122] have shown that for these two fissioning systems the average total fission fragment kinetics energies decrease with increasing incident neutron energy, by 1.33 MeV and 1.73 MeV in its energy range, respectively. This is because symmetric fission (SL fission mode) are increasing with increasing incident neutron energy and the total kinetic energies are at a minimum for symmetric fission [123]. Thus the extra TXE can be deduced from the experimental results of TKE, see Table 5.3. Then the partition of prompt γ-ray energy in this extra excitation energy can be deduced according to the energy conservation

$$\overline{TXE} = \overline{TXE}_n + \overline{TXE}_\gamma = \overline{\nu}_n(\overline{\epsilon}_n + \overline{S}_n) + E_{\gamma,tot} \quad , \tag{5.9}$$

where $\overline{\nu}_n$ is the average neutron multiplicity, $\overline{\epsilon}_n$ is the average neutron energy in center of mass system and $\overline{S}_n$ is the average neutron separation energy. $\overline{TXE}_n$ corresponds to the excitation energy released by neutron emission and $\overline{TXE}_\gamma$ by γ-ray emission. The neutron properties, namely neutron multiplicity and average neutron energy in laboratory system, can be obtained from JEFF-3.3 evaluated library [115]. The average neutron separation energy $\overline{S}_n$ has to be calculated using experimental masses [114] or theoretical masses [124] and weighted by the independent fission yields [115]. These numbers are presented in Table 5.2.

Table 5.2 – Summary of the prompt fission neutron properties extracted from JEFF-3.3 data library.

	E_n (MeV)	$\overline{\nu}_n$ (#)	$\overline{\epsilon}_{n,lab}$ (MeV)	$\overline{\epsilon}_{n,cm}$ (MeV)	$\overline{S}_n$ (MeV)	TXE_n (MeV)
^{238}U(n,f)	1.9	2.57	1.99	1.27	5.33	16.96
^{238}U(n,f)	4.8	2.97	2.07	1.34	5.40	20.02
^{239}Pu(n,f)	2.5e^{-8}	2.86	2.10	1.37	5.94	20.91
^{239}Pu(n,f)	1.8	3.14	2.13	1.41	6.08	23.52

Table 5.3 – Summary of the distribution of the excess excitation energy in prompt neutron and prompt γ-ray emission.

	ΔE_n (MeV)	ΔE^*_{CN} (MeV)	ΔTKE (MeV)	ΔTXE (MeV)	ΔTXE_n (MeV)	$\Delta TXE_{\gamma,calc}$ (MeV)	$\Delta TXE_{\gamma,exp}$ (MeV)
^{238}U(n,f)	1.9→4.8	2.9	-1.33	4.23	3.06	1.17	0.93±0.68
^{239}Pu(n,f)	2.5e^{-8} →1.8	1.8	-1.72	3.52	2.61	0.91	0.44±0.39

According to the calculated values of energy release in Table 5.3 for the two fission reactions, ∼70% of the excess excitation energy is evacuated by neutron evaporation and

only ∼30% for the photon emission, which means that the majority of the extra available TXE is dissipated by prompt fission neutron (PFN) emission. It is compatible with the measured values of the total energy release from prompt γ-ray emission within the uncertainties, supporting the conclusion that there is no significant energy dependence for the spectral characteristics of PFGS below the second chance fission.

Figure 5.21 and Figure 5.22 contains - as a function of incident neutron energy - the average values for each quantity from this work, together with results from GEF, FREYA and calculations based on systematics [125]. The calculated observables of PFG from GEF and FREYA have reasonable agreement with the experimental results and also exhibit a slightly increasing trend in terms of average γ multiplicity and total energy per fission, and no firm trend of the average γ-ray energy. It is also noted that the multiplicity and average energy quantities are very sensitive to the lower energy limit.

Some discrepancies are observed in the calculations based on systematics for the ^{238}U(n,f) reaction. We report much lower average γ multiplicity per fission, slightly lower total energy and higher average energy per fission, compared to the calculations based on systematics. A possible reason for the discrepancies is that these calculations are based on the assumption that the average total γ-ray energy and the multiplicity are linearly depending on the neutron multiplicity, whose coefficients are depending on the A and Z of the fissioning system. As a result, it highly relies on the fit with respect to the experimental PFG data to get the coefficients, where the number of experimental PFG data is still clearly insufficient.

Our observation of at most weak energy dependence of the PFG characteristics in this energy range is, within uncertainties, compatible with the results of J-M. Laborie *et al* [112]. It is also of importance for nuclear applications, since γ-ray heating accounts for a major source of energy deposition in certain reactor components, *e.g.* instrumentations and structural materials. In particular, the heating from γ rays is two orders of magnitude higher than neutron heating [3] in reactor reflectors and shielding, and needs to be estimated to a reasonable accuracy to avoid possible fracture and failure. The observed results facilitate the design for the fast reactors in Generation-IV which may not require significant changes in the modeling of γ heating transportation.

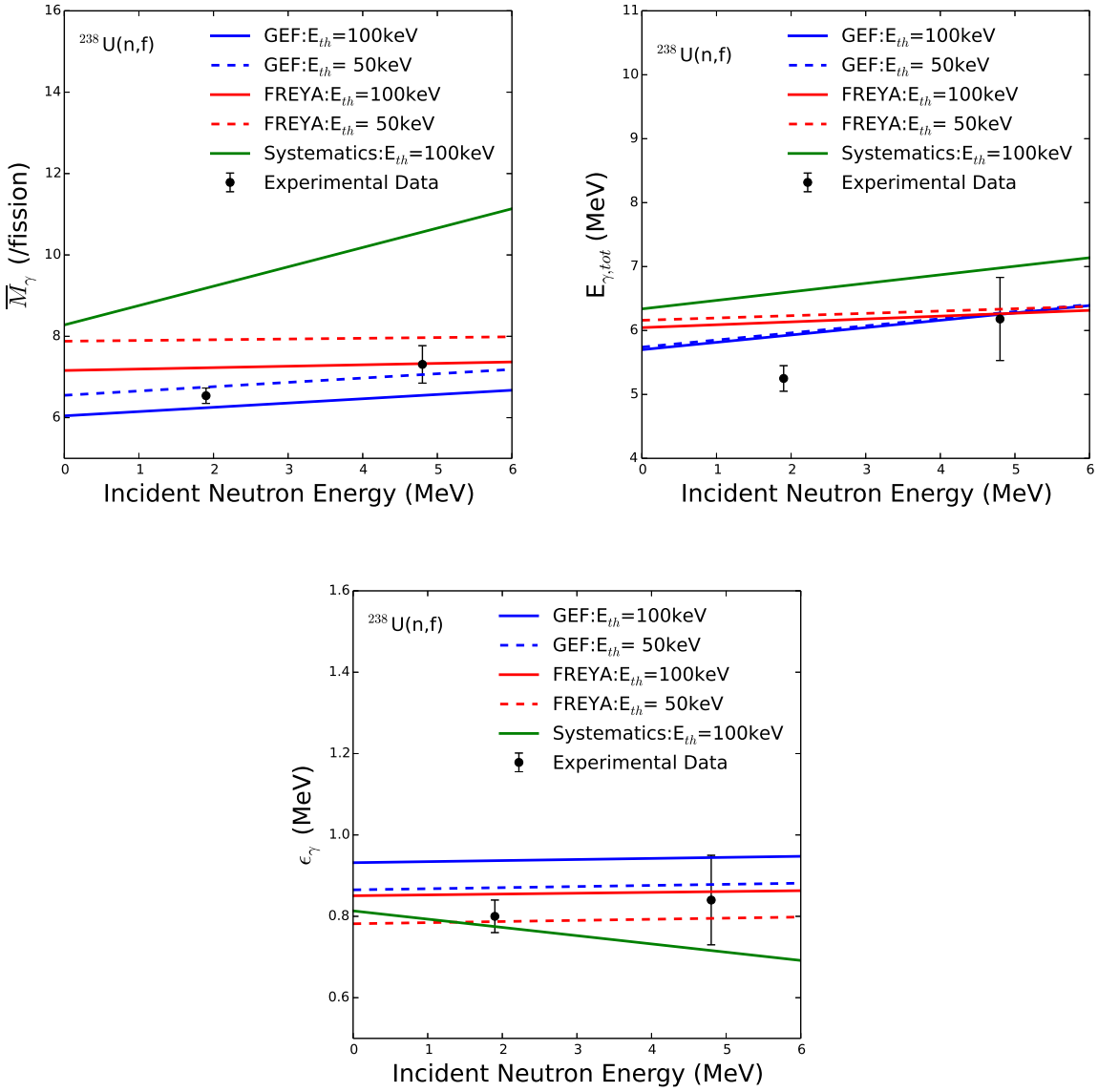

Figure 5.21 – Summary of the PFGS characteristics including average multiplicity $\overline{M}_\gamma$, average total energy $E_{\gamma,tot}$ and average γ-ray energy ϵ_γ, as a function of incident neutron energy, for fast-neutron induced fission of ^{238}U.

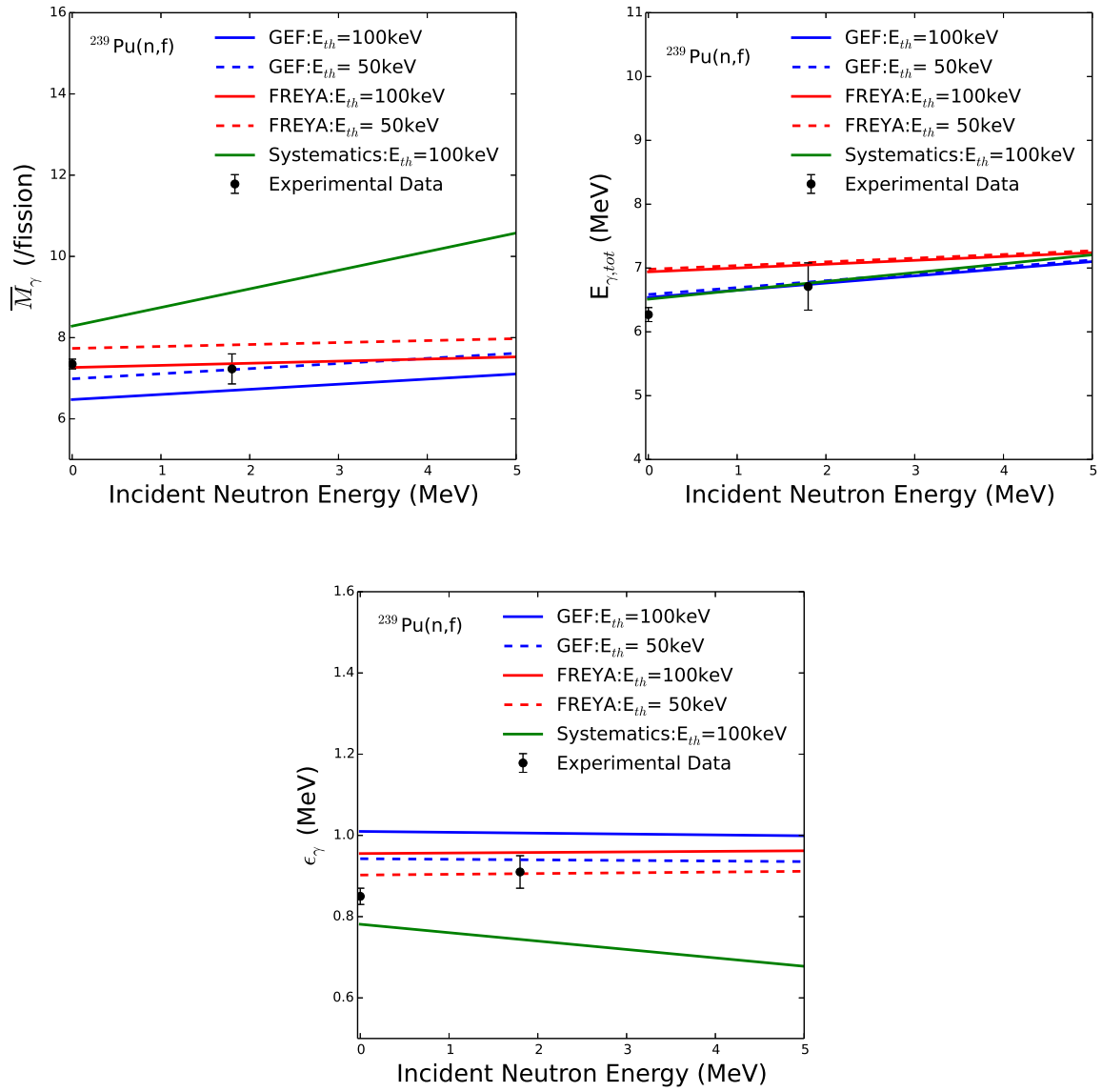

Figure 5.22 – Summary of the PFGS characteristics including average multiplicity $\overline{M}_\gamma$, average total energey $E_{\gamma,tot}$ and average γ-ray energy ϵ_γ, as a function of incident neutron energy, for fast-neutron induced fission of ^{239}Pu.

Three possible effects that may impact the prompt γ-ray emission are investigated in this chapter, including fission energetics, isotopic yields and angular momentum of the fission fragments. The comparison of the spectral characteristics in different fissioning systems reveals that the prompt γ-ray emission is constraint by its energetic conditions and thus related to the neutron separation energy. The slope of the PFGS at high-energy indicates that the prompt γ-ray emission also has dependences on the fragments yields. Lastly, the incident neutron energy denpendce of the prompt fission γ-ray emission is also investigated, which is observed to be very weak.

Conclusions and outlooks

The development of inverse kinematics neutron source, LICORNE, has opened up many new experimental possibilities, particularly related to the spectroscopy of the fission process and investigation into prompt emission of fast-neutron-induced fission. In this work, firstly, we developed the code to simulate the LICORNE neutron source and perform the experiments to validate the code. Secondly, we performed prompt fission γ-ray measurement for fast-neutron-induced fission and corresponding data analysis procedure to extract the spectral properties. Lastly, an investigation into different fission models have been carried out, by comparing the obtained experimental results to the calculations.

The simulation of the directional neutron generator LICORNE with p(^{7}Li,n)^{7}Be and p(^{11}B,n)^{11}C reactions have been implemented in GEANT4. The experimental differential cross section distributions are used in the kinematics calculations to better sample the angular distribution of the neutrons. The event biasing techniques, namely importance biasing and particles splitting, are implemented in GEANT4 without changing the tool kit itself, in order to decrease the calculation time. The code has been validated by comparing to the experimental results, including time-of-flight spectrum by using a liquid scintillation neutron detector and fission rate distribution by using an ionization chamber. Finally, the code has been used to understand the neutron spectrum and flux distribution in the space depending on different configuration of the LICORNE setup. These modifications and additions can help the design of future experiments for fundamental physics research and nuclear applications.

In this work, two experiments using the directional neutron source LICORNE have been carried out, namely measurement of prompt fission γ-ray spectra in fast-neutron-induced fission of ^{238}U and ^{239}Pu. Fission fragments were measured in an ionization chambers and discriminated with α particles depending on the differences of kinetic energies. The ionization chamber provides a fission tag and the coincident γ-ray are detected by different types of inorganic scintillation detectors, including LaB_3 and PARIS phoswich detectors. The prompt fission gamma rays are discriminated from prompt fission neutrons *via* time-of-flight technique. The measured γ-ray spectra were unfolded from the detection system response, which is simulated in GEANT4. Different unfolding techniques

were tested and iteration method has been chosen in consideration of stability especially in low statistics data set. The obtained results demonstrate a good performance of the PARIS phoswich detectors in this experiment when compared to $LaBr_3$. It was the first time that these detectors have been used in a physics experiment.

The spectral characteristics have been extracted from the PFGS with two important conditions: lower energy limit and the width of time window for PFG selection. The correlation between the spectral characteristics and these two conditions are obtained. The spectral characteristics in nominal conditions for the three fission reactions, *i.e.* ^{252}Cf(sf), ^{238}U(n,f) and ^{239}Pu(n,f), are also presented for easier comparison with other experiments and theoretical calculations. The γ multiplicity and total photon energy release for ^{238}U(n,f) reaction is much lower than the other two reactions. It reveals that the prompt γ-ray emission is constrained by its energetic conditions, which reflects the neutron separation energy distribution. These quantities in the fission process also have dependences on the fragment yields, *e.g.* the slope of the PFGS at high-energy region is sensitive to the mass yields around mass A=130-135. The initial angular momentum distribution of fission fragments may impact the prompt γ-ray emission, but it is difficulty to extract sufficient experimental evidence for further detailed study in this work. The possible energy dependence of the spectral characteristics have been investigated. The energy dependence of prompt γ-rays emission on incident neutron energy is observed to be very weak. However, a strong dependence on the particular fissioning system is observed. These results provide information on PFGS characteristics for important nuclides ^{238}U and ^{239}Pu in a reactor core. They also depict general features for prompt γ-ray emission in fast-neutron-induced fission.

In this work, the ionization chamber used is only capable of tagging fission events and was not designed to provide any mass information of the fission fragments. The PFGS obtained are the contributions from all the possible mass splits. As discussed in Chapter5, the relative contribution to the PFGS of each fission fragment is different. Future experiments may use ionization chambers that are capable of correlating PFGS with corresponding fission fragment mass information.

In the experiments described here, scintillation detectors were used to provide high detection efficiency for fast-neutron-induced fission. The cost of using scintillation detectors is that the energy resolution is not able to resolve the discrete γ lines of each individual fission fragment. The characteristic γ lines contain the spin and parity information, which enables extraction of the angular momentum of the fission fragments at scission. Hence, future experiments may use high purity Germanium detectors (HPGe) to measure the PFG with high energy resolution in order to access the rich information in the de-excitation process of the neutron-rich nuclides.

Information on the fission fragment properties at scission is crucial for the theoretical calculations, and at the same time is a challenge for experimental investigations. The

prompt neutron evaporation precedes the prompt γ-ray emission. In order to extrapolate the properties of fission fragments at scission (*e.g.* the excitation energy for each fragment at scission), not only prompt γ-rays but also prompt neutrons need to be measured. Thus, information of neutron/γ competition can be obtained directly. As a consequence, it would be interesting to measure the prompt neutrons and prompt γ-rays simultaneously.

Appendix A
Simulation interface

```
#Event biasing (default)
#Important biasing factor: 10000; split biasing factor: 100;
#GAS cell geometry
#cell length
/Licorne/cell/setLength 3.5 cm
#cell pressure
/Licorne/cell/setPressure 1.50 atmosphere
#foil thickness
/Licorne/foil/setThickness 0.0027 mm
#update the geo (important)
/Licorne/cell/update
#Define the primary beam (Lithium or Boron)
/Licorne/beam/setZ 3
/Licorne/beam/setA 7
/Licorne/beam/setEnergy 16.6 MeV
#Root file name (output)
/Licorne/hist/setName test.root
#Number of primary particles
/run/beamOn 10
```

Appendix B
Spectral characteristics of PFGS

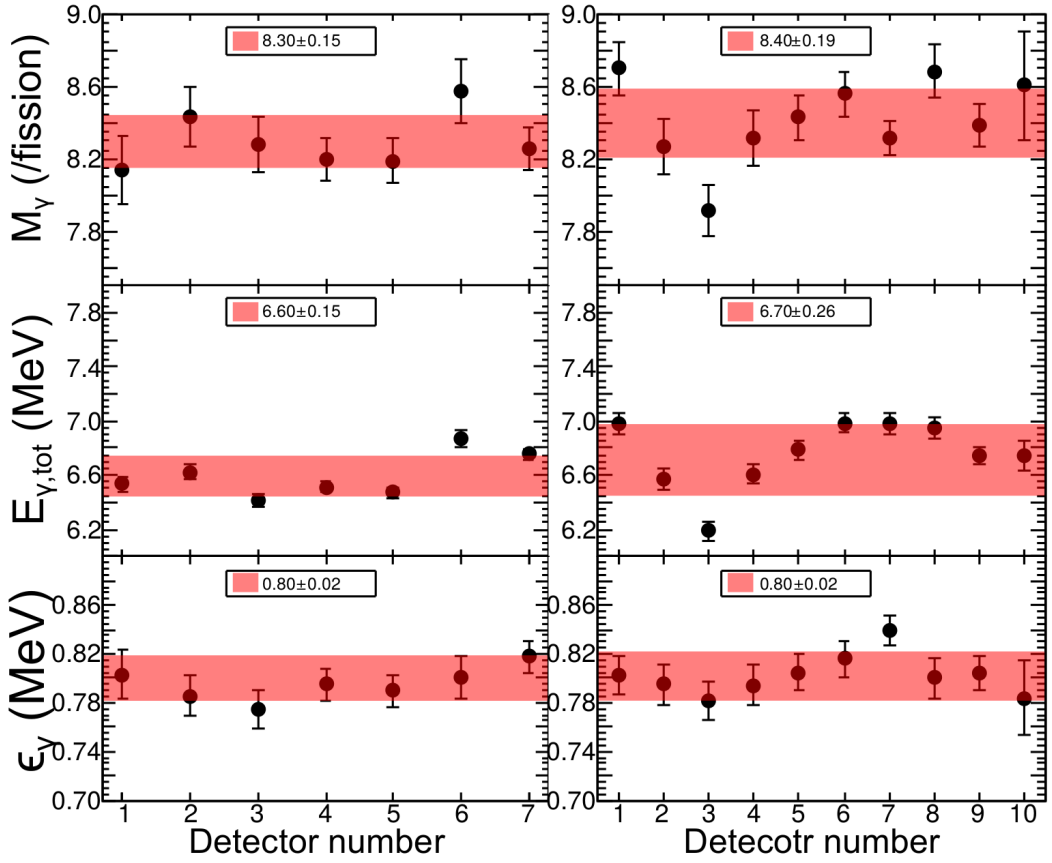

Figure B.1 – Spectral characteristics for each individual γ detector for $LaBr_3$ (left) and PARIS phoswich (right), respectively, in case of ^{252}Cf(sf).

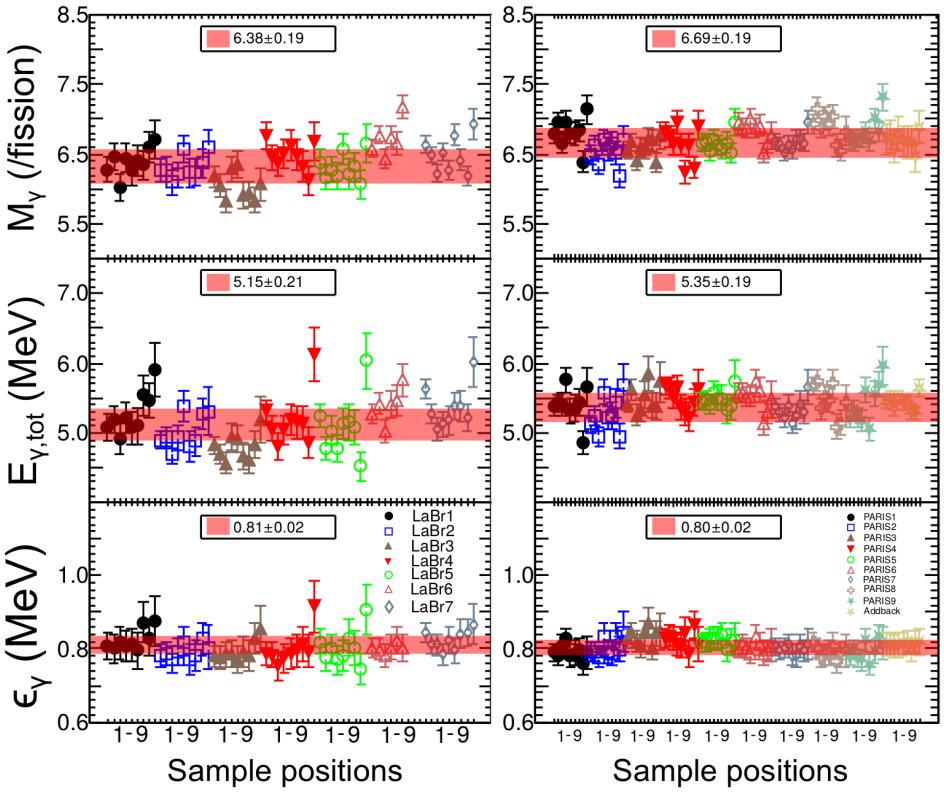

(a)

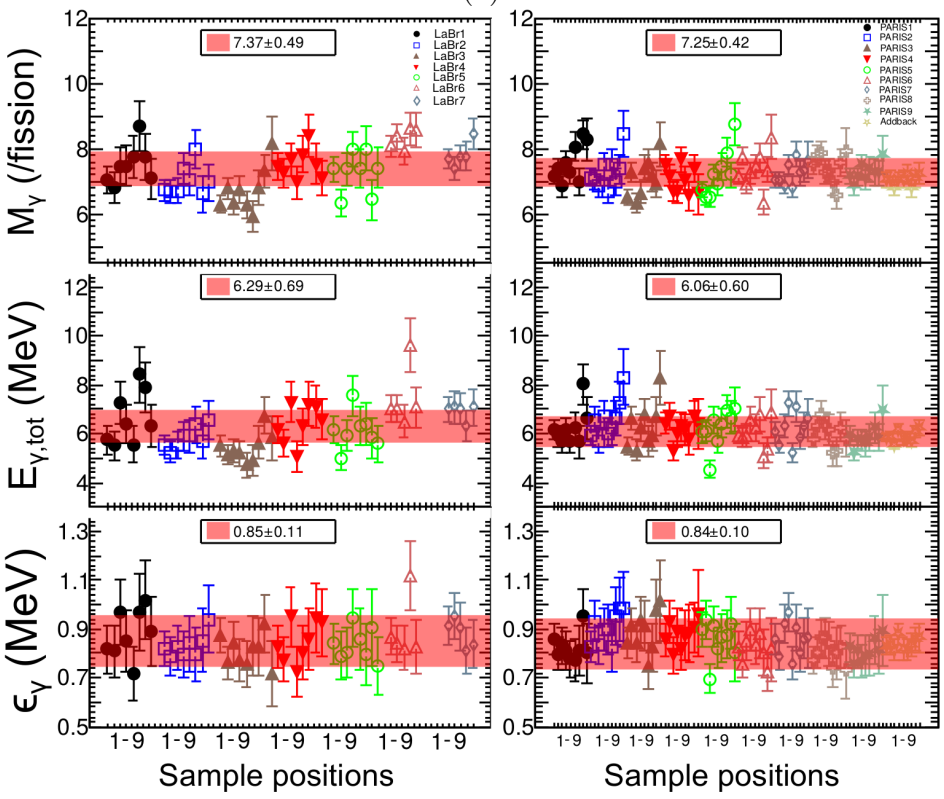

(b)

Figure B.2 – Spectral characteristics for each individual γ detector for $LaBr_3$ (left) and PARIS phoswich (right), respectively, in case of ^{238}U(n,f) at E_n=1.9 (a) and 4.8 MeV (b).

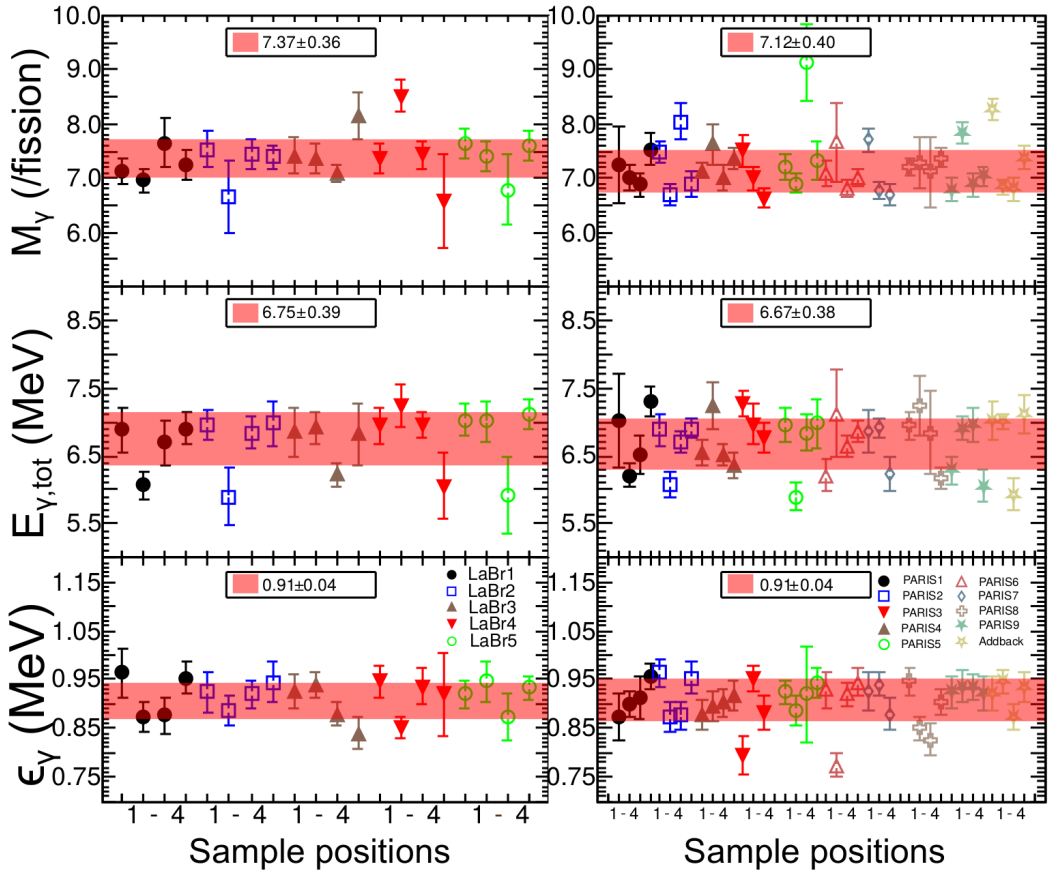

Figure B.3 – Spectral characteristics for each individual γ detector for $LaBr_3$ (left) and PARIS phoswich (right), respectively, in case of ^{239}Pu(n,f) at E_n 1.8 MeV.

Appendix C
Résumé en français

Le développement de la source de neutrons à cinématique inverse, LICORNE, a ouvert de nombreuses possibilités expérimentales, notamment en ce qui concerne la spectroscopie du processus de fission et l'étude de l'émission prompt de la fission induite par les neutrons rapides. Dans ce travail, nous avons d'abord développé le code pour simuler la source de neutrons LICORNE et effectuer les expériences pour valider le code. Deuxièmement, nous avons effectué des mesures la rayonnement γ prompt de fission induite par neutrons rapides et la procédure d'analyse des données correspondantes pour extraire les propriétés spectrales. Enfin, une étude sur différents modèles de fission a été réalisée, en comparant les résultats expérimentaux obtenus aux calculs.

C.1 Motivation physique

Le spectre de la rayonnement γ prompt de fission (PFGS) et ses caractéristiques spectrales, *i.e.* multiplicité de rayonnement γ, libération totale d'énergie de rayonnement γ et énergie moyenne de photon, sont des données nucléaires cruciales pour la physique des reacteurs. La rayonnement γ prompt (PFG) de fission ont un large éventail d'énergie, de peu de dizaines de keV à peu de dizaines de MeV. Elles peuvent échapper au coeur du réacteur et déposer l'énergie dans l'instrumentation et des matériaux d'armature. Le chauffage γ de ces matériaux est dominant au-dessus du chauffage de neutron [3], qui doit être prévu avec l'exactitude raisonnable pour éviter la fracture et l'échec possibles. Mais dans un réacteur expérimente récent, le chauffage de γ a été montré pour être sous-estimé par jusqu'à 28% cite HPRL. En outre, le développement réacteurs de Génération IV, visant pour la sécurité améliorée, exigent la mesure d'un PFGS plus précis et des caractéristiques spectrales.

D'autre part, l'information plus précise de PFGS est également utile d'un point de vue fondamental de physique. De nos jours, plusieurs codes concurrentiels de calcul essayent de reproduire toutes les propriétés des fragments de fission et des particules émises (neutron et rayonnement γ) pour un large éventail de systèmes fissioning. Ces codes

incluent GEF [5–7], FREYA [8–13], CGMF [14–17], FIFRELIN [18–20] etc. Beaucoup d'hypothèses et de modèles sont faits en ces codes, qui demeurent toujours controversés. PFGS contient un grand nombre d'informations sur le processus de fission et les nuclides neutron-riches (fragments de fission). Il peut mener à une meilleure compréhension le mécanisme de tri d'énergie d'excitation entre les fragments de fission naissants au scission [5, 18, 21], le mécanisme de génération de moment angulaire des fragments de fission naissants au scission [7, 13, 16, 18] et la concurrence de neutron-γ pendant le processus de déexcitation du fragments de fission [22–24].

Ces dernières années, une série de mesures a été effectuée pour obtenir des valeurs des caractéristiques spectrales plus précises, dans le fission induite par neutron thermique [25–27] et le fission spontané [28, 29]. L'information de PFG existe très peu pour la fission induite par neutron rapide. Le développement du source de neutron de LICORNE [30–32], par la production des neutrons rapides intense, expédient cinématiquement focalisés, effectue l'étude de la fission induite par neutron rapide plus accessible. Dans ce travail, nous visons à mesurer et étudier le PFGS a la fission induite par neutron rapide de ^{238}U et de ^{239}Pu. ^{238}U et ^{239}Pu sont les nuclides importants dans un coeur du réacteur. Ces résultats fournissent également des informations des caractéristiques de PFGS pour la fission induite par neutron rapide en général.

C.2 Simulation de la source de neutrons LICORNE

LICORNE utilise p(^{7}Li,n)^{7}Be et p(^{11}B,n)^{11}C pour focaliser cinématiquement les neutrons sortants dans une petite plage angulaire autour de zéro degré par rapport à la direction de l'axe du faisceau. Les avantages des réactions cinématiques inversées sont que les matériaux de blindage pour la collimation du faisceau ne sont pas nécessaires, ce qui limite le bruit de fond des neutrons diffusés, et le flux de neutrons est considérablement augmenté. Depuis sa création en 2013, la source de neutrons LICORNE est devenue un outil essentiel pour l'installation ALTO.

La simulation du générateur de neutron directionnel LICORNE avec p(^{7}Li,n)^{7}Be et p(^{11}B,n)^{11}C réactions ont été mis en application dans GEANT4. Les distributions expérimentales de section efficace différentielle sont employées dans les calculs de cinématique pour améliorer l'échantillon la distribution angulaire des neutrons. L'événement polarisant des techniques, polariser à savoir d'importance et particules se dédoublant, sont mis en application dans GEANT4 sans changer la trousse à outils elle-même, diminue le temps de calcul. Le code a été validé en comparant aux résultats expérimentaux, y compris le spectre de temps-de-vol à l'aide d'un détecteur de neutrons de scintillation liquide et la distribution de taux de fission à l'aide d'une chambre d'ionisation. En conclusion, le code a été employé pour comprendre le spectre de neutrons et la distribution de flux dans l'espace selon la configuration différente de l'installation de LICORNE. Ces modifi-

cations et additions peuvent aider la conception de futures expériences pour la recherche fondamentale de physique et les applications nucléaires.

C.3 Dispositif expérimental et analyse des données

Dans ce travail, deux expériences utilisant la source neutronique LICORNE ont été réalisées, à savoir la mesure des spectres de rayonnement γ prompt dans la fission induite par neutrons rapides de ^{238}U et ^{239}Pu. Le dispositif expérimental se compose principalement de chambres d'ionisation et de détecteurs de rayons γ. Les fragments de fission ont été mesurés dans des chambres d'ionisation et discriminés avec des particules de α en fonction des différences d'énergies cinétiques. La chambre d'ionisation fournit une étiquette de fission et les rayons coïncidents γ sont détectés par différents types de détecteurs à scintillation inorganique, y compris les détecteurs LaB_3 et PARIS phoswich. Les détecteurs à scintillation de $LaBr_3$(Ce) ont une excellente résolution temporelle (∼300 ps) et une bonne résolution énergétique (∼3% à 661 keV). PARIS est un tableau d'un nouveau type de détecteurs $LaBr_3$(Ce)-NaI(Tl) phoswich. La coquille intérieure est constituée de cristaux cubiques $LaBr_3$(Ce) et la coquille extérieure est constituée de cristaux rectangulaires NaI(Tl). En appliquant une discrimination de forme d'impulsion pour les signaux, les détecteurs phoswich PARIS bénéficient d'une énergie et d'une résolution temporelle supérieure de la partie $LaBr_3$(Ce), et d'une efficacité accrue, particulièrement à haute énergie, de la partie NaI(Tl) avec un coût économique inférieur à celui du $LaBr_3$(Ce) pur de taille identique. Les rayons gamma de fission rapide sont distingués des neutrons de fission rapide par la technique du temps de vol. La procédure d'analyse des données comprend:

1. γ caractérisation du détecteur
2. Détermination de l'énergie neutronique incidente;
3. Sélection des événements de fission;
4. Prompt fission γ-rays selection;
5. Déploiement de la fonction de réponse.

Les spectres de rayonnement γ mesurés ont été extraits du temps de vol par rapport aux histogrammes bidimensionnels de l'énergie des rayons γ avec une certaine fenêtre temporelle et une certaine plage d'énergie pour chaque γ détecteur. Chaque spectre de rayons gamma γ mesuré a été déplié à partir de la réponse du système de détection pour récupérer le spectre d'émission. La fonction de réponse aux rayons γ a été simulée dans GEANT4 et validée par des nucléides radioactifs dans le processus d'étalonnage. Différentes techniques de dépliage ont été testées et la méthode d'itération a été choisie en tenant compte de la stabilité, en particulier dans les ensembles de données statistiques faibles. Les résultats obtenus démontrent une bonne performance des détecteurs de phoswich PARIS dans cette

expérience par rapport à $LaBr_3$. C'est la première fois que ces détecteurs ont été utilisés dans une expérience de physique.

C.4 Résultats et discussions

Les caractéristiques spectrales ont été extraites du PFGS avec deux conditions importantes : la limite inférieure d'énergie et la largeur de la fenêtre temporelle pour la sélection PFG. La corrélation entre les caractéristiques spectrales et ces deux conditions est obtenue. Les caractéristiques spectrales dans des conditions nominales pour les trois réactions de fission, *i.e.* ^{252}Cf(sf), ^{238}U(n,f) et ^{239}Pu(n,f), sont également présentées pour faciliter la comparaison avec d'autres expériences et calculs théoriques. La multiplicité de γ et la libération totale d'énergie photonique pour ^{238}U(n,f) réaction est beaucoup plus faible que les deux autres réactions. Il révèle que l'émission de rayons γ est limitée par ses conditions énergétiques, qui reflètent la distribution de l'énergie de séparation des neutrons. ^{238}U est le nucléide stable le plus riche en neutrons et ^{238}U(n,f) la réaction produit plus de fragments de fission riches en neutrons que les deux autres réactions de fission. Ces quantités dans le processus de fission dépendent également des rendements des fragments. L'une des preuves est que la pente du PFGS dans la région à haute énergie est sensible aux rendements massiques autour de la masse A=130-135. La distribution initiale du moment angulaire des fragments de fission peut avoir un impact sur l'émission rapide de rayons γ, mais il est difficile d'extraire suffisamment de preuves expérimentales pour une étude plus détaillée dans le cadre de ce travail. La dépendance énergétique possible des caractéristiques spectrales a également été étudiée. La dépendance énergétique de l'émission de rayons gamma γ sur l'énergie neutronique incidente est très faible. Toutefois, on observe une forte dépendance à l'égard du système de fissionnement particulier. Ces résultats fournissent des informations sur les caractéristiques des PFGS pour les nucléides importants ^{238}U et ^{239}Pu dans le cœur d'un réacteur. Ils décrivent également les caractéristiques générales de l'émission rapide de rayons gamma γ dans la fission induite par neutrons rapides.

C.5 Conclusions et perspectives

Dans ce travail, nous avons développé un programme GENAT4 pour simuler la source de neutrons LICORNE. Le programme vise à reproduire la distribution de l'énergie neutronique et de flux dans l'espace à différentes configurations LICORNE, et dans un temps raisonnablement court. Les mesures expérimentales valident le programme et le programme a été utilisé dans de nombreuses expériences récentes. Des rayons γ de fission induite par neutrons rapides de ^{238}U et ^{239}Pu ont été mesurés, en utilisant des neutrons rapides générés à partir de la source LICORNE. Les caractéristiques spectrales de la fis-

sion rapide γ-rays sont comparées aux résultats des calculs du FEM et de FREYA, ce qui renforce l'importance de l'état de l'énergie d'excitation, des rendements isotopiques et du moment angulaire des fragments de fission pour l'émission rapide γ-ray.

Dans ce travail, la chambre d'ionisation utilisée est seulement capable de marquer les événements de fission et n'a pas été conçue pour fournir des informations sur la masse des fragments de fission. Les PFGS obtenus sont les contributions de tous les fractionnements de masse possibles. Comme nous l'avons vu dans le chapitre réfchap:fifth, la contribution relative de chaque fragment de fission au PFGS est différente. Les expériences futures pourraient utiliser des chambres d'ionisation capables d'établir une corrélation entre le PFGS et l'information correspondante sur la masse des fragments de fission.

Dans les expériences décrites ici, des détecteurs à scintillation ont été utilisés pour fournir une grande efficacité de détection pour la fission induite par neutrons rapides. Le coût de l'utilisation de détecteurs à scintillation est que la résolution énergétique n'est pas en mesure de résoudre les lignes discrètes γ de chaque fragment de fission individuel. Les lignes caractéristiques γ contiennent les informations de spin et de parité, ce qui permet d'extraire le moment angulaire des fragments de fission à la scission. Par conséquent, les expériences futures pourraient utiliser des détecteurs au germanium de haute pureté (HPGe) pour mesurer le PFG avec une haute résolution énergétique afin d'accéder à la riche information dans le processus de désexcitation des nucléides riches en neutrons.

L'information sur les propriétés des fragments de fission à la scission est cruciale pour les calculs théoriques et constitue en même temps un défi pour les études expérimentales. L'évaporation neutronique rapide précède l'émission de rayons gamma γ. Afin d'extrapoler les propriétés des fragments de fission à la scission (par exemple, l'énergie d'excitation pour chaque fragment à la scission), il faut mesurer non seulement les rayons γ, mais aussi les neutrons rapides. Ainsi, l'information de la compétition neutron/γ peut être obtenue directement. Par conséquent, il serait intéressant de mesurer simultanément les neutrons rapides et les rayons gamma γ.

Bibliography

[1] O. Hahn and F. Straßmann, "Über den nachweis und das verhalten der bei der bestrahlung des urans mittels neutronen entstehenden erdalkalimetalle," *Naturwissenschaften*, vol. 27, no. 1, pp. 11–15, 1939. https://link.springer.com/content/pdf/10.1007/BF01488241.pdf.

[2] L. Meitner and O. Frisch, "When man became god," *Nature*, vol. 143, pp. 239–240, 1939. https://sites.google.com/site/msacmagazinesparttwo/home/MANGOD1.pdf.

[3] A. Colombier, H. Amharrak, D. Fourmentel, S. Ravaux, D. Régnier, O. Gueton, J. Hudelot, and M. Lemaire, "Nuclear data production, calculation and measurement: a global overview of the gamma heating issue," in *EPJ Web of Conferences*, vol. 42, p. 04001, EDP Sciences, 2013. https://cea-proceedings.edpsciences.org/articles/epjconf/abs/2013/03/epjconf_wond2013_04001/epjconf_wond2013_04001.html.

[4] Nuclear Data High Priority Request List of the NEA (Req. ID: H.3, H.4), http://www.nea.fr/html/dbdata/hprl/hprlview.pl?ID=421 and http://www.nea.fr/html/dbdata/hprl/hprlview.pl?ID=422.

[5] K.-H. Schmidt and B. Jurado, "Entropy driven excitation energy sorting in superfluid fission dynamics," *Physical review letters*, vol. 104, no. 21, p. 212501, 2010. https://journals.aps.org/prl/abstract/10.1103/PhysRevLett.104.212501.

[6] K.-H. Schmidt and B. Jurado, "Final excitation energy of fission fragments," *Physical Review C*, vol. 83, no. 6, p. 061601, 2011. https://journals.aps.org/prc/abstract/10.1103/PhysRevC.83.061601.

[7] K.-H. Schmidt, B. Jurado, C. Amouroux, and C. Schmitt, "General description of fission observables: Gef model code," *Nuclear Data Sheets*, vol. 131, pp. 107–221, 2016. http://www.sciencedirect.com/science/article/pii/S0090375215000745.

[8] J. Randrup and R. Vogt, "Calculation of fission observables through event-by-event simulation," *Physical Review C*, vol. 80, no. 2, p. 024601, 2009. https://journals.aps.org/prc/abstract/10.1103/PhysRevC.80.024601.

[9] R. Vogt, J. Randrup, J. Pruet, and W. Younes, "Event-by-event study of prompt neutrons from pu 239 (n, f)," *Physical Review C*, vol. 80, no. 4, p. 044611, 2009. https://journals.aps.org/prc/abstract/10.1103/PhysRevC.80.044611.

[10] R. Vogt and J. Randrup, "Event-by-event study of neutron observables in spontaneous and thermal fission," *Physical Review C*, vol. 84, no. 4, p. 044621, 2011. https://journals.aps.org/prc/abstract/10.1103/PhysRevC.84.044621.

[11] R. Vogt, J. Randrup, D. Brown, M. Descalle, and W. Ormand, "Event-by-event evaluation of the prompt fission neutron spectrum from 239 pu (n, f)," *Physical Review C*, vol. 85, no. 2, p. 024608, 2012. https://journals.aps.org/prc/abstract/10.1103/PhysRevC.85.024608.

[12] R. Vogt and J. Randrup, "Event-by-event study of photon observables in spontaneous and thermal fission," *Physical Review C*, vol. 87, no. 4, p. 044602, 2013. https://journals.aps.org/prc/abstract/10.1103/PhysRevC.87.044602.

[13] J. Randrup and R. Vogt, "Refined treatment of angular momentum in the event-by-event fission model freya," *Physical Review C*, vol. 89, no. 4, p. 044601, 2014. https://journals.aps.org/prc/abstract/10.1103/PhysRevC.89.044601.

[14] T. Kawano, P. Talou, I. Stetcu, and M. Chadwick, "Statistical and evaporation models for the neutron emission energy spectrum in the center-of-mass system from fission fragments," *Nuclear Physics A*, vol. 913, pp. 51–70, 2013. http://www.sciencedirect.com/science/article/pii/S0375947413005952.

[15] I. Stetcu, P. Talou, T. Kawano, and M. Jandel, "Isomer production ratios and the angular momentum distribution of fission fragments," *Physical Review C*, vol. 88, no. 4, p. 044603, 2013. https://journals.aps.org/prc/abstract/10.1103/PhysRevC.88.044603.

[16] B. Becker, P. Talou, T. Kawano, Y. Danon, and I. Stetcu, "Monte carlo hauser-feshbach predictions of prompt fission γ rays: Application to n th+ 235 u, n th+ 239 pu, and 252 cf (sf)," *Physical Review C*, vol. 87, no. 1, p. 014617, 2013. https://journals.aps.org/prc/abstract/10.1103/PhysRevC.87.014617.

[17] I. Stetcu, P. Talou, T. Kawano, and M. Jandel, "Properties of prompt-fission γ rays," *Physical Review C*, vol. 90, no. 2, p. 024617, 2014. https://journals.aps.org/prc/abstract/10.1103/PhysRevC.90.024617.

[18] O. Litaize and O. Serot, "Investigation of phenomenological models for the monte carlo simulation of the prompt fission neutron and γ emission," *Physical Review C*, vol. 82, no. 5, p. 054616, 2010. https://journals.aps.org/prc/abstract/10.1103/PhysRevC.82.054616.

[19] O. Serot, O. Litaize, and D. Regnier, "Fission mode influence on prompt neutrons and γ-rays emitted in the reaction 239pu (nth, f)," *Physics Procedia*, vol. 59, pp. 132–137, 2014. http://www.sciencedirect.com/science/article/pii/S1875389214004969.

[20] O. Litaize, O. Serot, and L. Berge, "Fission modelling with fifrelin," *The European Physical Journal A*, vol. 51, no. 12, p. 177, 2015. http://link.springer.com/article/10.1140/epja/i2015-15177-9.

[21] S. Lemaire, P. Talou, T. Kawano, M. Chadwick, and D. Madland, "Monte carlo approach to sequential neutron emission from fission fragments," *Physical Review C*, vol. 72, no. 2, p. 024601, 2005. https://journals.aps.org/prc/abstract/10.1103/PhysRevC.72.024601.

[22] H. Nifenecker, C. Signarbieux, M. Ribrag, J. Poitou, and J. Matuszek, "Gamma-neutron competition in the de-excitation mechanism of the fission fragments of 252cf," *Nuclear Physics A*, vol. 189, no. 2, pp. 285–304, 1972. https://www.sciencedirect.com/science/article/pii/0375947472902965.

[23] D. Bleuel, L. Bernstein, J. Burke, J. Gibelin, M. Heffner, J. Mintz, E. Norman, L. Phair, N. Scielzo, S. Sheets, *et al.*, "Gamma-ray multiplicity measurement of the spontaneous fission of 252cf in a segmented hpge/bgo detector array," *Nuclear Instruments and Methods in Physics Research Section A: Accelerators, Spectrometers, Detectors and Associated Equipment*, vol. 624, no. 3, pp. 691–698, 2010. https://www.sciencedirect.com/science/article/pii/S0168900210021790.

[24] T. Wang, G. Li, L. Zhu, Q. Meng, L. Wang, H. Han, W. Zhang, H. Xia, L. Hou, R. Vogt, *et al.*, "Correlations of neutron multiplicity and γ-ray multiplicity with fragment mass and total kinetic energy in spontaneous fission of cf 252," *Physical Review C*, vol. 93, no. 1, p. 014606, 2016. https://journals.aps.org/prc/abstract/10.1103/PhysRevC.93.014606.

[25] A. Oberstedt, T. Belgya, R. Billnert, R. Borcea, T. Bryś, W. Geerts, A. Göök, F.-J. Hambsch, Z. Kis, T. Martinez, *et al.*, "Improved values for the characteristics of prompt-fission γ-ray spectra from the reaction 235 u (n th, f)," *Physical Review C*, vol. 87, no. 5, p. 051602, 2013. https://journals.aps.org/prc/abstract/10.1103/PhysRevC.87.051602.

[26] A. Gatera, T. Belgya, W. Geerts, A. Göök, F.-J. Hambsch, M. Lebois, B. Maróti, A. Moens, A. Oberstedt, S. Oberstedt, *et al.*, "Prompt-fission γ-ray spectral characteristics from pu 239 (n th, f)," *Physical Review C*, vol. 95, no. 6, p. 064609, 2017. https://journals.aps.org/prc/abstract/10.1103/PhysRevC.95.064609.

[27] A. Chyzh, C. Wu, E. Kwan, R. Henderson, J. Gostic, T. Bredeweg, A. Couture, R. Haight, A. Hayes-Sterbenz, M. Jandel, *et al.*, "Systematics of prompt γ-ray emission in fission," *Physical Review C*, vol. 87, no. 3, p. 034620, 2013. https://journals.aps.org/prc/abstract/10.1103/PhysRevC.87.034620.

[28] S. Oberstedt, T. Belgya, R. Billnert, T. Bryś, W. Geerts, F.-J. Hambsch, Z. Kis, T. Martinez, A. Oberstedt, L. Szentmiklosi, *et al.*, "Prompt fission γ-rays from the reactions 252cf (sf) and 235u (nth, f)–new data," in *EPJ Web of Conferences*, vol. 62, p. 02003, EDP Sciences, 2013. https://www.epj-conferences.org/articles/epjconf/abs/2013/23/epjconf_fission2013_02003/epjconf_fission2013_02003.html.

[29] S. Oberstedt, A. Oberstedt, A. Gatera, A. Göök, F.-J. Hambsch, A. Moens, G. Sibbens, D. Vanleeuw, and M. Vidali, "Prompt fission γ-ray spectrum characteristics from pu 240 (sf) and pu 242 (sf)," *Physical Review C*, vol. 93, no. 5, p. 054603, 2016.

[30] J. Wilson, M. Lebois, P. Halipre, B. Leniau, I. Matea, D. Verney, S. Oberstedt, R. Billnert, A. Oberstedt, G. Georgiev, *et al.*, "Licorne: A new and unique facility for producing intense, kinematically focused neutron beams at the ipn orsay," in *EPJ Web of Conferences*, vol. 62, p. 05006, EDP Sciences, 2013. https://cea-proceedings.edpsciences.org/articles/epjconf/abs/2013/23/epjconf_fissio n2013_05006/epjconf_fission2013_05006.html.

[31] J. Wilson, M. Lebois, P. Halipre, S. Oberstedt, and A. Oberstedt, "The licorne neutron source and measurements of prompt γ-rays emitted in fission," *Physics Procedia*, vol. 59, pp. 31–36, 2014. http://www.sciencedirect.com/science/article/pii/S1875389214004805.

[32] M. Lebois, J. Wilson, P. Halipré, B. Leniau, I. Matea, A. Oberstedt, S. Oberstedt, and D. Verney, "Development of a kinematically focused neutron source with the p (7 li, n) 7 be inverse reaction," *Nuclear Instruments and Methods in Physics Research Section A: Accelerators, Spectrometers, Detectors and Associated Equipment*, vol. 735, pp. 145–151, 2014. http://www.sciencedirect.com/science/article/pii/S0168900213010735.

[33] J. R. Nix, "Calculation of fission barriers for heavy and superheavy nuclei," *Annual Review of Nuclear Science*, vol. 22, no. 1, pp. 65–120, 1972. http://www.annualreviews.org/doi/pdf/10.1146/annurev.ns.22.120172.000433.

[34] A. Bulgac, P. Magierski, K. J. Roche, and I. Stetcu, "Induced fission of pu 240 within a real-time microscopic frame-

work," *Physical review letters*, vol. 116, no. 12, p. 122504, 2016. https://journals.aps.org/prl/abstract/10.1103/PhysRevLett.116.122504.

[35] N. Bohr and J. A. Wheeler, "The mechanism of nuclear fission," *Physical Review*, vol. 56, no. 5, p. 426, 1939. https://journals.aps.org/pr/abstract/10.1103/PhysRev.56.426.

[36] J. R. Nix, "Further studies in the liquid-drop theory on nuclear fission," *Nuclear Physics A*, vol. 130, no. 2, pp. 241–292, 1969. http://www.sciencedirect.com/science/article/pii/0375947469907301.

[37] G. Gamow, "Mass defect curve and nuclear constitution," *Proceedings of the Royal Society of London. Series A, Containing Papers of a Mathematical and Physical Character*, vol. 126, no. 803, pp. 632–644, 1930. http://www.jstor.org/stable/95297.

[38] C. v. Weizsäcker, "Zur theorie der kernmassen," *Zeitschrift für Physik A Hadrons and Nuclei*, vol. 96, no. 7, pp. 431–458, 1935. http://www.springerlink.com/index/QG3172J07HH4000N.pdf.

[39] S. Bjørnholm and J. Lynn, "The double-humped fission barrier," *Reviews of Modern Physics*, vol. 52, no. 4, p. 725, 1980. https://journals.aps.org/rmp/abstract/10.1103/RevModPhys.52.725.

[40] A. Karpov, P. Nadtochy, E. Ryabov, and G. Adeev, "Consistent application of the finite-range liquid-drop model to langevin fission dynamics of hot rotating nuclei," *Journal of Physics G: Nuclear and Particle Physics*, vol. 29, no. 10, p. 2365, 2003. http://iopscience.iop.org/article/10.1088/0954-3899/29/10/305/meta.

[41] S. Polikanov, V. Druin, V. Karnaukhov, V. Mikheev, A. Pleve, N. Skobelev, V. Subbotin, G. Terakopyan, and V. Fomichev, "Spontaneous fission with an anomalously short period. 1.," *SOVIET PHYSICS JETP-USSR*, vol. 15, no. 6, pp. 1016–1021, 1962.

[42] M. G. Mayer, "On closed shells in nuclei," *Physical Review*, vol. 74, no. 3, p. 235, 1948. https://journals.aps.org/pr/abstract/10.1103/PhysRev.74.235.

[43] H. Schatz, S. Gupta, P. Möller, M. Beard, E. F. Brown, A. T. Deibel, L. R. Gasques, W. R. Hix, L. Keek, R. Lau, *et al.*, "Strong neutrino cooling by cycles of electron capture and [bgr]-decay in neutron star crusts," *Nature*, vol. 505, no. 7481, pp. 62–65, 2014. https://www.nature.com/nature/journal/v505/n7481/abs/nature12757.html.

[44] A. J. Sierk, "Langevin model of low-energy fission," *Physical Review C*, vol. 96, no. 3, p. 034603, 2017. https://journals.aps.org/prc/abstract/10.1103/PhysRevC.96.034603.

[45] T. Ichikawa, A. Iwamoto, P. Möller, and A. J. Sierk, "Contrasting fission potential-energy structure of actinides and mercury isotopes," *Physical Review C*, vol. 86, no. 2, p. 024610, 2012. https://journals.aps.org/prc/abstract/10.1103/PhysRevC.86.024610.

[46] http://www.nuclear-power.net/nuclear-power/fission/.

[47] M. Caamaño and F. Farget, "Energy balance and deformation at scission in 240pu fission," *Physics Letters B*, vol. 770, pp. 72–76, 2017. https://www.sciencedirect.com/science/article/pii/S0370269317303155.

[48] P. Talou, B. Becker, T. Kawano, M. Chadwick, and Y. Danon, "Advanced monte carlo modeling of prompt fission neutrons for thermal and fast neutron-induced fission reactions on pu 239," *Physical Review C*, vol. 83, no. 6, p. 064612, 2011. https://journals.aps.org/prc/abstract/10.1103/PhysRevC.83.064612.

[49] http://www.khs-erzhausen.de/GEF.html.

[50] https://nuclear.llnl.gov/simulation/main.html.

[51] R. Capote, M. Herman, P. Obložinskỳ, P. Young, S. Goriely, T. Belgya, A. Ignatyuk, A. J. Koning, S. Hilaire, V. A. Plujko, *et al.*, "Ripl–reference input parameter library for calculation of nuclear reactions and nuclear data evaluations," *Nuclear Data Sheets*, vol. 110, no. 12, pp. 3107–3214, 2009. https://www.sciencedirect.com/science/article/pii/S0090375209000994.

[52] A. Göök, F.-J. Hambsch, and M. Vidali, "Prompt neutron multiplicity in correlation with fragments from spontaneous fission of cf 252," *Physical Review C*, vol. 90, no. 6, p. 064611, 2014. https://journals.aps.org/prc/abstract/10.1103/PhysRevC.90.064611.

[53] C. Manailescu, A. Tudora, F.-J. Hambsch, C. Morariu, and S. Oberstedt, "Possible reference method of total excitation energy partition between complementary fission fragments," *Nuclear Physics A*, vol. 867, no. 1, pp. 12–40, 2011. http://www.sciencedirect.com/science/article/pii/S0375947411005641.

[54] D. Aumann, W. Gückel, E. Nirschl, and H. Zeising, "Independent isomeric yield ratio of pm 148 in fission of the moderately excited u 236 compound nucleus as a measure of fragment angular momentum," *Physical Review C*, vol. 16, no. 1, p. 254, 1977. https://journals.aps.org/prc/abstract/10.1103/PhysRevC.16.254.

[55] N. Carjan, P. Talou, and O. Serot, "Emission of scission neutrons in the sudden approximation," *Nuclear Physics A*, vol. 792, no. 1, pp. 102–121, 2007. http://www.sciencedirect.com/science/article/pii/S0375947407005477.

[56] J. Terrell, "Distributions of fission neutron numbers," *Physical Review*, vol. 108, no. 3, p. 783, 1957. https://journals.aps.org/pr/abstract/10.1103/PhysRev.108.783.

[57] J. Terrell, "Fission neutron spectra and nuclear temperatures," *Physical Review*, vol. 113, no. 2, p. 527, 1959. https://journals.aps.org/pr/abstract/10.1103/PhysRev.113.527.

[58] V. Weisskopf, "Statistics and nuclear reactions," *Physical Review*, vol. 52, no. 4, p. 295, 1937. https://journals.aps.org/pr/abstract/10.1103/PhysRev.52.295.

[59] K. Skarsvåg, "Time distribution of γ-rays from spontaneous fission of 252cf at short times," *Nuclear Physics A*, vol. 253, no. 2, pp. 274–288, 1975. https://www.sciencedirect.com/science/article/pii/0375947475904820.

[60] P. Talou, T. Kawano, I. Stetcu, J. P. Lestone, E. McKigney, and M. B. Chadwick, "Late-time emission of prompt fission γ rays," *Physical Review C*, vol. 94, no. 6, p. 064613, 2016. https://journals.aps.org/prc/abstract/10.1103/PhysRevC.94.064613.

[61] K. Skarsvåg, "Differential angular distribution of prompt gamma rays from spontaneous fission of cf 252," *Physical Review C*, vol. 22, no. 2, p. 638, 1980. https://journals.aps.org/prc/abstract/10.1103/PhysRevC.22.638.

[62] R. Billnert, F.-J. Hambsch, A. Oberstedt, and S. Oberstedt, "New prompt spectral γ-ray data from the reaction 252 cf (sf) and its implication on present evaluated nuclear data files," *Physical Review C*, vol. 87, no. 2, p. 024601, 2013. https://journals.aps.org/prc/abstract/10.1103/PhysRevC.87.024601.

[63] F. Gunsing, U. Abbondanno, G. Aerts, H. Alvarez, F. Alvarez-Velarde, S. Andriamonje, J. Andrzejewski, P. Assimakopoulos, L. Audouin, G. Badurek, *et al.*, "Status and outlook of the neutron time-of-flight facility n_tof at cern," *Nuclear Instruments and Methods in Physics Research Section B: Beam Interactions with Materials and Atoms*, vol. 261, no. 1, pp. 925–929, 2007. http://www.sciencedirect.com/science/article/pii/S0168583X07006453.

[64] S. Oberstedt, G. Giorginis, F.-J. Hambsch, A. Krasa, A. Plompen, A. Al-Adili, A. Oberstedt, R. Billnert, and P. Castiñeira, "Nuclear research with mono-energetic neutrons at the jrc monnet facility," tech. rep., 2014. https://inis.iaea.org/search/search.aspx?orig_q=RN:46024668.

[65] F. Azaiez, S. Essabaa, F. Ibrahim, and D. Verney, "The alto facility in orsay," *Nuclear Physics News*, vol. 23, no. 2, pp. 5–10, 2013. http://www.tandfonline.com/doi/abs/10.1080/10619127.2013.797270.

[66] J. Wilson, M. Lebois, P. Halipré, S. Oberstedt, and A. Oberstedt, "Prompt emission in fission induced with fast neutrons," *Physics Procedia*, vol. 64, pp. 107–113, 2015. http://www.sciencedirect.com/science/article/pii/S1875389215001303.

[67] S. Agostinelli, J. Allison, K. a. Amako, J. Apostolakis, H. Araujo, P. Arce, M. Asai, D. Axen, S. Banerjee, G. Barrand, *et al.*, "Geant4—a simulation toolkit," *Nuclear instruments and methods in physics research section A: Accelerators, Spectrometers, Detectors and Associated Equipment*, vol. 506, no. 3, pp. 250–303, 2003. http://inspirehep.net/record/593382/files/fermilab-pub-03-339.pdf.

[68] M. M. Block, "Monte carlo phase space evaluation," *Computer physics communications*, vol. 69, no. 2-3, pp. 459–476, 1992. http://www.sciencedirect.com/science/article/pii/001046559290183Y.

[69] R. Brun and F. Rademakers, "Root—an object oriented data analysis framework," *Nuclear Instruments and Methods in Physics Research Section A: Accelerators, Spectrometers, Detectors and Associated Equipment*, vol. 389, no. 1-2, pp. 81–86, 1997. http://www.sciencedirect.com/science/article/pii/S016890029700048X.

[70] S. Elbakr, I. Van Heerden, W. McDonald, and G. Neilson, "Measurements of neutron angular distributions from the 7li (p, n) 7be reaction," *Nuclear Instruments and Methods*, vol. 105, no. 3, pp. 519–523, 1972. http://www.sciencedirect.com/science/article/pii/0029554X72903485.

[71] L. Van der Zwan and K. Geiger, "The 11b (p, n) 11c cross section from threshold to 4.9 mev," *Nuclear Physics A*, vol. 306, no. 1-2, pp. 45–52, 1978. http://www.sciencedirect.com/science/article/pii/037594747890310X.

[72] J. F. Briesmeister *et al.*, *MCNP–A general Monte Carlo code for neutron and photon transport.* Los Alamos National Laboratory, 1986. http://www.iaea.org/inis/collection/NCLCollectionStore/_Public/18/044/18044302.pdf.

[73] G. Collaboration *et al.*, "Physics reference manual," *Version: geant4*, vol. 9, no. 0, 2005. http://cds.cern.ch/record/2237422/files/geant4.pdf.

[74] I. Kawrakow, D. Rogers, and B. Walters, "Large efficiency improvements in beamnrc using directional bremsstrahlung splitting," *Medical physics*, vol. 31, no. 10, pp. 2883–2898, 2004. http://onlinelibrary.wiley.com/doi/10.1118/1.1788912/full.

[75] M. H. Mendenhall and R. A. Weller, "A probability-conserving cross-section biasing mechanism for variance reduction in monte carlo particle transport calculations," *Nuclear Instruments and Methods in Physics Research Section A: Accelerators, Spectrometers, Detectors and Associated Equipment*, vol. 667, pp. 38–43, 2012. http://www.sciencedirect.com/science/article/pii/S0168900211021541.

[76] W. R. Leo, *Techniques for nuclear and particle physics experiments: a how-to approach*. Springer Science & Business Media, 2012. http://cds.cern.ch/record/302344/files/0387572805_TOC.pdf.

[77] A. Maj, F. Azaiez, D. Jenkins, C. Schmitt, O. Stezowski, J. Wieleczko, D. Balabanski, P. Bednarczyk, S. Brambilla, F. Camera, *et al.*, "The paris project," in *Presented at the Zakopane Conference on Nuclear Physics*, 2008. http://paris.ifj.edu.pl/documents/main/AM_Zakopane2008.pdf.

[78] M. Zieblinski, M. Jastrzab, N. Dokania, V. Nanal, S. Brambilla, P. Bednarczyk, M. Ciemala, E. Dutkiewicz, M. Kmiecik, M. Krzysiek, *et al.*, "Testing of the paris labr3-nai phoswich detector with high energy gamma-rays," *Acta Physica Polonica B*, vol. 44, p. 651, 2013. http://adsabs.harvard.edu/abs/2013AcPPB..44..651Z.

[79] C. Ghosh, V. Nanal, R. Pillay, K. Anoop, N. Dokania, S. Pal, M. Pose, G. Mishra, P. Rout, S. Kumar, *et al.*, "Characterization of paris labr3 (ce)-nai (tl) phoswich detectors up to eγ 22 mev," *Journal of Instrumentation*, vol. 11, no. 05, p. P05023, 2016. http://iopscience.iop.org/article/10.1088/1748-0221/11/05/P05023/meta.

[80] http://faster.in2p3.fr/.

[81] http://www.srim.org/.

[82] J. F. Ziegler and J. P. Biersack, "The stopping and range of ions in matter," in *Treatise on Heavy-Ion Science*, pp. 93–129, Springer, 1985. http://link.springer.com/chapter/10.1007/978-1-4615-8103-1_3.

[83] J. F. Ziegler, M. D. Ziegler, and J. P. Biersack, *SRIM: the stopping and range of ions in matter*. Cadence Design Systems, 2008.

[84] W. J. Price *et al.*, "Nuclear radiation detection," 1958. http://agris.fao.org/agris-search/search.do?recordID=US201300378742.

[85] J. Taieb, B. Laurent, G. Bélier, A. Sardet, and C. Varignon, "A new fission chamber dedicated to prompt fission neutron spectra measurements," *Nuclear Instruments and Methods in Physics Research Section A: Accelerators, Spectrometers, Detectors and Associated Equipment*, vol. 833, pp. 1–7, 2016. http://www.sciencedirect.com/science/article/pii/S0168900216307070.

[86] G. F. Knoll, *Radiation detection and measurement*. John Wiley & Sons, 2010.

[87] https://www.nuclear-power.net/nuclear-power/reactor-physics/interactio n-radiation-matter/interaction-gamma-radiation-matter/.

[88] R. Lecomte, "Novel detector technology for clinical pet," *European journal of nuclear medicine and molecular imaging*, vol. 36, no. 1, pp. 69–85, 2009. https://link.springer.com/article/10.1007/s00259-008-1054-0.

[89] D. Guillemaud-Mueller, "Tours symposium on nuclear physics iii," in *AIP Conf. Proc.*, vol. 425, p. 290, 1997.

[90] http://www.lnl.infn.it/ annrep/read_ar/2016/contributions/pdfs/094_C_119_C114.pdf.

[91] A. Sardet, *Spectres en énergie des neutrons prompts de fission: optimisation du dispositif expérimental et application à l'*^{238}*U*. PhD thesis, Université Paris-Saclay, 2015. https://tel.archives-ouvertes.fr/tel-01274998/.

[92] https://www.mesytec.com/products/datasheets/MPD-4.pdf.

[93] G. Molnár, Z. Révay, and T. Belgya, "Wide energy range efficiency calibration method for ge detectors," *Nuclear Instruments and Methods in Physics Research Section A: Accelerators, Spectrometers, Detectors and Associated Equipment*, vol. 489, no. 1-3, pp. 140–159, 2002. https://www.sciencedirect.com/science/article/pii/S0168900202009026.

[94] J. G. Rogers, M. S. Andreaco, C. Moisan, and I. M. Thorson, "A 7–9 mev isotopic gamma-ray source for detector testing," *Nuclear Instruments and Methods in Physics Research Section A: Accelerators, Spectrometers, Detectors and Associated Equipment*, vol. 413, no. 2-3, pp. 249–254, 1998. https://www.sciencedirect.com/science/article/pii/S0168900298000977.

[95] https://www.nndc.bnl.gov/nudat2/decaysearchdirect.jsp?nuc=208TL&unc=nds.

[96] Z. Liu, J. Chen, P. Zhu, Y. Li, and G. Zhang, "The 4.438 mev gamma to neutron ratio for the am–be neutron source," *Applied Radiation and Isotopes*, vol. 65, no. 12, pp. 1318–1321, 2007. https://www.sciencedirect.com/science/article/pii/S0969804307001200.

[97] N. Kornilov, I. Fabry, S. Oberstedt, and F.-J. Hambsch, "Total characterization of neutron detectors with a 252cf source and a new light output determination," *Nuclear Instruments and Methods in Physics Research Section A: Accelerators, Spectrometers, Detectors and Associated Equipment*, vol. 599, no. 2-3, pp. 226–233, 2009. https://www.sciencedirect.com/science/article/pii/S0168900208015519.

[98] Z. Kis, B. Fazekas, J. Östör, Z. Révay, T. Belgya, G. Molnár, and L. Koltay, "Comparison of efficiency functions for ge gamma-ray detectors in a wide energy range," *Nuclear Instruments and Methods in Physics Research Section A: Accelerators, Spectrometers, Detectors and Associated Equipment*, vol. 418, no. 2-3, pp. 374–386, 1998. https://www.sciencedirect.com/science/article/pii/S0168900298007785.

[99] C. Gautherin, "Nuclear isomerism in fission fragments produced by the spontaneous fission of 252 cf," tech. rep., CEA Centre d'Etudes de Saclay, 1997. https://inis.iaea.org/search/search.aspx?orig_q=RN:31017434.

[100] P. C. Hansen, "Numerical tools for analysis and solution of fredholm integral equations of the first kind," *Inverse problems*, vol. 8, no. 6, p. 849, 1992. http://iopscience.iop.org/article/10.1088/0266-5611/8/6/005/meta.

[101] G. S. Brunson Jr, "Multiplicity and correlated energy of gamma rays emitted in the spontaneous fission of californium-252," tech. rep., Los Alamos National Lab., NM (USA), 1982. https://www.osti.gov/scitech/biblio/5187089.

[102] T. Materna, A. Letourneau, A. Marchix, O. Litaize, O. Sérot, W. Urban, A. Blanc, M. Jentschel, U. Köster, P. Mutti, *et al.*, "Study of fission fragment de-excitation by gamma-ray spectrometry with the ex-ill experiment," in *EPJ Web of Conferences*, vol. 146, p. 04041, EDP Sciences, 2017. https://epjwoc.epj.org/articles/epjconf/abs/2017/15/epjconf-nd2016_04041/epjconf
-nd2016_04041.html.

[103] H. Van der Ploeg, C. Laurens, J. Bacelar, A. Buda, J. Gaardhøje, G. van't Hof, N. Kalantar-Nayestanaki, A. van der Woude, and Z. Zelazny, "Study of the gamma emission probability accompanying the spontaneous fission of 252cf.," *Nuclear Physics A*, vol. 569, no. 1-2, pp. 83–91, 1994. https://www.sciencedirect.com/science/article/pii/0375947494900981.

[104] H. Makii, K. Nishio, K. Hirose, R. Orlandi, R. Léguillon, T. Ogawa, T. Soldner, F.-J. Hambsch, A. Astier, A. Pollitt, *et al.*, "Measurement of high-energy prompt gamma-rays from neutron induced fission of u-235," in *EPJ Web of Conferences*, vol. 146, p. 04036, EDP Sciences, 2017. https://epjwoc.epj.org/articles/epjconf/abs/2017/15/epjconf-nd2016_04036/epjconf
-nd2016_04036.html.

[105] B. A. Faddegon, I. Kawrakow, Y. Kubyshin, J. Perl, J. Sempau, and L. Urban, "The accuracy of egsnrc, geant4 and penelope monte carlo systems for the simula-

tion of electron scatter in external beam radiotherapy," *Physics in Medicine & Biology*, vol. 54, no. 20, p. 6151, 2009. http://iopscience.iop.org/article/10.1088/0031-9155/54/20/008/meta.

[106] S. Schmitt, "Tunfold, an algorithm for correcting migration effects in high energy physics," *Journal of Instrumentation*, vol. 7, no. 10, p. T10003, 2012. http://iopscience.iop.org/article/10.1088/1748-0221/7/10/T10003/meta.

[107] A. Hoecker and V. Kartvelishvili, "Svd approach to data unfolding," *arXiv preprint hep-ph/9509307*, 1995. https://arxiv.org/abs/hep-ph/9509307.

[108] A. László, "A linear iterative unfolding method," in *Journal of Physics: Conference Series*, vol. 368, p. 012043, IOP Publishing, 2012. http://iopscience.iop.org/article/10.1088/1742-6596/368/1/012043/meta.

[109] G. Zech, "Iterative unfolding with the richardson–lucy algorithm," *Nuclear Instruments and Methods in Physics Research Section A: Accelerators, Spectrometers, Detectors and Associated Equipment*, vol. 716, pp. 1–9, 2013. https://www.sciencedirect.com/science/article/pii/S0168900213003148.

[110] https://github.com/LiqiangQI
/LICORNE.git.

[111] A. Chyzh, C. Wu, E. Kwan, R. Henderson, J. Gostic, T. Bredeweg, R. Haight, A. Hayes-Sterbenz, M. Jandel, J. O'Donnell, *et al.*, "Evidence for the stochastic aspect of prompt γ emission in spontaneous fission," *Physical Review C*, vol. 85, no. 2, p. 021601, 2012. https://journals.aps.org/prc/abstract/10.1103/PhysRevC.85.021601.

[112] J.-M. Laborie, G. Belier, and J. Taieb, "Measurement of prompt fission γ-ray spectra in fast neutron-induced fission," *Physics Procedia*, vol. 31, pp. 13–20, 2012. https://www.sciencedirect.com/science/article/pii/S1875389212011893.

[113] V. Bunakov, I. Guseva, S. Kadmensky, and G. Petrov, "Angular anisotropy of neutrons evaporated from fission fragments," *BULLETIN-RUSSIAN ACADEMY OF SCIENCES PHYSICS C/C OF IZVESTIIA-ROSSIISKAIA AKADEMIIA NAUK SERIIA FIZICHESKAIA*, vol. 70, no. 11, p. 1853, 2006. https://www.researchgate.net/profile/I_Guseva/publication/288612955_Angular_anisotropy_of_neutrons_evaporated_from_fission_fragments/links/5687a06908ae19758398b204/Angular-anisotropy-of-neutrons-evaporated-from-fission-fragments.pdf.

[114] G. Audi and A. Wapstra, "The 1995 update to the atomic mass evaluation," *Nuclear Physics A*, vol. 595, no. 4, pp. 409–480, 1995. https://www.sciencedirect.com/science/article/pii/0375947495004459.

[115] JEFF-3.3 Nuclear Data Library ZA = 98252, MF = 5, MT = 18; 456; 456 (2017), https://www-nds.iaea.org/exfor/endf.htm.

[116] A. Hotzel, P. Thirolf, C. Ender, D. Schwalm, M. Mutterer, P. Singer, M. Klemens, J. Theobald, M. Hesse, F. Gönnenwein, *et al.*, "High-energy gamma-rays accompanying the spontaneous fission of 252 cf," *Zeitschrift für Physik A Hadrons and Nuclei*, vol. 356, no. 3, pp. 299–308, 1987. https://link.springer.com/article/10.1007/s002180050183.

[117] R. Vogt and J. Randrup, "Improved modeling of photon observables with the event-by-event fission model freya," *Physical Review C*, vol. 96, no. 6, p. 064620, 2017. https://journals.aps.org/prc/abstract/10.1103/PhysRevC.96.064620.

[118] T. Kawano, S. Chiba, and H. Koura, "Phenomenological nuclear level densities using the ktuy05 nuclear mass formula for applications off-stability," *Journal of nuclear science and technology*, vol. 43, no. 1, pp. 1–8, 2006. http://www.tandfonline.com/doi/abs/10.1080/18811248.2006.9711062.

[119] S. Mukhopadhyay, L. Danu, D. Biswas, A. Goswami, P. Prashanth, L. Kinage, A. Chatterjee, and R. Choudhury, "Prompt γ spectroscopic studies of fragment nuclei in thermal neutron induced fission of 235 u," *Physical Review C*, vol. 85, no. 6, p. 064321, 2012. https://journals.aps.org/prc/abstract/10.1103/PhysRevC.85.064321.

[120] N. Akimov, V. Vorob'eva, and V. Kabenin, "Effect of excitation energy on yields and kinetic energies of fragments at the fission of *sup*239 pu by neutrons.," tech. rep., and others), 1971. https://www.osti.gov/scitech/biblio/4043985.

[121] K. Nishio, Y. Nakagome, I. Kanno, and I. Kimura, "Measurement of fragment mass dependent kinetic energy and neutron multiplicity for thermal neutron induced fission of plutonium-239," *Journal of nuclear science and technology*, vol. 32, no. 5, pp. 404–414, 1995. http://www.tandfonline.com/doi/abs/10.1080/18811248.1995.9731725.

[122] D. Duke, F. Tovesson, A. Laptev, S. Mosby, F.-J. Hambsch, T. Bryś, and M. Vidali, "Fission-fragment properties in u 238 (n, f) between 1 and 30 mev," *Physical Review C*, vol. 94, no. 5, p. 054604, 2016. https://journals.aps.org/prc/abstract/10.1103/PhysRevC.94.054604.

[123] D. Madland, "Total prompt energy release in the neutron-induced fission of 235u, 238u, and 239pu," *Nuclear Physics A*, vol. 772, no. 3-4, pp. 113–137, 2006. https://www.sciencedirect.com/science/article/pii/S0375947406001503.

[124] P. Moller, J. Nix, W. Myers, and W. Swiatecki, "Nuclear ground-state masses and deformations," *Atomic data and nuclear data tables*, vol. 59, no. 2, pp. 185–381, 1995. https://www.sciencedirect.com/science/article/pii/S0092640X85710029.

[125] A. Oberstedt, R. Billnert, and S. Oberstedt, "Predictions of characteristics of prompt-fission γ-ray spectra from the n+ u 238 reaction up to e n= 20 mev," *Physical Review C*, vol. 96, no. 3, p. 034612, 2017. https://journals.aps.org/prc/abstract/10.1103/PhysRevC.96.034612.

université PARIS-SACLAY | ÉCOLE DOCTORALE PHENIICS

Titre : Étude des rayonnements gamma émis lors de la fission de ^{238}U et ^{239}Pu induite par neutrons rapides à l'aide de la source de neutrons LICORNE

Mots clés : fission, rayon gamma, source de neutrons

Résumé : Les spectres des rayons γ prompt de fission sont des données nucléaires importantes pour la physique des réacteurs, en tant qu'entrée pour les calculs de chauffage gamma, puisque l'effet de chauffage gamma peut être sous-estimé jusqu'à ~28% avec les données nucléaires actuelles. De plus, les nouvelles informations sur les rayons γ prompts de fission seront utiles du point de vue de la physique fondamentale, où les résultats peuvent être comparés à de nombreuses prédictions théoriques concurrentes pour affiner les modèles du processus de fission.

Les spectres des rayons γ prompts de fission ont été mesurés pour la fission induite par neutrons rapides de ^{238}U et de ^{239}Pu, en utilisant des neutrons rapides générés à partir de la source LICORNE. Le dispositif expérimental se composait d'une chambre d'ionisation et de différents types de détecteurs à scintillation, dont les détecteurs $LaBr_3$ et PARIS phoswich. Une procédure d'analyse, comprenant le unfolding et la simulation de la réponse aux rayons γ dans les détecteurs à scintillation, est mise au point pour extraire le spectre des rayons γ prompts de fission et les caractéristiques spectrales correspondantes.

Les résultats expérimentaux sont comparés aux codes de modélisation de fission GEF et FREYA. Cette comparaison révèle que les caractéristiques spectrales sont liées aux conditions énergétiques, aux rendements isotopiques et au moment angulaire des fragments de fission. La dépendance énergétique des caractéristiques spectrales montre que l'émission des rayons γ est tout à fait insensible à l'énergie neutronique incidente. Toutefois, on observe une forte dépendance à l'égard du système fissionnant particulier.

Title : Measurements of prompt gamma rays emitted in fission of ^{238}U and ^{239}Pu induced by fast neutrons from the LICORNE neutron source

Keywords : fission, gamma ray, neutron source

Abstract : Prompt fission γ-ray spectra are important nuclear data for reactor physics, as an input for gamma heating calculations, since the gamma heating effect can be under-estimated by up to ~28% with present nuclear data. Furthermore the new prompt fission γ-ray information will be useful from a fundamental physics point of view, where results can be compared with many competing theoretical predictions to refine models of fission process.

Prompt fission γ-ray spectra have been measured for the fast-neutron-induced fission of ^{238}U and ^{239}Pu, using fast neutrons generated from the LICORNE source. The experimental setup consisted of an ionization chamber and different types of scintillation detectors, including $LaBr_3$ and PARIS phoswich detectors. An analysis procedure, including unfolding and recovering the γ-ray response in the scintillation detectors, is developed to extract the prompt fission γ-ray spectrum and corresponding spectral characteristics.

The experimental results are compared to the fission modeling codes GEF and FREYA. This comparison reveals that the spectral characteristics are related to the energetic conditions, isotopic yields and angular momentum of the fission fragments. The energy dependence of the spectral characteristics shows that the prompt γ-rays emission is quite insensitive to the incident neutron energy. However, a strong dependence on the particular fissioning system is observed.

Université Paris-Saclay
Espace Technologique / Immeuble Discovery
Route de l'Orme aux Merisiers RD 128 / 91190 Saint-Aubin, France